



**Politecnico
di Torino**

Master's Degree Course in
Architecture for Sustainability
A.a. 2024/2025

3D digital documentation of the Pompeii archaeological site in Italy using geomatic surveying and analysis with applications of AI technique

- The submerged and underground environment in Regio II.

Relater
Antonia Teresa SPANO'
Co- Relater
Giacomo PATRUCCO

Candidate
Zhiguo WU

Index

1. INTRODUCTION.....	1
2. HISTORICAL FRAMEWORK: SUSTAINABILITY DEVELOPMENT IN POMPEII	3
2.1. HISTORICAL OUTLINE OF POMPEII	5
2.1.1. Pompeii: a living and prosperous city.....	6
2.1.2. Regio II: colorful civilian life.....	8
2.2. SUSTAINABILITY IN THE POMPEII	15
2.2.1. The Crisis of the Ancient City.....	16
2.2.2. Protective measures	17
2.2.3. Related work.....	18
3. PURPOSE OF THE THESIS AND METHODS OF ANALYSIS.....	12
3.1. GENERAL OBJECTIVES	21
3.1.1. Survey techniques: Geomatics applied to heritage.....	26
3.1.2. The GPS/GNSS system for the topographical survey	29
3.1.3. Photogrammetry	34
3.1.4. Lidar scanning.....	42
3.2. ANALYSIS ENVIRONMENT.....	48
3.2.1. The GIS environment.....	49
3.2.2. Machine learning system for Semantic Segmentation.....	52
4. MULTI-METHOD DOCUMENTATION: AMPHITHEATRE	55
4.1. 3D METRIC SURVEY OPERATIONS	57
4.1.1. The topographic survey related to the framing network.....	58
4.1.2. Aerial photogrammetric survey.....	60
4.1.3. Lidar scanner survey.....	61
4.1.4. SLAM survey	63
4.2. PROCESSING OF MULTI-DATA	65
4.2.1. Processing of LIDAR	66
4.2.2. Processing of Photogrammetry	69
4.2.3. Processing of SLAM data	72
4.2.4. Products merging and visualisation.....	73
5. MULTI-SCALE ELEMENTS DOCUMENTATION: RITI MAGICI.....	79
5.1. 3D METRIC SURVEY OPERATIONS	81
5.1.1. Topographic survey.....	82
5.1.2. Lidar scanner survey.....	84
5.1.3. Photogrammetric survey.....	85
5.2. PROCESSING OF MULTI-DATA	87
5.2.1. Processing of Lidar scans.....	88
5.2.2. Products visualisation.....	95
6. NON-VISIBLE INVESTIGATIONS: PRAEDIA OF IULIA FELIX	107
6.1. 3D METRIC SURVEY OPERATIONS	109
6.1.1. The topographic survey of the framing network	110
6.1.2. Aerial photogrammetric survey	112
6.2. PROCESSING OF PHOTOGRAMMETRY (VISIBLE DATASETS)	114
6.2.1. Processing of photogrammetric acquisitions (visible dataset)	115
6.2.2. Products visualisation (visible datasets)	119
7. ADVANCED ANALYSIS FOR MULTISPECTRAL DATA	127
7.1. ELECTROMAGNETIC RADIATION	129
7.1.1. Performance of objects under the electromagnetic radiation	130
7.1.2. Spectral signatures	132
7.1.3. Interpretation analysis	134
7.2. MULTISPECTRAL DATA PROCESSING.....	135
7.2.1. Processing of photogrammetric acquisitions.....	136
7.2.2. Product visualisation	139
7.3. ADVANCED MULTISPECTRAL ANALYSIS	141
7.3.1. Spectral indices	142
7.3.2. products visualisation with false colour.....	144
7.3.3. spectral anomalies detection from visual inspection	150
7.4. RESULTS OBTAINED AND COMPARATIVE ANALYSIS.....	154
7.4.1. Synthesis of comparison with geophysical survey.....	155
7.4.2. Synthesis of comparison with excavations.....	159
7.4.3. Summary of other significant anomalies	162
7.4.4. Discussion about the analysis	165
8. ENHANCEMENTS OF ANALYSIS FROM AI.....	167
8.1. AI SOLUTIONS FOR GEOMATICS RESEARCHERS.....	169
8.2. APPLICATION SCENARIOS	170
8.2.1. Block scale point cloud segmentation.....	171
8.2.2. Atypical architecture scale point cloud segmentation.....	174
8.2.3. Image segmentation on index maps.....	177
9. CONCLUSIONS.....	183
10. BIBLIOGRAPHY.....	185

1. Introduction

Archaeology is a discipline that was born out of interdisciplinary collaboration, with application of systematic excavation, observation, and documentation (Kristiansen, 2002). It is no coincidence that Remote Sensing technologies from airborne and space-borne sensors are widely used and well-documented in literature for the identification of new sites, the study of archaeological landscapes, and the monitoring of historical areas for their conservation (Tapete & Cigna, 2021) (Shin, 2023).

The development of new sensors and innovations in analysis techniques, combined with data fusion and the proven benefit of integrating multiple methods, can significantly enhance our knowledge of archaeological sites, enabling more accurate investigations. Apart from these, Artificial intelligence (AI) plays a growing role in Remote Sensing field, particularly Machine Learning algorithms, range from initial image processing to high-level data understanding and knowledge discovery (Zhang L. Z., 2022). These factors shape the futural directions of developing of strategies and methods in the field of remote sensing applied to archaeology.

As the Faro Convention emphasizes the value of cultural heritage and its potential as a resource for sustainable development, while seeking creative ways of developing and managing community heritage assets (Europe, 2005). It also focuses on promoting sustainability, access and the use of digital technology in the context of cultural heritage. So, more importance is attached on studying the advanced geomatic survey techniques promoted by AI undoubtedly.

Some of the most important archaeological remains in the world are founded underground due to various reasons (Baiocchi, 2020), like the succession of demolitions and reconstructions, or natural events. For example, *Pompeii*, as the well-known ancient city, had been completely covered by an eruption of Somma-Vesuvius in AD 79, covering with ash flow and surge deposits (Lirer, 2001). After excavating for centuries, on one hand, digital documentation is needed in *Pompeii* for the excavated remains during archaeological survey as the Faro Convention mentioned. And on the other hand, much of ancient Pompeii remains buried, and due to conservation and preservation issues, many ancient structures will probably remain unexcavated for the near future (Barone, Bellomo, Mattei, Lauro, & Pettinelli, 2011).

Therefore, the needs are aroused by these situations for revised techniques applying for non-invasive or micro-invasive surveys that enable a more precise documentation and its following element identification, which can push the survey to a more efficient way. As we know, traditional strategies usually need longer time, more cost and more labour.... But now, with the bases above, the innovation of strategies to

obtain the results with more accurate and informative information becomes reachable and workable.

The aim of this thesis is to discuss the enhancement of geomatics techniques for geomatic survey and analysis during digital archaeological documentation, especially the application in the submerged and underground environment. The main body of it presents the practical techniques, tools and disciplines related to Geomatics, such as Remote Sensing, Digital Photogrammetry and Geographic Information Systems (GIS), with the promoted analysis held manually based on different datasets and analysis aims. And then, in the following part, it steps into exploring how AI can integrate with those processes and analysis strategies, based on those different targets and datasets. Finally, it would finish with concluded comments about the advanced geomatics techniques, as well as suggestions for applying AI as interdisciplinary supporting tools in future.

2. Historical framework: sustainability development in Pompeii



2.1. Historical outline of Pompeii

Pompeii, a city that was preserved during unimaginable moments of destruction, is the impression that people usually have of it. However, based on in-depth archaeological research, this historic city has revealed its complex and multi-layered appearance. As the classicist Mary Beard said in her book, Pompeii is not just a Roman city frozen in time, but a more challenging and captivating place, with various traces of different histories (Beard, 2009).

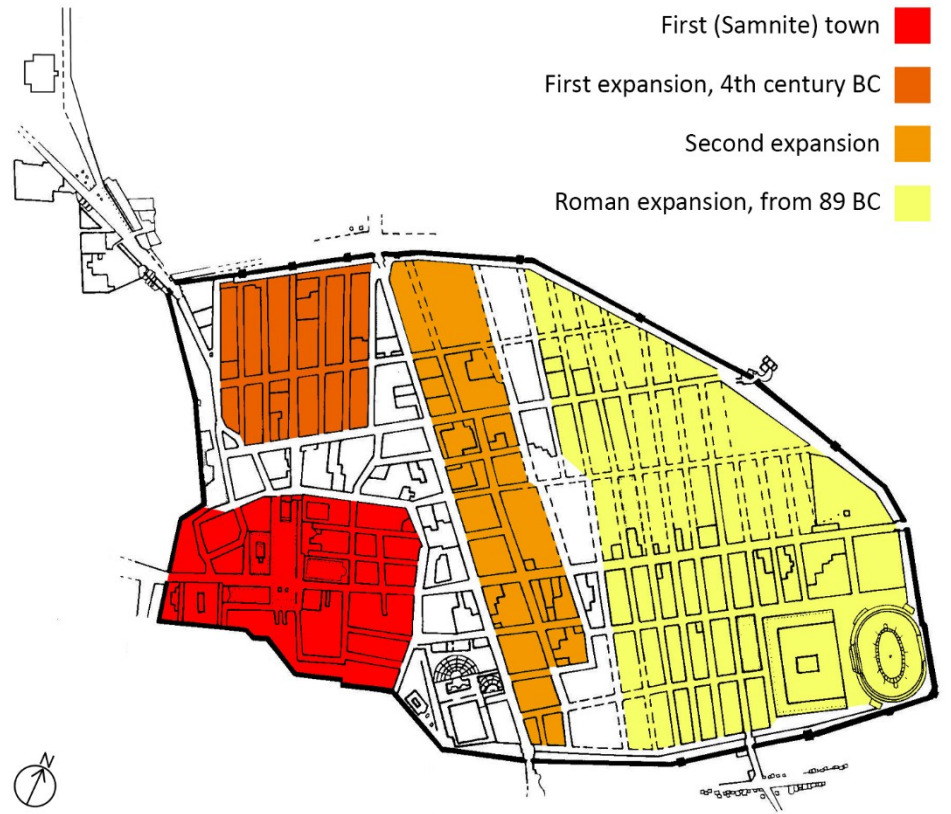
This paragraph is dedicated to telling the story of Pompeii and the vibrant lives of its citizens represented by the Regio II, although it is a division later made by researchers, through historical research and heritage interpretation. Obviously, such a short paragraph cannot fully describe the complex and diverse history of Pompeii, but it is hoped that the vivid life represented by the architectures mentioned in this thesis can truly connect modern people with this piece of heritage.

The first section would offer a historical background of Pompeii, emphasizing the general developing level of the city. And the second section will offer a small scale observation of citizens' public life based on the heritage in Regio II.

2.1.1. Pompeii: a living and prosperous city

As a city with a long history, the origin of Pompeii can be traced back to the 8th century BC, when the Oscans established five villages in the fertile Sarno Valley (De Vos & De Vos, 1982). And later in the 6th century BC, these villages merged as a single community, which was then encircled by a tufa city wall (Touring Club Italiano, 2008). During this period, the district had not only been influenced by the external culture and commerce of the surrounding areas, but its own wealth and importance had also fully grown, and even begun port construction and maritime trade (Etienne, 1992) (Zanker, 1993).

In the following 3 centuries, Pompeii underwent several power changes and eventually became a part of Rome. During this period, the city absorbed cultures from different regions and gradually developed and grew stronger. Especially after becoming a Roman colony, the fertile soil of the area, combined with the desirable location of the Bay of Naples became the main reason for the prosperity of this city (Roller, 2021). As a result, the wealth pushed the construction of numerous public works, including the Forum, the Large Theatre, the Basilica, and the renovations to the Temple of Jupiter and the Doric Temple (Torelli & Osanna, 2006).



◀ Figure 1 Settlement phases of Pompeii, modified from (Cyron,

The Romanization and prosperity of cities continued until a large-scale earthquake occurred in 62 AD (Wellesley College, 2017). This highly vibrant city had begun to undergo restoration and renewal: damaged

murals in private areas have been covered with new murals, while the planning of buildings and cities in public areas has changed, such as in the Roman Forum (Roller, 2021). Various signs indicate that the city was still thriving at the time, rather than struggling to recover from the earthquake.

This city was ultimately destroyed by a two-stage volcanic eruption in 79 AD: First, there was a pumice rain that lasted for about 18 hours but was escaped by most residents, and then a high-speed, dense, and scorching volcanic ash cloud formed by the volcano completely destroyed the entire city (Haraldur, Stanford, Cashdollar, & Stephen, 1982). Although there are numerous claims about the details of volcanic eruptions, it is widely accepted that the collapse is caused by volcanic eruptions.

2.1.2. Regio II: colorful civilian life

As destroyed, Pompeii was a wealthy town with a population estimated at 11,000 to 11,500 (Wilson, 2011). The city's prosperity was mainly built on a strong economy centered on agriculture and trade. The fertile volcanic soil and mild climate of the region allowed for the successful agriculture, making Pompeii a significant trading power in the Mediterranean, while the city's port guaranteed wealth, facilitating the export of goods like wine, oil, textiles, and cosmetics (Beard, 2009).

In Pompeii, it was a common scenery that citizens were found at the Forum, discussing the day's issues and conducting business (Beard, 2009), which is a strong evidence of the vibrant public life in that period. The extensive infrastructure, including aqueducts, water towers, and public fountains, provided piped water to homes, businesses, and public bathhouses (Notarian, 2023). For personal care, many people, including slaves, frequented the public bathhouses, which were cheap to use and served as a central hub for socializing, business, and exercise (Panella).



◀ Figure 2 Sports facilities and hot springs in Pompeii, modified from (Cyron, wikipedia: Pompeii, 2006)

The cases involved in this thesis are all located on the southeastern quadrant of Pompeii, which belong to Regio II according to the widely accepted modern research zoning. It is particularly notable for its concentration of significant public structures and large private estates. These include the Amphitheatre, the Complesso dei Riti Magici, and the

Praedia di Iulia Felix, which collectively offer invaluable insights into the diverse social, economic, and religious life of Pompeii. While a comprehensive general description of all characteristics of Regio II is not explicitly detailed in all available documentation, the presence of these prominent features underscores its critical importance in understanding the city's public entertainment, unique religious practices, and adaptive domestic economies.

The Amphitheatre

The Amphitheatre of Pompeii, strategically positioned in the southeastern quadrant of the ancient city near the Sarno Gate, holds the remarkable distinction of being the oldest surviving permanent stone amphitheatre in the Roman world. It was built over a century earlier than the iconic Colosseum in Rome (Pompei Online, 2025).

Built between 80 and 70 BCE, the amphitheatre was a key element in the city's Romanization. Its construction was financed by the private funds of two local magistrates, Quintus Valgus and Marcus Porcius, who also oversaw the adjacent palaestra (Beard, 2009). An inscription explicitly states their motivation: "to demonstrate the honour of the colony," (Wilkinson, 2019) highlighting the structure's importance in asserting Roman identity and influence within the newly Romanized city.



► Figure 3 View from the top passway of the Amphitheatre

Architecturally, the amphitheatre is an elliptical, entirely free-standing structure, built using the *opus incertum* technique with readily available local materials such as Sarno limestone and volcanic tufa (the Editors of the Madain Project, 2025). Unlike many Greek theaters or earlier Roman amphitheatres that utilized natural slopes for support, it used an innovative system of embankments and vaulted substructures to support its tiers of seating (the Editors of the Madain Project, 2025). Its main

function was to host gladiatorial games and other public spectacles, with an impressive capacity for approximately 20,000 spectators (Wilkinson, 2019), drawing audiences not only from Pompeii but also from surrounding areas.

The amphitheater's seating was arranged as expression of Rome's rigid social hierarchy. The structure was divided into three distinct sections, or *cavea*, each designated for a specific social class (Pompei Online, 2025):

- *Ima Cavea*: the lower section, was reserved for patricians and other upper-class citizens, providing them with the closest and most privileged view;
- *Media Cavea*: the middle section, was for the middle-class citizens;
- *Summa Cavea*: the top section, was designed for the poorest people, along with slaves and women.



◄ Figure 4 Fresco depicting the riot between Pompeians and Nucerians during a gladiatorial show in the Pompeii amphitheater, leading to many deaths and injuries, and the closing of the amphitheater, photo by Chappsnet

While primarily known for its blood sports, the Amphitheatre was a multifaceted venue that served as a central hub for community gatherings for hosting theatrical performances, ceremonies, political speeches, and athletic games (Seepompeii, 2025). This open accessibility, coupled with its central location in the southeastern suburbs of the city, undoubtedly became a shared experience for citizens to participate in reflecting the core values and culture of the Roman Empire.

Complesso dei Riti Magici

One of the most mysterious and compelling structure in Pompeii, is the complesso dei Riti Magici, a site appears different from the typical Roman *domus*. Its name, which translates to "Complex of Magical Rites," is derived from the unique and puzzling artifacts discovered within its walls, including bronze hands decorated with symbols and iron reproductions of snakes (Olivito & Anguissola, 2023).

The recent archaeological activities have refreshed people's understanding of this architectural complex. It has been confirmed to have been the site of a mysterious cult specifically that of the eastern god Sabazios (Berndt, 2018). Archaeological excavations have discovered a small but significant number of carbonized plant remains, including pomegranates and hazelnuts, indicating the existence of a sacrificial ceremony held in memory of this deity at that time (Olivito & Anguissola, 2023). This discovery provides a tangible connection to a specific religious ritual.



► Figure 5 A magical hand in bronze depicting the god Sabatius, Photo by Stilearte.

The complex's architecture offers a powerful corroboration of its function as a site for secret religious practice. Its peculiar layout, with large open courtyards and a series of small, isolated rooms, makes it difficult to identify as a simple domestic residence (Università di Pisa, 2023). This can be regarded as a sign of religious fusion in the Roman world. The presence of a private, non-traditional cult site alongside the public, state-sanctioned worship of deities like Venus and Hercules demonstrates that Pompeian society was home to a vibrant, diverse, and often hidden religious landscape (Agostinacchio, 2021). The Complesso dei Riti Magici is not merely a building but a testament to how eastern cults spread and

found a place in the Roman Empire, flourishing in private spaces and offering their followers unique spiritual experiences.



◄ Figure 6 View from the courtyard of the Complesso dei Riti Magici

Praedia di Iulia Felix

The Praedia di Iulia Felix, stands as a monumental residential-commercial complex that uniquely occupies a entirety *insula* in Pompeii. Its scale is particularly noteworthy, , covering a total surface area of approximately 5800 square meters (Lundgren, 2023).

The architectural design of the Praedia di Iulia Felix is a blend of indoor and outdoor spaces, centered around atria and courtyards, complemented by enclosed gardens and a private water supply (Drummond, 1993). Approximately one-third of the sprawling property was dedicated to the main house and its associated buildings, while the larger remaining area was utilized as an extensive vegetable garden (the Editors of the Madain Project, 2025).

It was originally a private residence and was first inhabited in the 2nd century BC (Archaeological Park of Pompeii). However, its most significant transformation was personally planned by Iulia Felix in the mid-1st century BC, ultimately turning into a revenue generating property (Dobbins & Foss, 2007). This business transformation was a direct

response to the devastating earthquake of 62 AD. The earthquake severely damaged the infrastructure of Pompeii, causing many public baths to be in disrepair or under construction (Archaeological Park of Pompeii). Iulia Felix cleverly exploited the urban crisis and market gap by transforming her luxurious private bathhouse into a public facility, thereby earning a considerable income. Further demonstrating her business view, she also rented out



► Figure 7 Garden with large pools surrounded by a colonnade of the Praedia di Iulia Felix (Archaeological Park of Pompeii)

The magnificent constructions and high-quality decorations found throughout the *praedia* clearly indicate that it was designed to attract and cater to "richer and higher status customers" (the Editors of the Madain Project, 2025). Iulia Felix's strategic actions, which was reflected by this heritage, leverage private wealth to address public needs and capitalise on commercial opportunities. It also provided valuable evidence for understanding the vibrant economic landscape of Pompeii. Furthermore, her social role as a landlord, entrepreneur, and public benefactor, as highlighted by her property's transformation, challenged traditional view of women's societal limitations in Roman society (D'Ambra, 2012), showcasing the significant opportunities and agency available to women of means. Despite its commercial function, Iulia Felix kept a portion of the house for her personal use, preserving a private area in her public project (Archaeological Park of Pompeii).



◄ Figure 8 Interior view of the praedia di Iulia Felix (Archaeological Park of Pompeii)

The architectural layout of the Praedia Di Iulia Felix, combined with its business functions, showcases a unique and innovative urban model. It blended the private and public space, transforming a private residence into a complex, multi-functional urban hub. Apart from the property of the space, the decisions hidden behind this are also of great social significance: this indicates that for cities after earthquakes, the citizens at that time also played a crucial role in the functional restoration after the disaster

2.2. Sustainability in the Pompeii

As a vibrant city that seems to have been alive yesterday, Pompeii is undoubtedly one of the most important legacies for us, supporting our understanding of past life, cities, and society. The only archaeological site in the world that fully displays the appearance of an ancient Roman city is actually facing the problem of how to protect and excavate it.

In this paragraph, Pompeii will be presented as the heritage which we need to stay with, instead of the ancient city belonging to the ancient people. And it will be divided into 3 sections:

The crisis that Pompeii has faced since its rediscovery, especially in contemporary times.

The protective measures taken by people in response to the Pompeii crisis include contributions made by geomatics.

Finally, the studies focusing on the cases in this thesis, or related works, will connect this background to the studies of this thesis.

2.2.1. The Crisis of the Ancient City

It is said that Pompeii has died twice: the first is a sudden death caused by the eruption in the history; and the second is a slow death since it began to be uncovered in the 18th century. Whether it's natural elements, damage caused by early excavators, or countless tourists every year, they have all contributed to the disintegration of this city. This is why this despairing process continues to occur.

Taking Amphitheatre as an example, like all other sites in Pompeii, it mainly faces the impacts of weathering, erosion, and increasingly severe climate change (Costanza, 2024). Prolonged drought periods stress ancient buildings, while heavy rainfall exacerbates damage to foundations and walls, leading to erosion and structural instability (Archaeological Park of Pompeii, 2021). Strong winds and storms also become a threat, potentially causing buildings to collapse and artifacts to erode.

Also the initial haphazard excavations further compromised the structural integrity of them, leaving vulnerabilities to the elements (Costanza, 2024). Meanwhile, the effect of this haphazard excavation appeared on another typical example, the Praedia di Iulia Felix. Early, inexperienced excavation practices, which often involved cutting out fragments without proper protective materials, brought another kind of damage to the painting areas (De Caro, 2015).

Overall, the crisis faced by Pompeii came from various aspects, and due to its enormous scale, its maintenance and preservation became extremely difficult. Therefore, the recording and archiving of heritage, such as murals, becomes as important as the protection and reinforcement of the heritage itself.

2.2.2. Protective measures

To deal with these threats, the Archaeological Park of Pompeii has adopted a complex, interdisciplinary approach to preservation. Key initiatives include the Great Pompeii Project (GPP) and the Pompeii Sustainable Preservation Project (PSPP) (Pompeii, 2025) (Mazzaglia, 2021). The GPP, launched in 2012 with €105 million in funding from the European Union and Italy, is a major program focused on comprehensive requalification of the site, with primary goals to reduce hydro-geological risk, secure unexcavated embankments, and consolidate and restore masonry and decorated surfaces (Pompeii, 2025). The PSPP, also launched in 2012, is a long-term, privately funded project dedicated to developing sustainable conservation strategies and promoting preventive maintenance across the site (Mazzaglia, 2021).

These projects became part of a broader "Sustainable Management Model" that prioritizes the careful allocation of resources and proactive maintenance to address the constant (Mazzaglia, 2021), slow decay caused by regular weather changes, as well as to mitigate the impact of extreme weather events (Archaeological Park of Pompeii, 2021). This modern approach is highly scientific and technologically advanced. For example, archeological studies of the mosaics in the Praedia di Iulia Felix have provided crucial guidance for restoration by identifying the local provenance of most materials and ensuring that new interventions are compatible with the original work (De Francesco, et al., 2025).

Based on these frameworks, some summer school activities have also become part of the restoration and protection work (Mazzaglia, 2021), such as the DIRECT team that completed all surveying projects for this thesis. In particular, the digital representation of three-dimensional physical space combines descriptive data of physical and spatial attributes (Mazzaglia, 2021), helping to preserve information that is difficult to archive in traditional surveying, and can be integrated into GIS platforms to facilitate information analysis and generation processes, as well as the sharing of acquired knowledge. And GIS platforms have indeed played a positive role in recent years when parks and civil engineering professionals use drones and real-time sensors to monitor climate change and predict the damage caused by such phenomena (Archaeological Park of Pompeii, 2021).

2.2.3. Related work

The PRAEDIA project, formally known as the Pompeian Residential Architecture: Environmental, Digital, Interdisciplinary Archive, was launched in 2016 with the clear goal of enhancing understanding of housing in Pompeii (Praedia Project, 2025). The original name of this project expressed its methodological concept of helping to understand the housing of Pompeii through interdisciplinary research on the crucial area of the Regio II ancient city structure (Archaeological Park of Pompeii, 2025). It highlights the necessity of integrating expertise from a broad range of fields, including archaeology, geophysics, geology, and material sciences, to construct a holistic narrative. This structured innovated approach is different from traditional archaeological methods, favoring a collaborative model for inquiry.

It officially began in 2016, with its initial focus squarely on the *Praedia Iulia Felix* (Archaeological Park of Pompeii, 2025). The investigations at this site laid the groundwork for the project's methodologies and initial findings. Following this phase, research was extended in Summer 2022 to include the "Complesso dei Riti Magici," also located within Regio II (Praedia Project, 2025).

A central component of the PRAEDIA project's investigation into the *Praedia Iuliae Felicis* was a geophysical survey of the complex's *hortus* (Redazione Web of University of Pisa, 2022). This non-invasive investigation was conducted in November 2016 and April 2018 and the researchers applied an integrated geophysical approach, combining Ground Probing Radar (GPR), Magnetometry, and Frequency Domain Electromagnetic Method (FDEM) (Urbini, et al., 2021).

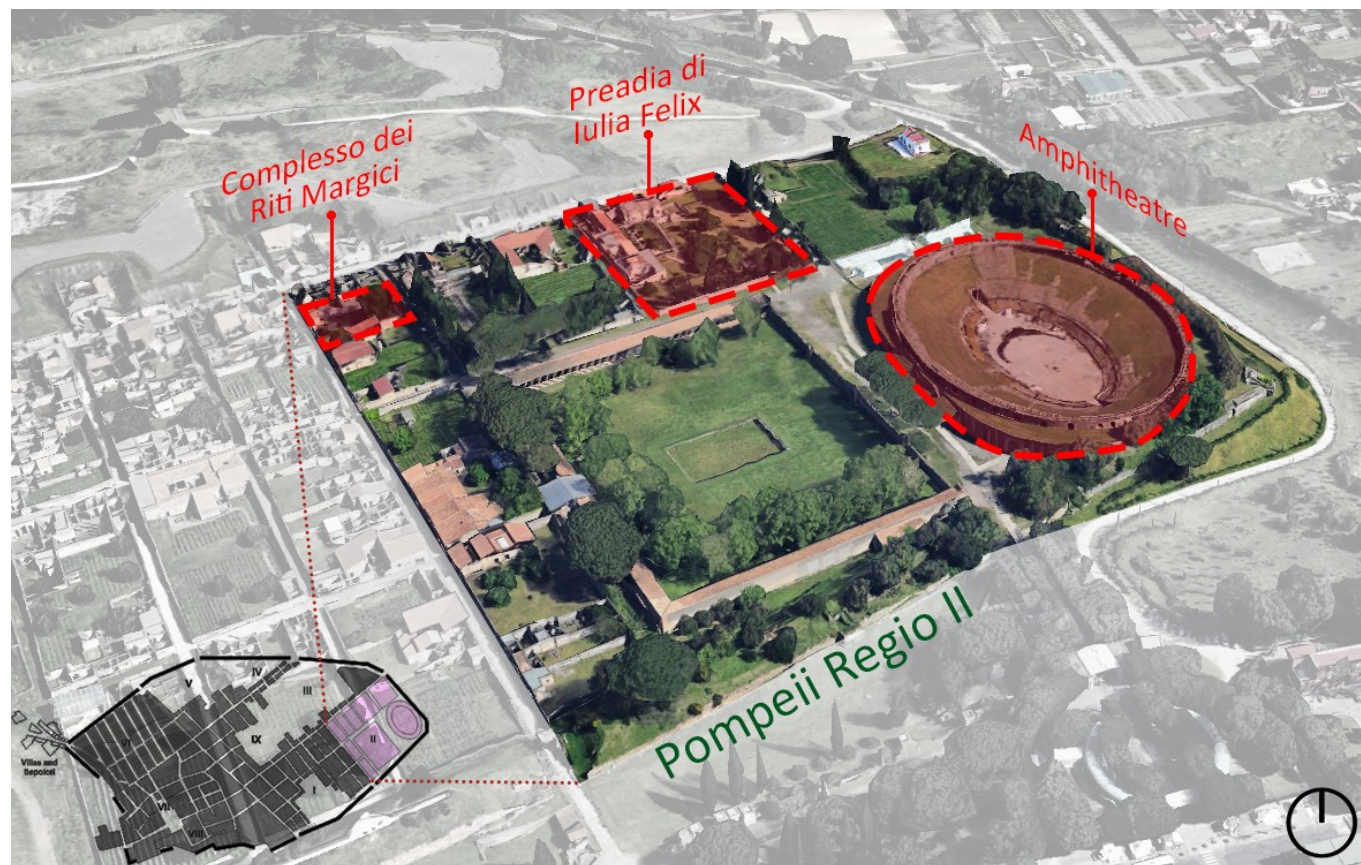
The application of geomatics within the PRAEDIA project is comprehensive. It begins with the initial data acquisition, such as LiDar acquisition of buildings and structures (Praedia Project, 2025), and also works with the geophysical datas—GPR, Magnetometry, and FDEM—to have other advanced analysis based on GIS. The data and the analysis are not the end in themselves; instead, will be a crucial component of a larger digital ecosystem serving the studies.

3. Purpose of the thesis and methods of analysis



3.1. General objectives

Based on the main objective and the history framework stated in the last two chapter, the idea of this thesis is to explore different submerged upstanding structures and underground environments with a group of analysis based on different datasets acquired in Pompeii *Regio II*, for exploring the advanced geomatics methods and possibility of AI supporting. The chosen cases are the Amphitheatre, *Complesso dei Riti Margici* and *Praedia di Iulia Felix*, which were surveyed by DIRECT student team in 2023 and 2024 with the support of the Laboratory of Geomatics for Cultural Heritage (G4CH Lab). Much experience and knowledge about the cases were developed during being a member of the DIRECT in 2024 and would be present in this thesis. From the advanced analysis held in those cases parallelly, comparative consideration about developing geomatic strategies will come out naturally during these survey and analysis processing. Also, the application of AI as an aid in geomatic survey and analysis can be explored as widely as possible.



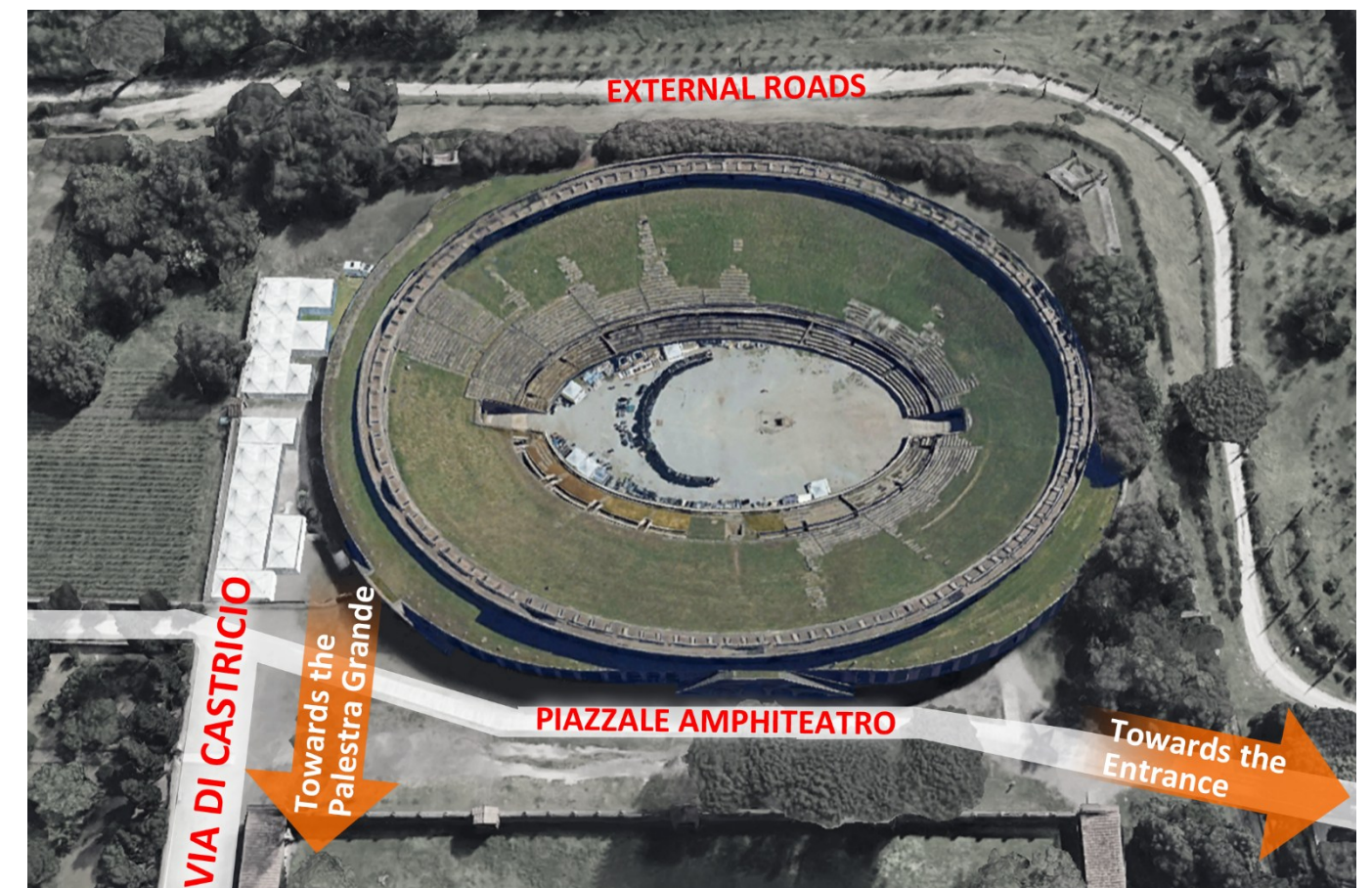
▲ Figure 9 Bird view of the cases in Regio II

Chapter 2 aims to introduce the historical frame work of the area related to this thesis, ranging from the ancient city Pompeii, Regio II and the 3 case building, for having a view of the culture heritage. Meanwhile, the related study works are also introduced as well as the sustainable development there.

As the base of the following application cases, Chapter 3 is structured to provide the principle of the survey and analysis, which are used in this thesis, as well as all the instruments and the analysis environments. But operations of the survey or analysis are not mentioned in this chapter.

In the following four chapters, the research cases are presented parallelly from site survey and data processing to documentation, and finished with analysis and brief comments for each of those 3 cases. In this phase, the detailed process and the problems appeared in the survey are stated, which will connect with the next step. More detailed, the cases are:

Chapter 4 introduces Amphitheatre, which is near *Praedia di Iulia Felix* built around 70 BC as one of the earliest Roman amphitheatres built of stone (Bomgardner, 2021). An integrated survey using rapid mapping methods with multiple data sources was applied there, which involves Mobile Mapping System (MMS), Terrestrial Laser Scanner (TLS) and UAV system. The typical architecture construction and the complex interior underground environments usually appearing with amphitheatres, will be documented under a detailed architectural scale. With the survey, an architectural analysis focusing on the space can be developed as well.



Chapter 5 concentrates on the case of *Complesso dei Riti Margici*, which is located on the northwestern corner of the Regio II and regarded as the

▲ Figure 10 photo of Amphitheatre, marks on the excavated area

place to hold magic ceremony, with its special space different from other houses in *Pompeii*. And the application case is also an integrated 3d documentation, but focus on the areas underground of this complex domus and special construction pattern, using TLS and close-range photogrammetry. During the work, the possibility of merging point clouds from different datasets could be explored in this chapter, aimed at uniformed documentation on an architectural scale. In addition to obtaining updated and more detailed, the texture and construction analysis of the excavated area in different positions also has the aim of obtaining information that, compared with each other and theoretical data, allowed us to develop an inference of the construction time scenario.



▲ Figure 11 photo of the insula the complesso dei Riti Margici located in, marks on the excavated area

Another case study is presented in chapter 6, which is *Praedia di Iulia Felix*, located near the vital area used for public entertainment including the Amphitheatre and the *Palestra Grande*, as the case of photogrammetry based on UAV systems in both the visible and non-visible ranges of the electromagnetic spectrum. In this case, the target is exploring non-visible investigation in archaeological sites through testing multispectral UAV photogrammetry. During this case, survey about photogrammetry focusing the remains submerged is presented with the anomalies appeared in the result comparison. And the comparison is held between

not only data with different spectrums but also data acquired from different time in the same day.



▲ Figure 12 photo of Praedia di Iulia Felix, marks on the survey interesting

Subsequently, chapter 7 presents the geomatics elaborations which plans to verify the use of the results of the multi-spectral photogrammetry from UAV, with the help of the Vegetation Indices and Soil Index calculated with relevant spectrums. In this chapter, the principle of spectrum selection and calculation is explained as well as the analysis verification based on those analysis held in GIS environment. In addition to obtaining detailed verified results through the non-invasive and non-destructive methods coherent with the intrinsic fragility of cultural heritage (CH), a sustainable efficient strategy to support archaeological investigations while defining excavation areas' perimeters can be defined with multiple result overlapped.

A final level of study, based on the practical cases above, machine learning, as the AI tool, is introduced in chapter 8 using in 3 different application scenarios, as well as, leading to different analysis targets: The first application series is 3D segmentation of point cloud is applied on the case of the Amphitheatre, which is supported by the open- source software. With the segmentation, surely the space analysis could be easily worked out, but in this case, the capability of segmentation for atypical architectural space will be tested. Similar to this application, the case of

Complesso dei Riti Margici would use the segmentation tool based on AI, which is equipped on the commercial software, to segment the point cloud with a block scale. machine learning on texture recognition of the excavated area. Apart from these, 2D segmentation of the abstract images that is the index maps calculated in the case of *Praedia di Iulia Felix*. The foreseeable result is that this method will greatly save the time consumed by repetitive work.

Finally, after the application of these promoting techniques to those cases, more specifically, the cases in the submerged and underground environment in Pompeii, the conclusion can be developed with the capability of presenting different application cases. Also, the difficulties and limitations during the work will be discussed as well as the future development prospects.

3.1.1. Survey techniques: Geomatics applied to heritage

The application of advanced geomatic techniques on heritage is becoming increasingly widespread to cope with the issues of documentation in past decades (Fritsch, 2018) (Hassani, 2015). And nowadays, geomatic research have become the powerful tool due to the development of innovation in survey techniques and digital data management, which can support the managing functions of diverse sectors authorities and corporations that need to control and use the geographically referenced information (Spanò & Sammartano, 2014).

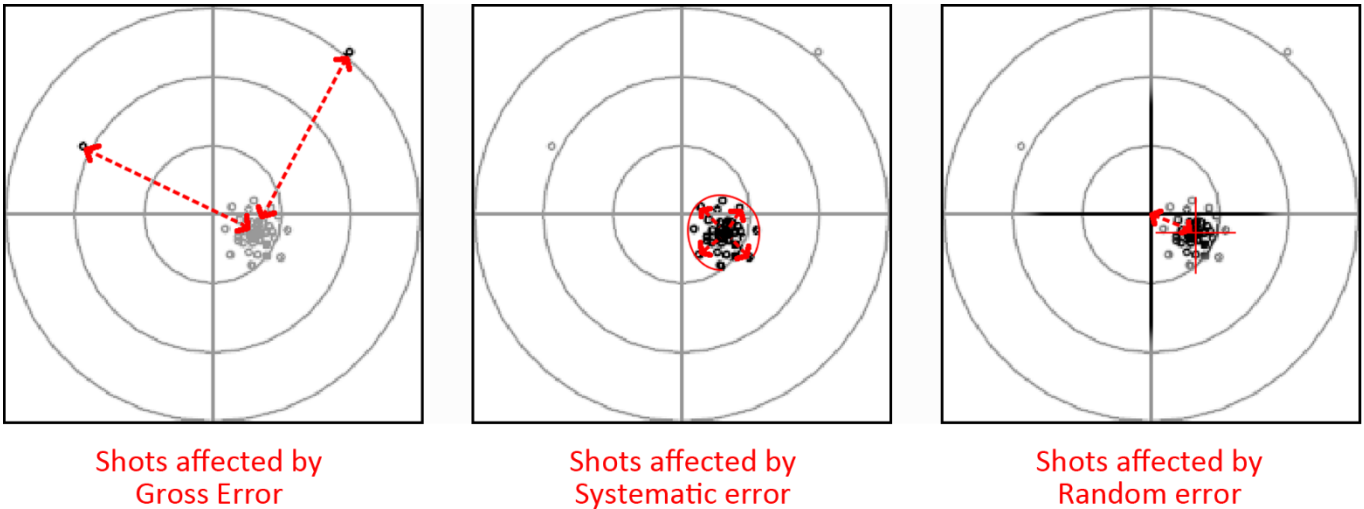
As the definition of the discipline of geomatics itself states, geomatics is a comprehensive discipline that brings together various disciplines, techniques and tools to "acquire, recover, analyse and manage metric or thematic data related to the Earth's surface or part of it, including urban environment, infrastructure and built heritage, which are determined by their spatial location and limited by the accuracy of the survey" (ISO/TR-19122, 2004). This thesis focuses on the application of geomatics to different submerged upstanding structures and underground environments in CH and emphasises its potential in multidisciplinary interactive work. In particular, the sub-disciplines such as land surveying, remote sensing (RS), cartography, GIS, global navigation satellite systems, photogrammetry, play important roles in this research.

During geomatic surveys, due to the complex and ever-changing field conditions and different surveying and mapping requirements, such as precision, pre-survey planning has become an essential step in the geomatic survey process. It includes a preliminary understanding of the object to be measured, the type of data expected to be obtained, the selection of the applied technology and the formulation of the surveying and mapping strategy. For example, for a photogrammetry survey based on UAV platforms, the parameters should be considered are: the scale of the survey, which determines the UAV category used in this survey; the average size of the pixel on the ground, allowing us to estimate the accuracy and the level of detail, which influence the flight planning greatly; accuracy demand, which determines the georeferencing strategies in this survey. (Spano, 2019) With the well-preparing survey plan, the survey can be hold with proper techniques, high efficiency, and great accuracy.

The data acquired during geomatic surveys, including coordinates, shape and geometry, and attributes, which refers to information that directly or indirectly linked to a specific geographic location on Earth, can be called spatial data. (Lee, 2021) It is most commonly processed and analysed by

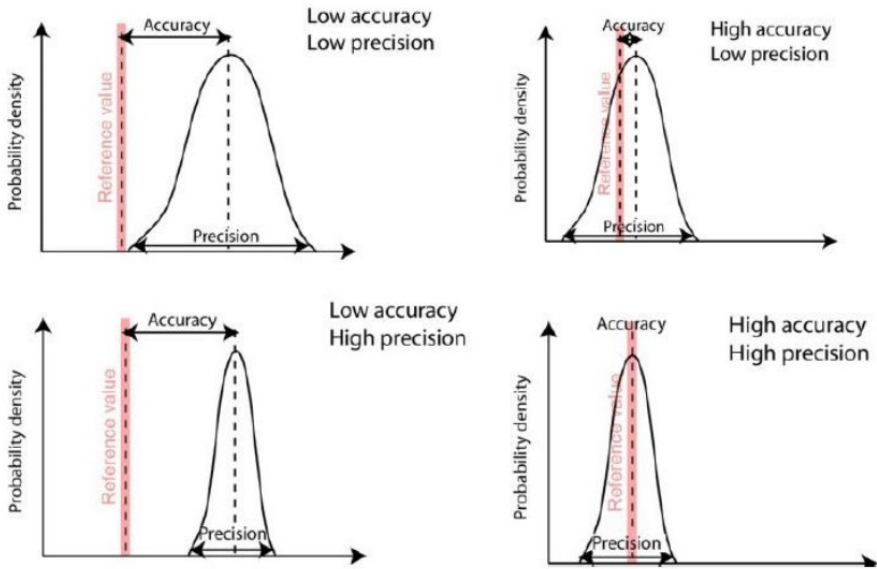
geographical information systems (GISes) to enable users in a wide range of fields of application to understand geographic context, patterns and relationships for further analysis, communications and decision-making. (Awati, Zola, & Fontecchio, 2024) As the base of analysis, the data is never exact and will always contain errors, no matter how carefully made, observed, or measured. (Spano, 2024) And the difference between the reality and the data is error, it can be propagated through computing by using the measurement with errors. Generally, due to the sources, errors can be classified into 3 types: natural errors, instrumental errors and personal errors. But according to the diverse nature, the total error can be formed by three different kinds:

- Gross errors (or mistakes): Errors tend to occur through carelessness, can be eliminated. (Suraci & de Oliveira, 2019)
- Systematic errors (or biases): Errors caused by the system, including surveying equipment, observation methods, and certain environmental factors, is difficult to be detected but can be corrected. (Spano, 2024) (The U.S. Geological Survey, 2024)
- Random errors: Errors caused by factors beyond the control of the observer, obey the laws of probability, and are even called accidental errors. (Spano, 2024)



▲ Figure 13 Schemes of different errors, modified from (Spano, 2024)

To understand the behaviour of survey result, accuracy and precision can be the parameter to evaluate the general situation. Accuracy is the closeness of an estimated value (for example, measured or computed) to the standard or accepted (true) value of a particular quantity, which commonly described by Root Mean Square or the Root Mean Square Error (RMSE). (Spano, 2024) Precision (connected with repeatability of measures) is the closeness with which measurements agree with each other, which can be presented as the standard deviation. (ASPRS, 2015)

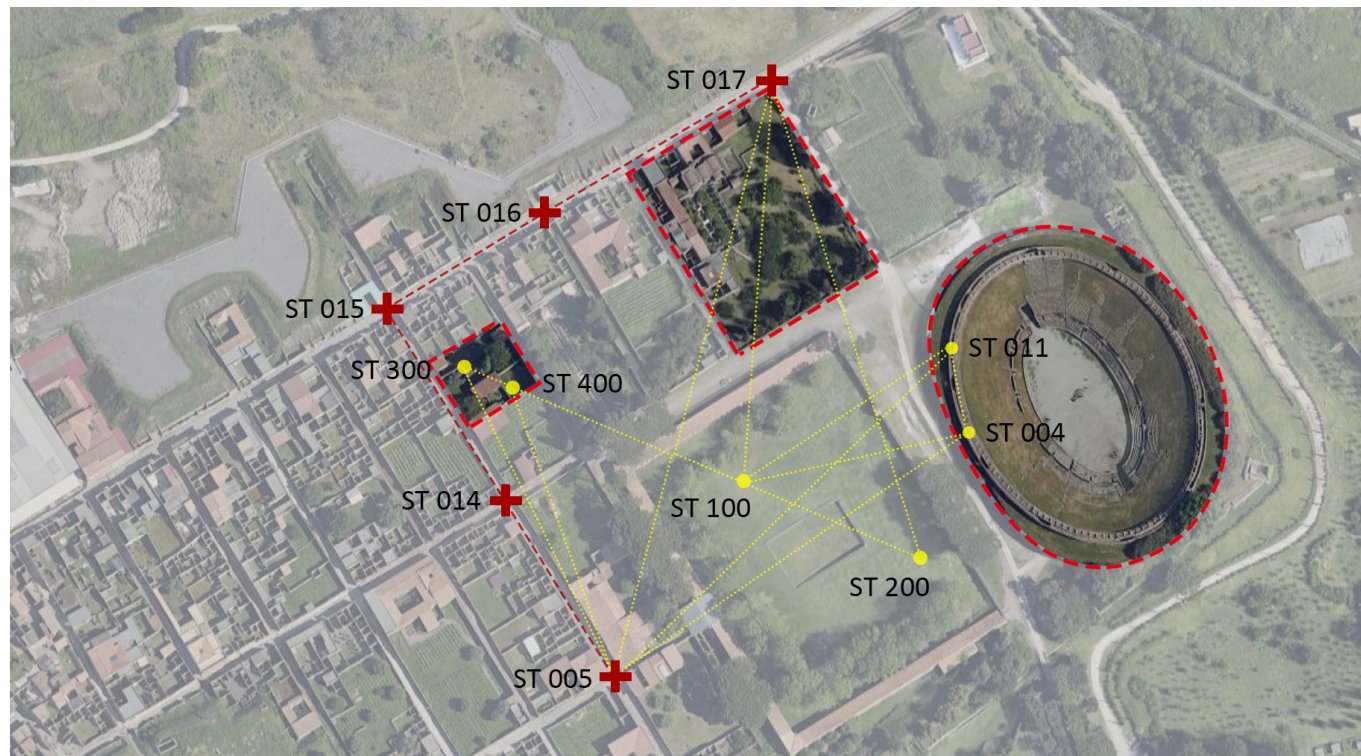


◀ Figure 14 Accuracy and precision (ASPRS, 2015)

3.1.2. The GPS/GNSS system for the topographical survey

As a subdiscipline of Geomatics, Topography is a combination of methods and instruments to comprehensively measure and represent details of the Earth's surface, including Planimetry, Altimetry, Tachymetry and Land surveying (Gomarasca, 2009). Operations called “topographical survey” is required for capturing the accurate location and characteristics of natural and man-made elements within a given region of land (Okwuenu, Igbokwe, & Anyadiiegwu, 2024), including site data acquisition, data processing and graphic restitution.

Topographical survey is deeply involved in detailed geomatics 3D survey using photogrammetry or laser scanning, as the measurements of topographic control network. In geomatics, a topographic control network is a system of established points with longitude, latitude and altitude, providing a reference framework to ensure accuracy and consistency in mapping and other spatial data. Furthermore, it plays an important role in the geomatics survey integrating multiple data sets.



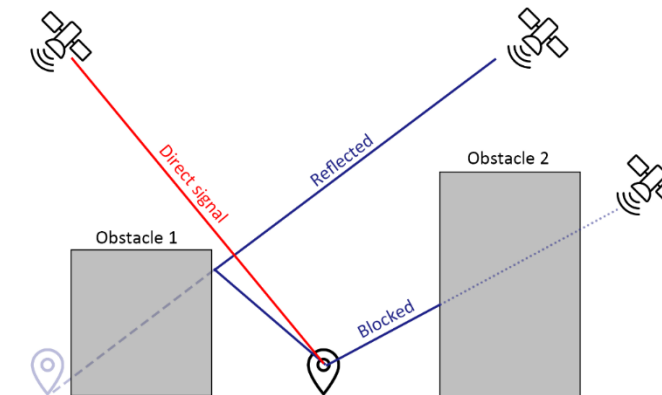
▲ Figure 15 Topographic control network of the case in Regio II

The instruments applied for the cases in this thesis include the most common techniques in this process: Global Navigation Satellite System (GNSS), Total Station and Real-time Kinematic (RTK).

GNSS

GNSS is a satellite navigation system using satellites to provide autonomous geo-positioning, which determines devices' location to high

precision using time signals transmitted along a line of sight by radio from satellites (Wikipedia: Satellite navigation, 2025). In essence, the measurements are taken by a GNSS receiver through measuring the transmitting time of GNSS signals emitted from 4 or more GNSS satellites, which are used to obtain its coordinates and reception time (Enge & Misra, 2006). However, to maintain the measure process, the constant communication with 4 or more satellites is mandatory, which is difficult to be kept in some complex environments or weather conditions. Based on this reason, to acquire high quality measurements, the collaboration with traditional systems relying on total stations can be considered.



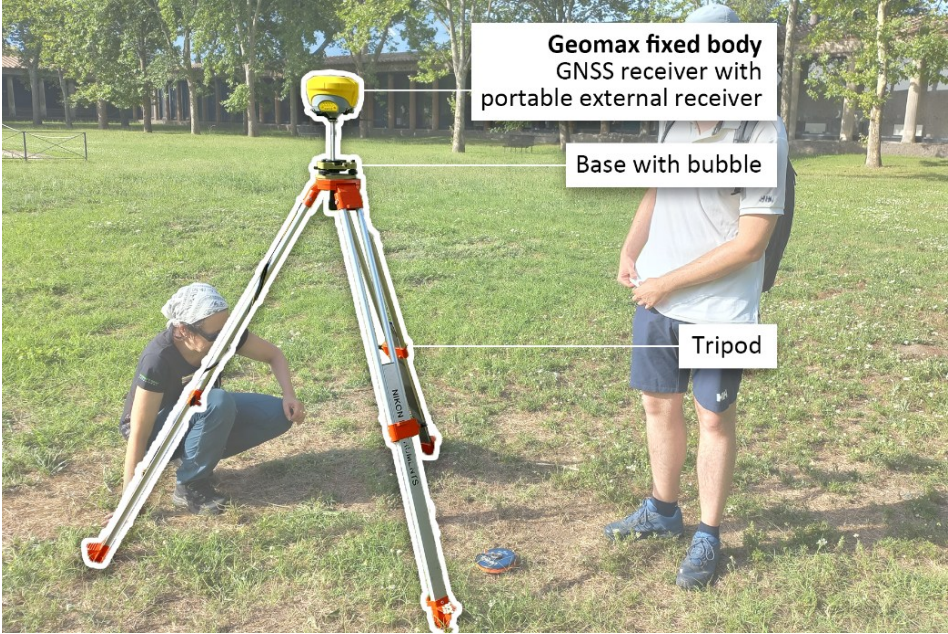
◀ Figure 16 Different working case of GNSS receiver

The global GNSS system currently includes the following satellite constellations:

- NAVSTAR GPS (NAVigation Satellite with Timing and Ranging Global Positioning System) built and managed by the US Department of Defence;
- GLONASS (GLObalnaya NAVigatsionnaya Sputnkikovaya Sistema) of the Russian Aerospace Defence Forces;
- GALILEO, the European positioning system;
- Chinese BeiDou or BDS (BeiDou Navigation Satellite System), the Chinese positioning system. (Kaplan & Hegarty, 2017)

In the cases of this thesis, the system applied is Global Positioning System (GPS). It now includes 31 active satellites that are approximately uniformly dispersed around six circular orbits with five or more satellites in each, which are inclined at an angle of 55° relative to the equator and are separated from each other by multiples of 60°. (Grewal, 2011) Theoretically, three or more GPS satellites will always be visible from most points on the earth's surface. But several factors can cause signal interference in GPS surveying, such as physical obstructions or reflections of Buildings nearby or trees, or bad atmosphere conditions with rain, fog or snow. (Global GPS Systems , 2023) Therefore, to achieve a higher quality measurement, the vertices of topographic control network should be measured in the open areas and clean atmosphere conditions.

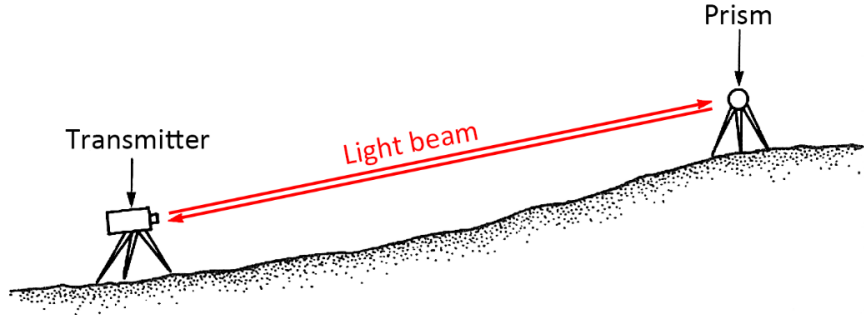
The reference system used is World Geodetic System84 (WGS84) with Universal Transverse of Mercator (UTM) cartographic projection, adopted as the world standard. From this comes the name of the reference system applied and cited in each map of this thesis WGS84 / UTM 33N where “33N” refers to the time zone in which the area under examination is located.



► Figure 17 GNSS receiver working in the site, with components annotated

Total Station

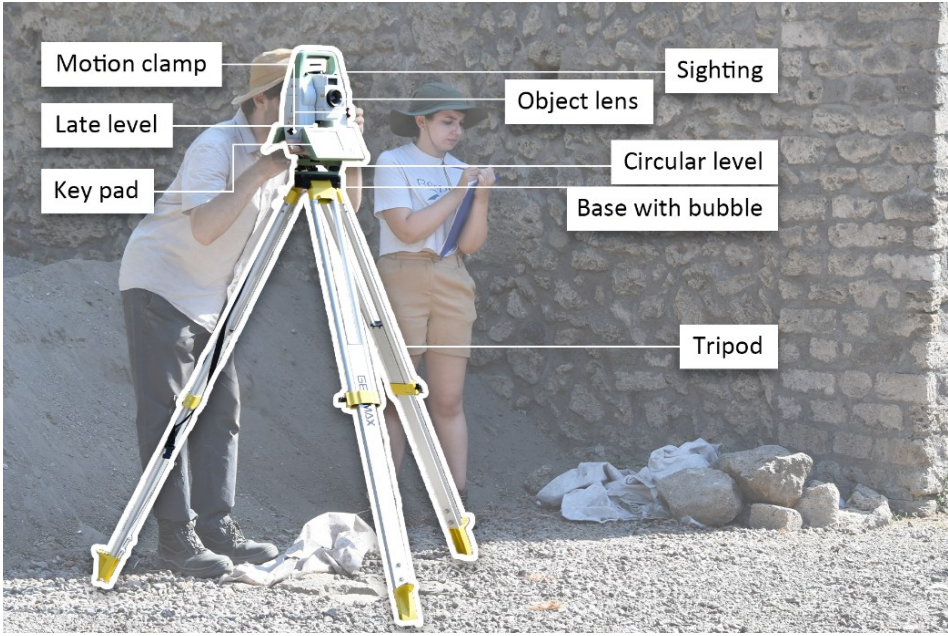
Total Station is a form of an electronic theodolite combined with an electronic distance measuring device (EDM), which mostly use a modulated near infrared light emitting diode which sends a beam from the instrument to a prism and the prism reflects this beam back to the instrument. (Okwuenu, Igbokwe, & Anyadiiegwu, 2024) Modern total stations are equipped with advanced electronic systems capable of precise angle and distance measurements, aided by computer technology, not only process and store data in real-time but can also transmit data directly to remote systems via wireless communication, significantly improving work efficiency and measurement accuracy. (Kang, 2024)



► Figure 18 Scheme of total station's working principle

In the cases of this thesis, to deal with the gap of data acquisition by GNSS Receivers, the total station survey can offer a solution with less error

produced and less time consumed than GNSS solution with low quality surveying.



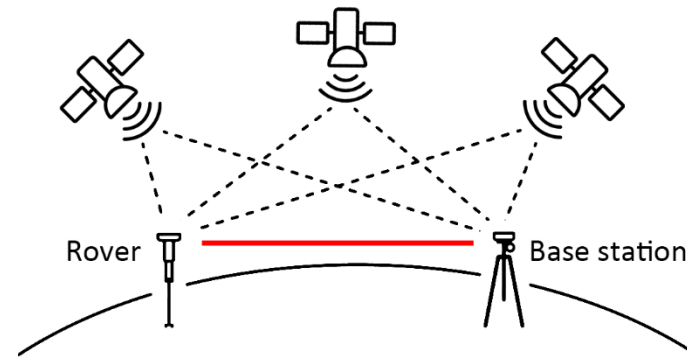
◄ Figure 19 Total station working in the site, with components annotated

RTK

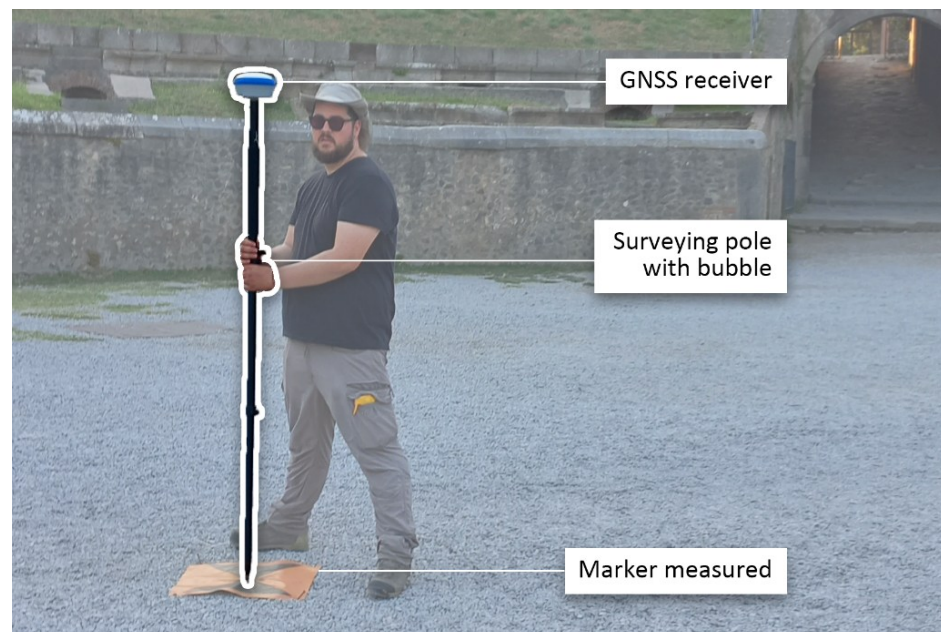
Post-processing kinematics is positioning process in which signals received from a mobile receiving device store location data can be adjusted using corrections from a reference station after data has been collected. (PIRTI, 2021) High production measurement and less surveying limitation than static observations can be provided as another substitute solution of topographic survey through measurement sessions lasting a few minutes.

RTK systems use a single base-station receiver and a number of mobile units: the base station re-broadcasts the phase of the carrier that it observes, and the mobile units compare their own phase measurements with the one received from the base station. (Riedorf, Daub, & Loef, 2006) These techniques are finding considerable diffusion due to the development of networks of GNSS stations, owned by public or commercial bodies, which allow obtaining differential measurements with the use of a single receiver, both in real time and in post-processing, in contact with the stations, thus allowing considerable savings in time and costs. (Teppati Losè, Chiabrando, & Giulio Tonolo, 2020) As regards, the availability of satellites guarantees a certain accuracy which supports the rapid measurement in the field.

► Figure 20 Scheme of RTK system working principle



Therefore, the measurement of GCPs, instead, took the use of the RTK techniques, with the use of two receivers: one on a fixed tripod positioned on a vertex with a known position and a mobile one, called a rover, mounted on a pole and transported to the various points to be surveyed by the operators of the various work groups.



► Figure 21 RTK rover working in the site, with components annotated

This technique is highly valuable and is currently widely applied in UAV photogrammetry. In this approach, the drone is equipped with a GNSS receiver, which allows for the accurate estimation of the projection centres of images captured during flight (Teppati Losè, Chiabrando, & Giulio Tonolo, 2020). This method, commonly referred to as direct photogrammetry, reduces the need for extensive ground control points and enhances the overall efficiency of data acquisition.

3.1.3. Photogrammetry

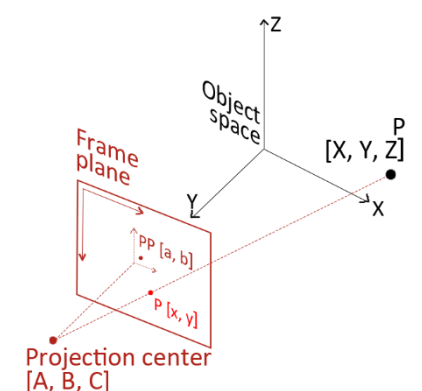
Photogrammetry is the art and science of determining the position and shape of objects from photographs (Kraus, 2007), with many successful and diverse applications can be found in a wide range of areas, like archaeology, architecture and geomatics (Alfonso, 2016)... In the field of geomatics, it's regarded as one of non-contact methods preferably used to map the landscape, providing a large amount of spatial data with high accuracy and detail, which capture parts, elements, and components. (Kovanič, et al., 2023) It's generally divided into two categories:

- Aerial photogrammetry: referring the recording of images of the ground from an elevated position, usually based on aircraft, Unmanned Aerial Vehicle (UAV) or other airborne platforms.
- Terrestrial photogrammetry: referring the recording of images acquired around an object, usually based on the cameras with a lesser distance to the object.

When it's applied for CH, time becomes the additional information out of the data itself: All the information can be recorded at a certain time, even the physical heritage is not available or still, the entire state is still kept in the document. Furthermore, comparing with the traditional methods like LIDAR scanning or satellite, high intensity data collection and flexibility allows users to define temporal and spatial resolution, with a lower cost and less labour. (Berra & Peppia, 2020) (Remondino, Barazzetti, Nex, Scaioni, & Sarazzi, UAV photogrammetry for mapping and 3D modeling: current status and future perspectives, 2011) A heritage study along the time scenario at any time interval can be held by means of comparing the survey results acquired efficiently. It can be illustrated deeper in the case studies of this thesis.

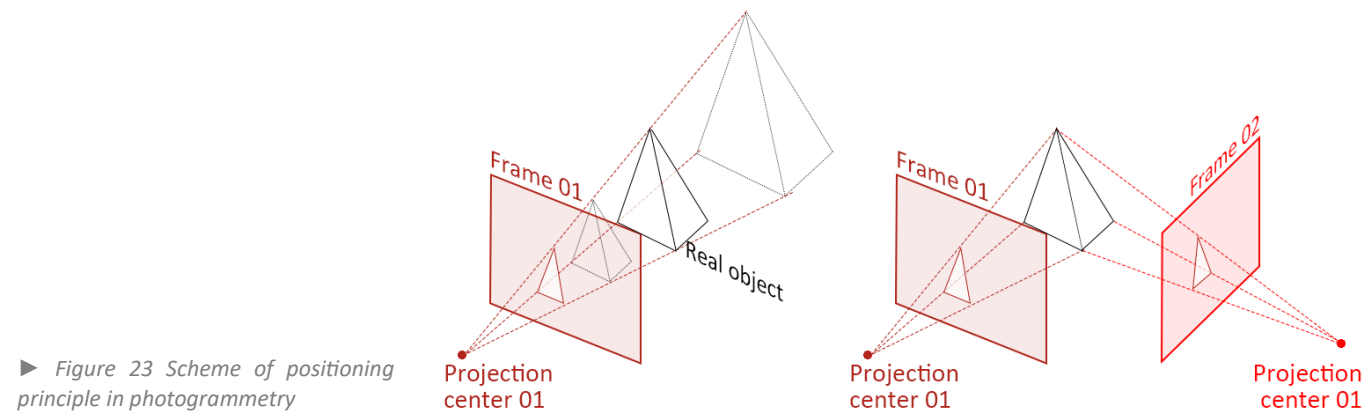
Principle of photogrammetry

To introduce the photogrammetry concepts, the explanation can be started with a single photo. Every photo can be regarded as a recording of the 3D object through similarity transformation of rotating, shifting and affine into 2D plane (Kraus, 2007). All the information is recorded according to this transformation into the planar coordinate system of the photo, which can be understood as a "central projection", as Figure 22 shown. Therefore, to obtain the information of the objects in photos, understanding the direction of the coordinate system, coordinates in the image coordinate system and the projection centre is necessary for the "reverse transformation".



▲ Figure 22 Relation between object space and Frame plane, modified from (Remondino, 2014)

But it's impossible to acquire more information like dimension by only one photo, since the certain position cannot be located on only one projection line (as Figure 23 shown). Instead, the intersection of the rays of the homologous points coming from the two frames, allows us to determine the position in space of the relative point through a mathematic way.



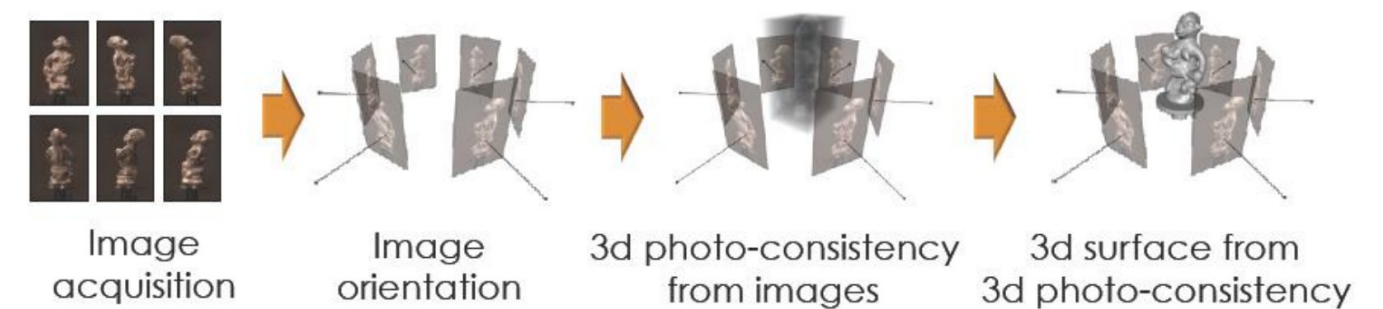
► Figure 23 Scheme of positioning principle in photogrammetry

Based on this principle, the concept of overlap becomes a fundamental element in the actual survey phase, which refers to that overlapping area between two frames, in which the homologous rays will define the coordinates of the common points. As a necessary and essential condition for photogrammetric surveying, the overlap must be around 60% or more. Also in the case of analytical surveying, to avoid that points remain visible in a single frame, reaching even 80-90% for current digital photogrammetry and increasing even more in cases of particular complexity of the analysed object.

After image acquisition, the next phase is orientating and placing, which involves interior relative orientation and absolute exterior orientation (Smith & Park, 2000). Interior orientation refers to the intrinsic properties of the camera and lens, while exterior orientation describes the camera's position and orientation in relation to the scene being photographed.

As regards, instead, the digital photogrammetry used in this thesis, its processing phase is entrusted to specific software that exploits the Structure From Motion (SFM) technology and the Image Matching algorithm using digital images (Spano, Sammartano, & Calantropio, 2019-2020). The orientation of interior and exterior can be hold simultaneously through SFM technology. The aforementioned technology allows to estimate the three-dimensional position of points represented in multiple images, reconstructing the geometry of the represented object (structure) and the position of the cameras (motion) even in the absence of a calibration of the cameras defined by the settings. (Lowe, 2004) It also implements the aforementioned internal and external orientation simultaneously and, in summary, can be schematized as follows:

1. collection of stereoscopic images with high overlap (80%-90%);
2. internal and external orientation of the images using the Image Matching algorithm as a starting point;
3. Estimation of the ability to recreate a dense point model starting from the images oriented in space;
4. Process of generating the dense cloud of points of the analysed object. (Spano, Sammartano, & Calantropio, 2019-2020)

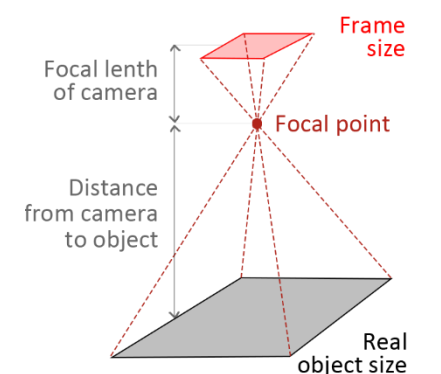


Having understand the basic principle, the workflow of photogrammetry can be summarized as:

1. Photography/Data Collection.
2. Data Processing/3D Model Development.
3. Further Improvement/Mesh Generation and Editing. (Rahaman, 2021)

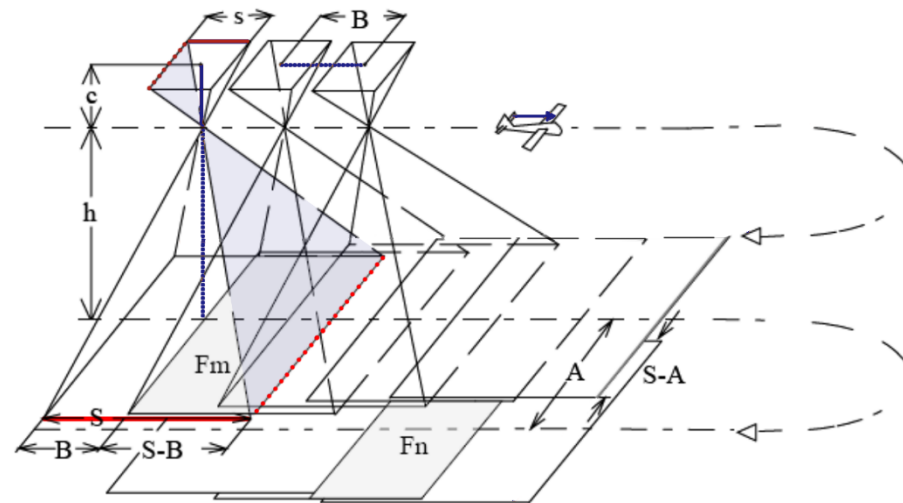
Photography actives as a base in photogrammetry, since the quality and number of photographs play a vital role in allowing the algorithm to process the surface, match points, and triangulate the visual features (Rahaman, 2021). Certainly, the more photos are captured, the greater chance of having an accurate model. (Rahaman, 2021) But considering the time and labour cost of the survey, it's necessary to hold a calculation to evaluate the density of the photography frames. During the photograph acquisition, the focal length and frame size is fixed, which let the calculation operatable to understand the overlap ratio of different frames and the scale of the object in each frame. As the frame shown, understanding the distance between the camera and the object, the scale of the object in a single frame can be discovered easily. According to this principle, this calculation also allows us to understand the ground width of a pixel in the photos, which represented as Ground Sampling Distance (GSD) in Aerial and terrestrial photogrammetry. One step more, the

▲ Figure 24 Scheme of Structure from Motion technology process (Spano, Sammartano, & Calantropio, 2019-2020) from (Remondio, 2014)



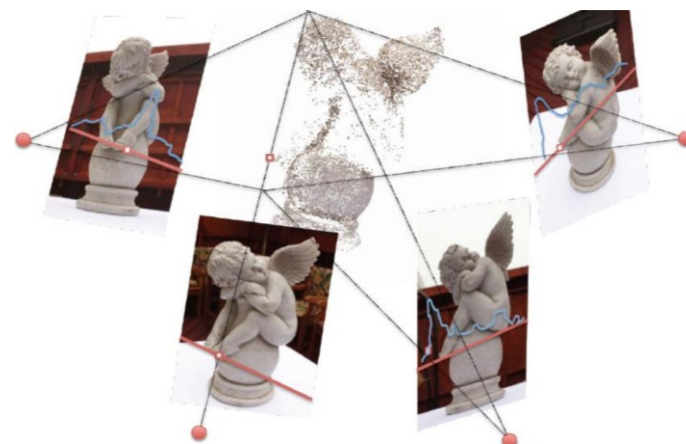
▲ Figure 25 Scheme of the relation between object & frame

distance between the positions where each frame is taken can be calculated for the survey plans, like the Figure 26 shows.



► Figure 26 Scheme of GSD in Aerial photogrammetry

During data processing, through recolonizing the relative positions among frames, the primary alignment of photos can be created, which leads to obtaining a 3D model of the object. But the model is in an arbitrary scale, with a generic spatial positioning free from the absolute reference system.



► Figure 27 Example of the rules of epipolar geometry in photogrammetry (Spano, Sammartano, & Calantropio, 2019-2020)

In the second phase of data processing, control points measured with Topographical methods can offer the correct geographical positions for the model and especially they enable to optimize the frames/images orientation in the space with high accuracy relating to the absolute reference system. Usually, the control points should be well-distributed on the object of interest to acquire the result with less errors.

Based on the 3D point cloud from data processing, further improvement allows us to create a series of metric products:

- digital surface model (including digital terrain model and digital elevation model)
- 3D mesh model

- orthophoto

UAV

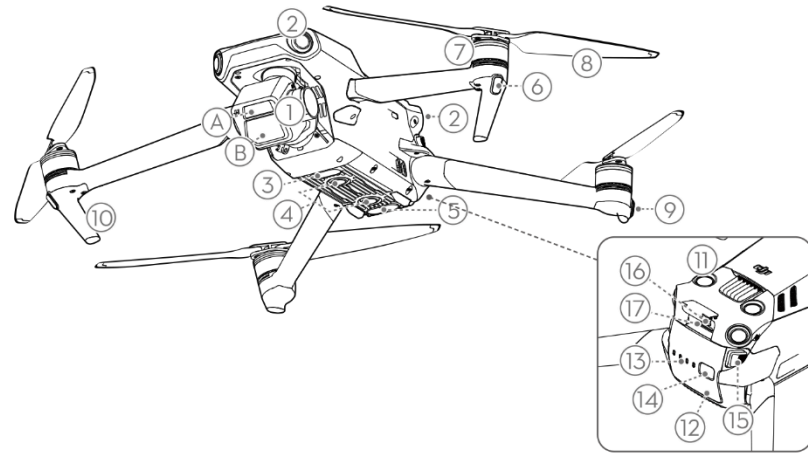
A new era of fine-scale RS has emerged with the arrival of light-weight consumer-grade UAVs (<10 kg). (Berni, Zarco-Tejada, Suarez, & Fereres, 2009) A UAV or unmanned aircraft system (UAS), widely known as a drone, is an aircraft with no human pilot, crew, or passengers onboard, but rather is controlled remotely or is autonomous. (Pan, Zahmatkesh, Rekabi-Bana, Arvin, & Hu, 2025) With the technology developed and lower cost, the use of UAVs had expanded to many applications, including aerial photography, area coverage, precision agriculture, forest fire monitoring, environmental monitoring, etc (Alvarado, 2021).

Combined with various sensors, UAVs have already become low-cost alternatives to the classical manned aerial photogrammetry, in the short-and close-range domain. (Remondino, Barazzetti, Nex, Scaioni, & Sarazzi, UAV photogrammetry for mapping and 3D modeling: current status and future perspectives, 2011) (Kovanič, et al., 2023) Comparing with satellite and aerial-based RS platforms, UAVs have three main advantages: high timeliness, flexibility and spatial resolution (Jiang, Jiang, & Wang, 2022). To be more specific, photogrammetry based on UAVs can perform surveys in a shorter time and a shorter time interval of target survey, which contributes to time-critical applications. Also, with the high flexibility of flight trajectories and view directions, it can bring data of complex target objects with higher resolution.

Classifications of UAVs become different according to different metrics, including aerodynamic layout, UAV weight, active radius, and flight height. (Jiang, Jiang, & Wang, 2022) Also, UAVs can be classified into 3 categories according to wings and rotors (Aptella Pty Ltd. , n.d.), which act differently and are suitable for various application scenarios:

- Fixed Wing Drones: greater covering distances, higher speed, longer flight time, energy efficient.
- Single Rotor Drones: good flying ability with heavy load.
- Multi-Rotor Drones – VTOL Helicopter UAVs: easier use, good availability, camera flexibility.

Multi-Rotor Drones are the UAV platform used in the cases of this thesis, carrying different sensors. Here are the parameters of the devices applied:

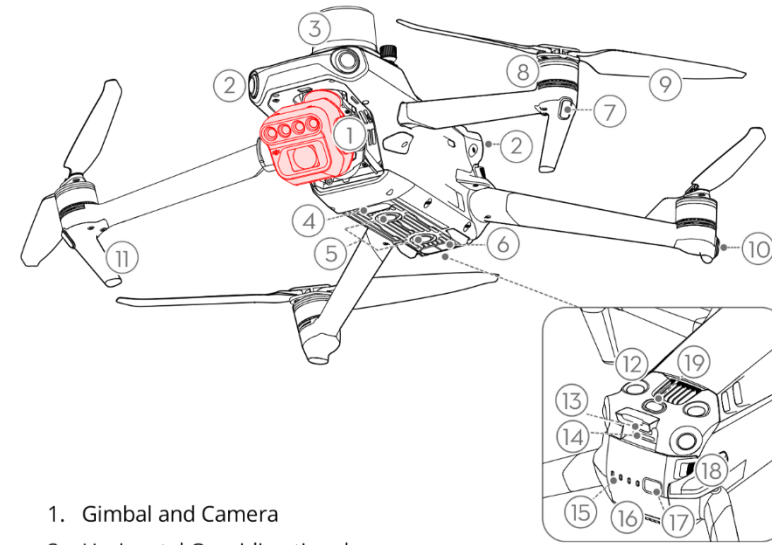


1. Gimbal and Camera
 - A. Tele Camera
 - B. Hasselblad L2D-20c Camera
2. Horizontal Omnidirectional Vision System
3. Auxiliary Bottom Light
4. Downward Vision System
5. Infrared Sensing System
6. Front LEDs
7. Motors
8. Propellers
9. Aircraft Status Indicators
10. Landing Gears (Built-in antennas)
11. Upward Vision System
12. Intelligent Flight Battery
13. Battery Level LEDs
14. Power Button
15. Battery Buckles
16. USB-C Port
17. microSD Card Slot

► Figure 29 Components of UAV system DJI Mavic 3

Aircraft	
Type	Multi-Rotor Drones
Maximum ascending speed	S Mode: 8 m/s; N Mode: 6 m/s
Maximum descent speed	6 m/s
Maximum speed	S Mode: 19 m/s; N Mode: 15 m/s
Max Flight Time (no wind)	46 mins
Flight autonomy	6,000 m
Operating temperature	-10° to 40° C
Camera	
Sensor	4/3 CMOS Effective Pixels: 20 MP
Lens	FOV: 84° Format Equivalent: 24 mm Aperture: f/2.8-f/11 Shooting Range: 1 m to ∞
Max Image Size	5280 × 3956
ISO Range	100-6400
Photo Format	JPEG/DNG (RAW)
Transmission	
Operating frequency	2.400-2.4835 GHz, 5.725-5.850 GHz
Max transmission distance	15 km (FCC), 8 km (CE/SRRC/MIC)

► Table 1 Basic parameters of UAV system DJI Mavic 3



1. Gimbal and Camera
2. Horizontal Omnidirectional Vision System
3. RTK Module (PSDK port)
4. Auxiliary Light
5. Downward Vision System
6. Infrared Sensing System
7. Front LEDs
8. Motors
9. Propellers
10. Aircraft Status Indicator
11. Landing Gears (Built-in antennas)
12. Upward Vision System
13. USB-C Port
14. Camera microSD Card Slot
15. Battery Level LEDs
16. Intelligent Flight Battery
17. Power Button
18. Battery Buckles
19. Spectral Sunlight Sensor

◀ Figure 28 Components of UAV system DJI Mavic 3

Aircraft	
Type	Multi-Rotor Drones
Maximum ascending speed	S Mode: 8 m/s; N Mode: 6 m/s
Maximum descent speed	6 m/s
Maximum speed	S Mode: 21 m/s; N Mode: 15 m/s
Max Flight Time (no wind)	43 mins
Flight autonomy	6,000 m
Operating temperature	-10° to 40° C
Camera	
Sensor	1/2.8" CMOS; Effective pixels: 5 MP
Lens	FOV: 73.91° Format Equivalent: 25 mm Aperture: f/2.0
Narrow Band Filter	Green (G): 560±16 nm, Red (R): 650±16 nm, Red edge (RE): 730±16 nm, Near-infrared (NIR): 860±26 nm
Image Size	2592×1944
Photo Format	JPEG/DNG (RAW)
Transmission	
Operating frequency	2.400-2.4835 GHz
Maximum transmission	15 km (FCC), 8 km (CE/SRRC/MIC)

◀ Table 2 Basic parameters of UAV system DJI Mavic 3M

Aerial photogrammetry based on UAVs follows the same basic principles and guidelines as introduced earlier, going through the same processes: photography, data processing and further improvement. In addition, a series of preventive measures should be taken through the image acquisition due to the operating characters of UAVs. During survey planning, the existing obstacles in the target area should be detected and avoided, as well as the weather condition like strong wind or rain. Meanwhile, the modes of flights should also be considered. Here are two flying modes of UAVs which can be applied during surveys:

- Manual Control: High flexibility, responding to irregular target areas or areas with unavoidable obstacles.
- Automatic Plan: Stable acquisition with less errors, responding to regular target areas without unavoidable obstacles.

In the case of this thesis, the flights were taken under a same automatic plan in both morning and afternoon in the same day, since there are no unavoidable obstacles in the flying altitude with the GSD demanded. Through this path, the cost of labour and time were reduced while more data related to a timescale can be collected.

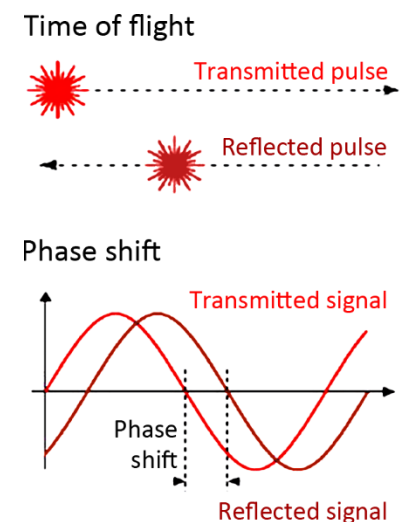
3.1.4. Lidar scanning

Lidar is an RS method implemented by using pulsed or modulated laser beams and laser detectors to determine precise distances to objects, which stands for “Light Detection and Ranging”. (Travis, 2019) (NOAA, 2024) This technique was derived from the 1960s, but was widely applied in the 1990s due to the introduction of direct geo-referencing and the general advancements in computer technology. (Shan & Toth, 2018) With the compacted dimension of the instrument, it can be regarded as a autonomic solution to acquire abundant data in a short time.

Basically, a lidar instrument consists of a laser, a scanner and a specialized GPS receiver, which records the reflected laser to measure the range combined with position and orientation data. (NOAA, 2024) The combination of orientation and distance is used to create a cloud of measured points located relative to the scanner. If the actual position and orientation of the scanner in real-world coordinates are known, these can be integrated with the scanner-relative measurements to produce a point cloud in real-world coordinates. (Harrap & Lato, 2010) The point clouds can be used to generate other geospatial products, such as DSM, building models, and contours.

The classifications of scanning systems are various. According to the scale and ranging, the scanning systems can be divided roughly as: long-range 3D laser scanning and short-range 3D laser scanning. There are two different types of scanners that are commonly used in long-range 3D laser scanning, referring to different working principles (Joncic & Jan, 2017) (Armesto-González, Riveiro-Rodríguez, González-Aguilera, & Rivas-Brea, 2010):

- Time of Flight (TOF) measurement: by sending a laser pulse of light and then measuring the time it takes to travel from the scanner to the object and back, allowing the scanner to calculate the distance. (Armesto-González, Riveiro-Rodríguez, González-Aguilera, & Rivas-Brea, 2010)
- Phase Shift (PS) method: by sending out a continuous laser beam with a modulated signal embedded in the laser and comparing the phase of the signal at the source with the phase of the laser light once it has travelled to the object and reflected to the scanner; the change of phase of the laser light is measured and this allows the scanner to calculate the distance. (Armesto-González, Riveiro-Rodríguez, González-Aguilera, & Rivas-Brea, 2010)



▲ Figure 30 Scheme of both working principle of LiDAR scanning (Wang, Tan, & Mei, 2020)

While long-range laser scanners are usually based on TOF technology, systems designed for short-range scanners, which appear as portable/handheld devices (Remondino, Barazzetti, Nex, Scaioni, & Sarazzi, 2011), often use the triangulation principle (Joncic & Jan, 2017). Triangulation systems is based on the laser or light emitted and returned to a specific location on a CCD array of an inboard camera. (Liebe & Coste, 2013) They typically have an operating range from 0.5 metres to few metres and can collect data with the micron-level accuracy. (Joncic & Jan, 2017)

For LiDAR, there are two types of accuracy specifications: relative LiDAR accuracy and absolute LiDAR accuracy (Njambi, 2021). Relative LiDAR accuracy refers to the internal quality of LiDAR elevation data without using surveyed ground control points. (Kim, Jason, Jeffrey, Jeffrey, & Seonkyung, 2022) It is concerned with how well points or features in the LiDAR data relate to each other, which can be promoted, in some cases, by a higher point density acquired. Absolute LiDAR accuracy refers to both the horizontal and vertical accuracy of LiDAR data by comparing the LiDAR data with ground surveyed checkpoints. (Kim, Jason, Jeffrey, Jeffrey, & Seonkyung, 2022) A high absolute accuracy often requires validation against GCPs or established reference datasets. (Elaksher, Ali, & Alharthy, 2023)

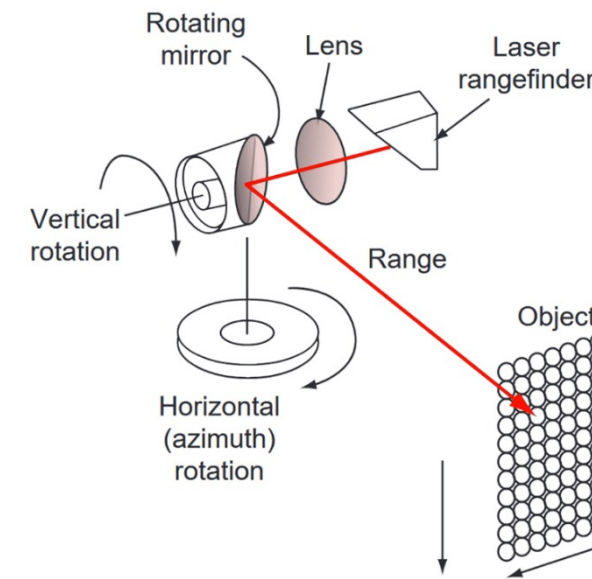
Terrestrial Laser Scanning (TLS)

Terrestrial Laser Scanning (TLS) is formally defined as a ground-based, active ranging method that rapidly acquires accurate, dense 3D point clouds of object surfaces through laser range finding. (Arianna, Teza, & Bonali, 2011) TLS is, in its essence, an improved version of the laser tachometric measurement toolkit (the so-called total station) that is based on the combination of distances and angles measured from a fixed point. (Petrie & Toth, 2009)

The operational mechanism of TLS involves the emission of laser beams towards target surfaces or areas surrounding the scanner. The system measures the target surfaces or areas through the simultaneous measurement of slant range by a laser rangefinder and the two associated angles by angular encoders in the horizontal and vertical planes passing through the centre of the instrument. (Petrie & Toth, 2009)

This synchronized measurement process results in the generation of millions of individual 3D points, collectively forming a "point cloud", with each point defined by its precise x, y, z Cartesian coordinates. (the U.S. National Science Foundation, n.d.) Most TLS are long-range devices used for 3D documentation of large landscape areas or complex structures.

To construct a complete 3D model through a survey based on TLS, multiple such range maps must be acquired from various perspectives to cover the entire object's surface. (Guidi, 2014) This process uses sets of dense point cloud acquired in each scan. Transforming this raw data into a final 3D model involves a structured workflow, supported by various specialized software.



◀ Figure 31 Scheme of the laser range and rotation when TLS working, modified from (Petrie & Toth, 2009)

Same as other geomatics surveys, the initial and crucial step is planning, where the ultimate purpose of the digital model dictates the required accuracy and resolution, directly impacting project budget and complexity. This phase also involves analysing the object's size, material, and shape.

While the acquisition of individual point clouds following the planning, the key considerations during this stage include optimal sensor positioning, which may require scaffolding or mobile platforms for large or fixed objects.

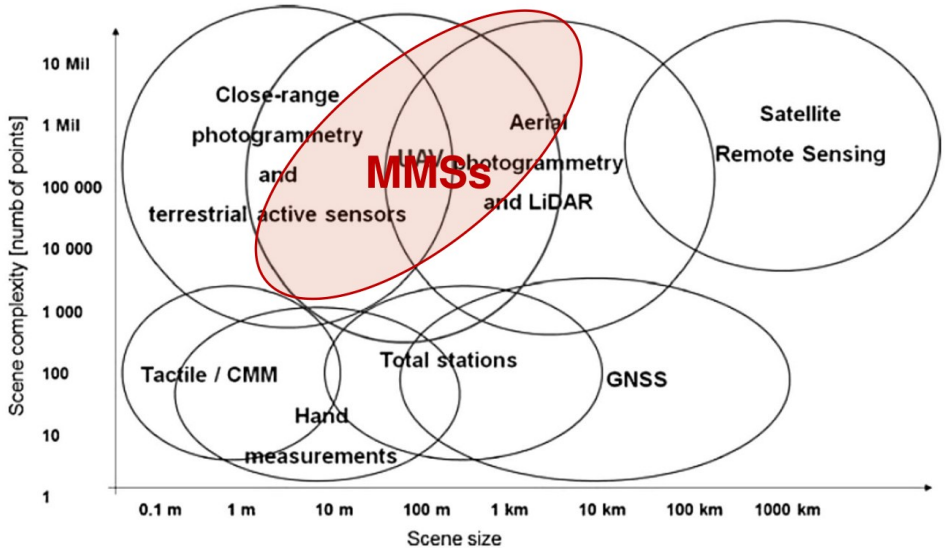
Finally, point-cloud and (geo) referencing of scans involves overlapping of scans. (Spanò A. , 2019) It's initially captured in their respective sensor coordinate systems, into a unified coordinate system, enabling the creation of a cohesive 3D model. They are aimed at containing the error propagation and the roto translation in the desired reference system. (Spanò A. , 2019) The process can be achieved in three different ways (Guidi, 2014):

- Alignment based on complementary 3D measurement equipment offering the position and orientation of ranging devices
- Alignment based on reference targets – topographic control points

- Alignment based on Algorithm ICP (iterative closest points)-refermentation shape

Mobile Mapping System (MMS)

MMS are fundamentally defined as integrated systems of mapping sensors mounted on a moving platform, designed to provide the platform's positioning while simultaneously collecting geospatial data. (Elhashash, Hessah, & Rongjun, 2022) These systems are versatile tools that combine various advanced technologies, such as GNSS, Inertial Measurement Units (IMU), LiDAR sensors, and high-resolution cameras, to efficiently map and create detailed 3D models of the surrounding environment. (Scolamiero, Boccardo, & Riccia, 2025)



► Figure 32 Geomatics techniques, sensors, and platforms for 3D recording, according to the scenes' dimensions and complexity (Spanò A., 2019), re-elaborated from (Nex & Remondino, 2013)

The evolution of MMS technology commenced in the late 1980s, propelled by significant advancements in mobile positioning technology, modern communication networks, spatial information systems, and embedded computing. (Wang, Liu, & Huang, 2009) Contemporary MMS technology is characterized by a blend of multi-discipline combination, multi-platform compensation, multi-sensor integration, and multi-data fusion capabilities. To be more specifically, it combines different data collecting technologies, along with advancements in communication and embedded technology, representing a convergence of diverse technological fields. (Elhashash, Hessah, & Rongjun, 2022)

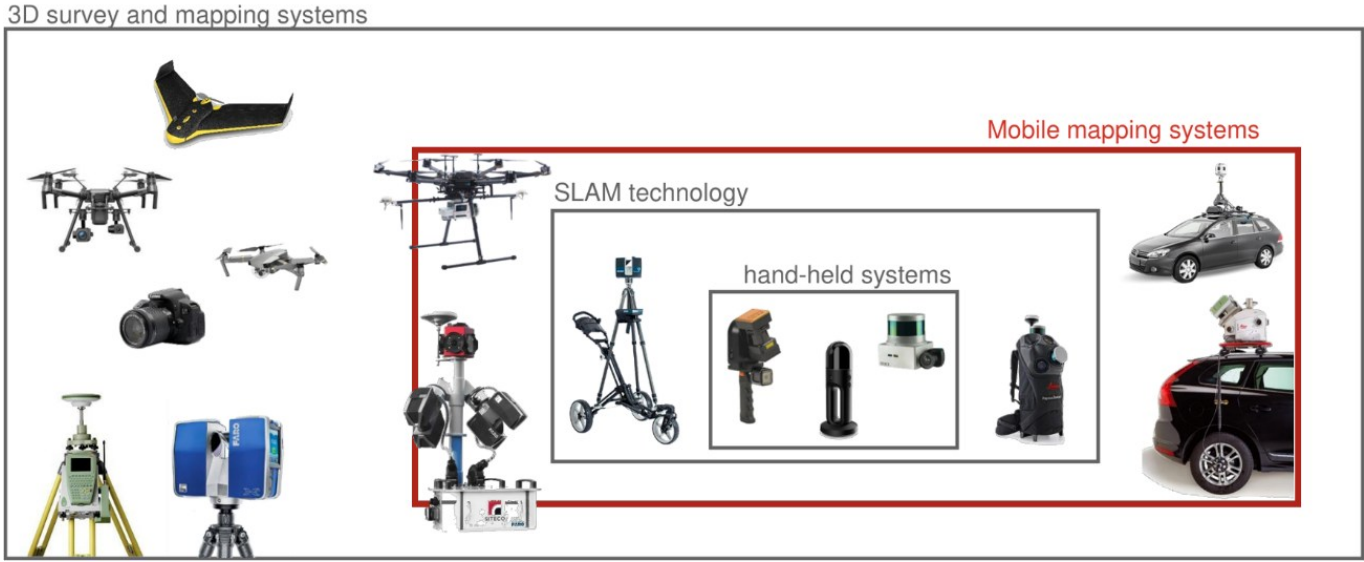
MMS provides highly valuable assets for a wide array of applications. Its versatility extends to numerous other fields, including natural resource monitoring and management, comprehensive mapping and map updating, urban asset inventory, intelligent transportation systems, precision agriculture, general field surveying, environmental engineering, gamification and virtual reality applications, autonomous driving systems, and indoor collision avoidance systems. (Sammartano & Spano, 2018) As

the complex applications, the devices of MMS appears variously with more special classification as Figure 33 shown.

Hand-held systems based on SLAM System

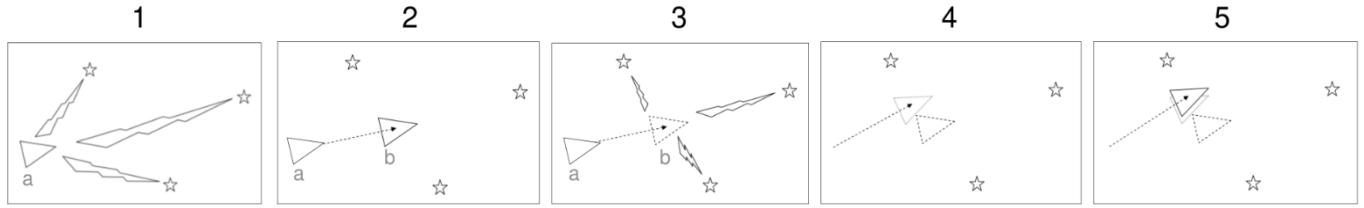
The device used in the case of the Amphitheatre in this thesis is a hand-held system based on SLAM technology. Because GNSS suffers from signal loss in urban canyons and indoors (Elhashash, Hessah, & Rongjun, 2022),

▼ Figure 33 Device examples in the classifications of 3D survey and mapping systems (Spanò A., 2019)



which cause problems when the survey needs to be held in underground environments, bulky MMS system with GNSS technology couldn't appear well. In contrary, characters of SLAM system (Simultaneous Localization And Mapping) lead the surveys in this environments to be more efficient and accurate.

SLAM systems are based on ICP-like techniques, leveraging inertial platforms that monitor the linear and angular movements of the instrument that is transported manually (or on a trolley) by an operator. (Riisgaard, 2005) SLAM systems simplify data collection, providing an avenue for scanning both internal and external environments (seamless positioning) without the need to have a connection to GNSS positioning systems (FARO).



- The scanning sensor (triangle), initially measures (arrows) in (a) the position of the reference points (stars), corresponding to geometric characteristics of the environment;

▲ Figure 34 Scheme of SLAM working principle (Riisgaard, 2005)

- The new position of the sensor in (b), provided by the odometry, is at an estimated position distance;
- The sensor measures the position of the reference points again and detects that they do not match the original ones;
- The sensor now uses the data obtained from the actual location of the reference points to determine where it is located (prevails over odometry). The initial estimated position is the dotted triangle;
- The final position estimate by the sensor combines measurement and odometry. The dotted triangle represents where it thought it was; the dotted triangle where it said odometry; and the last triangle where it is actually located. (Riisgaard, 2005)

This newly analysed is a continuous process that increases and optimizes with the movement of the operator and the algorithm. Therefore, it serves as a solution for both the positioning and the mapping of the 3D geometry of the detected object. Considering its operational characteristics, this type of device works best in environments rich in geometric elements and irregularities and the execution of a closed path is critical to the final adjustment of the SLAM.

Like other geomatics surveys, the survey using Hand-held systems also begins with a preliminary phase of preparation of the survey, as mentioned, to have a prior knowledge of the object to be analysed. However, apart from this, the survey process also follows the steps (Elhashash, Hessah, & Rongjun, 2022):

- Data Acquisition: Following the meticulous planning of the survey route and configuring the appropriate platforms and sensors.
- Sensor Calibration and Fusion: Achieving accurate localization, precise geometric reconstruction, and proper data alignment.
- Georeferencing: basing on the fused IMU positioning data after the calibration among data collection sensors.
- Returning and editing results.

3.2. Analysis environment

3.2.1. The GIS environment

GIS is a computer system for capturing, storing, querying, analysing, and displaying geospatial data (Chang, 2019), which represents a framework comprising computer software, hardware, data, and skilled personnel, all working in concert to facilitate the entry, manipulation, analysis, and presentation of information intrinsically linked to locations on the Earth's surface. It is designed for the collection, storage, management, analysis, and visual representation of geo-referenced data, ultimately serving as a robust platform for informed decision-making. (Ershad & Ali, 2020)

The conceptual underpinnings of GIS began to take shape in the early 1960s, building upon nascent ideas of automated cartography. (Esri, 2025) The field experienced substantial growth from the late 1980s into the early 1990s (Maguire, 1991), with the concept of "Geographic Information Science" (GIScience) came out in 1992 (Schuurman & Cinnamon, 2013). From its origins in specialized, large-scale government systems like CGIS, GIS has evolved to desktop applications and cloud-based platforms, such as Google Maps and Google Earth, making it accessible to individual professionals. (Wikipedia, Geographic information system software, n.d.)

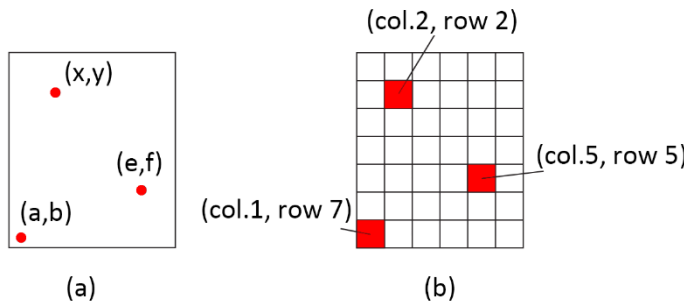
As a complex system, GIS includes various functional components besides geospatial data, which are essential for the comprehensive capabilities of a GIS (Chang, 2019) (Ershad & Ali, 2020):

- **Hardware:** Referring the physical computing infrastructure required for GIS operations, including computers, servers for data processing and storage, workstations for user interaction.
- **Software:** As the core of any GIS, providing the tools and functionalities necessary for data entry, manipulation, analysis, visualization, and output, including various types.
- **People:** Referring to the individuals who interact with the GIS—the users, managers, analysts, and developers.
- **Organization:** GIS operations exist within an organizational environment; therefore, they must be integrated into the culture and decision-making processes of the organization for such matters as the role and value of GIS, GIS training, data collection and dissemination, and data standards.

In addition to the above elements, the basic element of GIS is of course to organize and geographically register data in a single reference system, which is defined by users and varies according to geographical regions. For example, in Pompeii, people had used different reference frames for

surveying activities, such as the Italian Gauss Boaga coordination system. The more commonly used reference system in Italy is the SR WGS84 (World Geodetic System) for the 32N and 33N time zones, represented by EPSG (European Petroleum Survey Group) codes 32632 and 32633. WGS8433N is the reference frame used for all cases in this article.

Finally, geospatial data is a key point of GIS, since the ability of a GIS to handle and process geospatial data distinguishes GIS from other information systems and allows GIS to be used for integration of geospatial data and other data (Chang, 2019). It can describe both the locations and characteristics of spatial features. And GIS primarily utilize two fundamental types of data models to represent the real world: vector and raster, as Figure 35 shown.



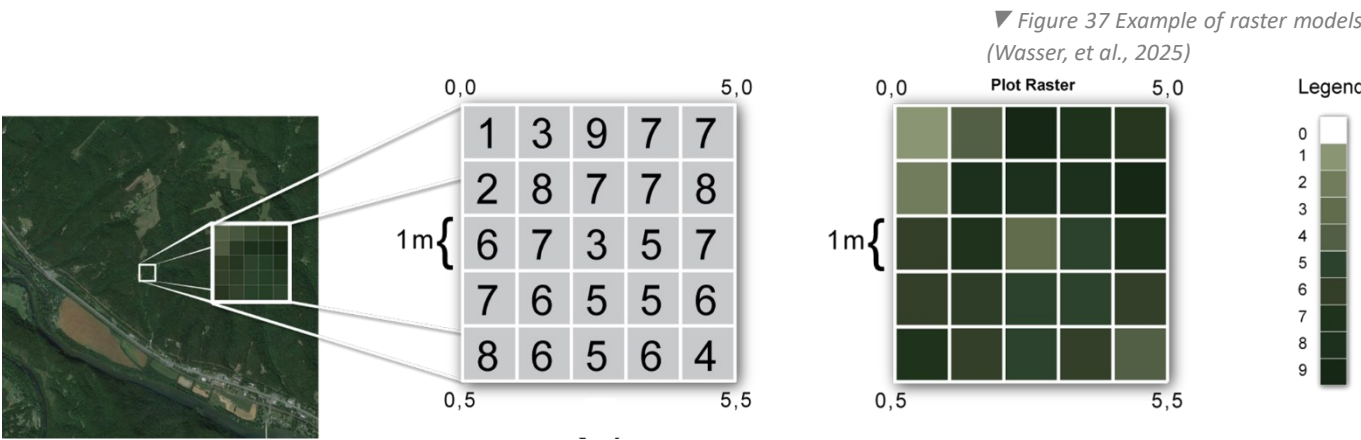
◀ Figure 35 The vector data model uses x-, y-coordinates to represent point features (a), and the raster data model uses cells in a grid to represent point features (b), modifying from (Chang, 2019)

The vector data model uses points, lines, and polygons to represent spatial features with a clear spatial location and boundary such as streams, land parcels, and vegetation stands. Each feature is assigned an ID so that it can be associated with its attributes.



◀ Figure 36 Examples of vector models (Chang, 2019)

The raster data model represents spatial information as a grid of equal-sized cells, often called pixels. Point features are represented by single cells, line features by sequences of neighbouring cells, and polygon



▼ Figure 37 Example of raster models (Wasser, et al., 2025)

features by collections of contiguous cells. The cell value corresponds to the attribute of the spatial feature at the cell location. Raster data are for continuous features such as elevation and precipitation.

The methods of acquisition and visualization, as well as the spatial queries and analyses that can be performed, may vary depending on the data type used to represent certain information.

There are many sources of errors that may affect the quality of a GIS dataset (Ndehedehe, 2013), it's mandatory to attach attention to them for a more accurate result. Apart from the inherent imprecision in cartography beginning with the projection process and its necessary distortion of some of the data (Jean-Michel, Jean-François, Ana-Maria, & David, 2019), errors can be divided into three main categories (Burrough & McDonnell, 1998):

- Obvious sources of error, like density of observations and data relevance to the result.
- Errors resulting from natural variations or from original measurements.
- Errors arising through processing, like numerical, digitizing and geo-coding Errors.

QGIS

QGIS is a famous GIS software distinguished by its fundamental characteristic of being free and open source. (wikipedia, 2025) It empowers users to comprehensively create, edit, visualise, analyse, and publish geospatial data. It functions as a full-fledged desktop GIS, providing a robust and comprehensive suite of processing and analytical tools for intricate geospatial data handling. (Sparks, 2025)

This software provides great accessibility and cost-Effectiveness, due to its free entry and online resources. And the open-source nature of QGIS inherently fosters continuous innovation, leading to a constant influx of new features and significant improvements. As a key component of the broader open-source GIS ecosystem, QGIS excels in its interoperability and seamless integration capabilities with other software tools. This is powerfully supported by its ability to read and write nearly all prevalent geospatial data formats. (QGIS community)

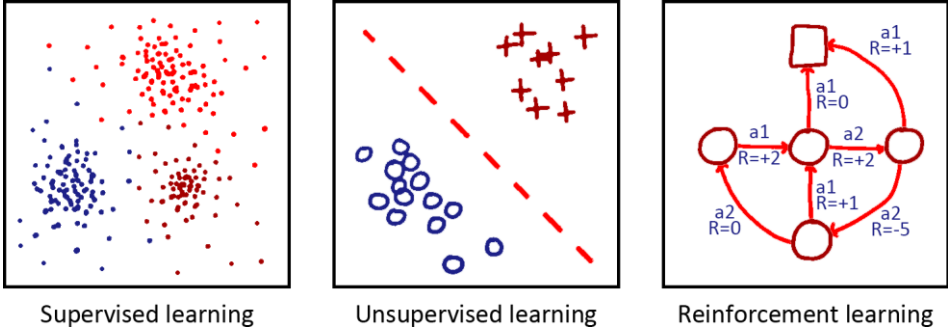
QGIS offers robust and intuitive capabilities for viewing and exploring geospatial data. It supports both traditional 2D and advanced 3D map rendering, allowing for comprehensive and multi-dimensional visualization of spatial information. (QGIS community) In the cases of this thesis, QGIS offers a GIS environment for presenting and analysing the results.

3.2.2. Machine learning system for Semantic Segmentation

Machine learning (ML) is a field of study in AI concerned with the development and study of statistical algorithms that can learn from data and generalise to unseen data, and thus perform tasks without explicit instructions. (Koza, Bennett, Andre, & Keane, 1996) ML algorithms are generally able to model complex class signatures, can accept a variety of input predictor data, and do not make assumptions about the data distribution. (Maxwell, Warner, & Fang, 2018) This discipline encompasses a range of tasks towards images and point clouds, including classification, object detection, and segmentation labelling, all of which are instrumental in fostering a machine's capacity for complex scene understanding. (Simeone, 2018). (Guo, et al., 2021)

These algorithms form the bedrock of contemporary AI, catalysing breakthroughs across a multitude of domains. They can be categorised into three major classes usually (Rosidi, 2023):

- Supervised Learning: training data used contains the required answers
- Unsupervised Learning: making predictions without labels in the data
- Reinforcement Learning: learning by making mistakes and getting more and more accurate as learning from the data



◀ Figure 38 Scheme of 3 main classes of ML, modified from (Rosidi, 2023)

This thesis will study the basic applications of ML focusing on “semantic segmentation” of images and point cloud, evolving supervised learning and unsupervised learning.

Semantic segmentation's capacity to deliver pixel-level scene understanding renders it an indispensable technology across an extensive range of domains, enabling precise and autonomous operations, such as medical image analysis, autonomous driving, virtual or augmented reality, etc. (Cheng, Li, Li, Hua, & Sheng, 2022) In recent decades, ML technologies, especially semantic segmentation, have significantly advanced the field of CH documentation and allows for detailed, efficient, and non-invasive methods of recording and analysing CH sites. (Argyrou & Agapiou, 2022) (Yang, Hou, & Li, 2023)

Semantic segmentation on images

The explanation of semantic segmentation begins with the concept on images. Semantic segmentation is a fundamental computer vision task wherein the objective is to categorise each pixel within an image into a predefined class or object. (Csurka, Volpi, & Chidlovskii, 2022) The outcome of this process is a dense, pixel-wise segmentation map, where every individual pixel is assigned a specific semantic label, thereby facilitating a comprehensive understanding of the scene. (Ankareddy & Delhibabu, 2025)

Unlike image classification, which assigns a singular label to an entire image, semantic segmentation provides a granular understanding by labelling each pixel individually. Similarly, while object detection identifies objects and delineates them with bounding boxes, semantic segmentation advances this by precisely outlining the boundaries and assigning a class to every pixel within those boundaries, including the background elements. (Simeone, 2018)

This work basically relies on feature engineering for images, extracting relevant and distinctive information from raw image data to create representations of key characteristics or patterns. (Faster Capital, 2025) The common features used are including colour, texture, shape and edges...

To make the feature engineering, it's mandatory to process the data before the analysis, including noise reduction, edge detection, and normalization of pixel intensity values to ensure consistency. (Widyaningsih, Priyambodo, Wibowo, & Kamal, 2023) Also, dimensionality reduction is another option to distil the essential information, enhance the performance of machine learning models, and achieve more efficient storage and processing. (Faster Capital, 2025) After these processes, the derived features are then served as inputs to various ML models.

One of the common methods is "K-Means" Clustering algorithm, which is an unsupervised machine learning algorithm. It partitions an image into a predefined number of K clusters based on the similarity of pixel attributes (Nielsen & Nock, 2003), such as colour, intensity, texture, spatial location. The algorithm aims to minimize the squared or absolute difference between each pixel and its assigned cluster centre. K-means is widely recognized for its simplicity and relatively low computational complexity. (Tatiraju & Mehta, 2008)

While the algorithm grouping pixels based on their statistical similarity in the feature, the groupings do not automatically guarantee

correspondence to real-world semantic objects. (Nielsen & Nock, 2003) Therefore, the semantic interpretation of the resulting clusters often necessitates a subsequent post-processing step or relies heavily on the discriminative power of the chosen value of K.

Semantic segmentation on point cloud

As a concept similar to the image semantic segmentation, the point cloud semantic segmentation categorises each point in the point cloud into a predefined class or object. The different elements become from the type of data, as point clouds are unstructured irregular collections of 3D points, each typically possessing X/Y/Z coordinates and potentially other attributes like intensity, normal vectors. (Harshit, Kushwaha, & Jain, 2022)

In consequence, the features used for clustering are not only colour or texture, but also position, normal and intensity. (Chen, et al., 2023) To be more specific, it focuses on 3D geometric properties and local descriptors that capture 3D spatial relationships and surface characteristics. The unstructured and irregular nature of point clouds significantly complicates the process of feature extraction compared to images, which makes it challenging to define consistent local neighbourhoods and extract robust features that generalize well. (Harshit, Kushwaha, & Jain, 2022)

One of the common methods is random forests algorithm, which will be applied in this thesis. It involves extracting a rich set of handcrafted features from the point cloud data, as referred, including points' position, normal, intensity and other properties. (Shahraki, Elamin, & El-Rabbany, 2025) Once these features are engineered, the algorithms will be trained to classify each point based on its feature vector into predefined semantic categories. It can be regarded as learning a mapping from the high-dimensional feature space to the discrete class labels.

While these approaches can achieve reasonable accuracy for specific, well-defined tasks, particularly with limited datasets, they face significant limitations. They are prone to overfitting, especially with limited or imbalanced datasets, which reduces their generalization to new data.

Also, there are many softwares have equipped the AI functions for point cloud semantic segmentation, which will be tested in this thesis.

4. Multi-method documentation: Amphitheatre



4.1. 3D metric survey operations

As the last chapter explained, 3D metric survey contributes to the geography information of the project, defining the shape, therefore the morphological characteristics, of an architectural space or object and quantifying its dimensional attributes.

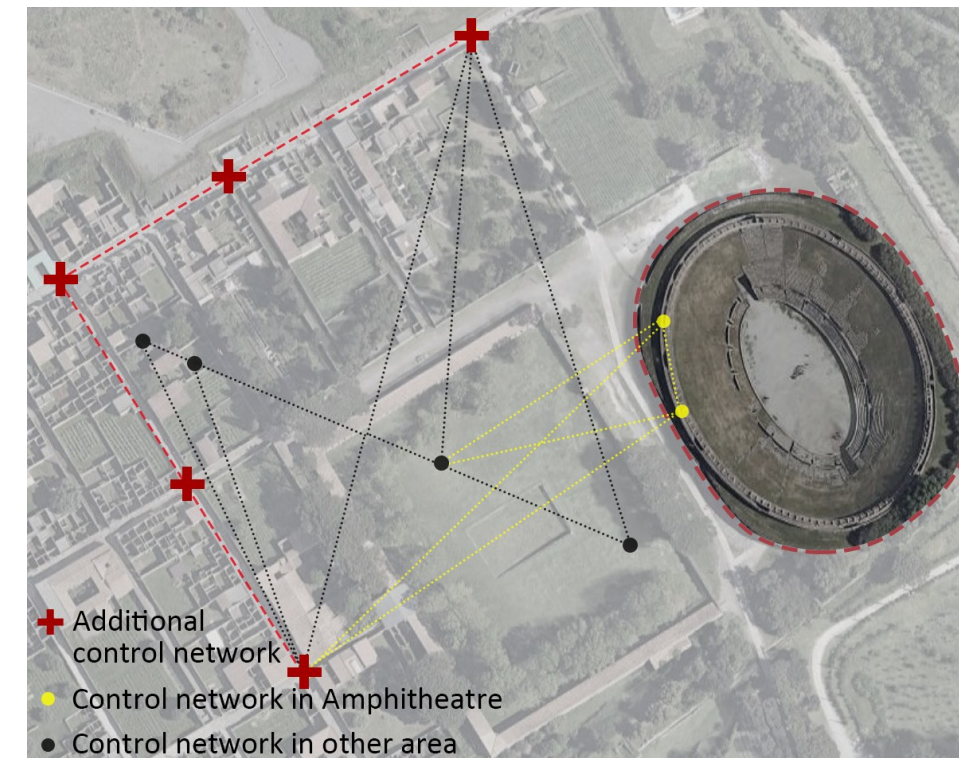
This 3D metric survey campaign, carried out in the summer of 2023 and 2024 in Pompeii, obtained different type of data with high accuracy focusing the amphitheatre. And this survey campaign was carried out by 2 generations of the DIRECT Team in these 2 years, saw the contribution of topography, UAV photogrammetry, lidar scanning, slam mapping, with 4 different objectives:

- A 3D survey of the points well distributed in the building and the ground;
- An aerial photogrammetric survey of the external space of the building using visible camera;
- A lidar survey focusing the external space of the building;
- A SLAM survey focusing the spaces of the building, especially the internal narrow spaces.

In the following paragraphs, the strategies, tools and operational workflows that led to the development of a series of value-added metric products will be presented with more details, which were used in the graphic restitutions.

4.1.1. The topographic survey related to the framing network

As all the three projects are close to each other, located in Regio II, a common topographic control network was planned additionally to have all the projects' documentation in the same reference space.



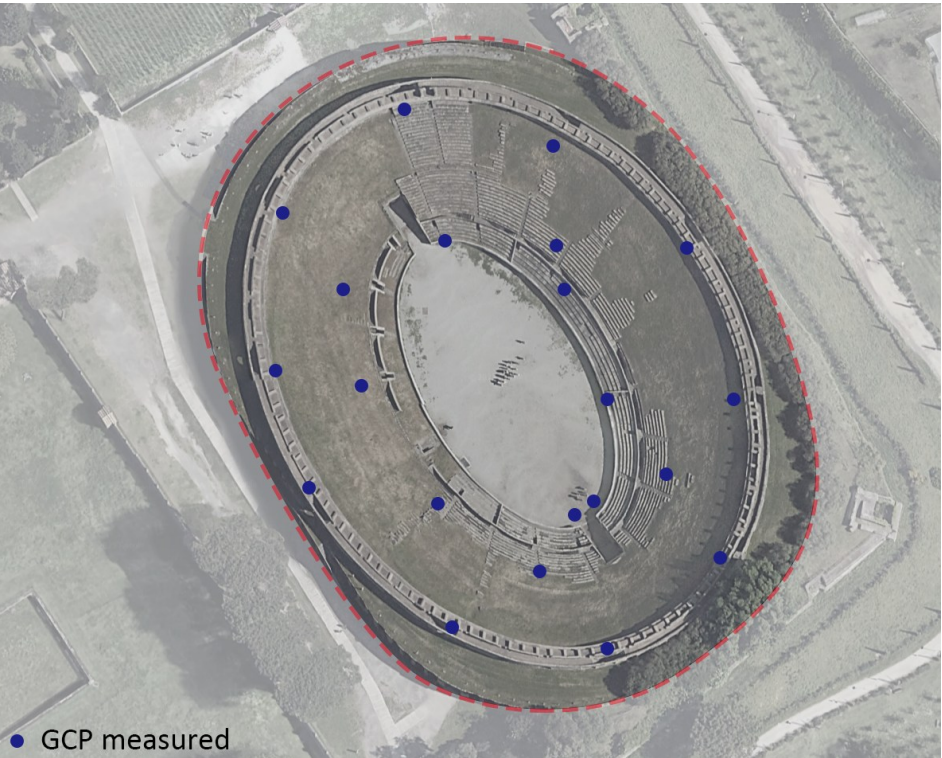
◀ Figure 39 Scheme of the topographic control networks, including the additional common control network, showing the relation with the Amphitheatre

For georeferencing each project, a triangle consisting of vertices measured should be set. With the base of the common control network, the baseline for each survey project were built with the vertices in the common network and the new vertices located in each survey area, as Figure 39 shows. As the baseline, the control vertices were measured on the first day of the survey campaigns using a total station.

This series of surveys is focusing on the amphitheatre itself, including the internal and external spaces. Apart from the baseline, the topographic survey of this case also involves measuring the ground control points, which should be well scattered in the areas of interest, to offer accurate geo-information to the whole project.

According to the plan, the ground control points were divided into 3 groups: one group on the top circle of the building, one group on the lower circular surface, and the last group on the ground area. As the Figure 40 shows, here are 20 control points positioned on the top with markers or natural feature points in the survey area. So, the vertices can be measured efficiently and attach convincing information to this photogrammetry area. And they were measured through RTK methods to determine the

coordinates by positioning the receiver installed on the pole.

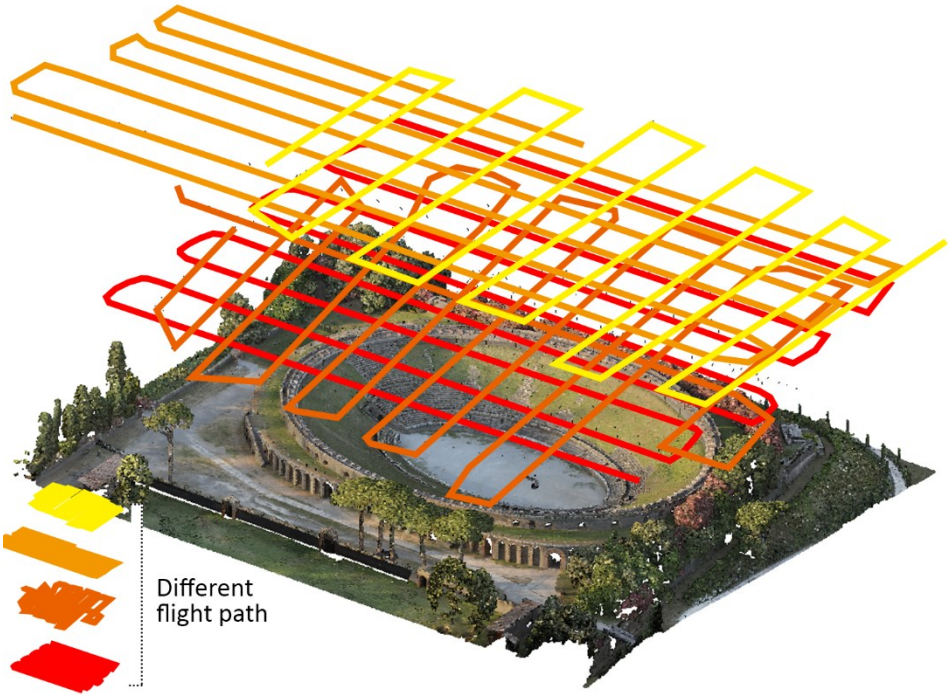


► Figure 40 Distribution of the vertices serving as ground control points

The control points in this project allows for geographic registration of all type of data obtained through different techniques during the acquisition process. In this case, during each survey, the ground control points set on the building would be captured by the sensors related to the data acquisition techniques. Thereby it enables geographic registration of different measurement products of this survey area.

4.1.2. Aerial photogrammetric survey

During the survey campaign of this case, to acquire the exact shape of the building, including the vertical and decline surfaces, with a higher data confidence, the flight was performed partially with different shooting angle. With the high-resolution camera, most of the frames were taken at the altitude of 60 meters but the survey still ensured achieve a GSD of approximately 0.9 cm.



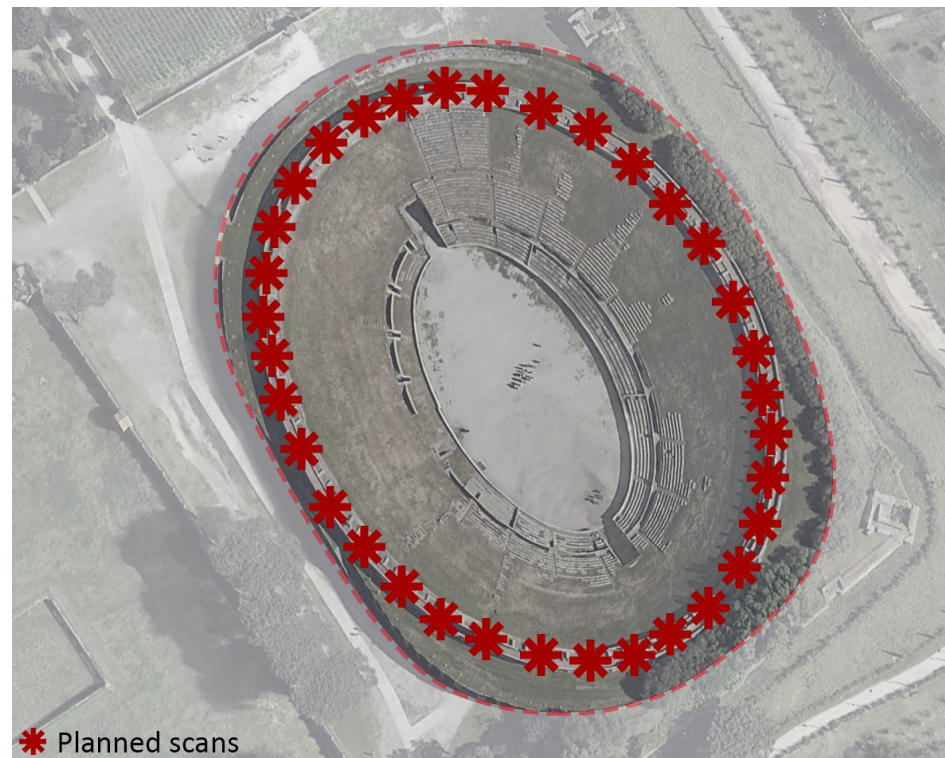
◄ Figure 41 Scheme of the flight plan in this case

These elements guarantee a proper resolution and an ideal level of detail for the photogrammetry part. And the frames acquired were processed with the aim of creating value-added metric products from the survey area. These steps will be presented in the following paragraph.

4.1.3. Lidar scanner survey

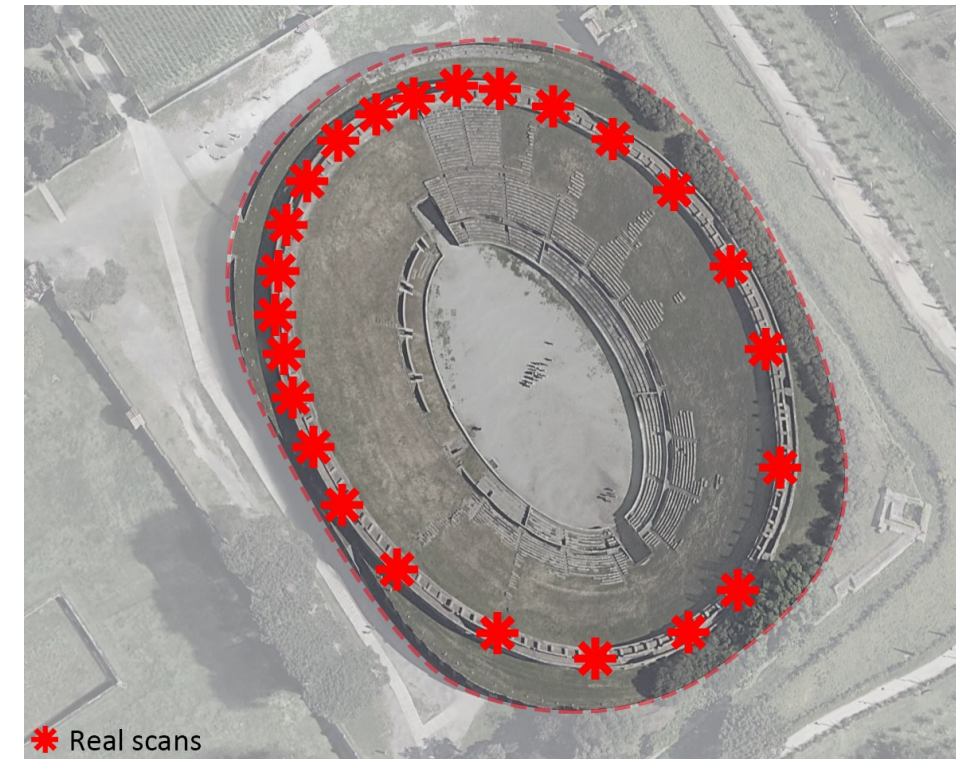
As for the survey using Lidar on the ground, the survey plan acts more important. The consideration is not directly connected to the resolution but appears as the elements like the scan position, scan density and sweeping angle. As the correspondence, time of the survey becomes an important control element in this time limited survey.

In the plan stage, the scans were planned in a relatively higher dense, as the Figure 42 shows, each of them are approximately 10-metre-close to each other. Also, the parameter of the scans was taken in a custom value to fulfil the survey need.



► Figure 42 Scheme of planned scans of Amphitheatre

But due to the special shape of the building, the strategy for the survey is exceeding and more time consuming. So, after several scans, the team gradually moved the plan to race against the limited time: fewer scans in a certain area and less scan dense. As a result, the dense of the scans were not uniformed, which caused a series problems in processing step that will be discuss in the following paragraph.



◄ Figure 43 Scheme of the real scans excuted during the survey

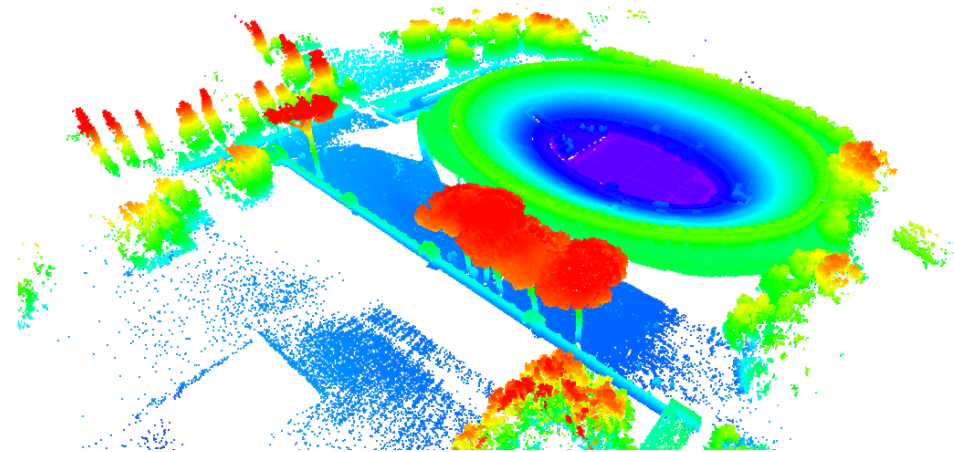
Another problem is, after the long continuing work under the high temperature environment, errors happened to the visible sensor carried on the scanner, which caused the texture disappeared on a half of the scans. Thus, the working time is an “invisible element” of having the acquisition without losing detail or information.

Based on these situations, the scans were collected completely along the highest circular pathway, the following paragraph will present the processing and the point cloud merging with SLAM. The data merging will be an important part of this case.

4.1.4. SLAM survey

While the open area of the amphitheatre was measured by Lidar scanning, GeoSLAM was applied to deal with the long narrow spaces and complex shapes such as arches distributed on the facades. This mobile mapping system carried by the operator, can generate a real-time preview on the connected device.

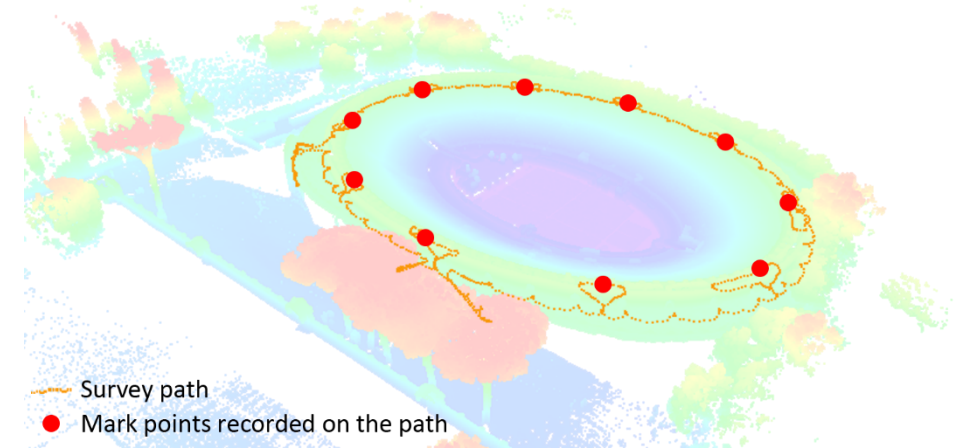
The entire survey was decided into 6 mapping paths to cover all the spaces of interests. Each of the mapping path were performed as closed paths, starting from one point and ending at the same point. For clear recognising the position during survey and better georeferencing the point cloud of the scans, the points are usually picked from the planned control point measured in the topographic survey.



► Figure 44 One of scans performed by SLAM, with height visualisation

In fact, as already highlighted in the previous chapters, this instrument is not equipped with a GNSS receiver, therefore all the point clouds created are oriented in a local reference system and independent from each other, which is why it will be necessary to both register them with each other and to roto-translate them in a unique reference system.

Based on the method of data acquisition, the reference points used for registration are recorded by pausing for a few seconds at the corresponding position. Therefore, during the survey campaign, attention should not only be paid to the starting point of the closed-loop path, but also to the path design that connects as many reference points as possible. For data collection, uniform travel along paths outside the reference point can provide a better base for accurate identification of the reference point position.



◄ Figure 45 One of the survey paths recorded by the scanner with reference points marked on it, overlapping on the point cloud semi-transparent

Though with the considerate plan, problems still happened during the survey and processing. Especially those long scans with duration more than 20 minutes, is particularly heavy to process for the software and the device.

4.2. Processing of multi-data

As stated in the last paragraph, each technique was applied for measuring a different part of the building, instead using a single technique to deal with all the problems, especially the long interior corridor under the structure. So, this paragraph will not only review the processing of the data, but also will discuss how to merge the data to achieve the value-added result which fulfil the survey's aim.

In the first 3 sections of this paragraph will focus on the data processing of each single technique. Beyond the operation, the errors will also be discussed as an important part.

After understanding the errors of each dataset, the last section will present the method to merge the data, not only the point cloud, to achieve a clean result with confidence.

4.2.1. Processing of LIDAR

The process was held in Scene, the commercial software supporting the Lidar scanner used in this survey, with the aim of registering the Lidar point cloud and georeferencing them. The workflow basically divided into 3 registrations: manual registration, ICP registration and GCP registration.

Since the raw data was randomly placed in the virtual space of the software when imported, usually each scan is far away from the others, it's mandatory to move the scans as close as possible to the corresponding ones, which offers a base for correct and easy ICP registration. There is no critical for this process, instead, it can be regarded as a preparation of the next step.

After rough manual registering, the precise registration, ICP registration, can be processed automatically by the software. This registration is based on matching the same feature of the point clouds. In this step, the point cloud was completed with the shape but without the location information in the real world.

As the Figure 46 shows, the result of ICP registration contains relative higher errors. Through checking and reasoning, it was because of the changing scan dense. When there is less overlap ratio between 2 near scans, the common feature can be found by the software would decrease a lot. Based on this situation, the result with medium value about 12mm was the best result can be achieved and it could be regarded as acceptable.

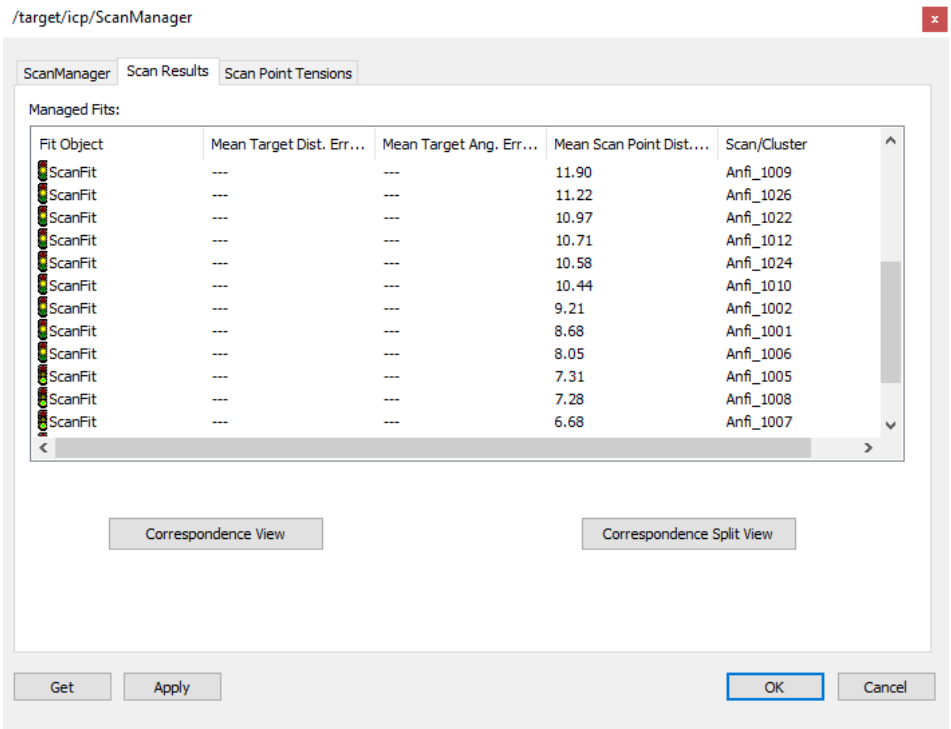
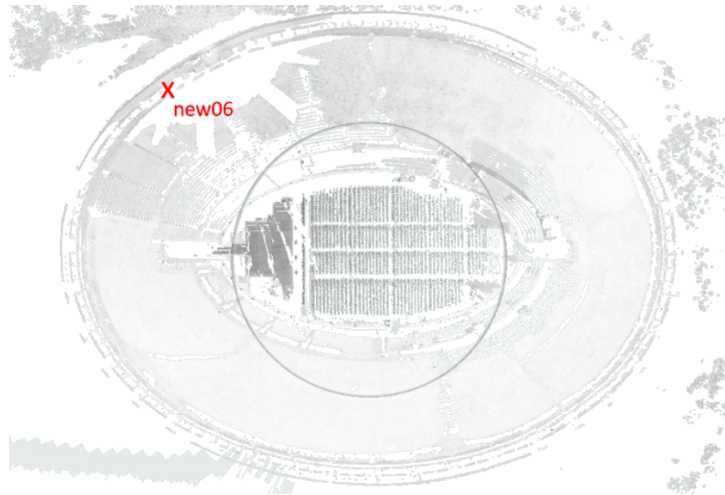


Figure 46 The result of the ICP registration, ranking by error distance in descending order

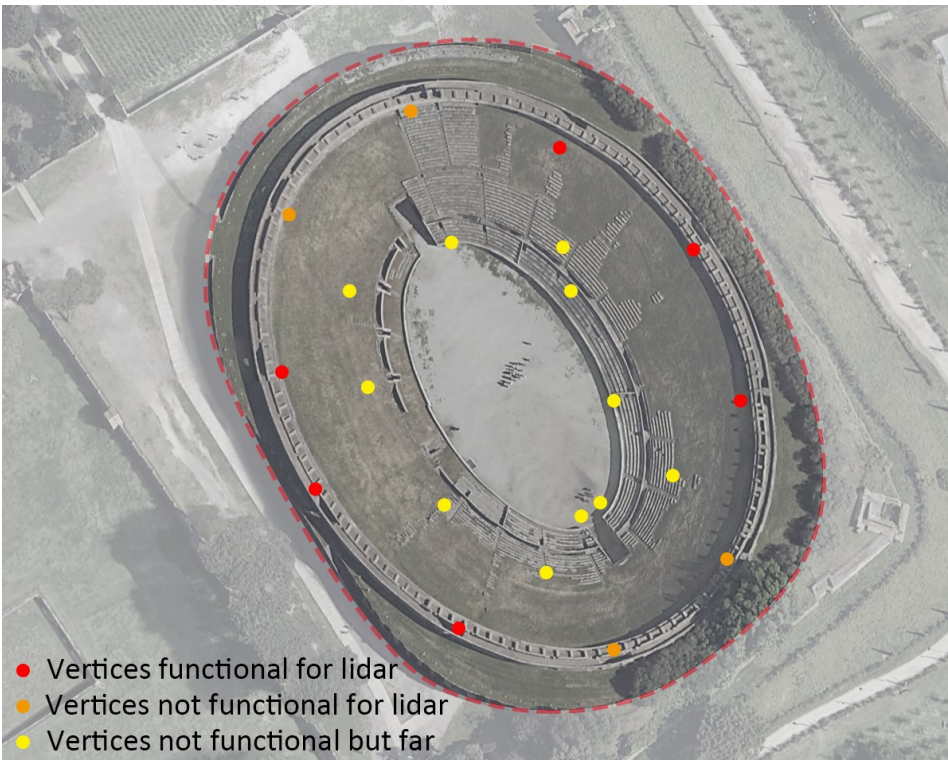
As the final step, the GCP registration using the ground control points allows the accurate georeferencing operation. By making the projection of the measured control points, the blocked point cloud is oriented and roto translated by the related points and the algorithm.

But during this step, the problem from the survey comes to the processing. The scans were taken on the highest circular path and above the ground approximately 1.4 metres, and the scanning points were not very overlapped with the markers' position placed on the half wall. As a result, the control points were not easy to be located in the scans.



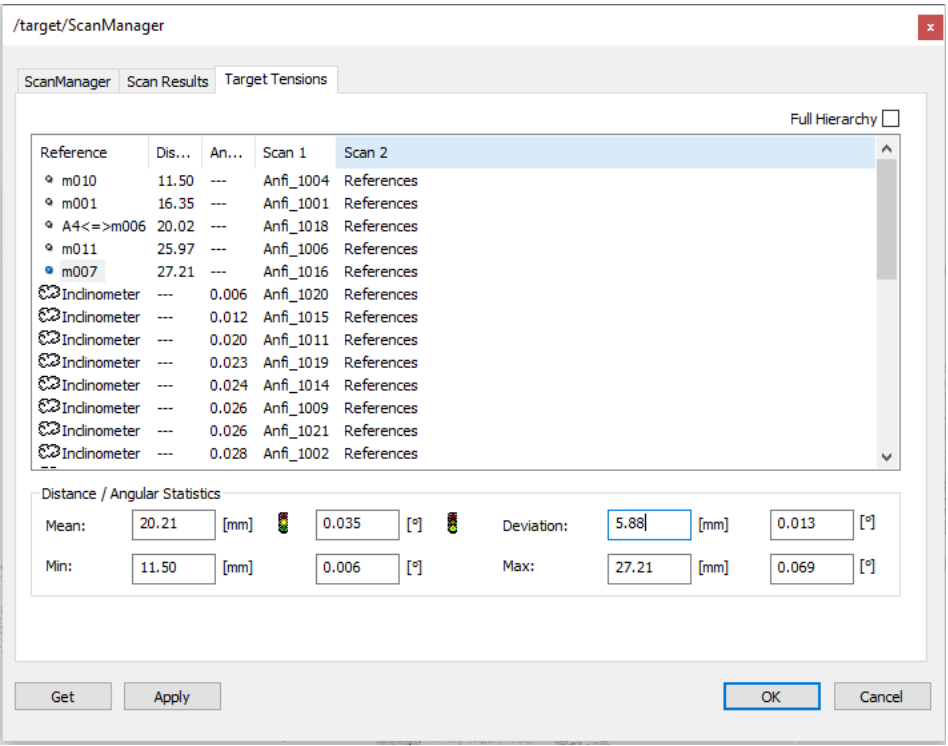
► Figure 47 A reference point marked on the point cloud

And another problem is that in the last half of the survey, as running against the limited survey time, the dense of scans decreased than the ones in the first half, which pushed the visibility problem of the control point more serious. Therefore, the control point with the real function in this project are only 6, as the Figure 48 shown.



► Figure 48 Scheme showing if the vertices functional or not, considering the distance

According to the result reported in the figure by the software, the best result achieved in this process, with the medium value as 20mm, still could be regarded as fulfilling the demand of this survey.



◀ Figure 49 The result of the target based (GCP) registration, showing the final errors of this set of point cloud

4.2.2. Processing of Photogrammetry

Phase involves the use of Agisoft Metashape Pro, a commercial software that performs photogrammetric processing of digital images and generates 3D spatial data to be used in various fields: from the documentation of cultural heritage to the production of visual effects, for analysis in a GIS environment or, again, for indirect measurements.

The first stage is loading all the images in the software, including all the flight of this survey. After all the images were imported, the relevant coordinates information attached on the images should be removed from the calculation as the precision of the receiver integrated in the drone applied here cannot fulfil the demand of this survey to scale and georeferencing the metric products.

Starting with the photos, the photo orientation can be executed by the software which returned tie points as the result. The tie point clouds were generated with the precision High, which is the most detailed option can be chosen in the program interface. It took about 40 minutes to compute the result, which includes 1,685,908 points with the file size 3.61 Gb.

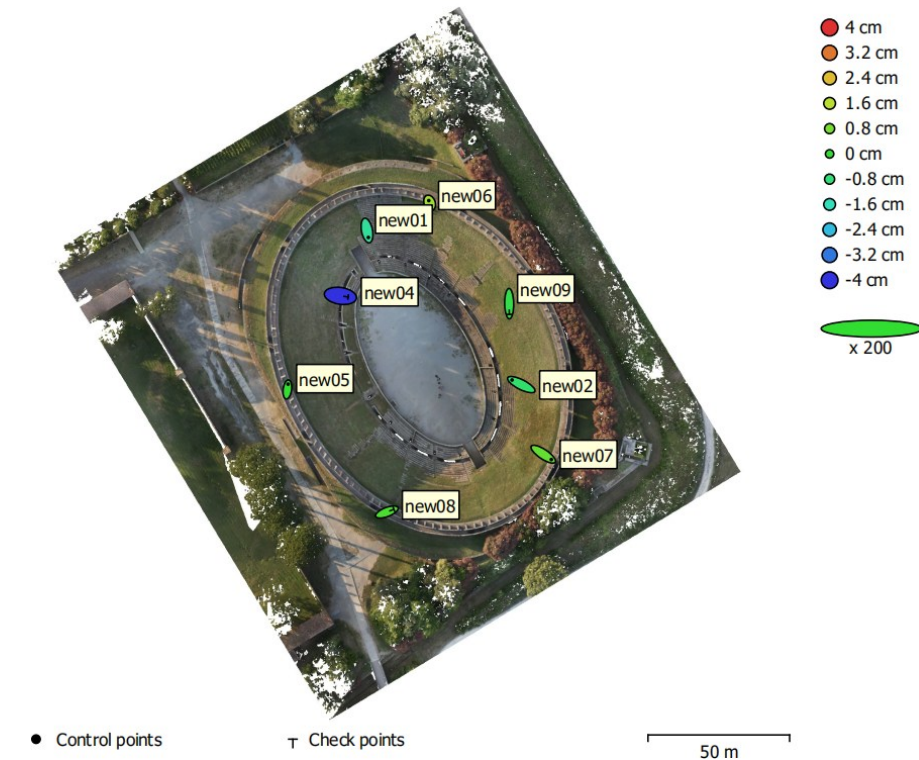
After the preliminary orientation, the model still doesn't have the geoinformation and correct dimension. Control points with their coordinates can be the reference of orientating and scaling. Under the correct reference system named EPSG:32633 – WGS 84 / UTM zone 33N, the CSV file containing the coordinates of the vertices and displayed in the program in tabular form should be imported into each project.

As the project spans over one period, the photogrammetry survey was performed in 2023, as a result, there is some problem for merging the metric products. To solve this problem and achieve a relative accurate result, the point cloud, the metric products from Lidar data process, was used as the base of georeferencing of this stage: the natural feature points were extracted from the Lidar point cloud, with good visibility of both 2 acquisition views, as the Figure 50 shown.

▼ Figure 50 One of selected point marked in both datasets



The principle of point picking is similar to the control point selecting in the real survey campaigns. Overcoming the visibility of both data sets, the control points picked for this process is well distributed in this project as the Figure 51 shown. After that, each of the points was collimated in the frames, which are 8 points in total, the maximum amount can be achieved.



◀ Figure 51 Distribution of GCPs and CPs in the project, with the visualisation of error

With the collimating work, the errors of CP and GCP are low and similar, lower than 5cm, which already fulfilled the demand of this survey and have a high confidence of merging the data.

Label	X error (cm)	Y error (cm)	Z error (cm)	Total (cm)	Image (pix)
new01	0.483529	-2.43905	-1.23395	2.77586	0.901 (26)
new02	-3.24819	1.63782	-0.67081	3.69908	2.784 (19)
new05	0.246597	1.87898	0.0341686	1.8954	1.166 (15)
new06	-0.305568	0.806074	1.29605	1.55656	1.175 (16)
new07	2.82363	-1.88382	0.574537	3.44264	1.461 (15)
Total	1.94482	1.8089	0.892593	2.80199	1.634

◀ Table 4 RMSE summary of GCPs

Table 5. Control points.
X - Easting, Y - Northing, Z - Altitude.

Label	X error (cm)	Y error (cm)	Z error (cm)	Total (cm)	Image (pix)
new04	2.73249	-0.407526	-3.99456	4.85686	0.794 (15)
new08	2.46542	0.949476	0.310425	2.66011	0.801 (16)
new09	0.0548809	-3.78351	-0.28343	3.79451	1.552 (16)
Total	2.12507	2.2644	2.319	3.87572	1.114

◀ Table 3 RMSE summary of CPs

Table 6. Check points.
X - Easting, Y - Northing, Z - Altitude.

As for the dense cloud, the time required for the high quality was about 10 hours and a half by the software for a result from 1125 photos and consisting of more than one hundred million points.

Control points RMSE [m]	0.028
Check points RMSE [m]	0.038
Dense cloud	159,520,960
File size [GB]	3.29

► Table 5 Parameters of the point cloud generated by photogrammetry)

The dense cloud thus georeferenced is ready to be used as a source for the processing of other metric products with added value. In this case, the point cloud of the entire out appearance with full colour information attached, will offer the colour information to the point cloud collected by scanners. Furthermore, a DSM and the visible colour orthophoto were created also.

DEM	13,404 x 13,839
Resolution of DEM [cm/pixel]	1.82
Orthophoto	27,064 x 27,942
Estimated GSD [cm/pixel]	0.9

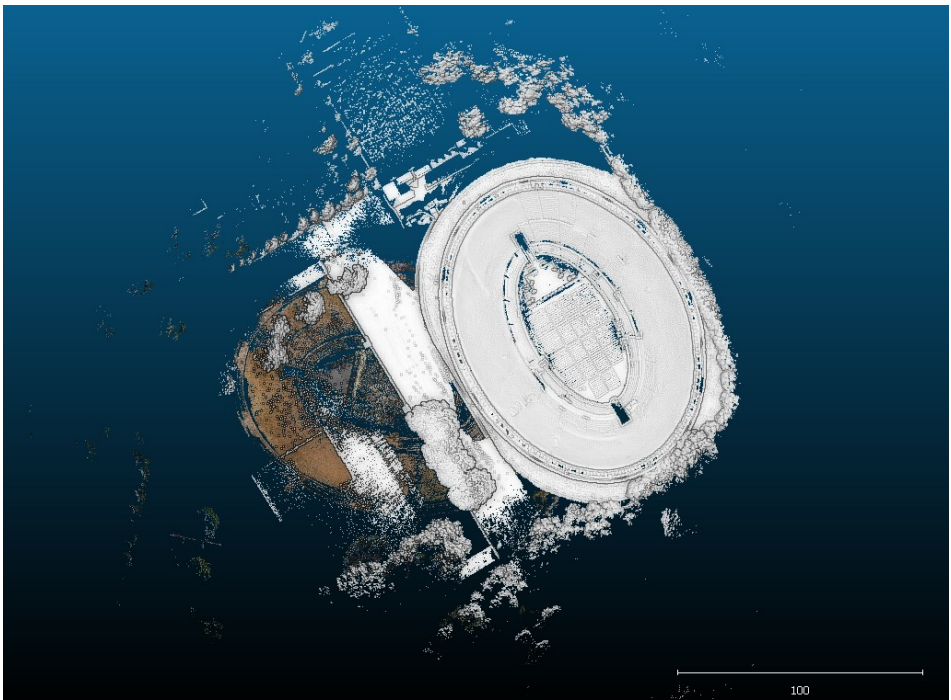
► Table 6 Parameters of other value-added metric products)

4.2.3. Processing of SLAM data

During the acquisition, a point cloud of the artefact was derived from each scan performed, as well as the close survey path performed by the operator. The process was executed by Go pro, the software supporting the SLAM scanner applied in this survey.

The aim of this processing basically is to record the various clouds of each work in the same (local) coordinate system and georeferencing the point cloud through the control point marked in the mapping path. However, the scans performed in this survey, especially those long ones, are mostly incomplete clouds and with a series of errors and drifts.

There were only 3 scans can be successfully processed with point clouds, even one of them could not be georeferenced and the last 2 were losing colour. For these reasons, the data should be used as much as possible through registering, colourizing and merging, as will be seen later.



◄ Figure 52 Final view of point clouds processed successfully

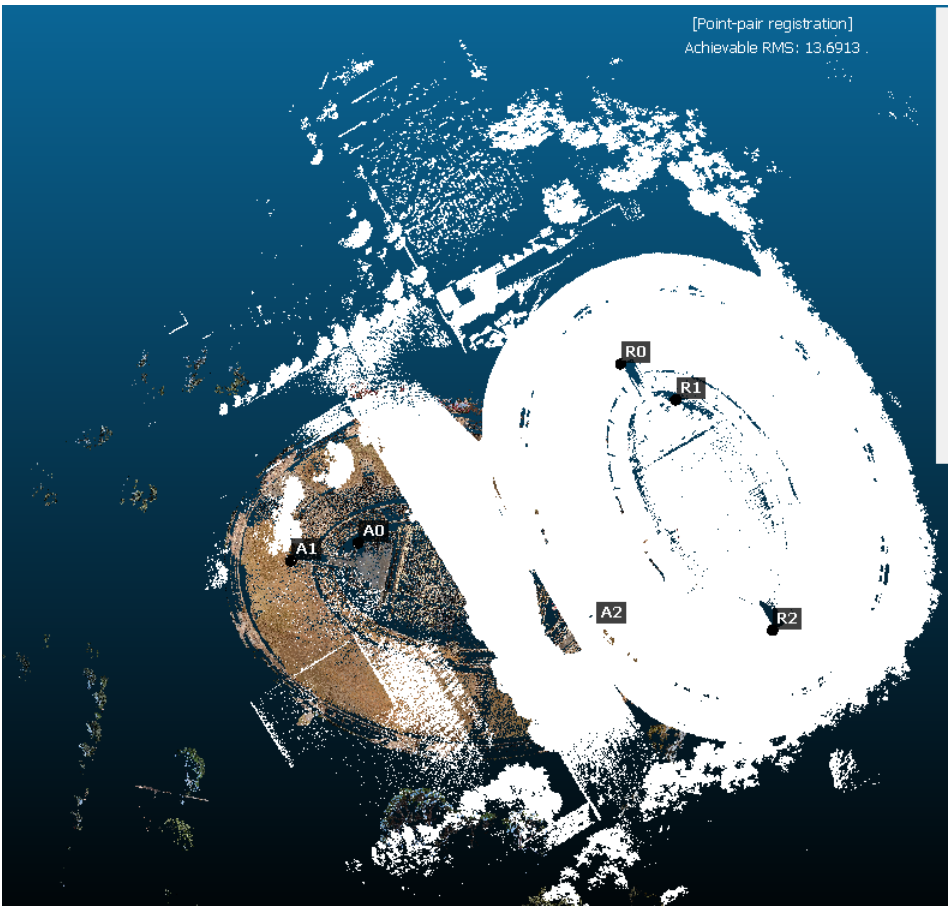
4.2.4. Products merging and visualisation

After processing of these 3 data sets of the survey, the products are:

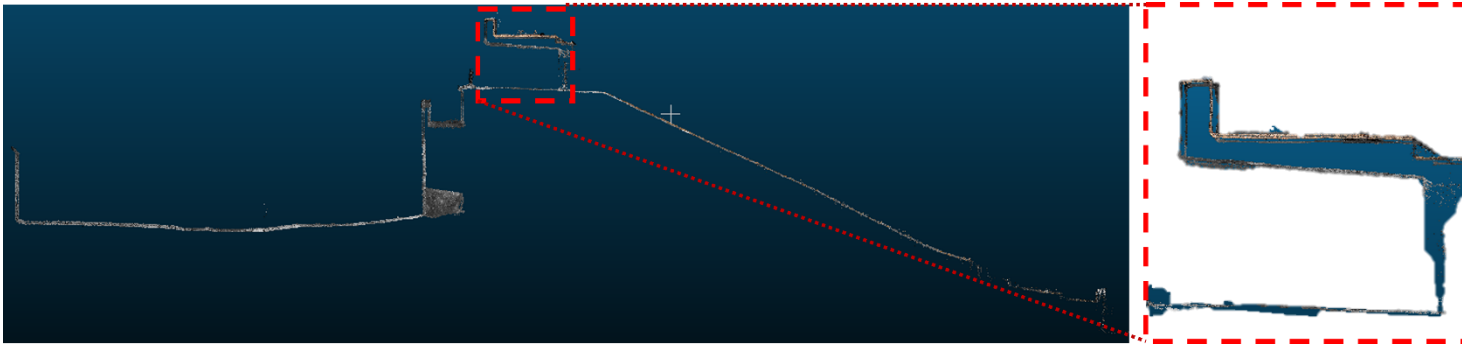
- 1 point cloud of the out appearance from UAV, with colour but lower dense.
- 1 point cloud scanned from the highest circular path of the building, lost colour but high dense.
- 3 point clouds scanned the corridor inside the building and the arches, one is not georeferenced.

To merge and complete the metric products, the point clouds firstly should be registered and merged as an entire block. As all the point clouds were georeferenced except one, the issue can be solved by using ICP registration to register the flying point cloud to the georeferenced ones in cloud compare, an open-source software to edit point clouds.

The operating logic is similar to the registration in Scene, the process for Lidar point cloud, to offer a better base for automatic ICP registration the software allows registering by manual picking the same feature points both in target point cloud and the reference one. After this step, two point clouds can be overlapped visibly to each other though it was not seamless.

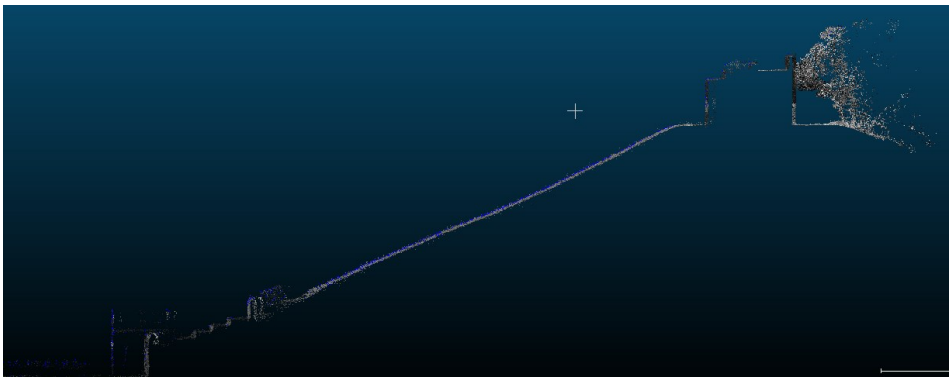


► Figure 54 Common feature picked from point clouds for registration



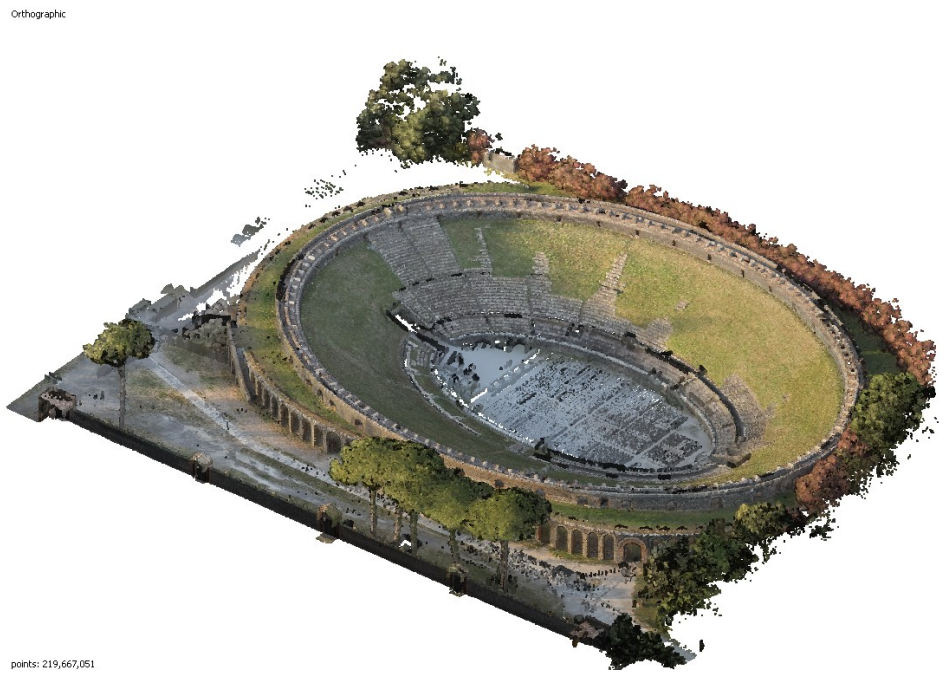
▲ Figure 53 Section view of the point clouds after manual registration

ICP registration can be performed automatically with different overlapped ratios can be set. After ICP registration, the point cloud was seamless with the target one, as the Figure 55 shows. and then, all the point clouds can be merged together as a block.



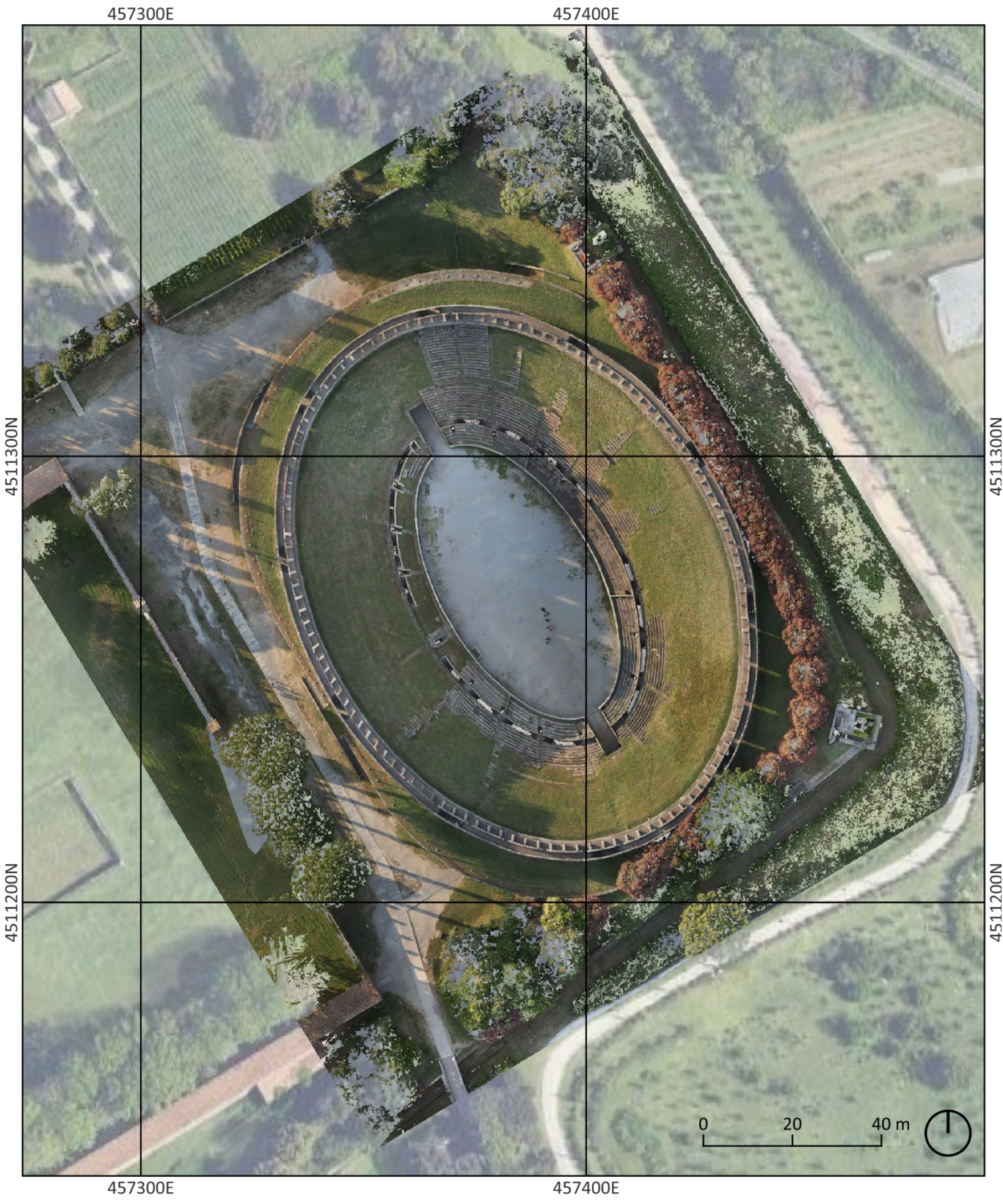
◀ Figure 55 Section view of the point clouds after ICP registration

As mentioned, the colour information was completely recorded in the data set of photogrammetry, which can be the source of colourizing. Agisoft Metashape Pro allows colourizing the point cloud according to the relation of the points' position and their photo source. After imported the merged point cloud, the colour information was attached through the relation between the point cloud and the photos.

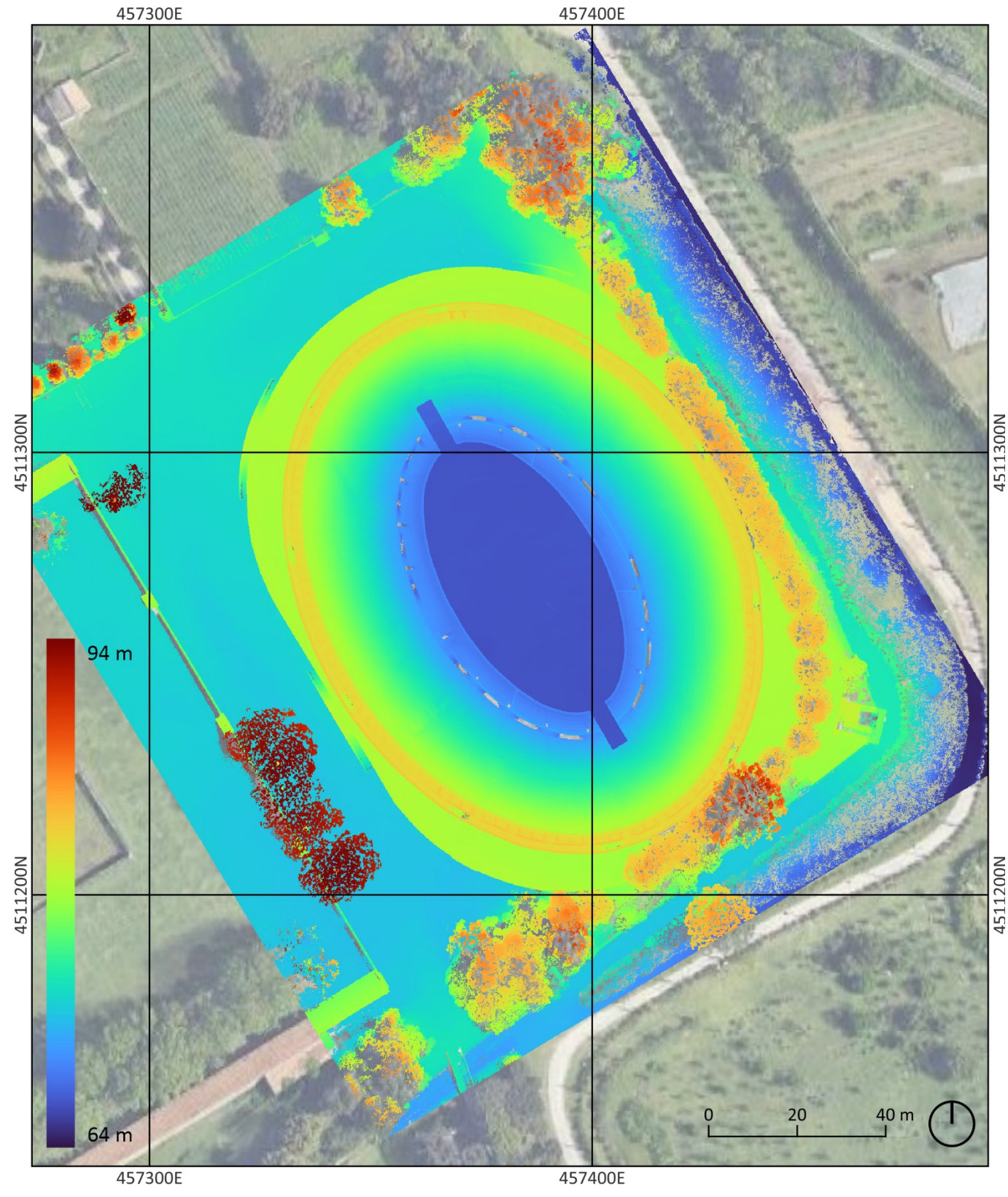


◀ Figure 56 Isometric view of the final point cloud coloured by the photogrammetry dataset

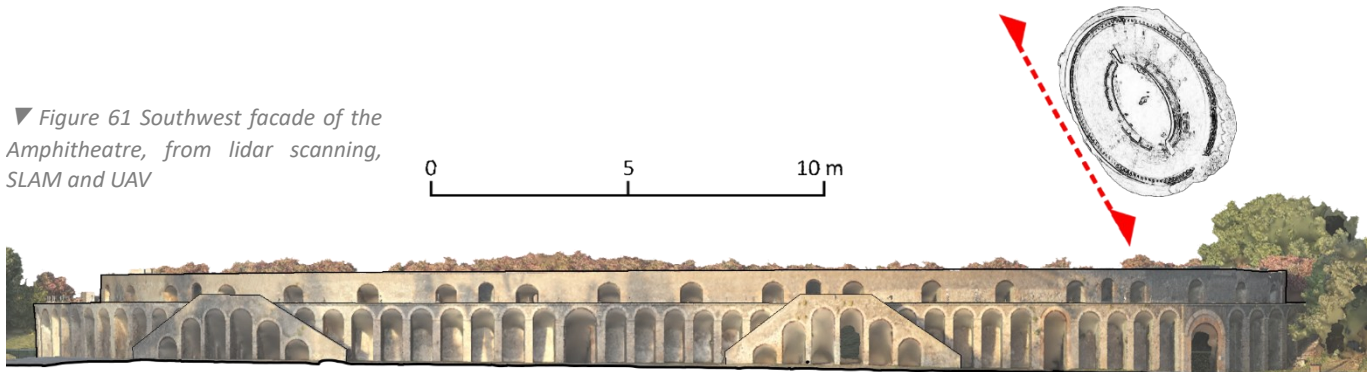
▼ Figure 57 Orthophoto of the Amphitheatre, from UAV photogrammetry



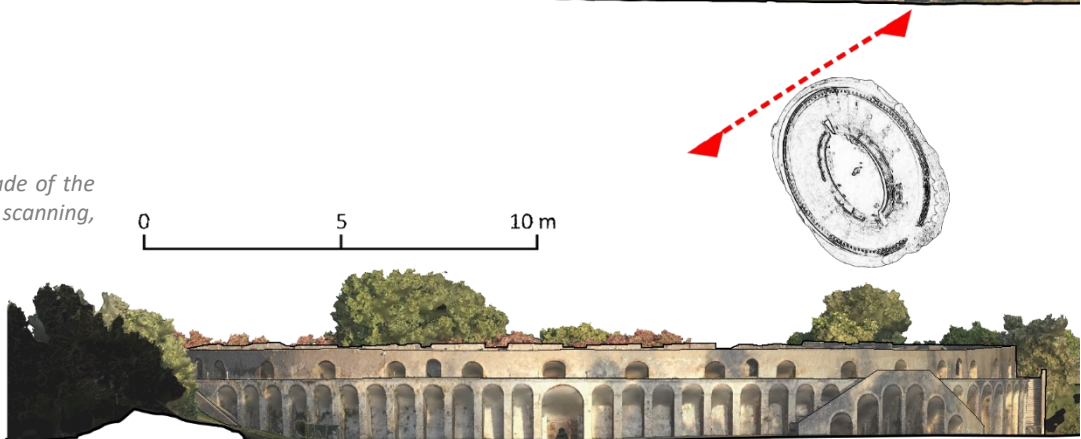
▼ Figure 58 DEM of the Amphitheatre, from UAV photogrammetry



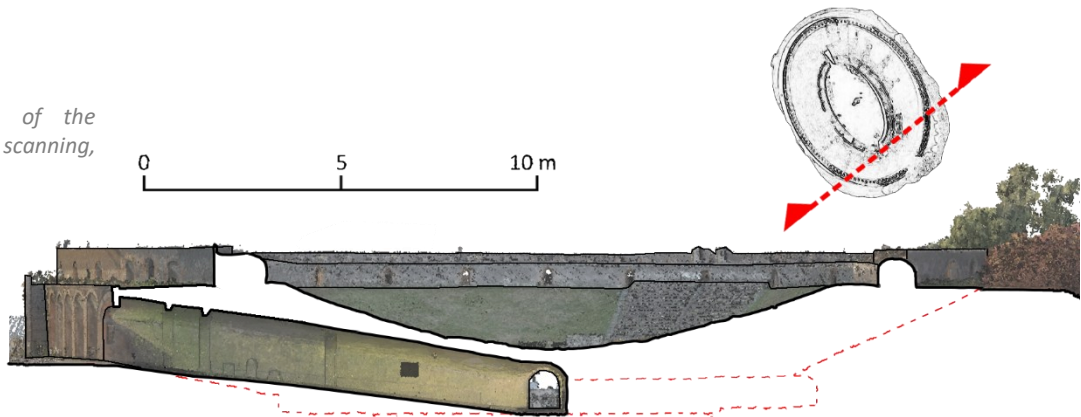
▼ Figure 61 Southwest facade of the Amphitheatre, from lidar scanning, SLAM and UAV



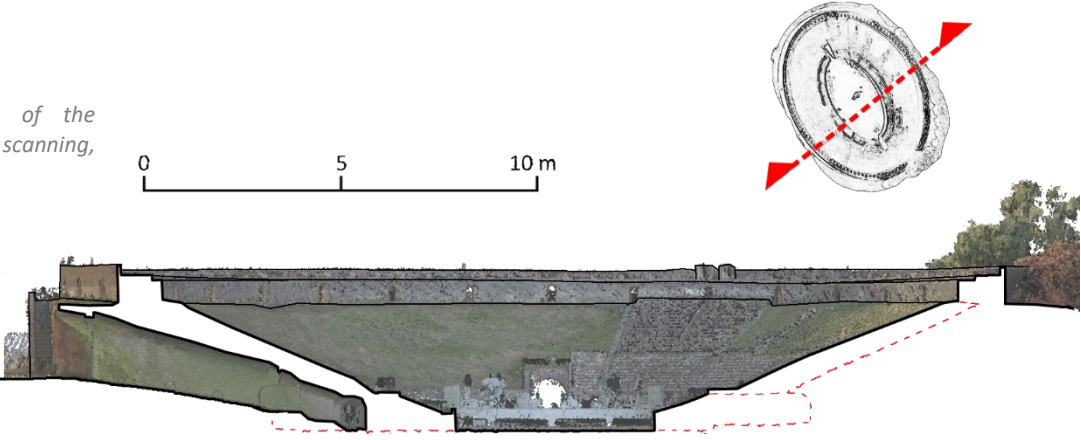
► Figure 60 Northwest facade of the Amphitheatre, from lidar scanning, SLAM and UAV



► Figure 59 Section A of the Amphitheatre, from lidar scanning, SLAM and UAV



► Figure 62 Section B of the Amphitheatre, from lidar scanning, SLAM and UAV



5. Multi-scale elements documentation: Riti Magici



5.1. 3D metric survey operations

Same as the case in the last chapter, 3D metric survey offers the geographic information, dimension and shape information as the base to define the project in the virtual space. This 3D metric survey campaign spanned 2 years, from 2023 to 2024 summer, purchasing various data by 2 generations of the DIRECT Team, including topography work, lidar scanning, UAV photogrammetry and close-range photogrammetry.

The objectives of this campaign are:

A 3D survey of the points well distributed on the building and the ground;

A lidar survey focusing the entire Complesso dei Riti magici;

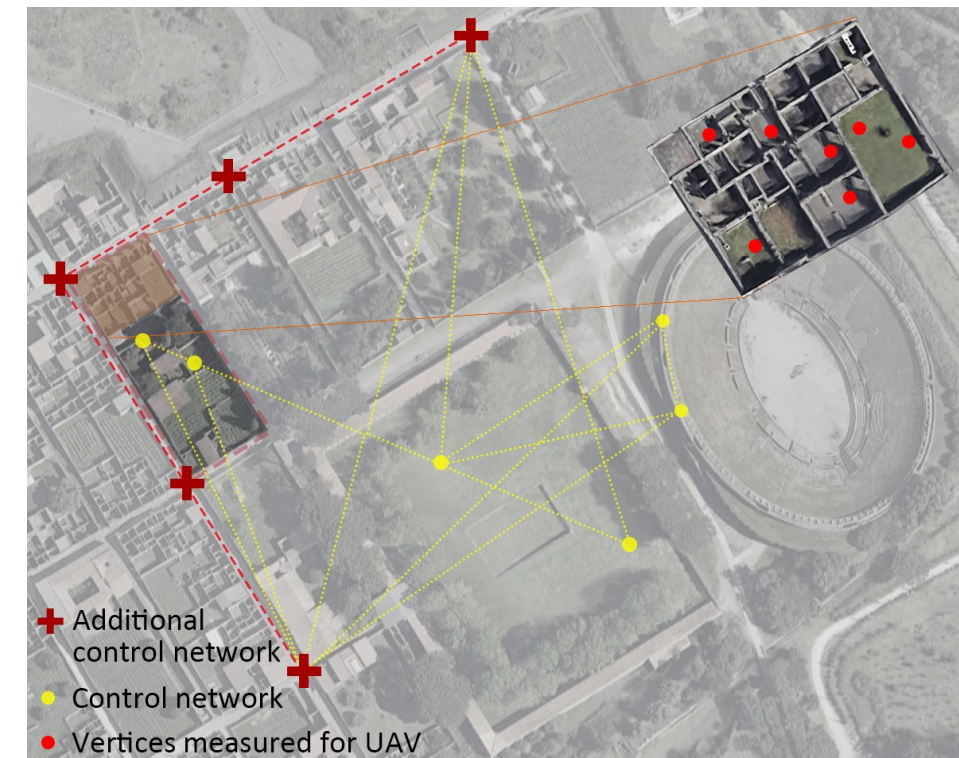
An aerial photogrammetric survey of the block which Riti magici located in using visible camera;

Several close-range photogrammetry surveys focusing the special archeological site and the room with colorful painting.

The workflow will be presented in the following paragraphs, as well as the strategies and the tools applied, to develop the value-added metric products.

5.1.1. Topographic survey

Same as the last case, the preliminary planning of the survey was held before proceeding with the topographic survey and, more generally, with the metric survey. As for this case, the different techniques were used for different serving areas, which are much different from each other. So the control points for control each survey area should be planned not only relating to the planned control network, but also should according to the specific survey area.



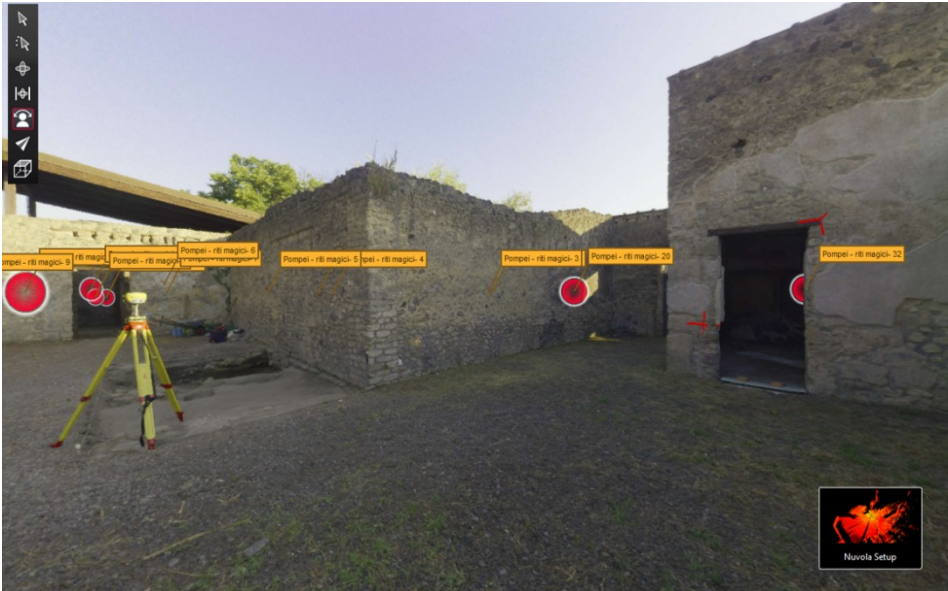
◀ Figure 63 Scheme of the topographic control networks, including the additional common control network, showing the relation with the Complesso dei Riti Magici

[Scheme of the survey areas, showing the relation between each other and the control network]

The strategy to deal with this situation, was developing 2 sets of control points relying on the common control network measured for all the cases in this thesis, one is focusing on the entire block and the other is only scattered in the Complesso dei Riti magici.

As for the vertices focusing on the entire block, planned for a relative flat case they were placed on the ground of the open area, with a great distribution. They were measured using RTK methods to determine the coordinates by positioning the receiver installed on the pole.

The survey focusing on the domus, especially the features can be measured from the ground, needs control vertices control with different altitude, instead of the vertices distributed on the ground. To offer a higher accuracy for the project, more vertices were placed with markers and measured using total station based on the point measured by GNSS technique.

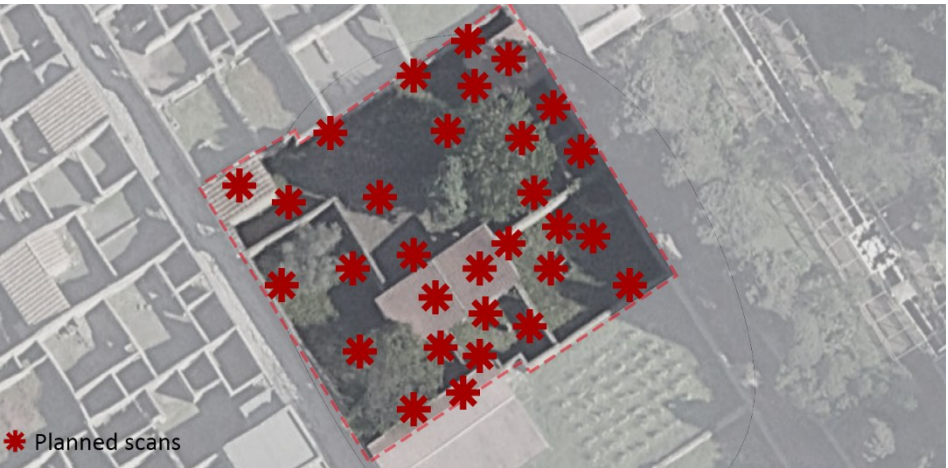


► Figure 64 the reference points located in the domus in a scene, appeared as red crosses

For the surveys of the projects with small scale, they include an interior space and two archaeological sites. For performing the survey more efficiently and getting a great overlapping ratio, the control points can be picked from the lidar dataset georeferenced, which were applied also in the last case.

5.1.2. Lidar scanner survey

As for the survey for this domus, the stage of planning was simple since the space is open and regular. The survey was held following the plan and the parameter of the scans were taken in a custom value to fulfil the survey need.



◄ Figure 65 Scheme of the planned scan position for the domus

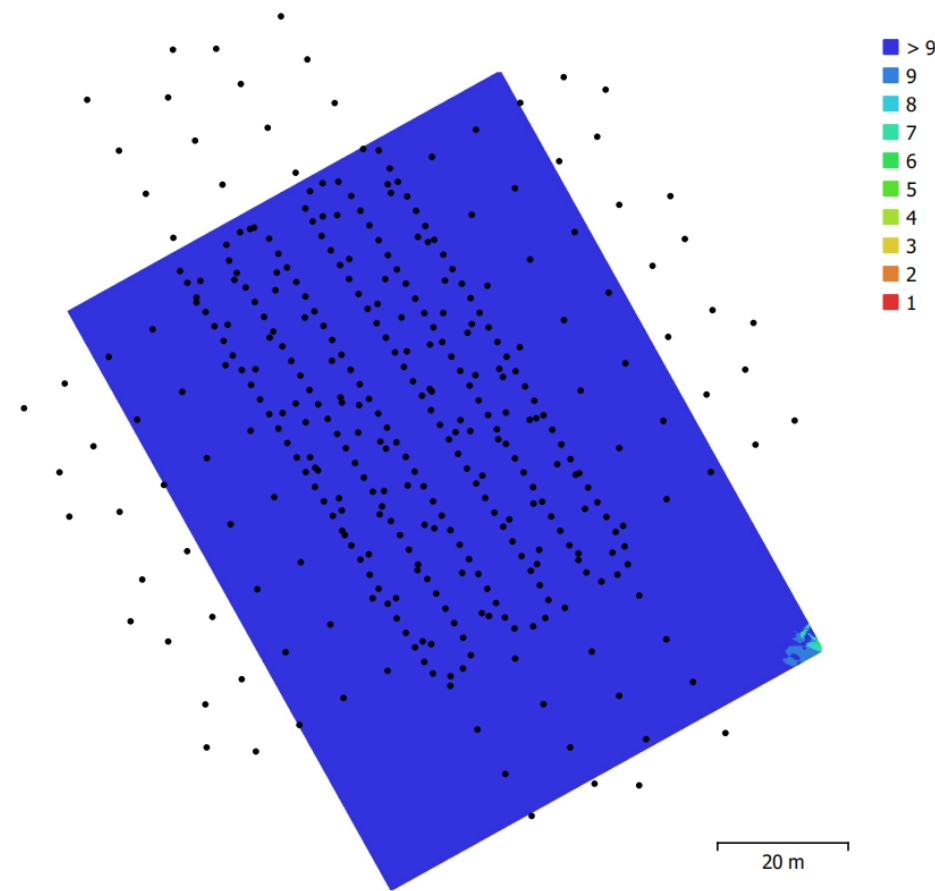
With the survey performed without any accident, the data was collected with a great quality. It offered a solid base for the following process of the lidar data and also a reliable data source for further operation, which will be presented in the following paragraphs.

5.1.3. Photogrammetric survey

This stage was including 2 series of surveys: the first part was Aerial photogrammetry, taking a longer time for a project with an automatic planned flight path in 2024; the other was close range photogrammetry, containing 3 areas of interests and 2 of them were performed in 2023. They'll be stated according to the type instead of the performed time.

Aerial photogrammetry covering the block

To acquire the result with a higher confidence but also consider the efficiency, the flight path was planned as 3 parts: 2 were planned as a cross shape with relatively sparse shooting for covering the entire survey area and the surroundings; 1 was planned covering the area of interests with dense shooting during the survey for acquiring a high confidence. With the high resolution camera, most of the frames were taken at the altitude of 38.5 metres but the survey still ensured achieve a GSD of approximately 1.1 cm.



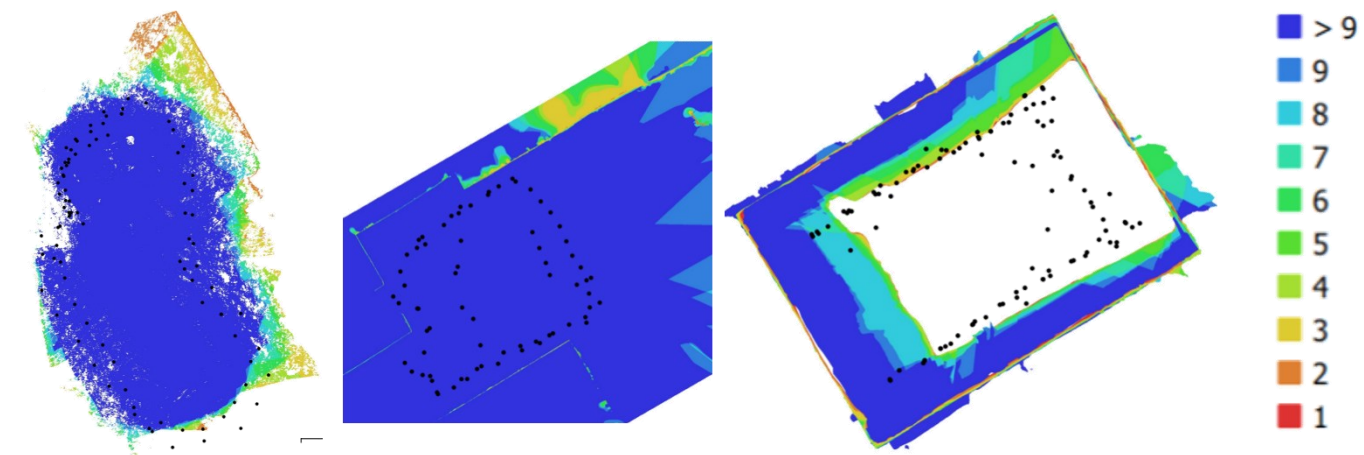
► Figure 66 Survey plan of camera position and the data confidence map of UAV photogrammetry

Close range photogrammetry

During the survey of big scale projects, the survey focusing on the small interesting points with great archaeological study value was performed. Because of the complex geometry or the close interior space shape, close range photogrammetry became the most efficient acquisition method with a high accuracy.

Following the principle stated before, the frames were taken with a fixed lens and camera parameters, which ensured a good overlapping ratio. As the dimensions were small, all of them got the resolutions, regarded as GSD in aerial photogrammetry, less than 1mm per pixel, which easily fulfilled the demand of the survey.

▼ Figure 67 Survey plan of camera position and the data confidence map of 3 close range photogrammetry projects



The data collected were processed to creating value-added metric products with an ideal level of detail, which will be stated in the following paragraphs.

5.2. Processing of multi-data

With the data collected during the survey campaign, the processing work, as this paragraph stating, can be concluded with a series of valued-added products. Also it will present how to register different point clouds and the results.

In the following sections, the statement follows the techniques' type, instead of the scale of projects. Apart from the operation itself, the differences and the links between the projects can be understood during this part.

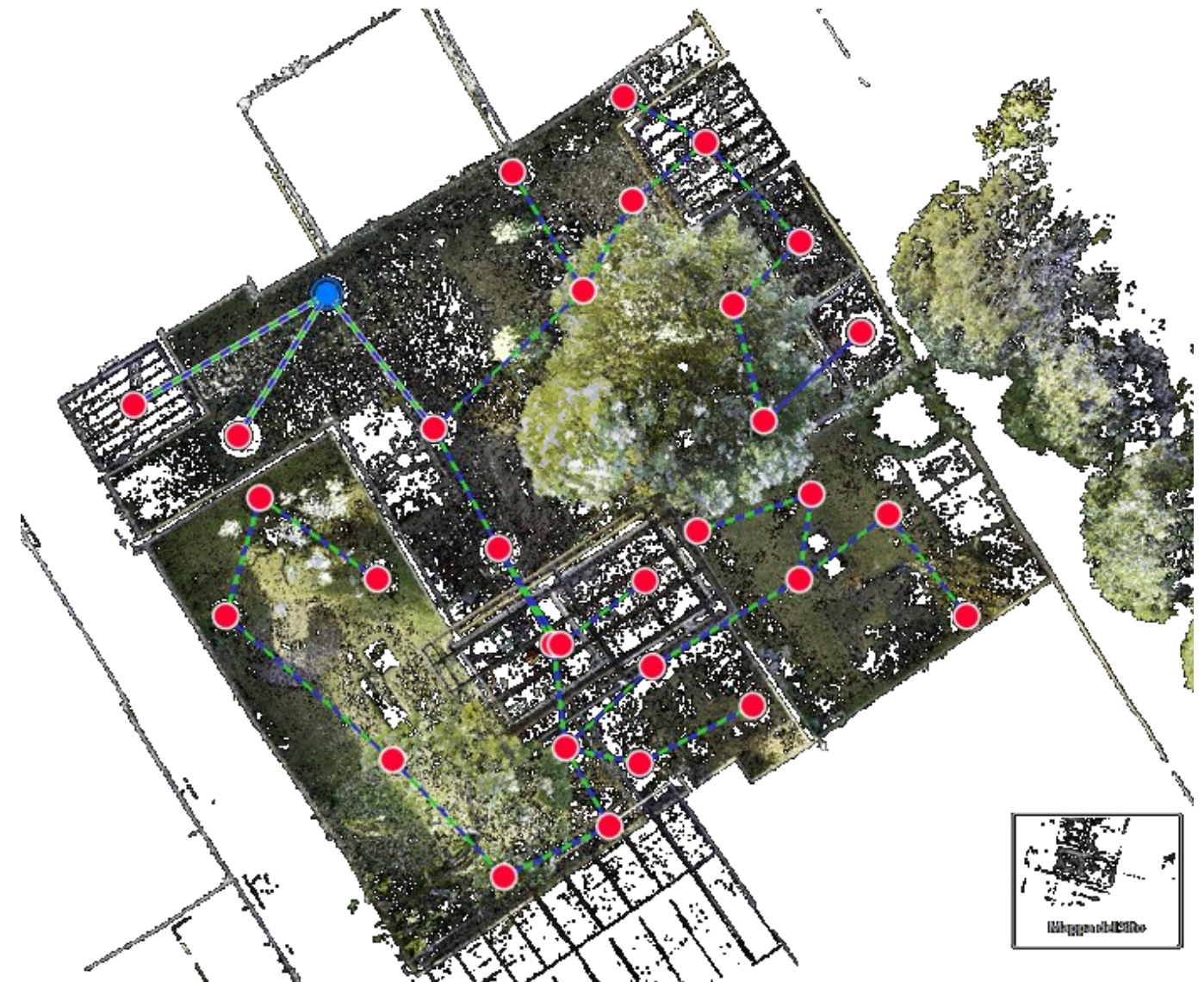
After processing, the final result with high level of detail will be present in the last section.

5.2.1. Processing of Lidar scans

This process was held in Leica Cyclone register 360, another commercial software supporting the Lidar scanner applied in this survey, which was different from the one used in the last case. This software allows registering and geofencing the scans acquired in the survey, along a similar working method, which basically relays on 3 registering ways: manual registration, ICP registration and GCP registration.

What was different in the operation is that the manual registration appeared as "linking the connection between different scans" with the help of algorithm instead of moving the scans manually, which can be regarded basically as a semi-automatic process. After connecting all the scans along the survey sequence, the ICP registration can be executed by the software. With the operation above, the point cloud had become a point cloud which included all the features in the space but without any geographic information such as its position in the real world.

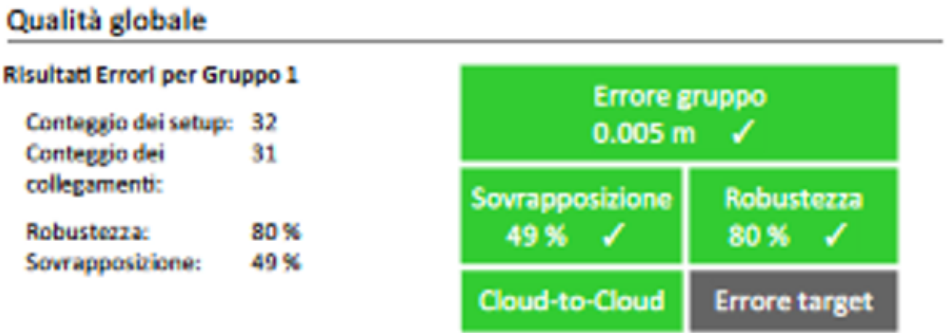
▼ Figure 68 Top view of the scans linked, with the point clouds related



As the last step, GCP registration allows importing the coordinates of the ground control points measured during the topographic survey. Through making the projections of the points, the accurate registration according to the control points would complete with the point cloud.



► Figure 69 Vertices used for GCP registration, with labels showing the informations



► Figure 70 the final accuracy of the registration, which showing the error of the result is less than 0.005m

Processing of photogrammetry

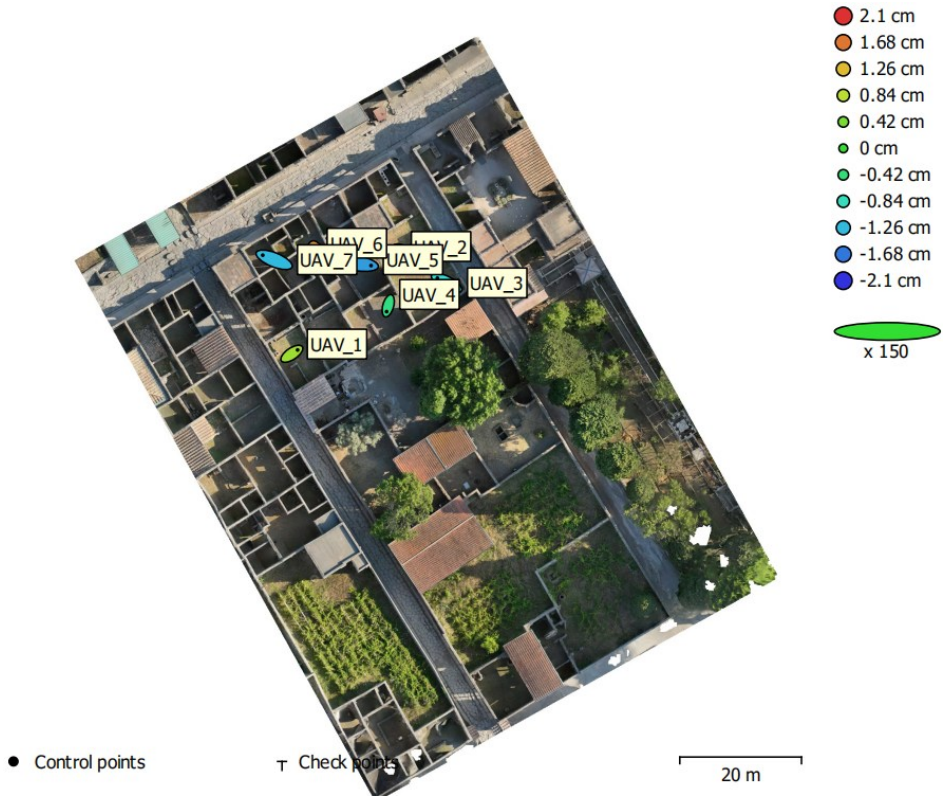
This process, same as the last case, was held in Agisoft Metashape Pro, but will be presented in 2 parts due to the small differences in the process: It will start with the process of Aerial photogrammetry covering the entire building block with GCP measured, and then the rest small interesting points measured with close range photogrammetry.

Aerial photogrammetry

After the first operation, importing all the relevant pictures acquired during the survey, the attached coordinates information should be removed also, which is same for all the aerial photogrammetry processing in this thesis.

Photos can be aligned by the software automatically, with adjustable precision setting in the interface. In this case, the high precision was selected to generate a series of detailed tie points. It took only about 9 minutes to compute the result, which includes 592,662 points with the file size 1.15 Gb.

After alignment, the model was completed with geometry shape but without the correct position or dimension. Control points can be imported in the project with their coordinates and act as the reference of orientating and scaling. Under the needed reference system named EPSG:32633 - WGS 84 / UTM zone 33N, the CSV file containing the coordinates of the vertices and should be imported into the project.



◀ Figure 71 Plan view of GCPs applied for georeferencing in the UAV photogrammetry

The collimation used 7 points in total, which distributed in the plain ground of the target area, as the Table 7 shows. And the average error of the project is 2.36 cm, which is perfectly fulfill the survey demand.

Label	X error (cm)	Y error (cm)	Z error (cm)	Total (cm)	Image (pix)
UAV_1	1.25808	0.840865	0.659861	1.65083	0.632 (11)
UAV_2	0.227357	-0.297387	2.05882	2.09257	0.689 (10)
UAV_3	-2.00896	1.05332	-1.02255	2.48817	0.618 (10)
UAV_4	-0.358512	-1.27858	-0.483156	1.41306	0.485 (10)
UAV_5	3.09833	-0.505476	-1.44663	3.45657	1.031 (10)
UAV_6	0.283725	-0.815558	1.50467	1.73484	0.721 (10)
UAV_7	-2.50003	1.00282	-1.27099	2.97846	0.926 (10)
Total	1.76187	0.883665	1.30523	2.36403	0.748

► Table 7 RMSE summary of GCPs of the UAV photogrammetry

After the collimation, the dense cloud with high precision can be derived by the software after 2 hours computing, which consisted 48,792,054 points.

Control points RMSE [m]	0.024
Dense cloud	48,792,054
File size [GB]	0.71
DEM	5,204 x 5,650
Orthomosaic	10,408 x 11,300

► Table 8 Parameters of the value-added metric products achieved)

This dense point cloud would offer the base of other value-added metric products. With the result, the points can be classified into different identities by manual selecting and classifying.

Close range photogrammetry

There were 3 small projects in this case using the data acquired in 2023 and 2024. Due to the repeated workflow, the statement will be only once and in general but with all the detail reported in the figures or tables.

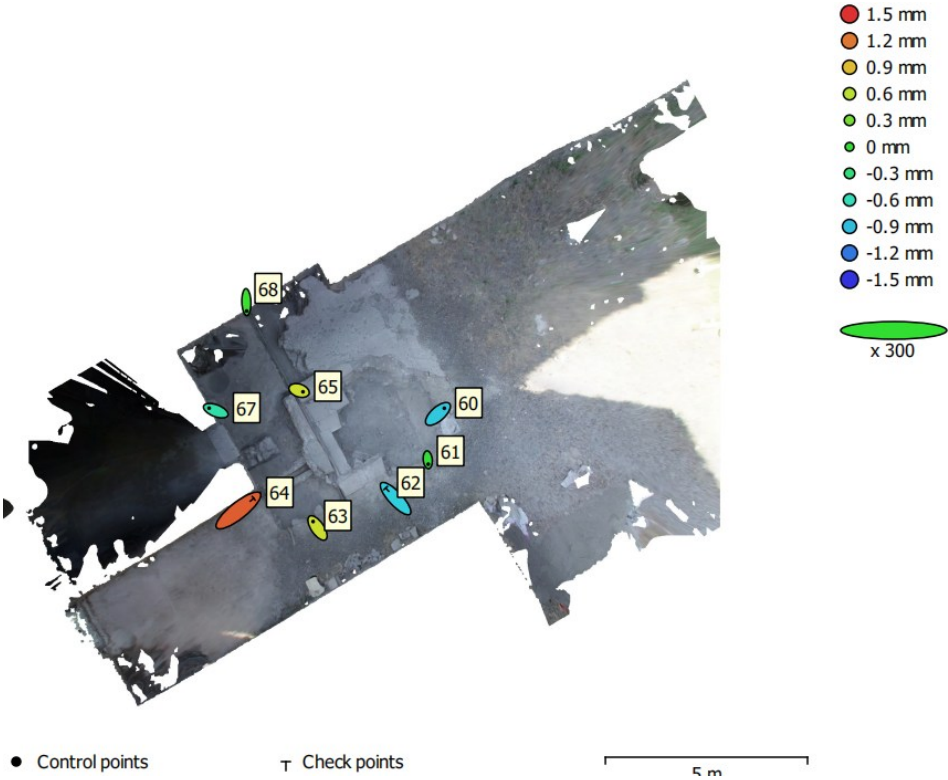
The first step was importing the frames related to the projects, same as aerial photogrammetry. A difference was that there was no coordinate information attached on the frames. As a result, the photos were directly aligned by the software without any operation.

	Pit 2024	Pit 2023	Room
Aligned cameras	70	95	102
Tie points	180,003	205,526	101,367
File size [MB]	230.18	315.68	335.41

► Table 9 Parameters of other value-added metric products)

To offer the position and dimension information to the projects, collimation using the control points was mandatory for them. But due to

the limited survey time and the working sequence of different survey teams, there was only a group of control points in the excavation pit of 2024 was measured during the survey campaign. As a result, control vertices of the rest 2 projects should be acquired.



◀ Figure 72 Plan view of GCPs measured for the archeological excavation in 2024

The method is same as the one applied in the last case: as there was a georeferenced point cloud as mentioned in the last section, it was workable to extract the coordinates of the single points in the entire scene through cloud compare, the open source software using for editing point clouds. Obeying the principle of selecting control points, natural feature points were extracted as well as their coordinates under the reference system used in other projects of this thesis.



◀ Figure 73 Isometric view of GCPs applied for georeferencing the painting room

The additional notice was that, the natural points was some solid and recognisable feature in the point cloud. As for the excavation pit in 2023, the selectable area for the control points were very limited since more than half of it was constructed by soil without a stable shape, the points were selected only on the bare stones instead of any other scattered points.



► Figure 74 Isometric view of GCPs applied for georeferencing the archeological excavation in 2023

After collimation using the points and the coordinates, RMSE or error, became the most important parameter to praise the result. As the figures below shows, all of the projects reached an accurate result.

Label	X error (mm)	Y error (mm)	Z error (mm)	Total (mm)	Image (pix)
60	1.05691	0.931934	-0.843928	1.64249	0.236 (10)
61	0.0734982	-0.731127	-0.0342255	0.735609	0.468 (10)
63	-0.730906	1.06194	0.666517	1.45127	1.451 (10)
65	0.644659	-0.216255	0.678644	0.960682	0.642 (12)
67	-1.09502	0.420436	-0.509987	1.27903	0.454 (5)
68	0.0508559	-1.46693	0.0429784	1.46844	0.519 (7)
Total	0.738682	0.904266	0.55978	1.29488	0.766

Table 5. Control points.
X - Easting, Y - Northing, Z - Altitude.

Label	X error (mm)	Y error (mm)	Z error (mm)	Total (mm)	Image (pix)
62	-1.62287	1.74069	-0.810472	2.51408	0.661 (10)
64	2.52806	1.99886	1.30952	3.47871	1.023 (8)
Total	2.12424	1.87423	1.08897	3.03496	0.841

Table 6. Check points.
X - Easting, Y - Northing, Z - Altitude.

► Table 10 RMSE of the close range photogrammetry projects: Archeological excavation in 2024

Label	X error (mm)	Y error (mm)	Z error (mm)	Total (mm)	Image (pix)
RA01	0.0294341	0.112774	0.118742	0.166385	0.124 (5)
RA02	-2.8401	0.776229	4.03066	4.99149	0.469 (5)
RA03	2.05829	-0.876068	-3.93967	4.53046	0.428 (5)
RA04	3.21526	0.739406	1.86629	3.79047	0.787 (5)
RA05	-4.39377	4.06015	-2.78241	6.59786	0.853 (5)
RA06	2.52286	-1.69497	6.57018	7.23913	0.378 (5)
RA07	1.79253	0.686605	-4.74421	5.11782	0.167 (5)
RA08	0.225731	-0.0268943	-0.633128	0.672702	1.122 (5)
RA09	-2.61024	-3.77724	-0.486459	4.61709	1.373 (5)
d0	0.441209	-0.908791	-1.80485	2.06834	0.010 (1)
point 2	0.936475	0.670977	2.35935	2.62559	0.012 (1)
Total	2.32497	1.84152	3.27723	4.42006	0.735

Table 4. Control points.
X - Easting, Y - Northing, Z - Altitude.

Label	X error (cm)	Y error (cm)	Z error (cm)	Total (cm)	Image (pix)
GA01	-1.3012	0.927945	0.23545	1.61544	0.352 (5)
GA02	0.700234	-1.09896	0.32292	1.34251	7.391 (5)
GA03	0.603812	0.593267	0.0600404	0.848622	0.890 (5)
GA04	0.0194371	0.0379648	1.57235	1.57293	3.812 (5)
GA05	-0.349799	1.09782	-0.686889	1.34141	1.720 (5)
GA06	-1.08316	0.590078	-1.23127	1.74283	1.150 (5)
GA07	1.41067	-2.14811	-0.2726	2.58432	0.612 (5)
Total	0.912924	1.10776	0.819211	1.65278	3.267

Table 4. Control points.
X - Easting, Y - Northing, Z - Altitude.

◀ Table 11 RMSE of the close range photogrammetry projects: Painting room

◀ Table 12 RMSE of the close range photogrammetry projects: Archeological excavation in 2023

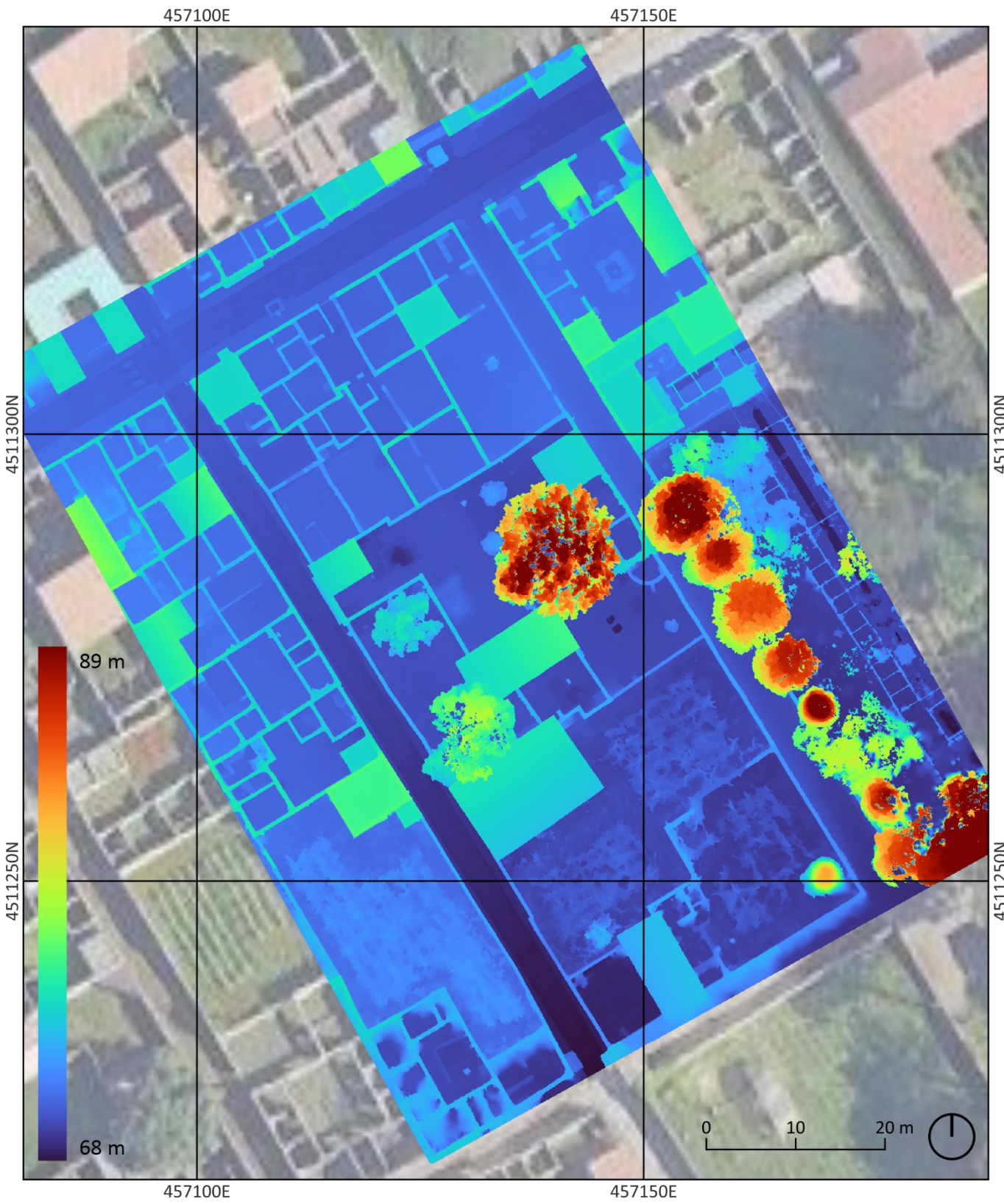
With the work above, a series of metric products could be developed, which will be presented in the next section. And some of them for example, point cloud, can be merged into the entire point cloud of the domus without additional registration.

5.2.2. Products visualisation

▼ Figure 75 Orthophoto of the insula
Complesso Riti Magici located in, , from
UAV photogrammetry



▼ Figure 76 DEM of the insula
Complesso Riti Magici located in, , from
UAV photogrammetry

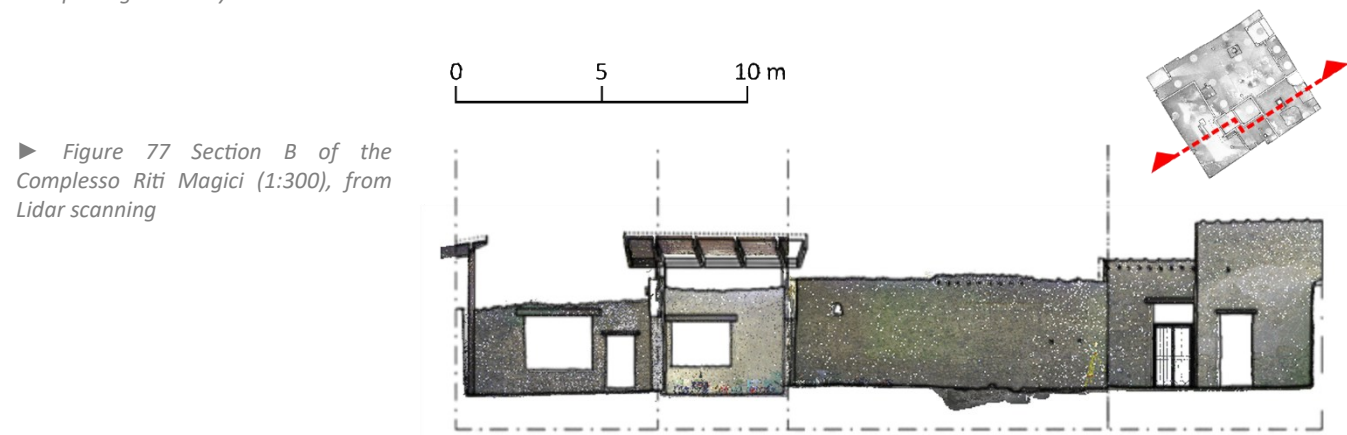




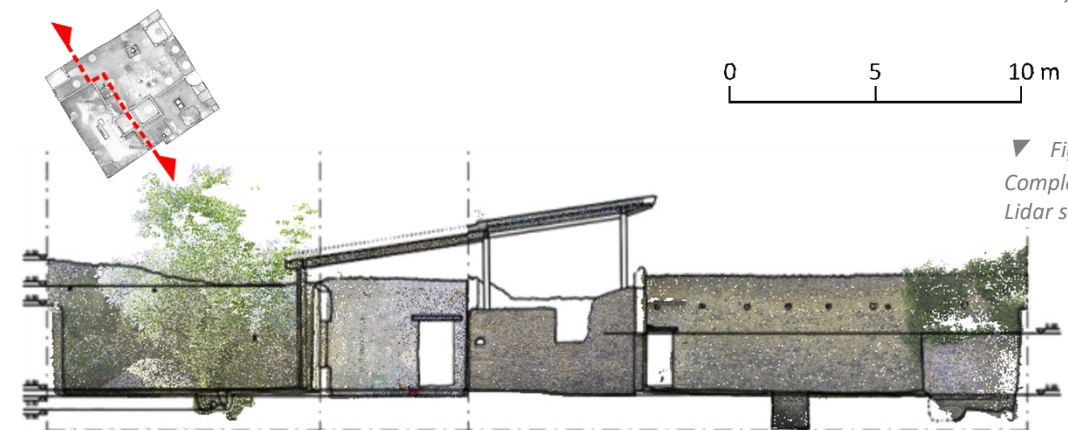
▲ Figure 78 Orthophoto of the Complesso Riti Magici located in, from UAV photogrammetry



▲ Figure 80 Plan of the Complesso Riti Magici (1:300), from Lidar scanning, overlaying on the UAV map



► Figure 77 Section B of the Complesso Riti Magici (1:300), from Lidar scanning



▼ Figure 79 Section B of the Complesso Riti Magici (1:300), from Lidar scanning



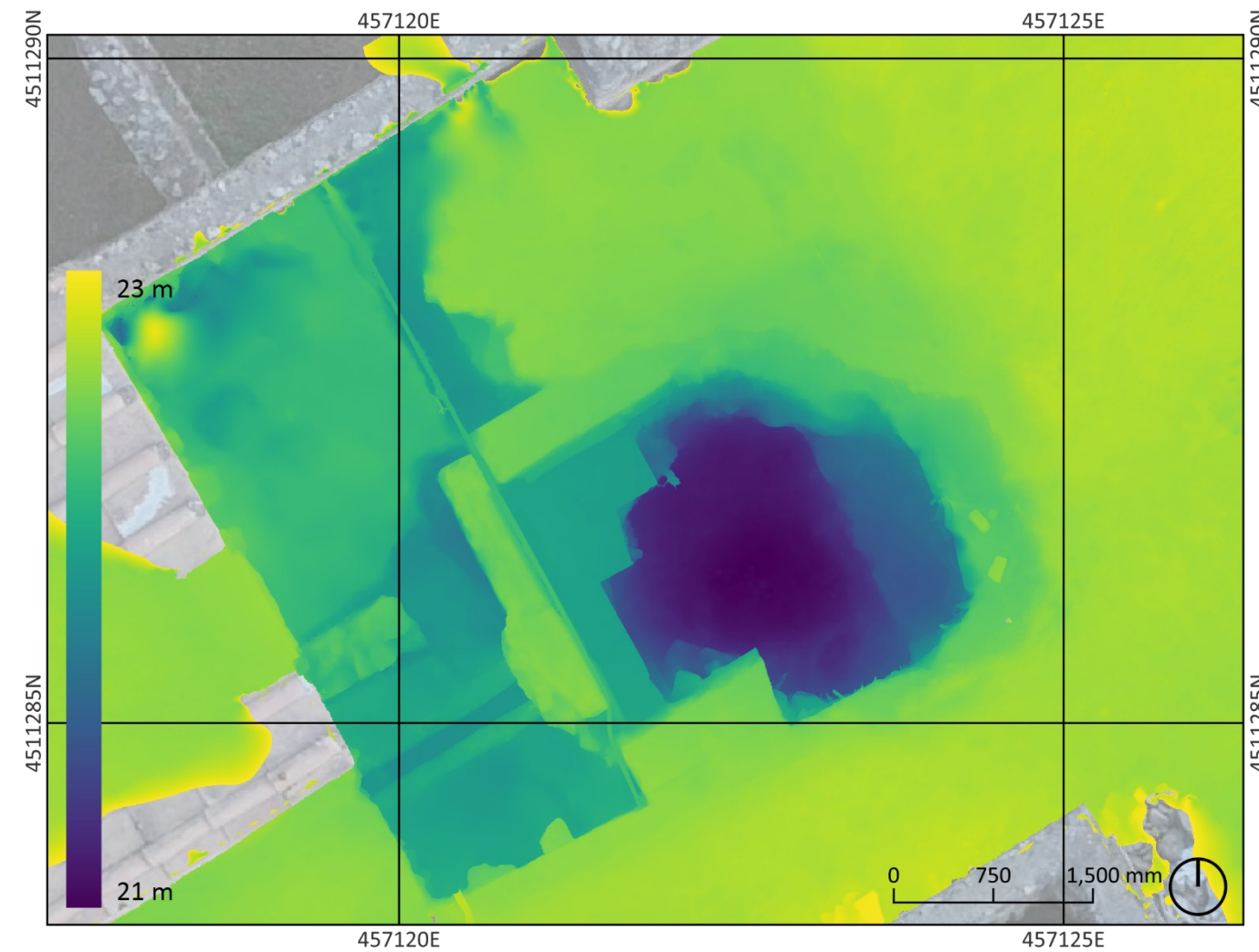
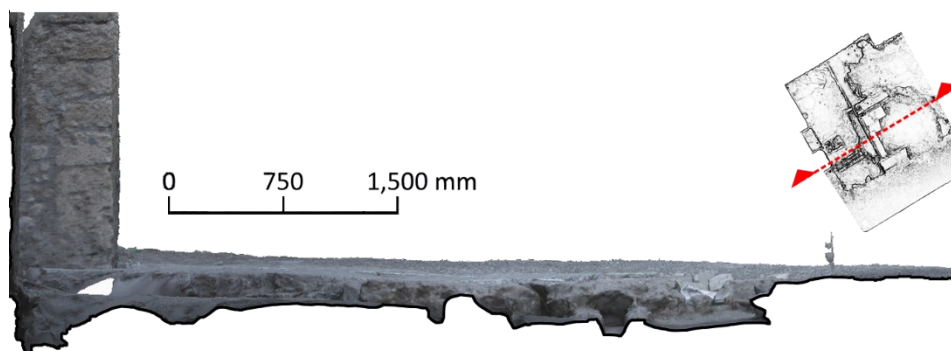
▲ Figure 81 Orthophoto of the archaeological excavation in 2024 in Complesso Riti Magici, from close range photogrammetry

0 750 1,500 mm

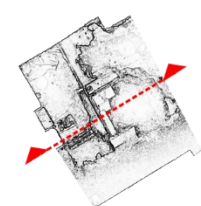
► Figure 83 Section A (1:50) of the archaeological excavation in 2024 in Complesso Riti Magici, from close range photogrammetry



► Figure 82 Section B (1:50) of the archaeological excavation in 2024 in Complesso Riti Magici, from close range photogrammetry



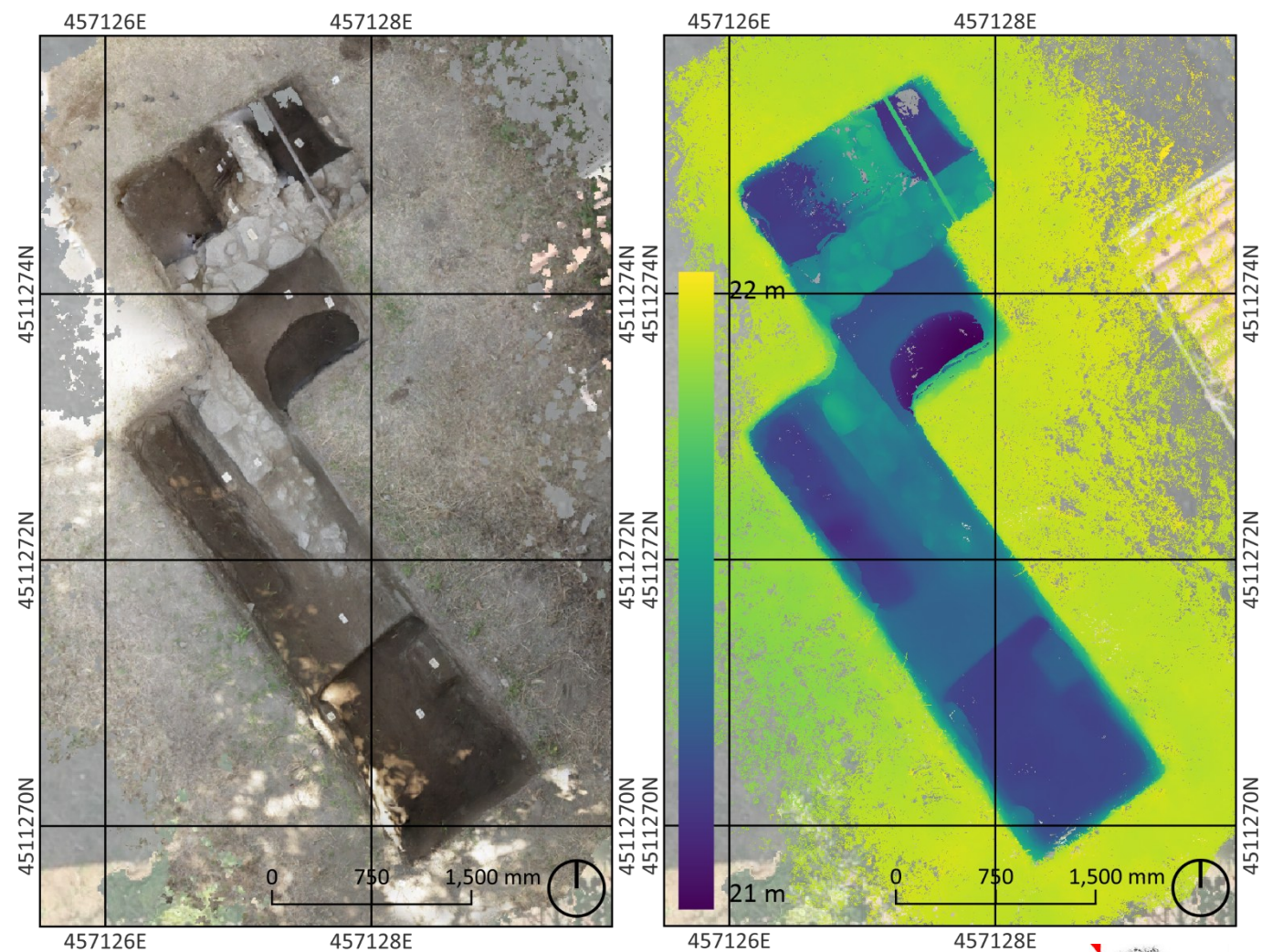
▲ Figure 85 DEM of the archaeological excavation in 2024 in Complesso Riti Magici, from close range photogrammetry



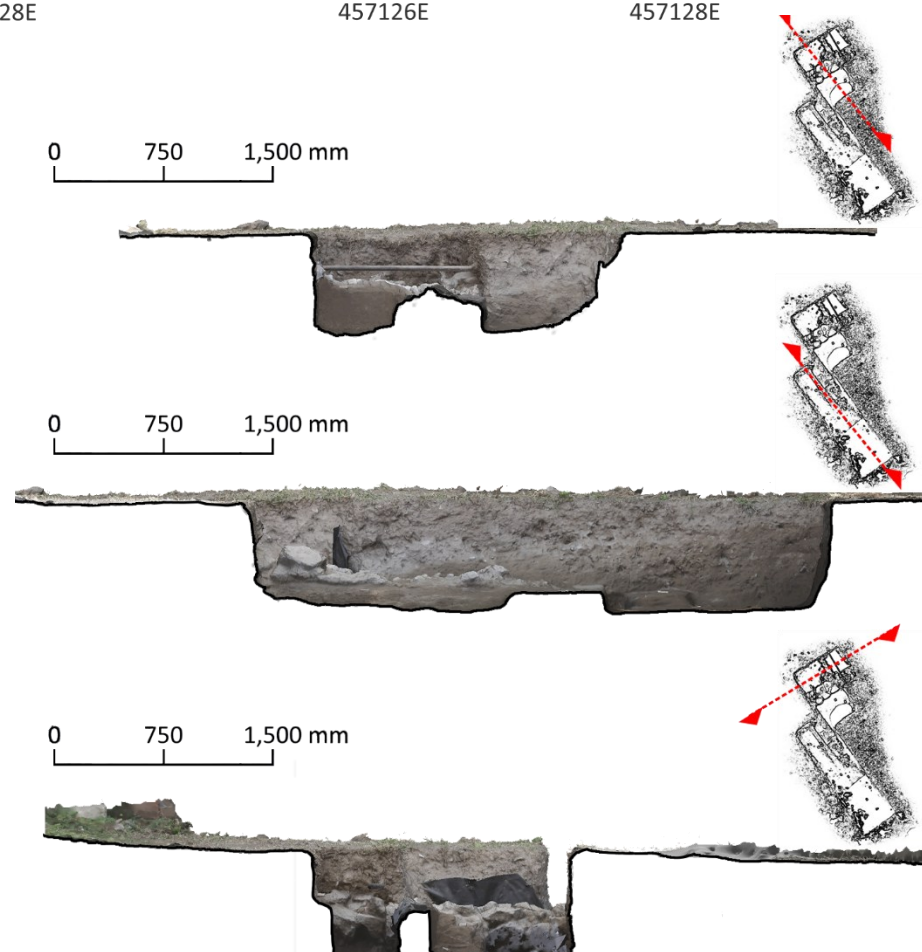
0 750 1,500 mm

◄ Figure 84 Section C (1:50) of the archaeological excavation in 2024 in Complesso Riti Magici, from close range photogrammetry

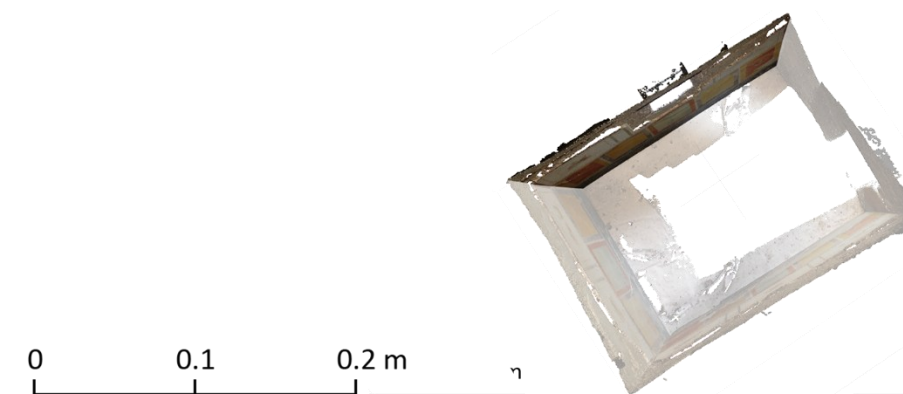




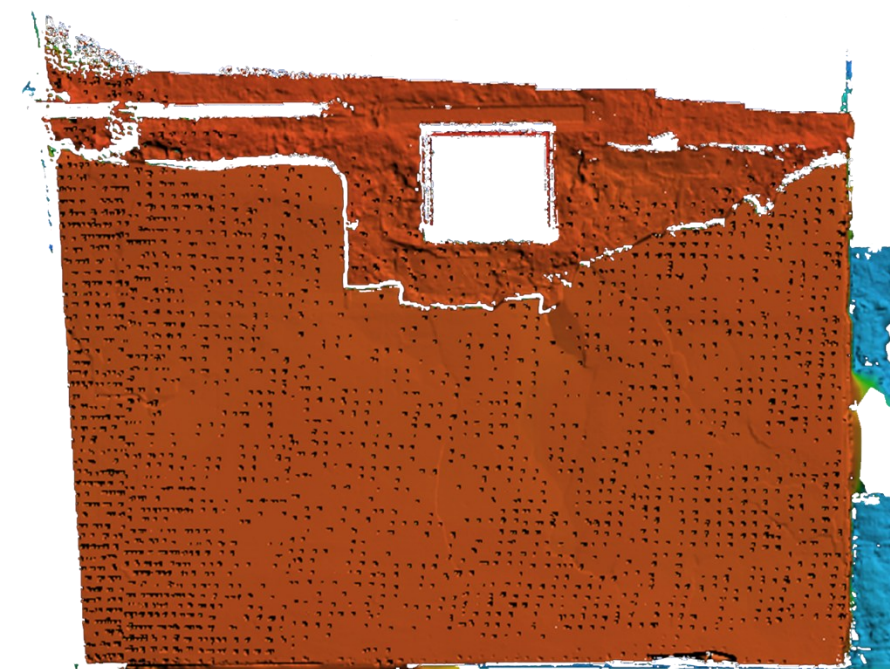
▲ Figure 87 Orthophoto (left) and DEM (right) of the archeological excavation in 2023 in Complesso Riti Magici, from close range photogrammetry



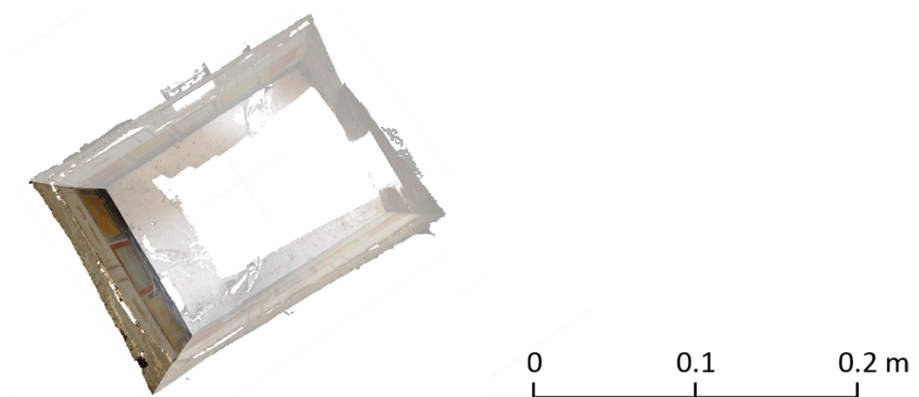
► Figure 86 Section A, B, C (1:50) of the archeological excavation in 2023 in Complesso Riti Magici, from close range photogrammetry



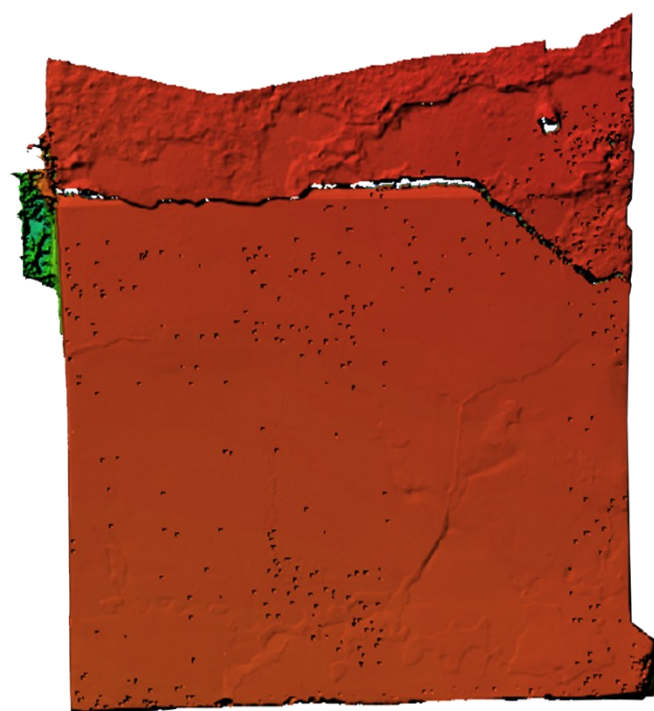
◀ Figure 88 Interior elevation A (1:50) of the painting room in northwest of Complesso Riti Magici, from close range photogrammetry



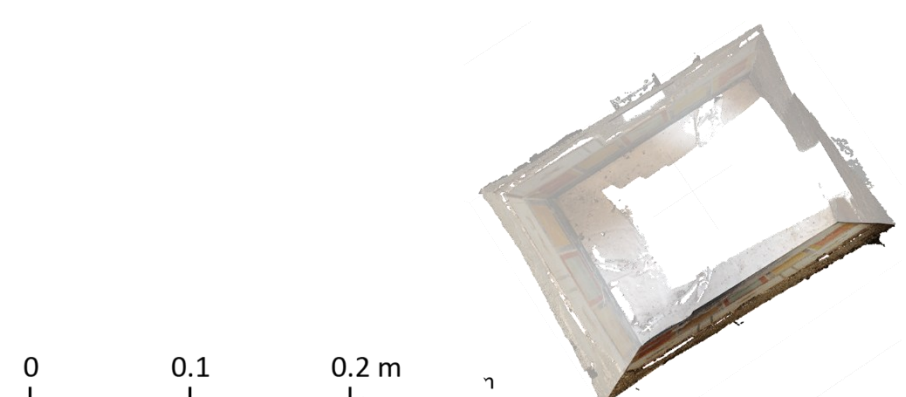
◀ Figure 89 Interior elevation A's DEM (1:50) of the painting room in northwest of Complesso Riti Magici, from close range photogrammetry



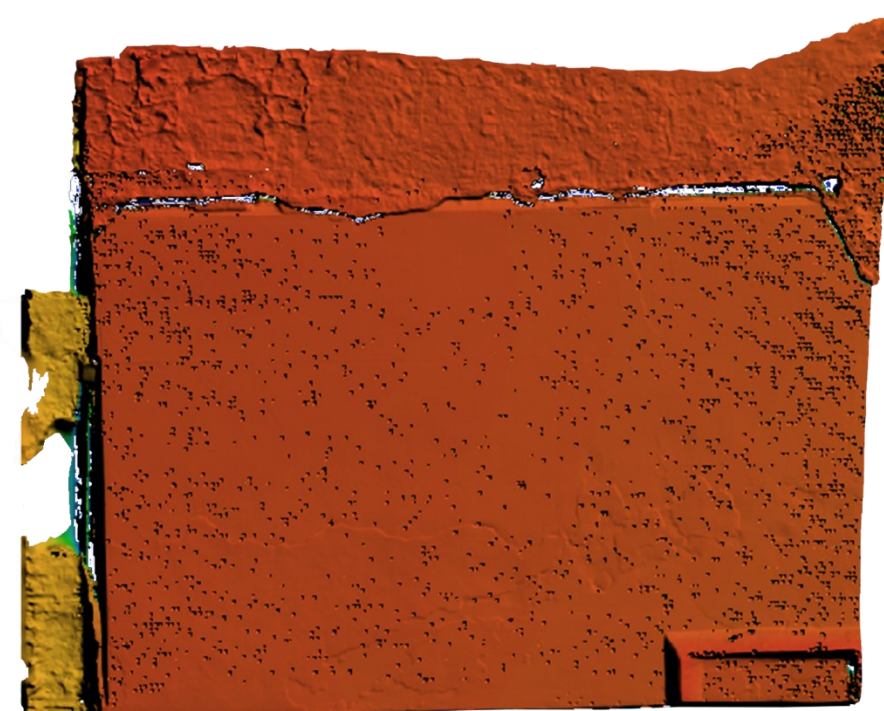
► Figure 90 Interior elevation B (1:50) of the painting room in northwest of Complesso Riti Magici, from close range photogrammetry



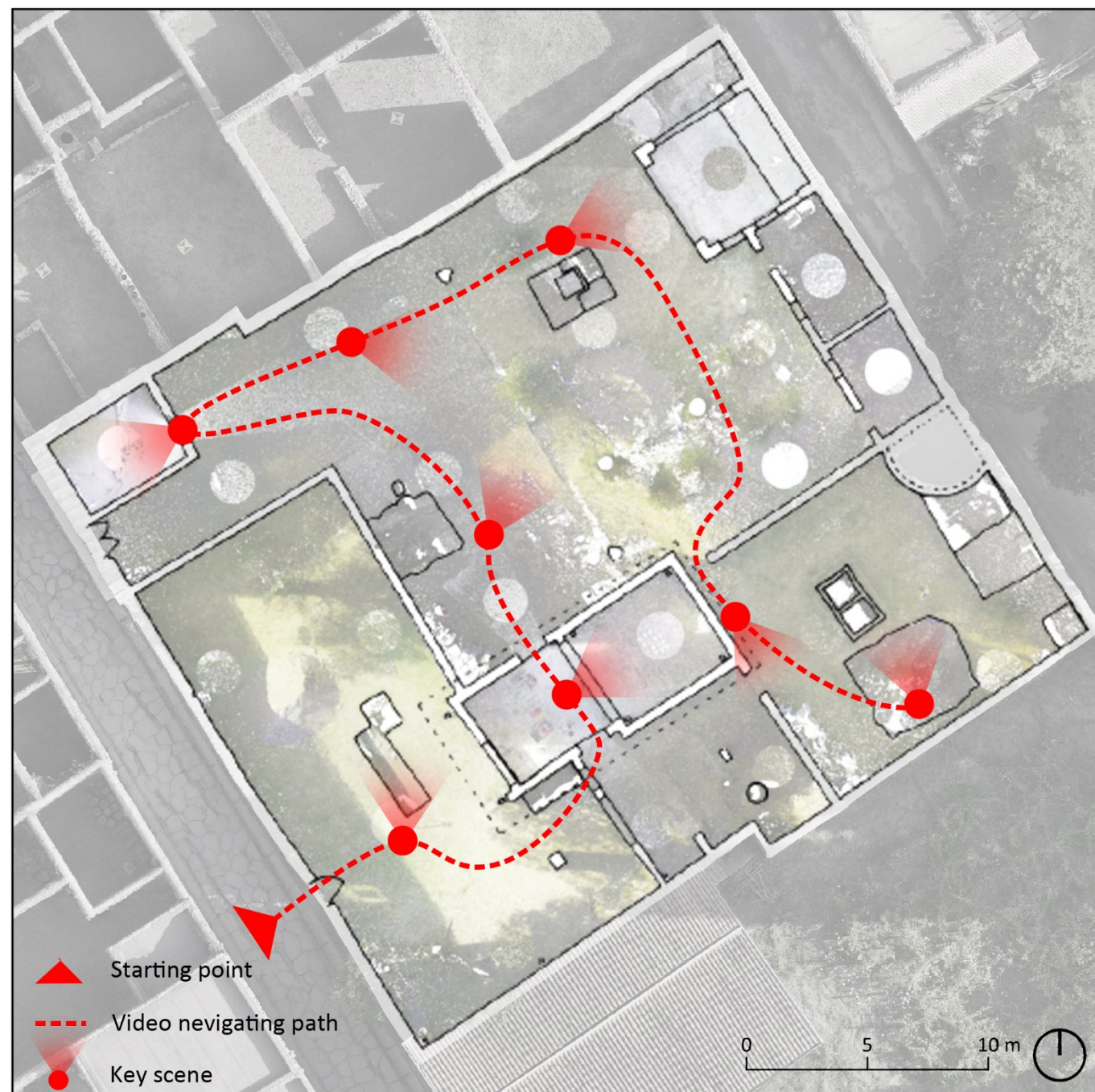
► Figure 91 Interior elevation B's DEM (1:50) of the painting room in northwest of Complesso Riti Magici, from close range photogrammetry



◄ Figure 93 Interior elevation C (1:50) of the painting room in northwest of Complesso Riti Magici, from close range photogrammetry



◄ Figure 92 Interior elevation C's DEM (1:50) of the painting room in northwest of Complesso Riti Magici, from close range photogrammetry



▲ Figure 94 Video plan of navigating tour in the complesso dei Riti Magici, with key scenes posed



► Figure 95 Screenshot of video frames in Recap pro

6. Non-visible investigations: Praedia of Iulia Felix



6.1. 3D metric survey operations

As the previous chapters presented, 3D metric survey offers the geography information of the project, as well as its shape and dimension, through the data collected by different techniques.

The 3D metric survey campaign, carried out in the summer of 2023 in Pompeii, followed these principles, combining the application of different technologies to obtain an accurate survey of the area and the heritage there. As mentioned, this survey campaign, carried out by professors, researchers and students, members of the DIRECT Team, saw the contribution of topography and UAV photogrammetry, with 2 different objectives:

- A 3D survey of the points well distributed in the area connected to the case;
- An aerial photogrammetric survey of the area containing Praedia of Iulia Felix, with both visible camera and multispectral camera.

In the following paragraphs, the strategies, tools and operational workflows that led to the development of a series of value-added metric products will be analysed in greater depth, which were then used in the graphic restitutions of the various elements surveyed.

6.1.1. The topographic survey of the framing network

Same as the previous cases, the preliminary planning of the survey should be held before proceeding with the topographic survey and, more generally, with the metric survey.

The survey area is covering Praedia of Iulia Felix, Palestra Grande and their surrounding area, extending for about 250m in the south-east and 150m in the north-west, as Figure 96 shown.

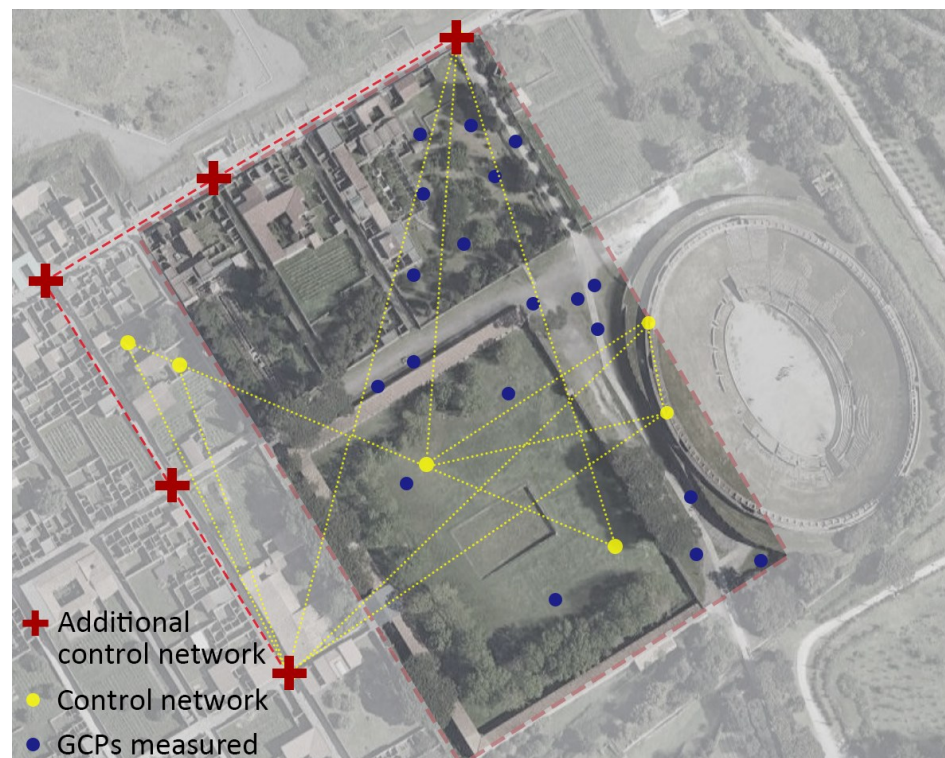


◀ Figure 96 Survey area of case Praedia Felix

Same as the previous cases, the topographic survey of this case still based on the topographic control network consisting of 6 topographic vertices established in Regio II. It enabled the management of all the 3D spatial data, even they become from different cases, within a same reference system.

With this general base, ground control points are planned well scattily in this survey. Same as other cases in this thesis, the vertices were positioned with markers or natural feature points within the area of the topographic control network. So, the points can be measured efficiently and attach convincing information to this photogrammetry area. As the Figure 97 presenting, here are 18 vertices covering the whole survey area.

► Figure 97 Scheme of the topographic control networks, including the additional common control network, showing the relation with the area of interests



The positioning and measurement of vertices in this area were carried out on the first day of the survey campaign. And the measurement was divided into two different stages: the first stage, as described in previous chapters, focused on using static GNSS methods to measure the added vertices of the topographic control network, they were combined with the vertices measured in past years to build up the topographic control network using in this case. The second stage used RTK methods to determine the coordinates of the other GCPs, where the operator positioned the receiver installed on the pole to each individual point.



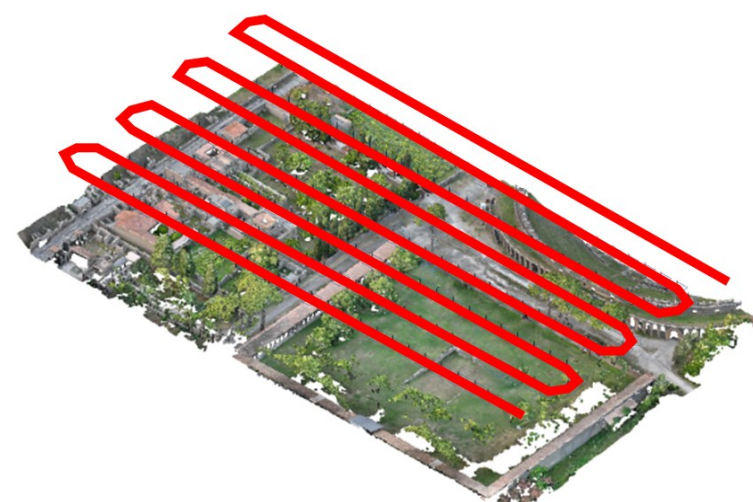
▲ Figure 98 Photo of a vertex located in the survey area

Measuring control points in the same reference frame allows for geographic registration of all data obtained from different 3D measurement methods used during the acquisition process, thereby enabling geographic registration of different measurement products held in Pompeii Regio II. In this case, during each different UAV flight, the measurement markers placed on the ground are accurately captured by the camera installed on the drone, and therefore also appear in the frame.

6.1.2. Aerial photogrammetric survey

During the survey campaign for this case, different photogrammetry acquisitions were undertaken by UAV, with the main objective to carry out an extensive survey of the entire area, by performing plural acquisition flights. Particularly, in this case, a total of 4 flights were carried out with the same cover area, on different time point and based different UAV systems.

During the survey campaign, the acquisition flights were carried out in couples, allowing the acquisition of frames with both visible and multispectral sensor, namely, in the Red Edge (RE) and Near Infrared (NIR) band. For this task, the DJI Mavic visible UAV system and DJI Mavic 3M multispectral UAV system were employed, so that the same automatic



◀ Figure 99 Scheme of the flight plan in this case

flight path can be arranged easily due to the similar system.

The visible UAV system is equipped a Complementary Metal-Oxide-Semiconductor (CMOS) sensor focusing RGB bands with a higher resolution. While the multispectral UAV system is equipped 4 CMOS sensors that allow the acquisition of single-band images at specific wavelengths: Green ($560 \text{ nm} \pm 16 \text{ nm}$), Red ($650 \text{ nm} \pm 16 \text{ nm}$), RE ($730 \text{ nm} \pm 16 \text{ nm}$), and NIR ($860 \text{ nm} \pm 26 \text{ nm}$). In this regard, it should be underlined that the photogrammetric acquisitions using all five sensors were performed simultaneously to ensure that the sunlight conditions on the ground remained as consistent as possible.

Additionally, repeating the flights both in the morning and afternoon can enhance the ability of the reflected radiation response from wavelengths in the non-visible spectrums to identify possible submerged structures. It is allowed for a comparison between the effects of different sunlight conditions on the ground.

The flight planning was carried out considering several crucial aspects. Due to the presence of trees, the flight altitude was planned to avoid interference with the foliage, while ensuring a GSD of approximately 1.5 cm, as regards the traditional visible images, and 2.5 cm, as regards the multispectral photogrammetric block. This was done to guarantee an appropriate resolution and the desired level of detail. The flight altitude that ensured a balance between these two parameters was approximately 50 m, based on the sensors of the applied system's cameras.

During the acquisition phase, the camera underwent radiometric calibration, which helps adjust camera settings to avoid reaching maximum reflection values, thereby avoiding image saturation and information loss. Usually, radiation calibration is performed through a calibration panel placed on the ground of the flight area, where the surface has known reflection values. Therefore, camera calibration is achieved by establishing a linear relationship between the DN value of the obtained image and the reflection value of the panel.

Because of the different weather conditions during the flights and the short possible flying times in the famous archaeological park, this flight has been realised in a much faster and more expeditive manner without setting up a radiometric calibration panel.

The frames obtained were processed with the aim of creating value-added metric products from which to derive both the graphic restitutions of the survey area and the subsequent analyses. These processes will be described in the next paragraph.

6.2. Processing of photogrammetry (visible datasets)

In the actual surveying activity, after the data acquisition process using the techniques and tools described in the last paragraph, the processing of data and the results achieved naturally become the focus of this paragraph's discussion.

The first section of this paragraph will explore the main aspects related to photogrammetric processes, focusing on the processing of visible data, and the generation of dense point clouds and related measurement products through these processes.

Meanwhile, the multispectral data processing will be presented in the next chapter, as well as more detailed explanation.

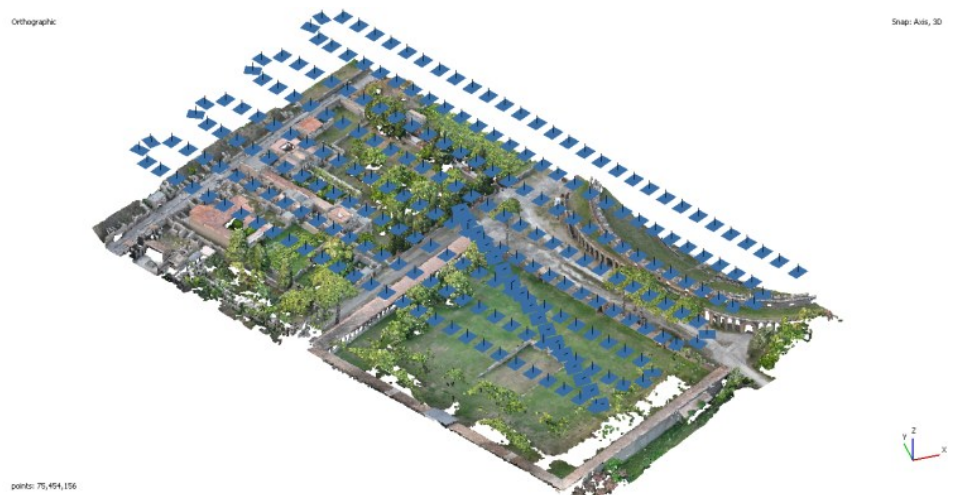
The final section will focus on exploring the survey products created and critically evaluating the results obtained and key issues encountered.

6.2.1. Processing of photogrammetric acquisitions (visible dataset)

The data processing procedures obtained from photogrammetric acquisitions with a UAV system will be analysed. This section will only refer to the operational workflow implemented in the case of frames acquired in the visible field, while the processing of multispectral images will be discussed in the next section.

This phase involves the use of Agisoft Metashape Pro, which can process both visible colour images and multispectral images. That’s why it was used for the processing of this type of data, as will be explored in the next section.

As the first step, the images acquired by UAVs should be loaded in this software, each flight in a single chunk or project. After all the images were imported, the relevant coordinates information attached on them need to be removed from the project, since the precision of the receiver integrated in this type of drone is not sufficient for the demand of this survey to scale and georeferencing the metric products.



► Figure 100 isometric view of photogrammetric dense cloud and camera centres

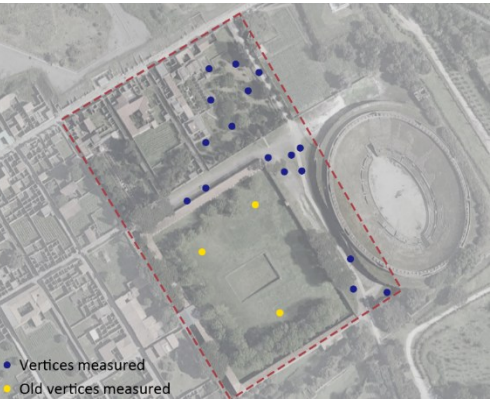
Start from the data above, the photo orientation can be carried out by the software which returned tie points as the first result. Also, during this step, the photos which cannot be recognized due to inclined shots near the works or were overexposed could appear out of the alignment. The tie point clouds were generated with High precision, the most detailed option can be chosen in the program’s input window. In both visible projects, it took about 50 minutes to compute the result, with the result described in Table 13.

	Visible dataset (Morning)	Visible dataset (Afternoon)
Aligned cameras	260	260
Tie points	504,410	508,131
File size [MB]	854.96	854.96

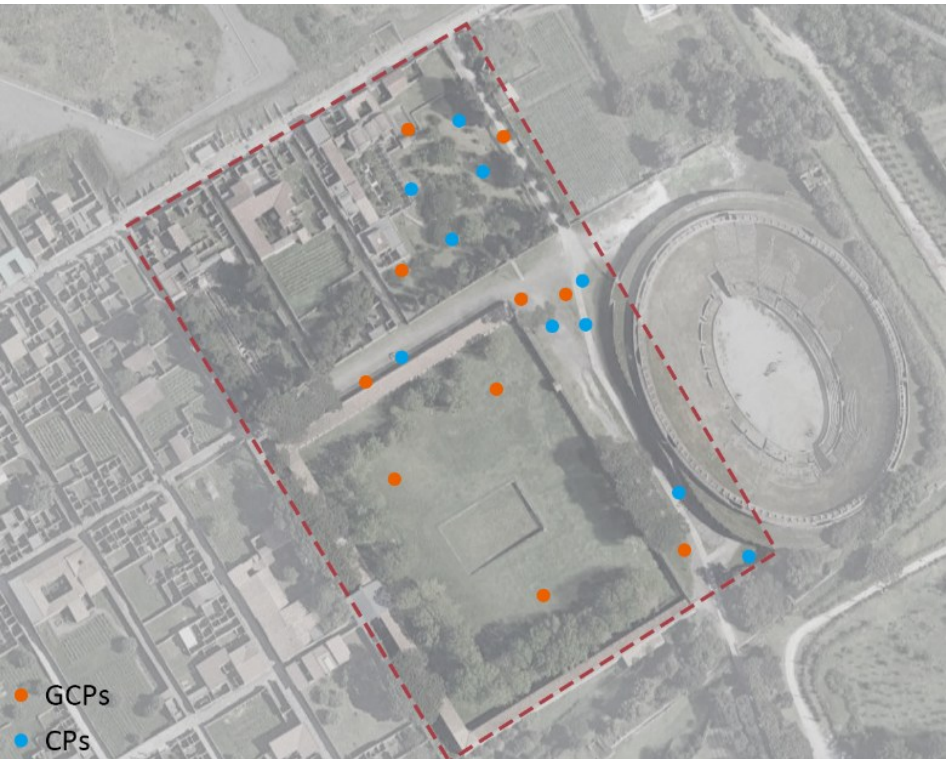
◄ Table 13 Parameters of tile points (visible datasets)

To offer the geoinformation to the project in the precision needed, as well as the real dimension, the coordinates of the ground control points should be located in the project. After setting the correct reference system, as same as the previous cases, namely the EPSG: 32633 – WGS 84 / UTM zone 33N, the CSV file containing the coordinates of the vertices and displayed in the program in tabular form was imported into each project. Each of them was collimated in the frames, which are 21 points in total (18 new vertices and 3 old vertices converted).

This process had been executed twice: one with only the coordinates measured in this coordinate system, the other with the additional coordinates converted from a different reference system Gauss Boaga. Thanks to the high resolution of the photos and adjustment of the projections, the errors are quite similar and low, which perfectly fulfil the accuracy demand of this project: both errors of the control points and check points are close to each other and lower than 5cm. For a result more convincing, as the control points scattering in the whole interesting area, the process with additional coordinates was taken for the next step.



▲ Figure 101 Scheme of vertices measuring time



◄ Figure 102 Distribution of GCPs and CPs in the project selected

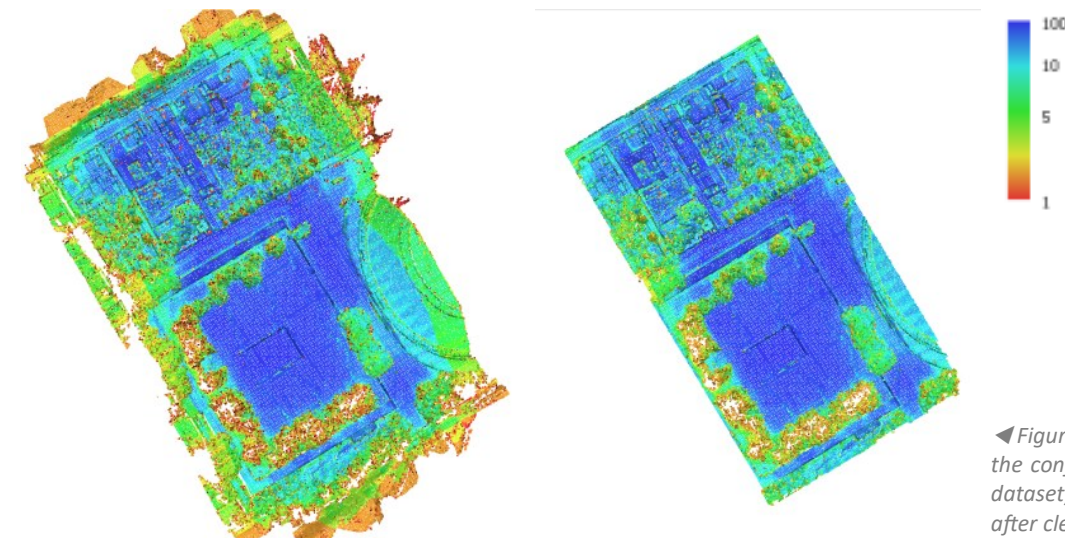


▲ Table 14 Errors of each GCPs and CPs in the visible datasets

► Table 15 RMSE summary of visible datasets (visible datasets)

		RMSE			
		X [m]	Y [m]	Z [m]	XYZ [m]
Visible dataset (Morning)	GCPs [12]	0.008	0.013	0.015	0.017
	CPs [9]	0.015	0.013	0.020	0.035
Visible dataset (Afternoon)	GCPs [12]	0.007	0.008	0.009	0.014
	CPs [9]	0.003	0.006	0.026	0.027

As for the dense cloud, the generation with high quality required about half an hour of work by the software for a result consisting of millions of points and an overall file weight of almost 2 GB. Furthermore, since there are various high vegetation distributing in the survey area, to acquire a result more reliable, the point clouds were cleaned by removing points indicated in only one frame.



◀ Figure 103 Dense point clouds under the confidence view (Afternoon visible dataset). Left: before cleaning; Right: after cleaning

	Visible dataset (Morning)	Visible dataset (Afternoon)
Control points RMSE [m]	0.017	0.014
Check points RMSE [m]	0.035	0.027
Dense cloud	125,686,901	125,679,904
Dense cloud (after cleaning)	73,615,418	77,032,851
File size [GB]	1.77	1.76

◀ Table 16 Parameters of dense clouds (visible datasets)

The dense cloud thus georeferenced is ready to be used as a source for the processing of other metric products with added value. For this case of visible data, a DSM and the visible colour orthophoto were created for each project, as well as a DTM.

	Visible dataset (Morning)	Visible dataset (Afternoon)
DEM	9,892 x 11,098	10,124 x 11,351
Resolution of DEM [cm/pixel]	2.75	2.73
Orthophoto	27,190 x 30,505	27,662 x 31,014
Estimated GSD [cm/pixel]	1	1

◀ Table 17 Parameters of other metric products (visible datasets)

DEM (Digital Elevation Model) will serve as a computational basis for multispectral data and will be mentioned in the next section. Meanwhile the orthophotos and DTM, when appropriately imported into the GIS environment, will become a part of the data sources for GIS analysis and the background of the work, as will be seen in the next chapter.

6.2.2. Products visualisation (visible datasets)

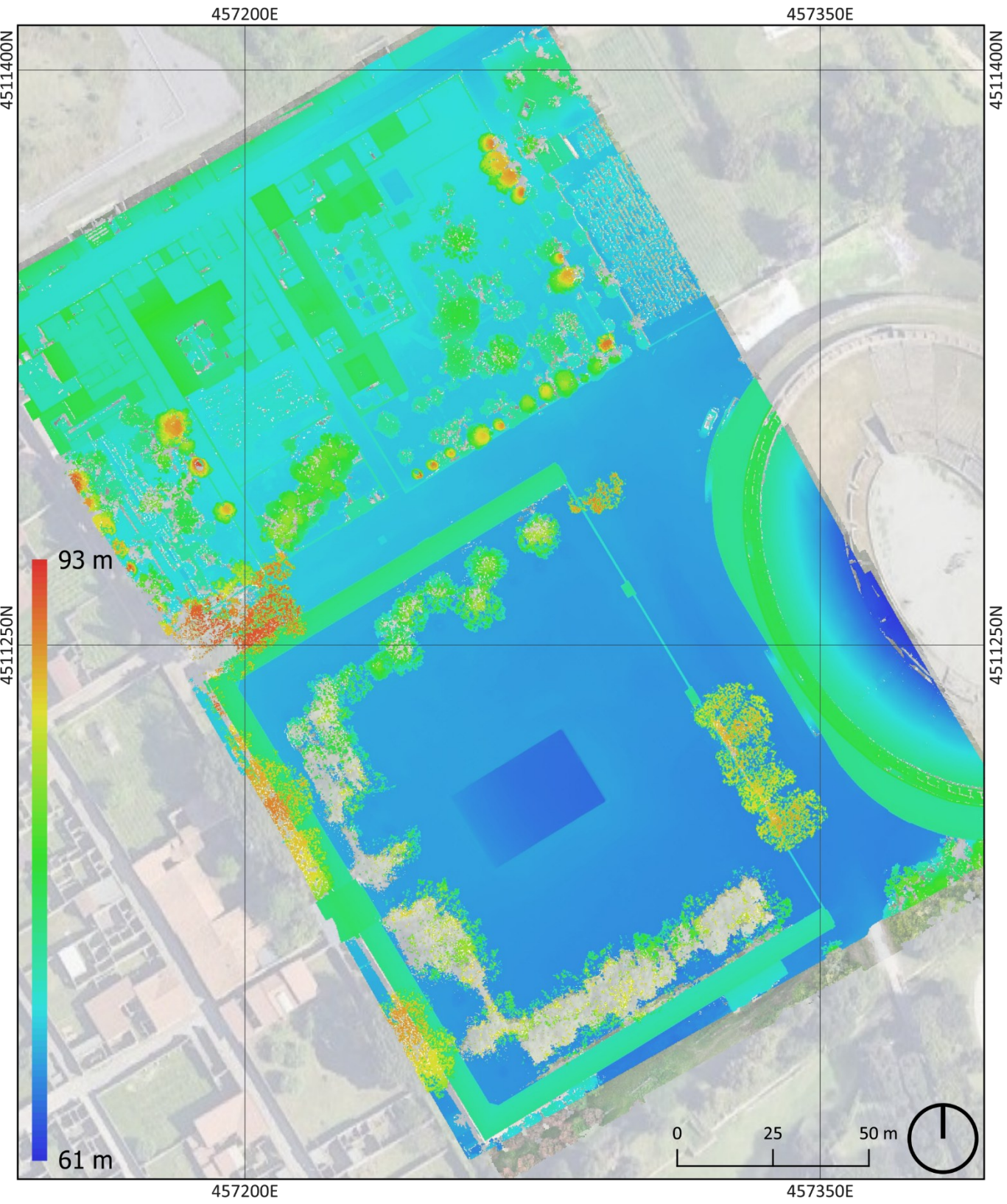
▼ Figure 104 Orthophoto of the whole survey area generated by Metashape (afternoon dataset)



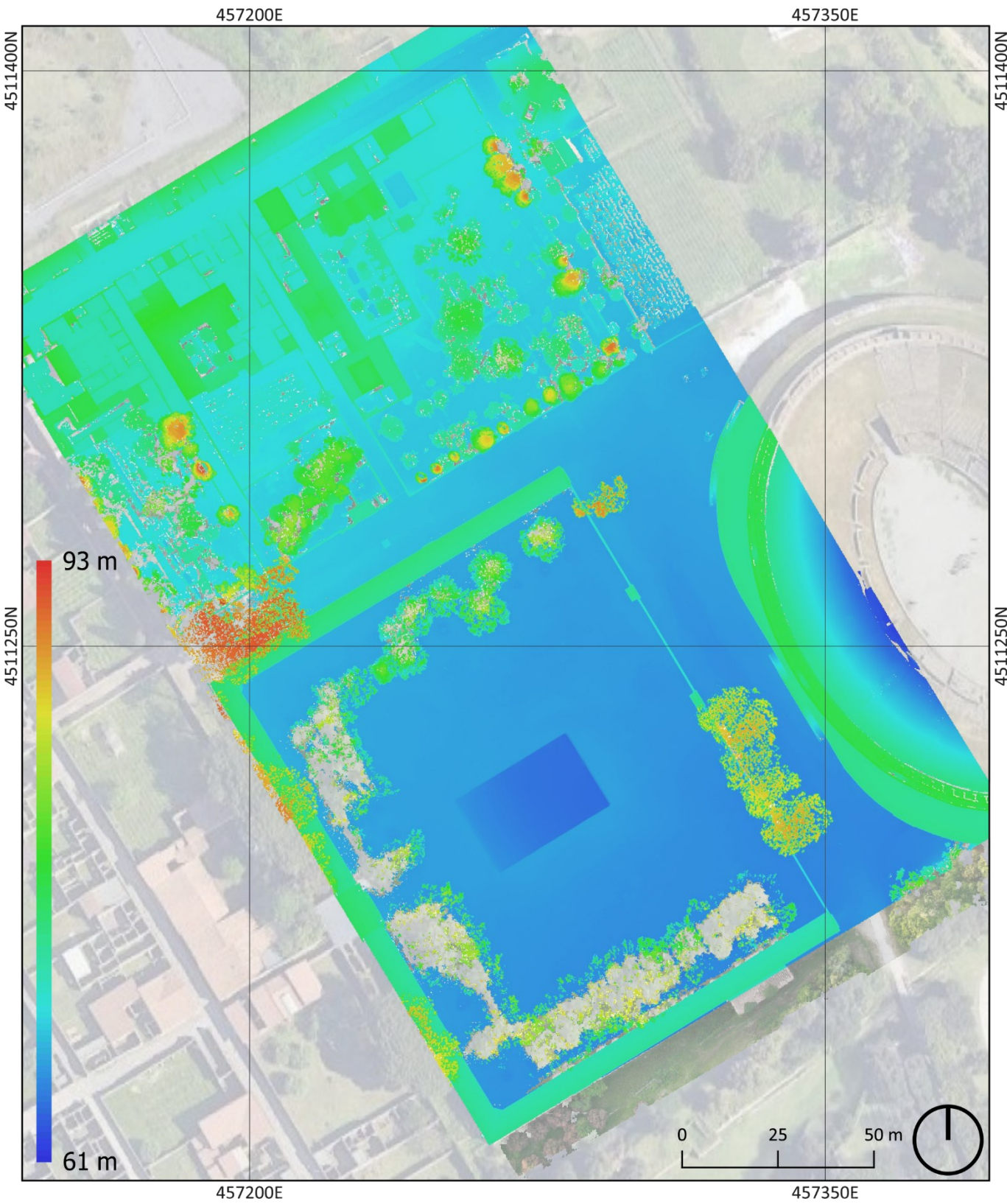
▼ Figure 105 Orthophoto of the whole survey area generated by Metashape (afternoon dataset)



▼ Figure 106 DSM of the whole survey area generated by Metashape (morning dataset)



▼ Figure 107 DSM of the whole survey area generated by Metashape (afternoon dataset)



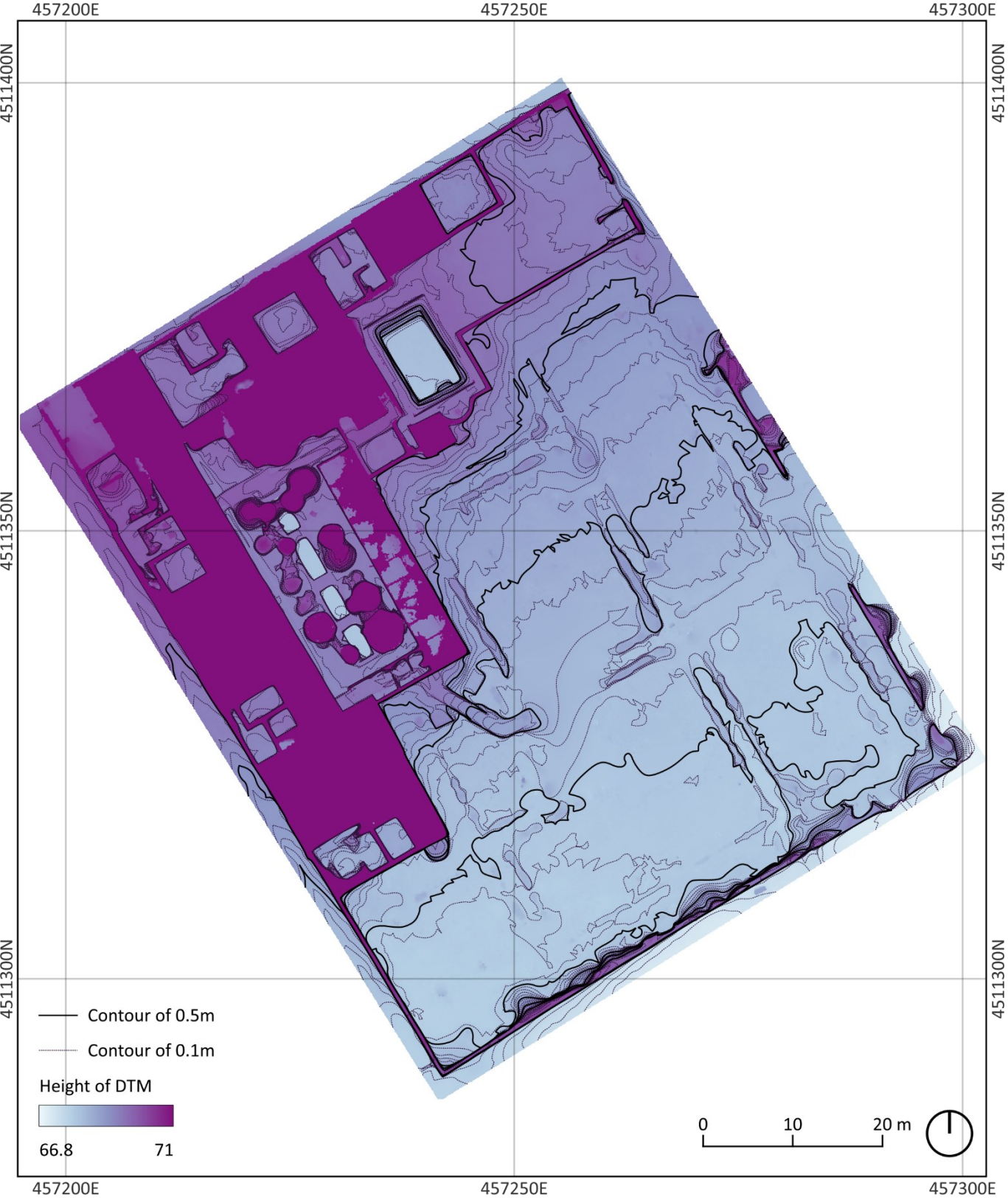
▼ Figure 108 Orthophoto of Praedia of Iulia Felix (afternoon dataset, locating in QIS)



▼ Figure 109 DSM of Praedia of Iulia Felix(afternoon dataset, locating in QIS)



▼ Figure 110 DTM of Praedia of Iulia Felix(afternoon dataset, locating in QIS)



7. Advanced analysis for Multispectral data



7.1. Electromagnetic radiation

Continuing with the last chapter, this chapter still focuses on the case of Praedia di Iulia Felix, but instead of the visible data set, it will discuss the processing and analysing of the multispectral data of photogrammetry.

In the first part of this paragraph, a base of the essential knowledge about the reaction under the electromagnetic radiation will be introduced briefly. The important concept, electromagnetic wave, will come out with its classification and special characters.

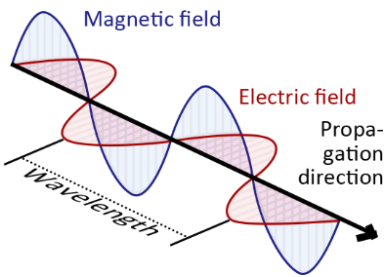
One step more, the performance of different item under the electromagnetic radiation, to be more specific, light and invisible light, will be compared and discussed. From this point of view, the relevant applications will be also state, which is the base of the analysis methodology of this case.

With the bases above, the main idea of multispectral data analysis can be explained clearly.

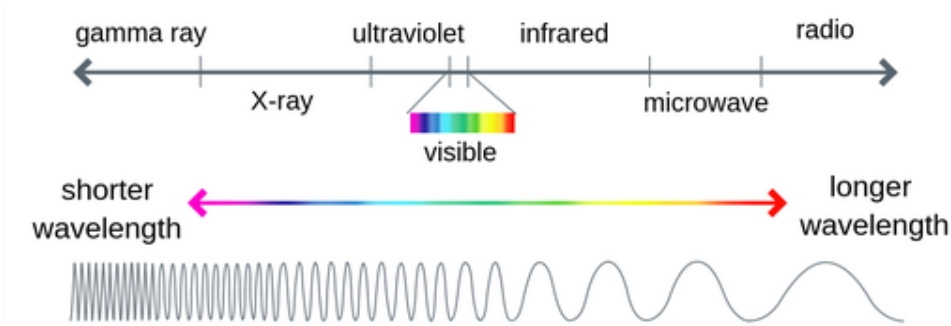
7.1.1. Performance of objects under the electromagnetic radiation

Visible light is electromagnetic radiation that can be perceived by the human eye (CIE, 2020), produced by accelerating charged particles such as from the Sun and other celestial bodies or artificially generated for various applications (Bettini, 2016). In physics, electromagnetic radiation is a self-propagating wave of the electromagnetic field that carries momentum and radiant energy through space. (Helmenstine, 2025) Thus, it can be effectively represented by periodic waveforms that alternate between positive maximum and negative minimum values

The electromagnetic spectrum is a continuum of all electromagnetic waves arranged according to their wavelength, and frequency. (Labster, 2025) In order to understand electromagnetic radiation of different wavelengths, it is divided into different regions, known as "spectral bands", with wavelengths ranging from kilometres per centimetre (radio) to less than one picometer (gamma rays).



▲ Figure 111 The electric and magnetic oscillating field vectors, modified from (Labster, 2025)



◀ Figure 112 Electromagnetic spectrum with visible light highlighted (Labster, 2025)

As shown in Figure 112, the visible light band is also included in these bands and is defined as the "visible spectrum". It is located in the central part of the electromagnetic spectrum, with a wavelength range from 380 nm (purple) to about 760 nm (red), corresponding to frequencies between 400 THz and 790 THz (Britannica 2025), composed of the wavelength range of light and its colours perceivable by the human eye. The wavelength below this range is called ultraviolet (UV), while the wavelength above this range is infrared (IR).

While the ordinary cameras can capture visible light across red, green and blue bands (RGB) which can be used for RS analysis, spectral imaging encompasses a wide variety of techniques that go beyond RGB. Multispectral cameras are able to capture data within specific wavelength ranges across the electromagnetic spectrum. The wavelengths will be separated by filters or detected with the use of sensors to wavelengths, including infrared radiation and ultraviolet. Additional information the

human eye fails to capture can be extracted and analysed through this method.

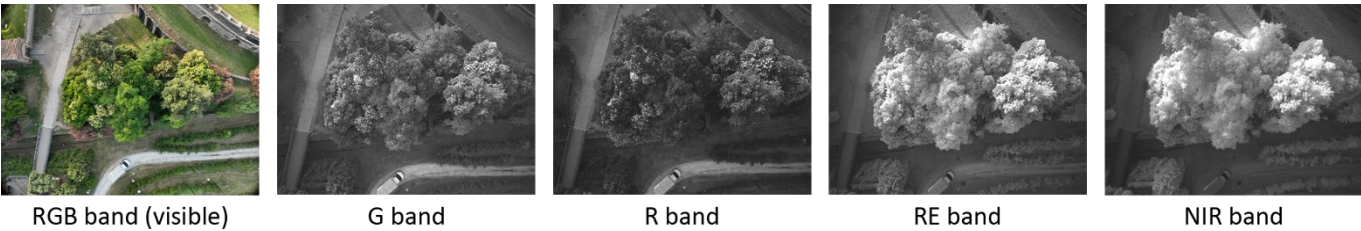
However, it doesn't exist a common and exact division of the spectrum, due to different standards or instruments. And here is one of the typical bands' divisions (Ohlinger, 2021) (UP42, 2025):

Band	Wavelength Range
Ultraviolet (UV)	100 - 400 nm
Blue (B)	400 - 520 nm
Green (G)	500 - 600 nm
Red (R)	600 - 680 nm
Red Edge (RE)	680 - 750 nm
Near Infrared (NIR)	750 - 1000 nm
short-wave infrared (SWIR)	1000 - 2500 nm
Thermal Infrared (TIR)	8000 - 14500 nm

► Table 18 Typical spectral bands and their wavelengths

As the section 3.1.3 mentioned, the multispectral data acquired in this case is: G, R, RE and NIR. Each band appears as a single band grayscale image, which is different from the visible datasets.

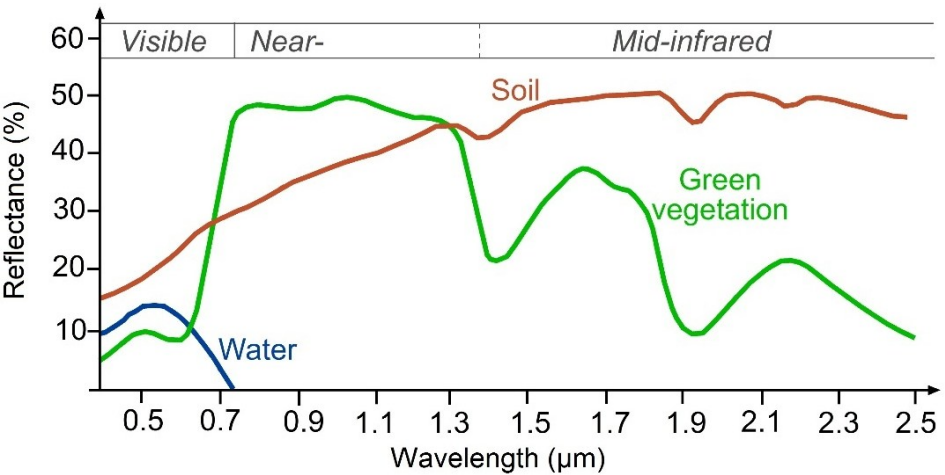
▼ Figure 113 Set of RGB image + multispectral grayscale images



7.1.2. Spectral signatures

Continuing with the example frames in the last section, it can be noticed that different objects with different materials can appear different reflectance in various spectral frames. For example, as the Figure 113 shows, the treetop appears strong (light) in the frame NIR while appearing weak (dark) in the frame R. In these same frames, the appearance of the road acts reversely to the treetop. To describe this phenomena, it's mandatory to import a concept, spectral signature.

Spectral signature is the variation of reflectance of a material with respect to wavelengths (European Space Agency, 2009). It can be presented through a functional graph using wavelength and reflectance ratio as the axis effectively. And as different objects varies the reflectance of different wavelength, the spectral signature can be various. As a result, it's workable to identify elements through their spectral signature. For example, healthy vegetation has a high reflectance ratio of infrared bands, especially in the region of NIR, while in the same graph, the peak of reflectance ratio appears in the visible light region.



◀ Figure 114 Spectral signature graph of vegetation, soil and water (European Space Agency, 2009)

To be more detailed, there are 2 important bands quite meaningful for analysing the spectral signature of vegetation. One is called Red Edge (RE), a band located at the edge of the visible spectrum and near to the band R. It's a narrow range, but it's an important feature for analysing vegetation as it's a turning point of the graph. And the other is band NIR, located between 750 - 1000 nm, which is often used for analysing vegetation, especially when classifying. Therefore, these bands and band R become the essential band applied in this analysis.

Spectral signatures and band RE and NIR have widely applied for environmental survey and archaeology field, but the application is still being developed (Santoro, Patrucco, Lingua, & Spano', 2023). The essence

of the archaeological application is analysing how submerged structures or residuals cause influence to the vegetation on the ground or the covering soil, which can be regarded as the key link between spectral signature study and the submerged heritage investigation.

In fact, the residual underground could lead to differences in height and colour between the exposed soil and the vegetation above, which may help to trace any archaeological remains, starting from the interpretation of images acquired in the NIR and RE bands. (Verhoeven, Smet, Poelman, & Vermeulen, 2009)

7.1.3. Interpretation analysis

As referred, the calculation of the data can be held in QGIS, which is not only able to manage various data in the same space, but also link them according to the geographical informations. After the operation of the data, how to analysis the result and explain the information, become the most important part of this case.

This case adopts visual interpretation analysis, because compared to converting complex standards into rules that can be recognized by the program under the premise that the methods and analysis values have not been studied, the visual interpretation analysis is a one-time thing in the early stage of research. It means for exploring these complex pattern of the analysis, especially the starting stage, visual interpretation relying on the operators with professional view is still the most effective choice, but after the pattern got generalised method with AI techniques like machine learning could be a better choice.

The aim of this interpretation analysis, is detecting the “anomalies” which are the blocks appearing in the vegetation areas with a readable difference from the surrounding areas. In the index maps achieved in this case, it’s like some small areas with different colours from the surrounding under a suitable visualising scale. Also, in the studied elements of this case, the spacial distribution or pattern is another useful element can be considered.

During the analysis, the negative elements can lead to errors are still need to be cared, such as the canopies, shrubs or the traces of human activities, which will be presented in the following sections.

7.2. Multispectral data processing

This paragraph concerns the multispectral photogrammetry processing, as well as its product visualisation.

The first section is about the processing workflow itself, which is similar to the one in the last chapter processing the visible datasets. It will not discuss the general operations very detailedly, instead, the special process towards multispectral data will be emphasized.

With the product from photogrammetry processing, the second section will discuss about the basic false colour visualisation, the way to convert the invisible data to visible information in the images. Also, the products will be shown.

7.2.1. Processing of photogrammetric acquisitions

After processing visible spectrum data, similar operations will be applied to multispectral data, as multispectral sensors only capture specific types of light that are not recognizable by the human eye. This section will introduce the operational workflow implemented in the case of frames acquired in the multispectral field. Similar to the processing of the visible datasets, the task is executed using Agisoft Metashape Pro.

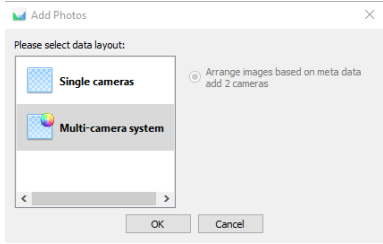
Through the processing, the operation is similar to the visible data but except only one specific step, because of the special setting of the software. It allows the bonding of different single band frames acquired at the same point, so that the typical photogrammetry operation is not mandatory to be repeated each time for each band.

After the first stage of importing images, the automatic alignment recognizing the corresponding points in the images displaying the same object, can be performed once but is valid for all the bands in this project. Comparing to the visible projects, it took longer time to compute the result since the alignment was for each bands' data, and the result described in Table 19.

	Multispectral dataset (Morning)	Multispectral dataset (Afternoon)
Aligned cameras	260*4	260*4
Tie points	2,180,367	2,396,987
File size [GB]	2.87	2.79

As for the geographic registration of the project, the situation is same as the visible projects in section 6.2.1: the accuracy of the GNSS receiver doesn't not fulfil the demand of this case considering the GSD and the scale. Therefore, in order to correctly register the point clouds with each other point clouds obtained for the same area, it's mandatory to have geographic registration using the control points like the section 6.2.1.

The coordinates are imported into the software in the form of CSV files under the same coordinate reference system EPSG: 32633 – WGS 84 / UTM zone 33N and need to be projected one by one into images of different bands. It should be noted that in this stage, each band can be considered as an "independent project", and all band images require a corresponding number of projection markers, for correcting any misalignment and/or registration errors between different spectral bands. Although the collimation of points in all four projects is certainly time-consuming, it greatly enhances the co-registration of the different blocks



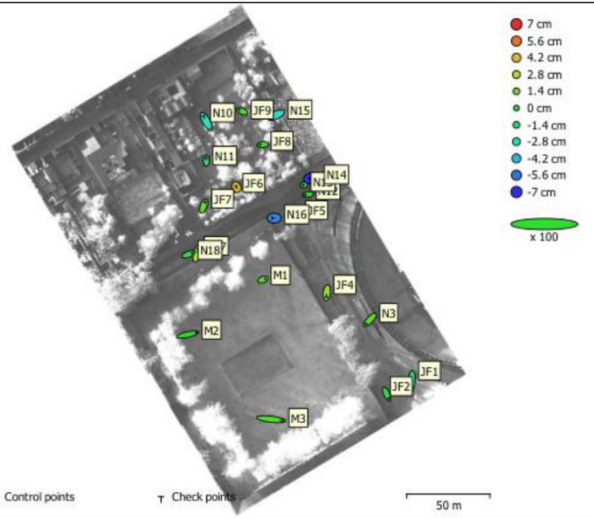
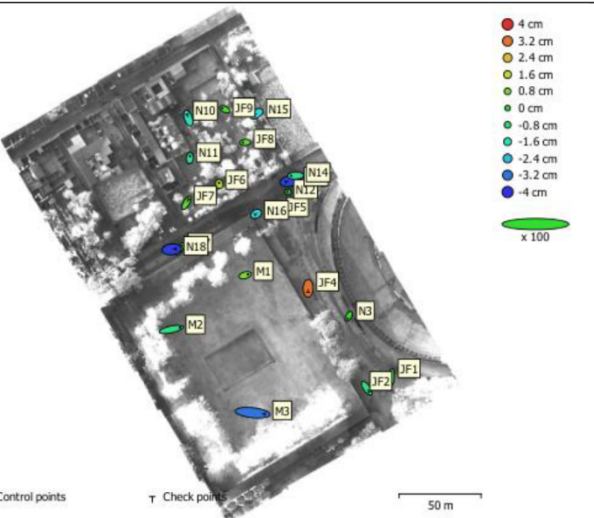
▲ Figure 115 Interface of importing the multispectral data

◀ Table 19 Parameters of tile points (multispectral datasets)

of multispectral single-band images, which otherwise could be slightly misaligned, particularly when using commercial sensors.

This process used the same coordinates as the one used for visible datasets, but RSME of both the multispectral datasets are relatively higher than the ones of the visible datasets. This is due, on one hand, to the fact that the GSD of the multispectral dataset is higher (with an approximate 2:1 ratio), and on the other hand, to the fact that, in this case, the photogrammetric process is characterised by greater complexity. However, considering that the goal of this research is to explore the

▼ Table 20 Errors of each GCPs and CPs in the multispectral datasets

Multispectral dataset (Morning)						Multispectral dataset (Afternoon)					
											
Label	X error (cm)	Y error (cm)	Z error (cm)	Total (cm)	Image (pix)	Label	X error (cm)	Y error (cm)	Z error (cm)	Total (cm)	Image (pix)
JF2	2.35055	-5.0491	-0.504344	5.59222	0.544 (49)	JF1	-0.349507	-6.98136	-0.0895869	6.99068	0.611 (32)
N3	-4.66655	-4.8307	0.960405	6.78489	0.855 (34)	N3	-1.69596	-2.93922	-0.011948	3.39345	0.335 (32)
JF5	-3.15757	-2.08287	-0.42499	3.80646	0.396 (54)	JF5	-2.42768	-2.20243	0.0960296	3.27926	0.445 (44)
JF7	1.63815	4.58739	1.25191	5.02941	0.375 (48)	JF6	-0.257075	1.18988	1.44252	1.88753	0.487 (44)
JF8	-3.33347	-0.244307	0.513931	3.38169	0.440 (54)	JF8	-2.86193	-0.194433	0.502766	2.91226	0.514 (48)
JF9	-3.50616	1.50251	0.658103	3.87089	0.337 (48)	JF9	-3.05235	1.44421	0.271228	3.38765	0.400 (48)
N11	0.0202481	2.629	-1.01109	2.8168	0.528 (49)	N11	0.215468	2.41012	-1.1678	2.68679	0.511 (44)
N12	-3.28371	-0.553534	-0.0925072	3.33132	1.401 (40)	N12	-0.553599	0.0876743	-0.104034	0.570071	0.296 (37)
N13	-0.689259	0.00635211	-0.755112	1.02241	0.453 (32)	N14	-5.51177	-0.225605	-1.25766	5.65794	0.873 (32)
N18	4.37879	1.72638	-0.606411	4.74573	0.605 (32)	N17	2.30874	4.05463	0.357287	4.67953	0.668 (40)
M1	2.62348	1.01426	0.986011	2.98053	0.456 (40)	M1	3.50584	1.04112	0.83923	3.75222	0.522 (36)
M2	10.249	2.30887	0.0101042	10.5058	0.867 (32)	M2	10.6798	2.31541	-0.878027	10.9632	1.143 (32)
Total	4.14042	2.78518	0.739537	5.04453	0.646	Total	3.96735	2.80655	0.762878	4.9192	0.591
Table 8. Control points. X - Easting, Y - Northing, Z - Altitude.						Table 8. Control points. X - Easting, Y - Northing, Z - Altitude.					
Label	X error (cm)	Y error (cm)	Z error (cm)	Total (cm)	Image (pix)	Label	X error (cm)	Y error (cm)	Z error (cm)	Total (cm)	Image (pix)
JF1	-0.802596	-9.02545	-1.7675	9.23184	0.320 (32)	JF2	3.22894	-4.66453	-0.91094	5.74575	0.432 (48)
JF4	-0.589273	-5.17205	2.152	5.6328	0.313 (48)	JF4	-0.0799187	-4.94137	3.21178	5.89398	0.337 (44)
JF6	-0.646326	1.42214	4.17429	4.457	0.269 (60)	JF7	2.61191	4.54636	0.439585	5.26162	0.507 (44)
N10	-3.47957	6.1021	-2.80847	7.56509	1.133 (44)	N10	-1.67861	4.98392	-1.65877	5.5144	0.850 (40)
N14	-4.18673	-0.613375	-6.98986	8.17087	0.568 (33)	N13	-6.23151	-1.35586	-3.77137	7.40901	0.491 (32)
N15	-5.69413	-2.49732	-2.95801	6.88546	0.425 (36)	N15	-3.13767	-2.0057	-1.98067	4.21792	0.270 (32)
N16	-2.63277	0.00249028	-5.23489	5.85965	1.352 (51)	N16	-1.6646	-0.950191	-1.98607	2.76011	0.316 (32)
N17	1.32113	5.35092	2.56916	6.08098	0.482 (44)	N18	5.1951	0.506724	-3.85553	6.48929	0.513 (32)
M3	13.85	-1.65116	0.730837	13.9672	0.361 (32)	M3	15.1441	-1.65701	-3.20761	15.5685	0.494 (36)
Total	5.41569	4.53919	3.72997	7.99041	0.714	Total	6.03556	3.35742	2.61055	7.38344	0.499
Table 9. Check points. X - Easting, Y - Northing, Z - Altitude.						Table 9. Check points. X - Easting, Y - Northing, Z - Altitude.					

potential presence of buried structures in the subsoil, the computed mean RSME values of ≤ 0.050 m and ≤ 0.080 m for the GCPs and CPs, respectively can be considered acceptable.

		RMSE [m]			
		X [m]	Y [m]	Z [m]	XYZ [m]
Multispectral (Morning)	GCPs [12]	0.041	0.028	0.007	0.050
	CPs [9]	0.054	0.045	0.037	0.080
Multispectral (Afternoon)	GCPs [12]	0.040	0.028	0.008	0.049
	CPs [9]	0.060	0.034	0.026	0.074

◀ Table 22 RMSE summary of visible datasets (multispectral datasets)

As for the dense cloud, the generation with high quality required only 10 minutes' work by the software for a result consisting of millions of points and an overall file weight of about 800 MB. After cleaning the points indicated in only one frame, same as the process for visible datasets, the DEM derived from the visible datasets was imported into the multispectral dataset projects as the best source for the height data. Overall, an orthophoto was generated for each photogrammetric block. These orthophotos will serve as primary data for the analyses presented in the following sections.

	Multispectral dataset (Morning)	Multispectral dataset (Afternoon)
Control points RMSE [m]	0.050	0.049
Check points RMSE [m]	0.080	0.074
Dense cloud	38,121,831	39,101,160
File size [MB]	797.42	818.23
Orthophoto	10,875 x 12,201	11,165 x 12,581
Estimated GSD [cm/pixel]	2	2

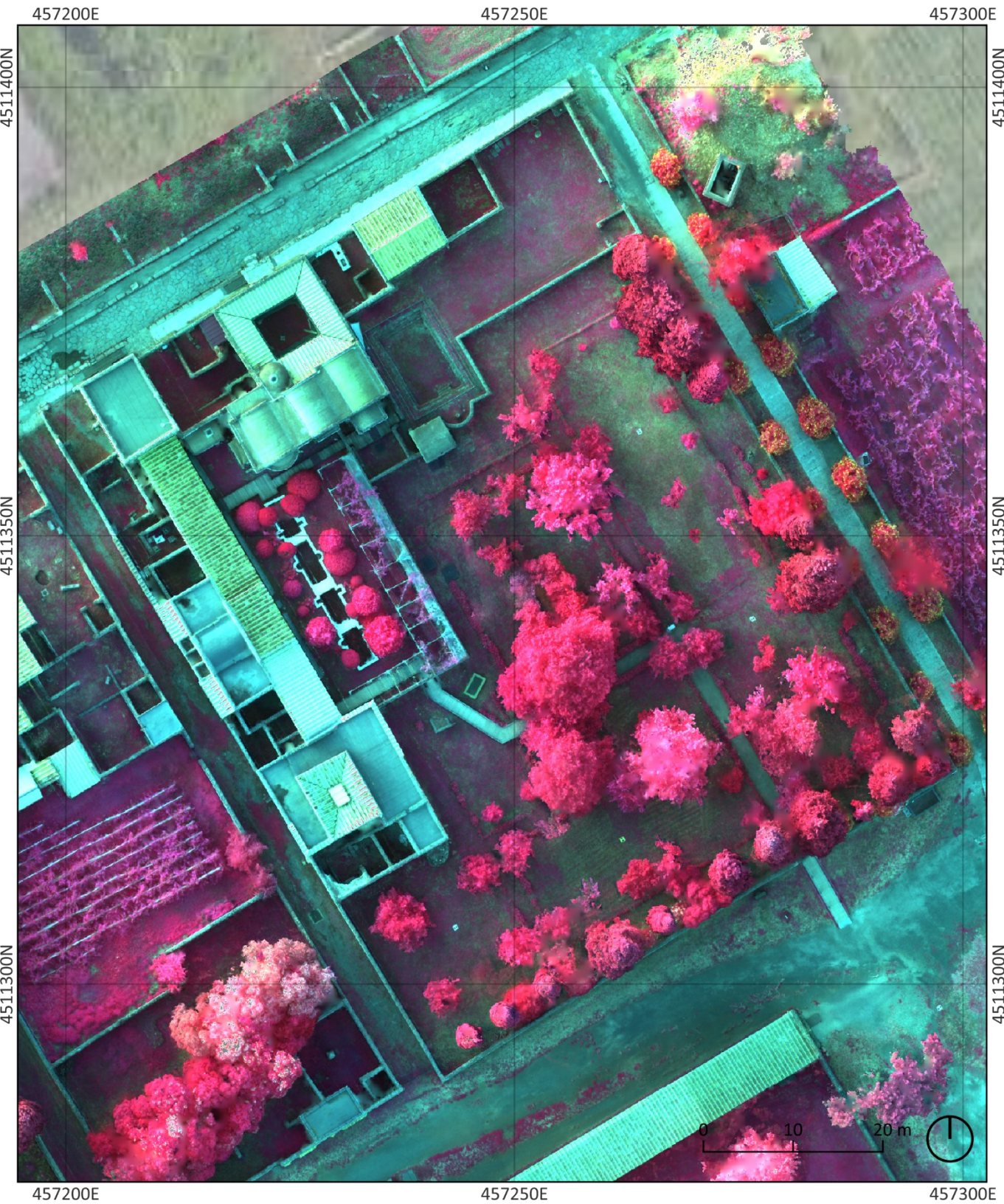
◀ Table 21 Parameters of dense point clouds and other metric products (multispectral datasets)

7.2.2. Product visualisation

To proceed with the analysis of the orthophoto obtained by the photogrammetric process, it is necessary to implement the grayscale display, thus making it more easily interpreted by the human eye.

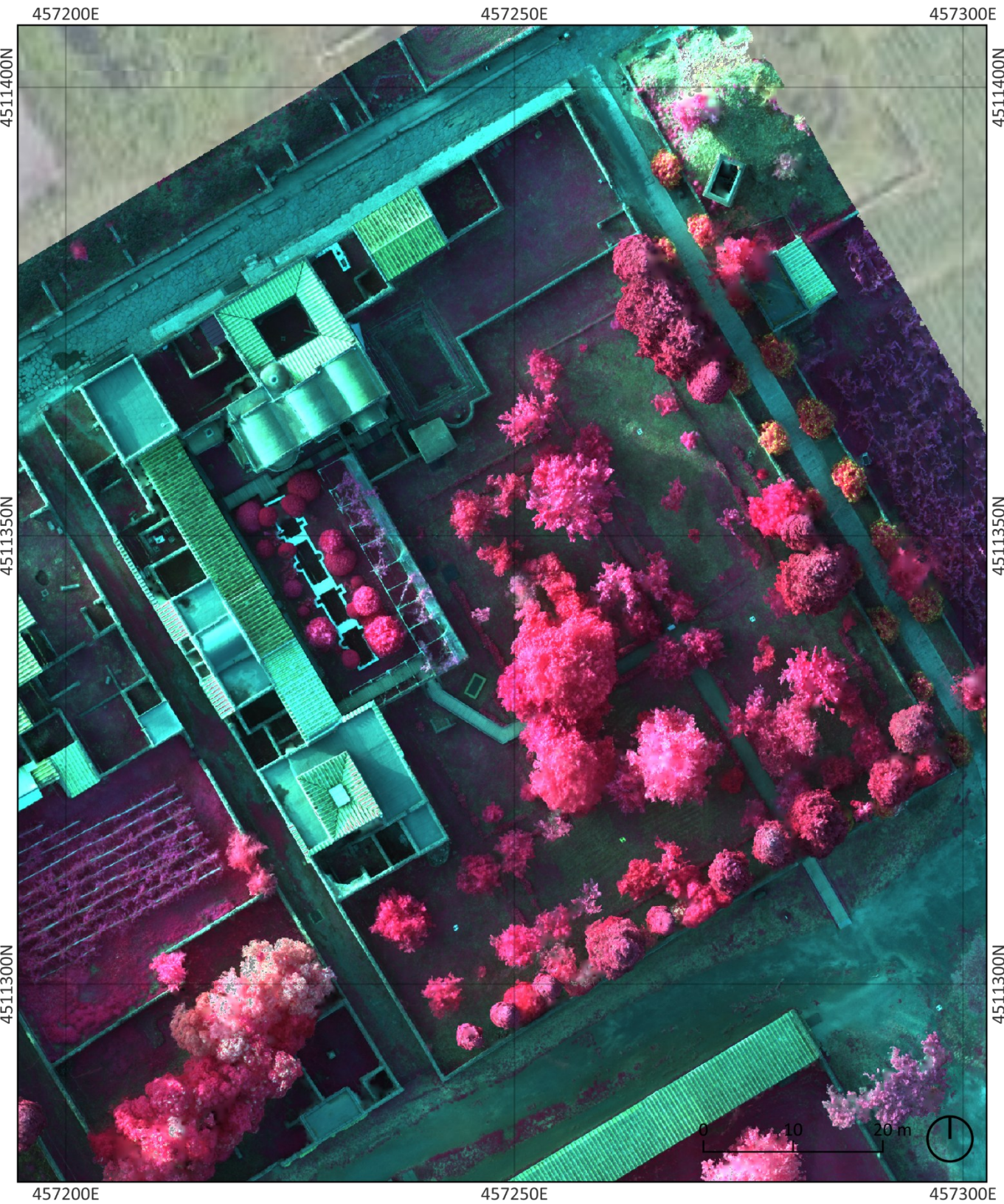
Based on the principle of trichromacy (Byrne and Hilbert 1997), the vision

▼ Figure 116 NRG Orthophoto in false colour display (morning dataset)



ability of human eyes, three spectral bands are commonly combined into a false-colour image. Similar to the true colour mapping RGB bands to the corresponding RGB channels, traditional false-colour satellite images of Earth an "NRG→RGB" mapping is used, with "N" being the near-infrared spectral band – this yields the typical "vegetation in red" false-colour images. It allows to highlight certain phenomena, favouring the interpretative process.

▼ Figure 117 NRG Orthophoto in false colour display (morning dataset)



7.3. Advanced multispectral analysis

This paragraph will push the study deeper from the literal bases and the survey products to the real application. A complete workflow showing the analysing method will be stated in this paragraph.

The first section will present the understanding and selecting of VIs (vegetation indice). The concept and principle of the VIs will be explained, which was the essential part of this analysis.

The products computed using the selected VIs will be presented, and the selection of visual colour scale will be also discussed in this section.

In the last section of this section, the anomalies detected by visual inspection will be shown on the semi-transparent orthophoto of the survey area, which expressed some interesting pattern for archaeological studying.

7.3.1. Spectral indices

As mentioned earlier, vegetation research, particularly in the red-edge and near-infrared bands, has been applied to precision agriculture and identifying cultural relics in soil. Advances in sensors and the availability of large amounts of data have pushed the analysis of this data and the development of several research indices, including the "Vegetation Index," which "numerically analyses reflectance and synthesizes information from the original bands."

Different vegetation densities and species, etc., determine the vegetation index used for analysis, as the biological parameters that cause the index to vary. Therefore, these spectral indices generally simplify the reading and understanding of the data acquired by the sensor and emphasize the colour differences of vegetation compared to surrounding elements.

However, like vegetation, other elements can also reflect energy and can be captured and analysed by sensors. Therefore, similar to VIs, other indices for soil, rock, glacier, etc. are widely used in remote sensing. They involve different spectral bands and provide different results based on the reflectivity of each material.

In this case, the soil index is a useful indicator because it takes into account factors such as humidity and the presence of nitrates, and can be used to determine the presence of underlying remains by looking at changes in the soil. In fact, in the case of archaeological sites, the soil over the site often has different moisture and nitrate content than the surrounding area. (Carmona, Quirós, Mayoral, & Charro, 2020)

The choice of index is not random, but strictly depends on the characteristics of the analysis area. For the area analysed in this case study, a key point is that the vegetation types in the area are complex and the biomass varies greatly. Therefore, more indices will be tested in the study.

The following is a summary table of the indices examined:

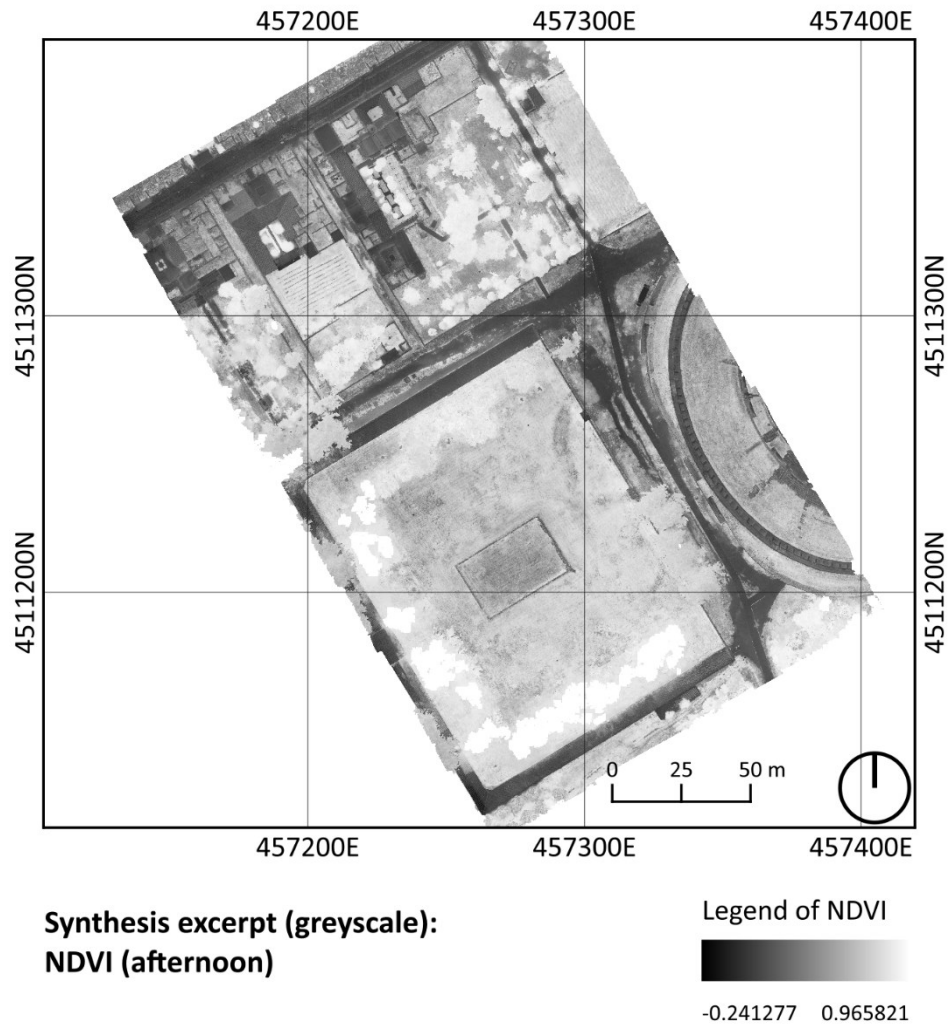
VI	Formular
NDVI	$NDVI = \frac{(NIR - RED)}{(NIR + RED)}$
EVI2	$EVI\ 2 = 2.5 \times \frac{(NIR - RED)}{NIR + (2.4 \times RED) + 1}$
NDRE	$NDRE = \frac{(NIR - RE)}{(NIR + RE)}$
BI2	$BI2 = \sqrt{(RED^2 + GREEN^2)}/2$
RN	$RN = RED + NIR$

◀ Table 23 Summary of the indices applied in this case, as well as the fomulars

In this case, the application of spectral indices begins with the different spectral bands of the orthophoto. Essentially, the thresholds of the different spectral bands contained within each pixel are appropriately combined using an exponential formula to obtain a single numerical value associated with that pixel. The resulting mapping between these numerical values creates a raster image that differs from the previous one, highlighting specific elements compared to the previous one.

To achieve this, the open-source software QGIS was used as the platform for processing the multispectral orthophotos obtained from the photogrammetric processing. It also allows for interpretive analysis through advanced tools for managing bands and their representation.

The Raster Calculator in the software allows you to process the data of different bands in the raster by entering different expressions. After the calculation is completed, the exported output raster will be displayed in grayscale. They will be processed into a form that is easier to effectively identify in the next section.

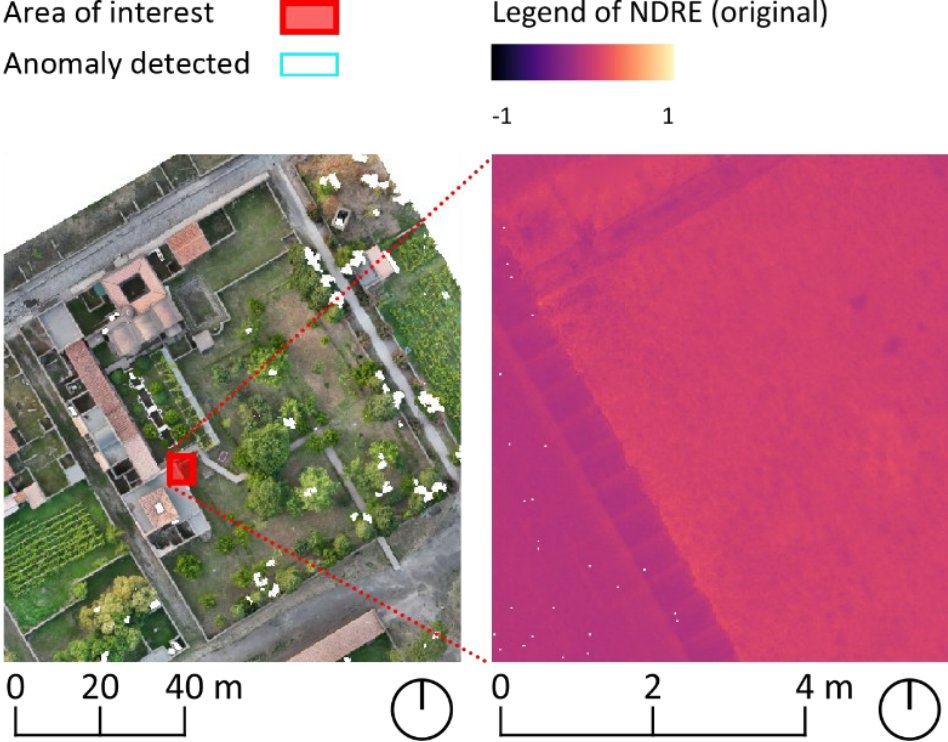


► Figure 118 NDVI index map calculated by QGIS without any visualisation promotion

7.3.2. products visualisation with false colour

After achieving the greyscale display result, the visualisation can be promoted by the software with false colour display. It can change the greyscale to colour display through the mapping relations. Furthermore, it also allows "stretching" to visualise a certain range of data, for a clearer analysis.

Usually a index map is describing all the elements exposed in the view, like rocks, bricks, and water. And a larger difference always appears on some different material. It is foreseeable that the stronger colour sign is more likely happen on a rock on the lawn, instead of a group of unhealthy vegetations on the lawn. Here is an example of NDRE index map with the original colour scale. With this scale, the effect of visualisation is not ideal, the strongest part is not related to the target and the anomalies in vegetation areas are not readable.



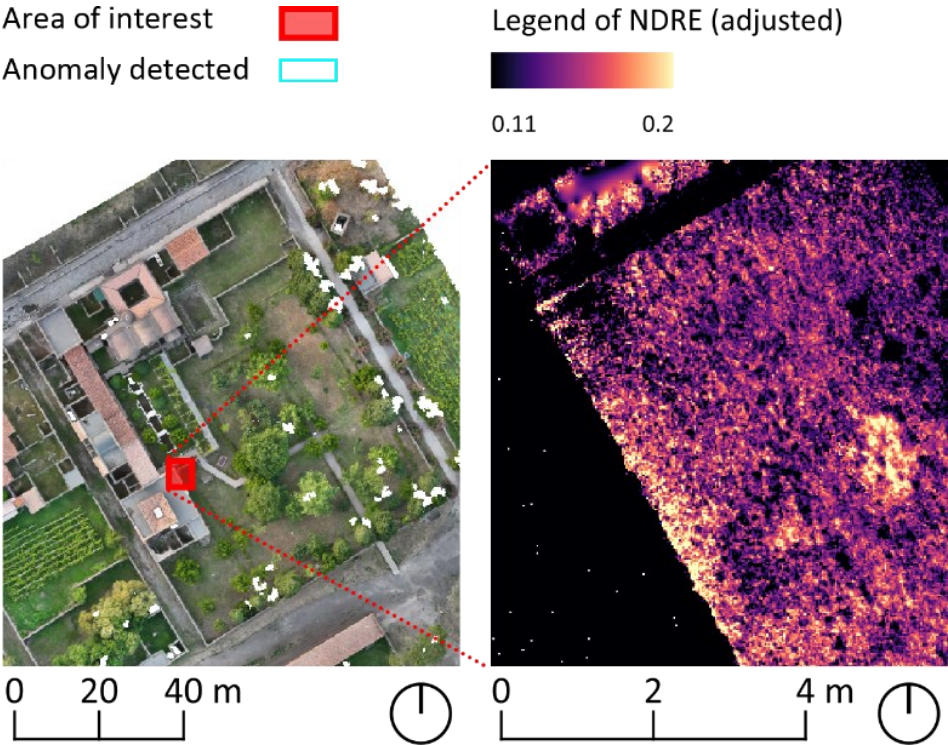
◀ Figure 119 A sample of the unadjusted NDRE index map, showing the position on the UAV visible map

Therefore, this study modified the colour scale values to better highlight the contrast between adjacent regions, which enabled us to obtain more effective images during the interpretation process.

The colour scale can be modified through the Layer Properties window, the most convenient way of doing this is to switch the mode from "Entire Raster" to "current view". This will update the range of displayed values by zooming in the interesting area of the orthophoto, and thus the colors of the image, to fit within the portion contained in the screen frame.

To better understand how the visualisation of orthophotos can be

improved by this method, the example of the NDRE index map updated is shown below. Instead of the original colour scale from -0.2 to 1, it was modified as "From 0.1 to 0.25". As the figure shows, the difference in the vegetation areas became recognisable by human eyes, while the difference between vegetation-covered areas and rocky areas was more obvious than before also.



► Figure 120 The same sample area of the adjusted NDRE index map, showing the position on the UAV visible map

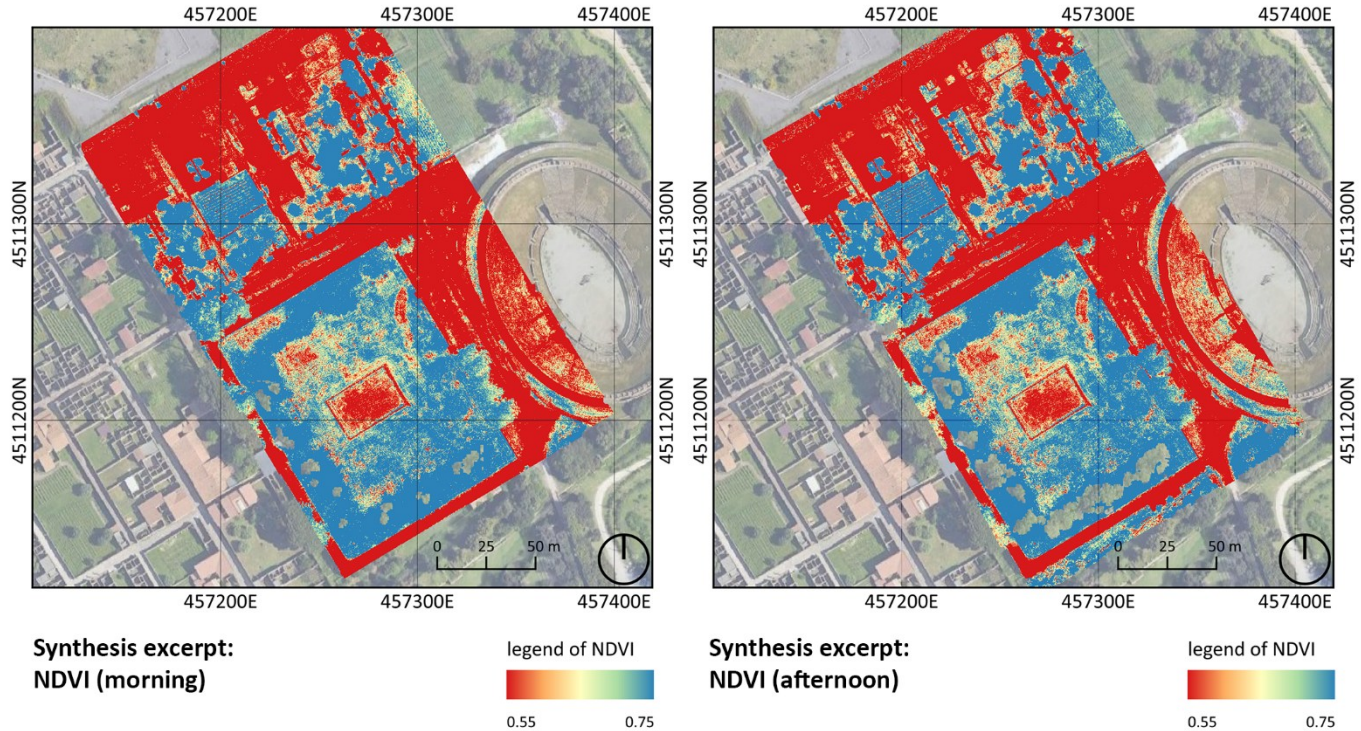
In the following part, all the index maps of the entire survey area will be presented one by one, as well as brief statements about the indices.

Among the VIs, NDVI is one of the most widely used spectral indices in Remote Sensing applications, from vegetation study to archaeological investigations (Zhao & Qu, 2024) (Agapiou, Hadjimitsis, & Alexakis, 2012). It expresses the normalised ratio between the reflected energy in the R absorbed by the chlorophyll, and the reflected energy in the NIR, which is due to the scattering of light by the leaves. This can be regarded as an indicator of the health and greenness of the vegetation (Delegido, et al., 2013).

NDVI values range from -1 to +1: values close to 0 or lower usually indicate inorganic materials such as water bodies, rocks, sand, or concrete, while positive values are connected with various types of vegetation, including crops, shrubs, grasses, and forests. As the values higher, the vegetation represented becomes healthier, denser, and in good condition (Huang, Hupy, Wang, & Shao, 2021).

While this index, at a certain degree, eliminates some influence from noise, observing view, terrain, etc, there are still some disadvantages (Huete & Justice, 1999):

- Oversaturation problem. When the vegetation coverage exceeds a certain level, NDVI begins to gradually saturate and is no longer sensitive to the continued growth of vegetation;
- Canopy background contamination. NDVI is very sensitive to soil moisture, soil roughness and even soil components on the canopy surface. It is generally believed that this impact is the greatest when the vegetation coverage is around 50%. The saturation problem of NDVI is actually the influence of the soil background (HUETE, JACKSON, D., & POST, 1985).
- Atmospheric influence. The atmospheric transmission process affects the red band and the near-infrared band in opposite ways, which can easily lead to an underestimation of the vegetation growth status.



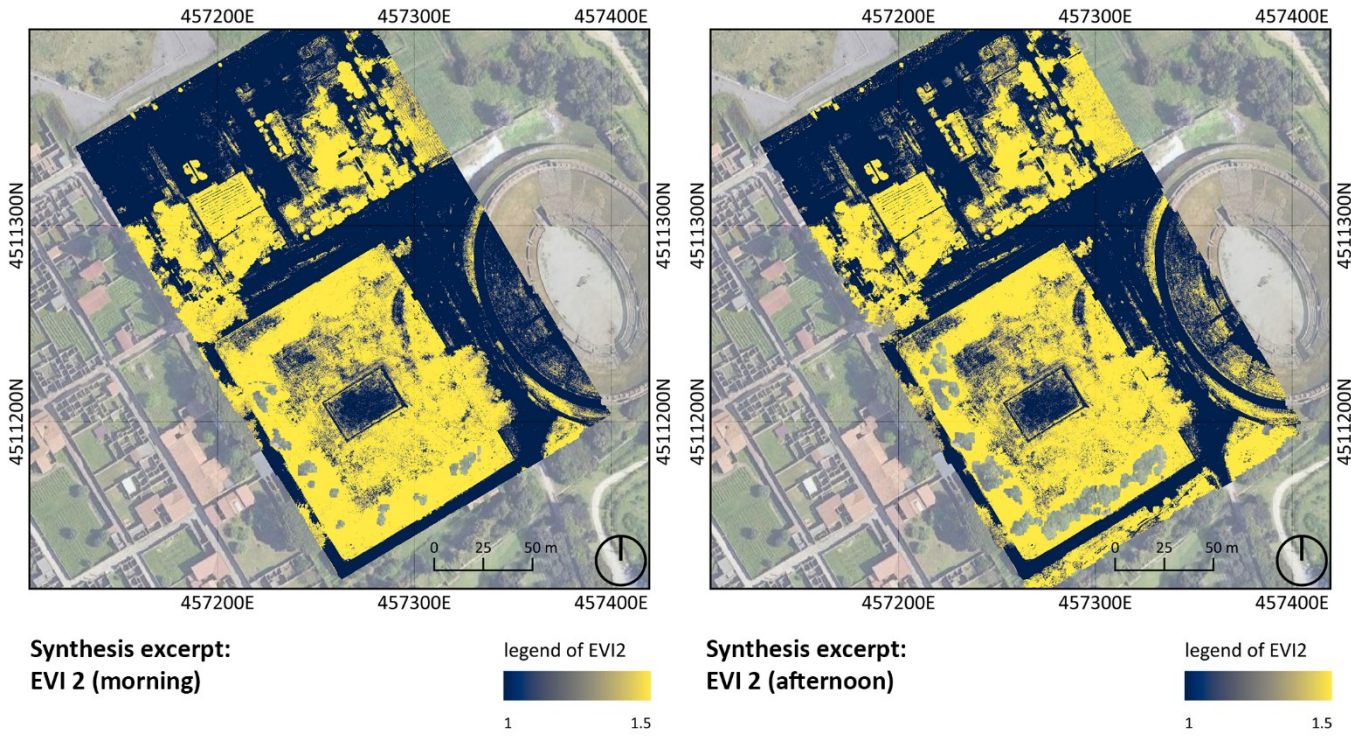
▲ Figure 121 Sythesis excerpts of NDVI calculated from both datasets, ranging the entire survey area

The EVI 2 is derived from the Enhanced Vegetation Index (EVI) which takes the relation between red band and blue band into consideration to reduce the influence of the atmosphere (Jiang, Huete, Didan, & Miura, 2008). But EVI 2 excludes the Blue band from the calculation, instead, it uses the fixed parameters showing the relation between red and blue bands to omit using the data of blue band. It allows the index to be calculated even when the acquiring sensors, such as the one used in this case, cannot capture the Blue band. EVI 2 considers environmental factors such as atmospheric conditions and soil background, offering improved

vegetation monitoring (Matsushita, Yang, Chen, Onda, & Qiu, 2007) (Jiang, Huete, Didan, & Miura, 2008).

Similar to the NDVI, EVI-2 yields positive values for vegetated areas and values close to zero or negative for inorganic surfaces. Especially, the positive values of EVI-2 allow for a more precise discrimination of vegetation greenness, increasing sensitivity to variations among high values approaching +1, which are often challenging to interpret using NDVI (Jiang, Huete, Didan, & Miura, 2008).

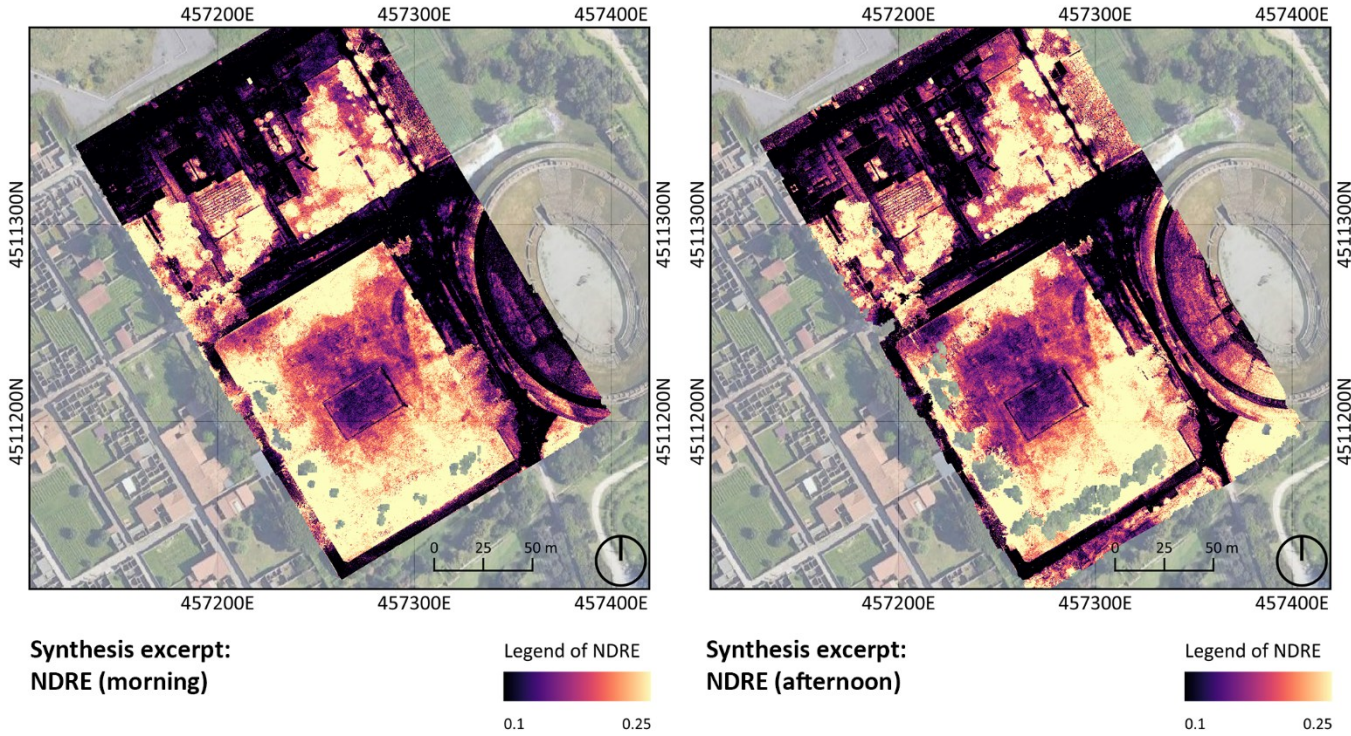
▼ Figure 122 Sythesis excerpts of EVI 2 calculated from both datasets, ranging the entire survey area



Apart from the indices studying R and NIR bands, the Normalized Difference Red Edge (NDRE) considering the contribution of the RE band is particularly effective for monitoring crop health through the chlorophyll content (Ronchi, 2020), which also has capability to explore the health of the vegetation.

NDRE values typically range between -1 and +1. Values from -1 to 0.2 generally correspond to inorganic surfaces, while values between 0.2 and 0.6 are indicative of unhealthy vegetation. Values above 0.6 up to 1 are usually associated with healthy and mature crops (Marx, et al., 2024).

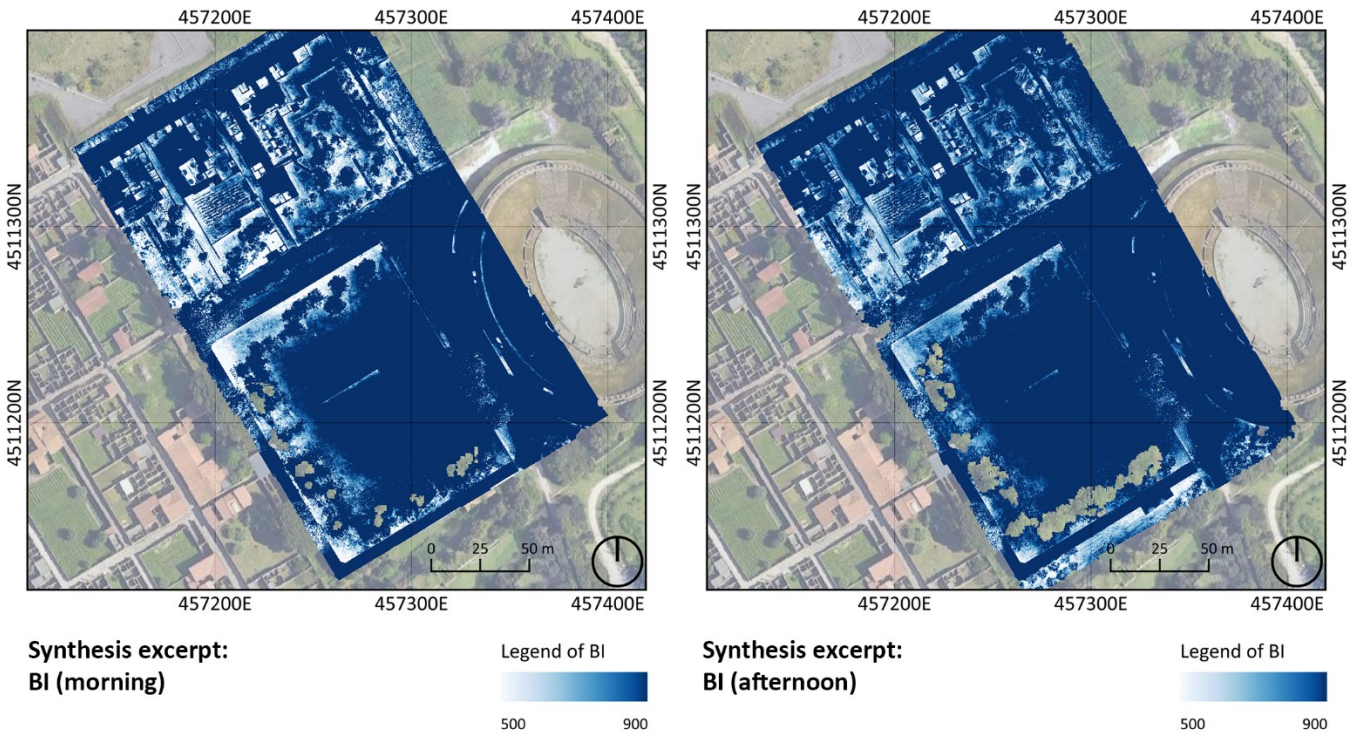
Because the conditions in the mapped areas are varied, some areas have only very sparse vegetation due to human activities or lack of living space,



which led the use of SIs become powerful. Specifically, the Brightness Index (BI) is calculated to study characteristics of soil in areas with irregular rainfall, for example Pompeii, have achieved good results in identifying archaeological structures (Carmona, Quirós, Mayoral, & Charro, 2020).

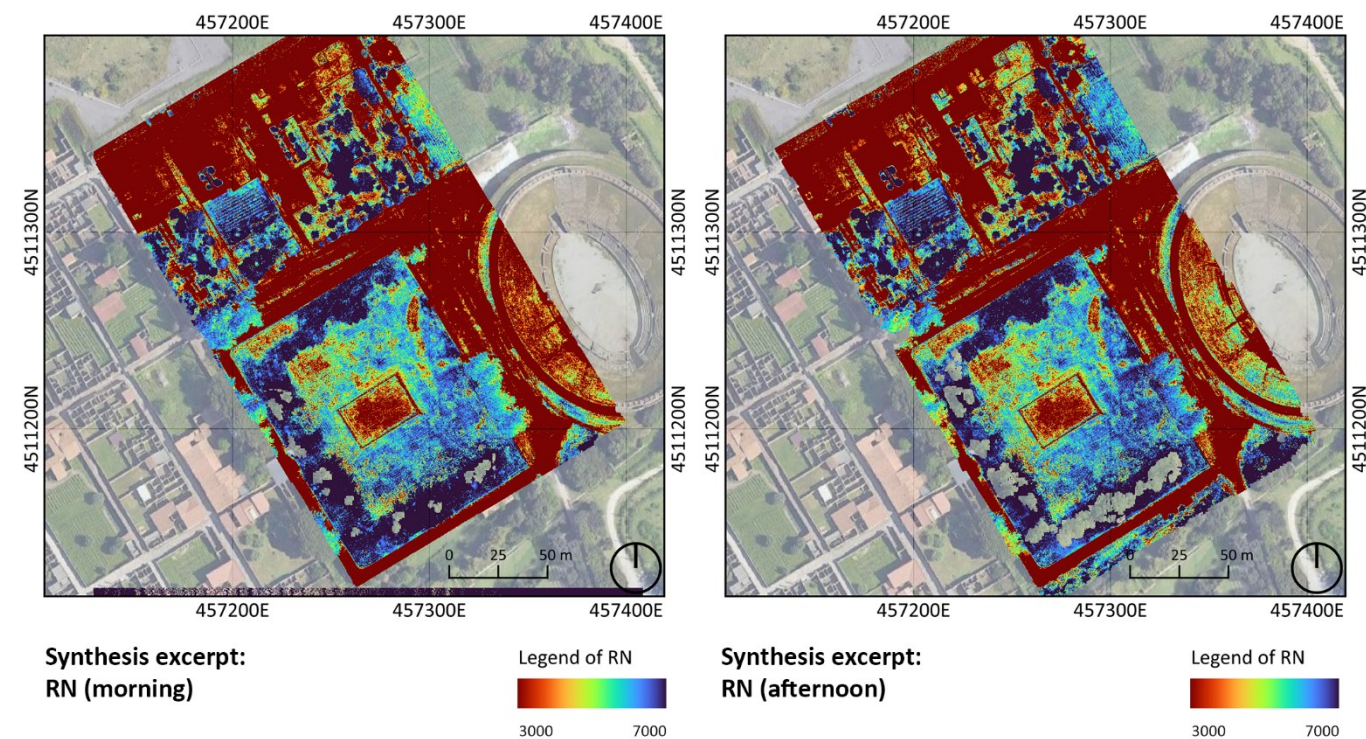
The calculated index indicates the conditions of the soil surface, ranging from non-vegetated mineral surfaces, bare soil, soil with sparse vegetation, to the areas covered by dense vegetation (Abderrazak, Kadhem, El Battay, Mohamed, & Rouai, 2016).

▲ Figure 123 Sythesis excerpts of NDREcalculated from both datasets, ranging the entire survey area



▼ Figure 124 Sythesis excerpts of BI calculated from both datasets, ranging the entire survey area

Additionally, in this case, another index was tested to explore more possibilities. In other archaeological contexts, this index has shown particularly promising results in detecting non-visible features associated with underground structures. The RN index (R + NIR) was successfully applied in a previous archaeological study using satellite imagery. It combines the R and NIR bands to evaluate the spectral characteristics of vegetation in these wavelengths (Zanni & De Rosa, 2019).



▲ Figure 125 Sythesis excerpts of RN calculated from both datasets, ranging the entire survey area

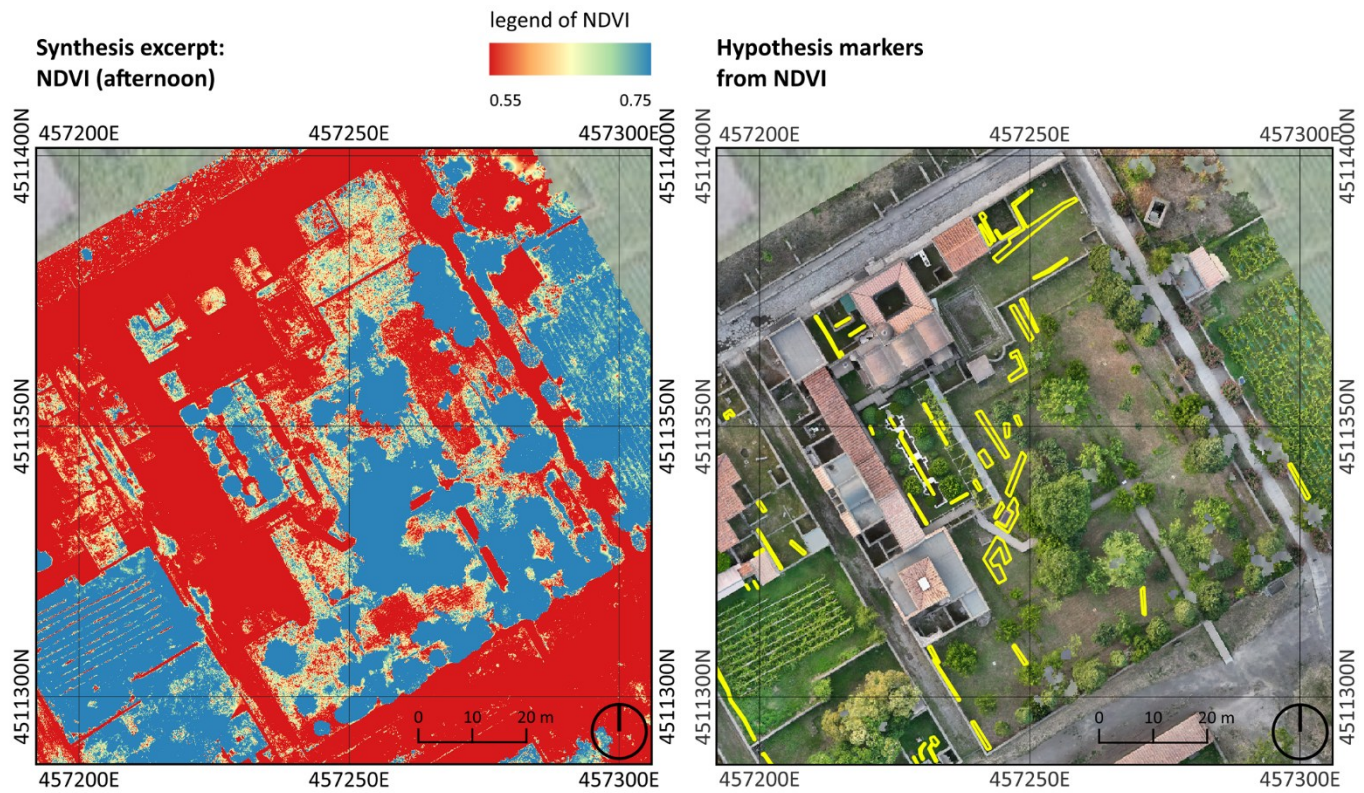
An preliminary result from the interperation of different index maps is that using more than one index map to find anomalies works effectively. It is because each index is calculated in a different way and uses different spectral bands, so they react differently to elements like biomass, vegetation thickness, and plant variety in the area. For example, the EVI 2 index map was made to distinguish small differences between healthy and thick vegetation. Because of this, it can detect anomalies better in cases where the normal NDVI index does not work as well. In this case, where the hortus has many kinds of plants to show the possible ancient state of crops and gardens (Anguissola & Olivito, Introduzione, 2022), it is useful to use these indices together, since they reflect the different vegetation types compared to the nearby fields.

7.3.3. spectral anomalies detection from visual inspection

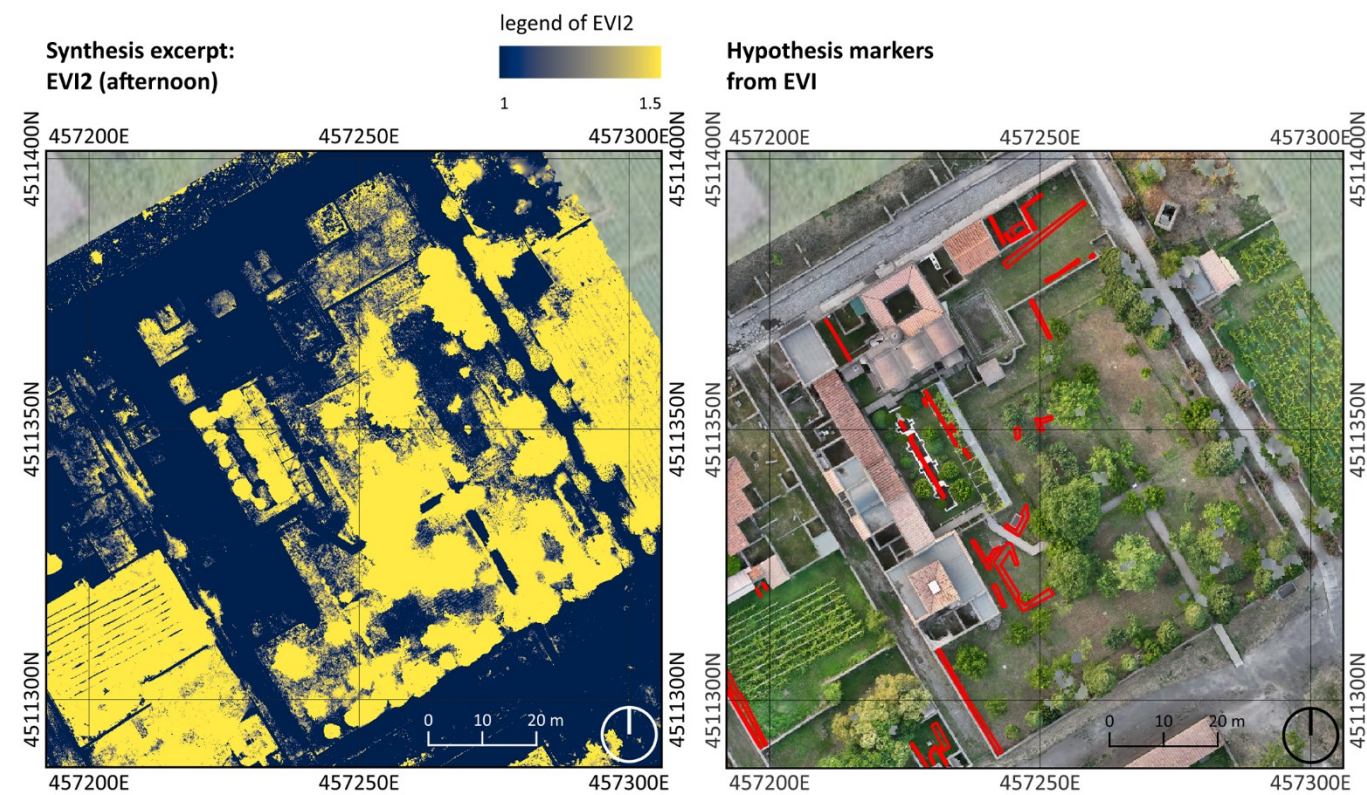
This section contains a series of index map with the anomalies detected, which were organised in couples for easier comparative analysis. The left figure in a couple displays the index maps of Praedia di Iulia Felix, while the right one presents the identified anomalies overlaid on the visible orthophoto, in order to provide better contextualisation for the detected anomalies. All the index maps in this section are extracted from the afternoon datasets, which exhibit a richer presence of spectral anomalies when compared to the corresponding index maps derived from the morning flight.

The NDVI index map highlights several linear anomalies distributed across the insula. At the northern edge, they appear close to the buildings once used for commercial purposes. Within the viridarium—the central garden featuring a fountain with geometrically shaped mixtilinear basins—further anomalies are detected, which may correspond to modern water supply infrastructures. Additional anomalies are visible immediately south of the viridarium and near the southern entrance to the praedia, aligned along a northeast–southwest axis. Another anomaly runs along the perimeter wall that separates the hortus from the alley of the praedia on the southwest side of the insula. Finally, a series of anomalies can be observed in the southern sector, following the line of maximum slope of the land.

▼ Figure 126 Sythesis excerpts of NDVI calculated from afternoon datasets, ranging the Praedia di Iulia Felix (left). Summary of the anomalies marked from NDVI index map (right).

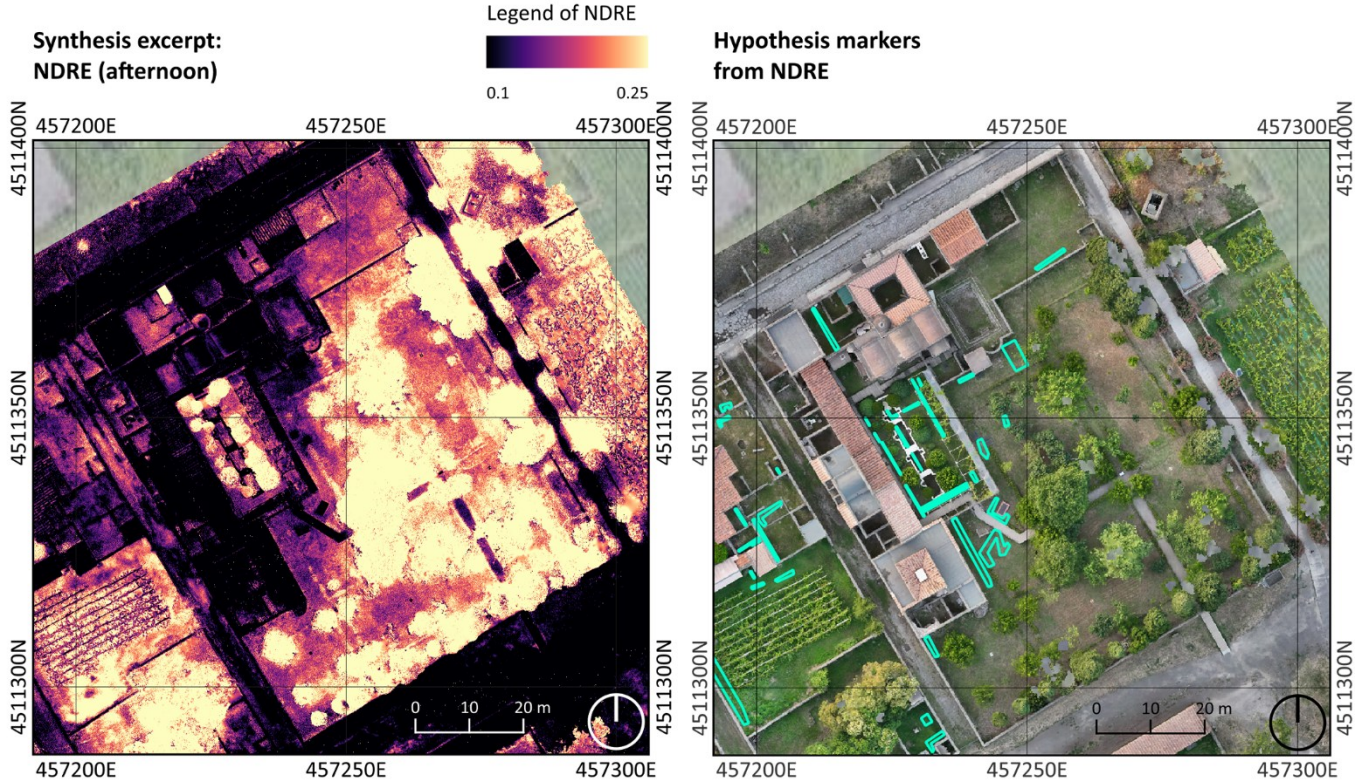


The EVI 2 index map reveals a situation broadly comparable to the NDVI map, yet with some notable distinctions in the central area of the hortus. While the NDVI map shows a denser concentration of anomalies, the EVI 2 map indicates that these features are less numerous, especially in the vicinity of the entrance walkway leading from the garden into the praedia. Despite being fewer, the anomalies maintain a northeast–southwest orientation, but they appear as more elongated marks that bend at right angles. Their configuration corresponds more directly with the main structural alignments of the praedia walls, suggesting that the EVI 2 index may be better suited to emphasising such architectural relationships.



▲ Figure 129 Synthesis excerpts of EVI 2 calculated from afternoon datasets, ranging the Praedia di Iulia Felix (left). Summary of the anomalies marked from EVI 2I index map (right).

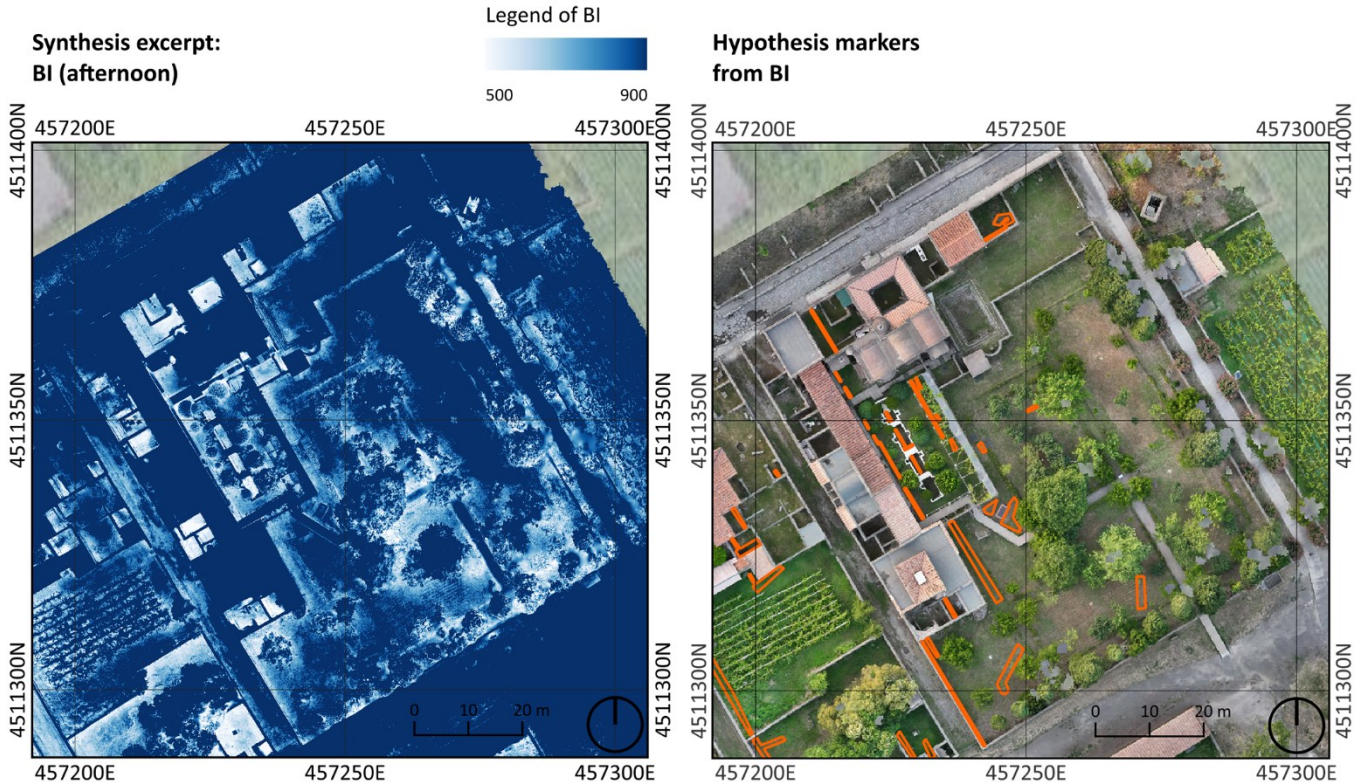
The NDRE index map presents a pattern only partly comparable to those of the NDVI and EVI 2 maps. In this case, the anomalies in the areas of the commercial shops and the thermal complex are noticeably reduced. A clear linear anomaly is still visible along the northern edge of the terrace, while an areal spectral anomaly is also evident at the base of the terrace's height change, to the south of the natatio of the thermal buildings. This feature is of particular interest, as Parslow had previously identified drainage systems in the same location through trench excavations (Anguissola & Olivito, Introduzione, 2022). In the central zone, near the entrance walkway leading into the praedia, the spectral anomalies already observed in the other maps are confirmed, though here they appear in smaller numbers.



The BI index map largely confirms the anomalies already detected in the previous analyses, distributed across the same areas that had been highlighted before. In particular, it provides strong confirmation of the marks in the southern sector of the hortus, which remain clearly aligned with the direction of the maximum slope of the land. It also reinforces the evidence of the anomaly running along the boundary wall that separates

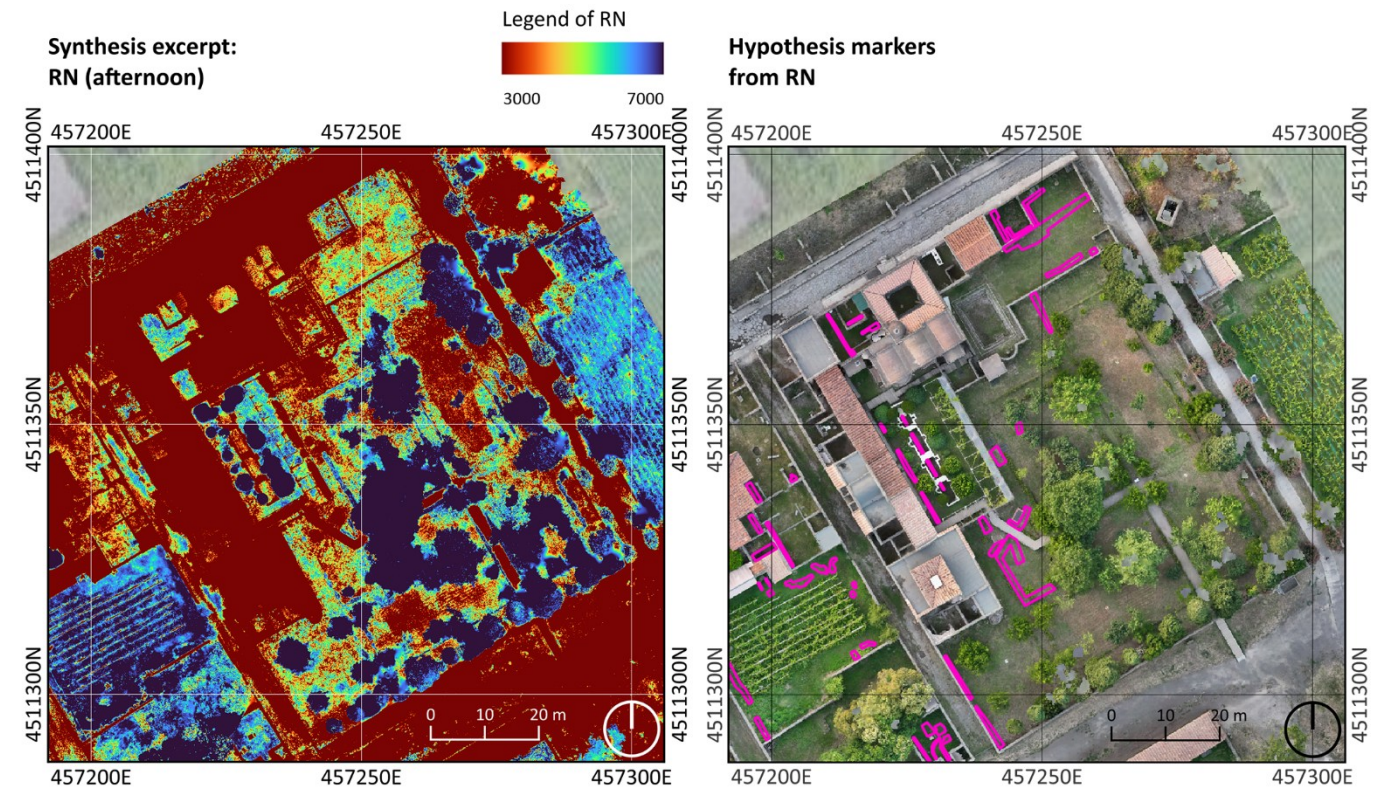
▲ Figure 127 Synthesis excerpts of NDRE calculated from afternoon datasets, ranging the Praedia di Iulia Felix (left). Summary of the anomalies marked from NDRE index map (right).

▼ Figure 128 Synthesis excerpts of BI calculated from afternoon datasets, ranging the Praedia di Iulia Felix (left). Summary of the anomalies marked from BI index map (right).



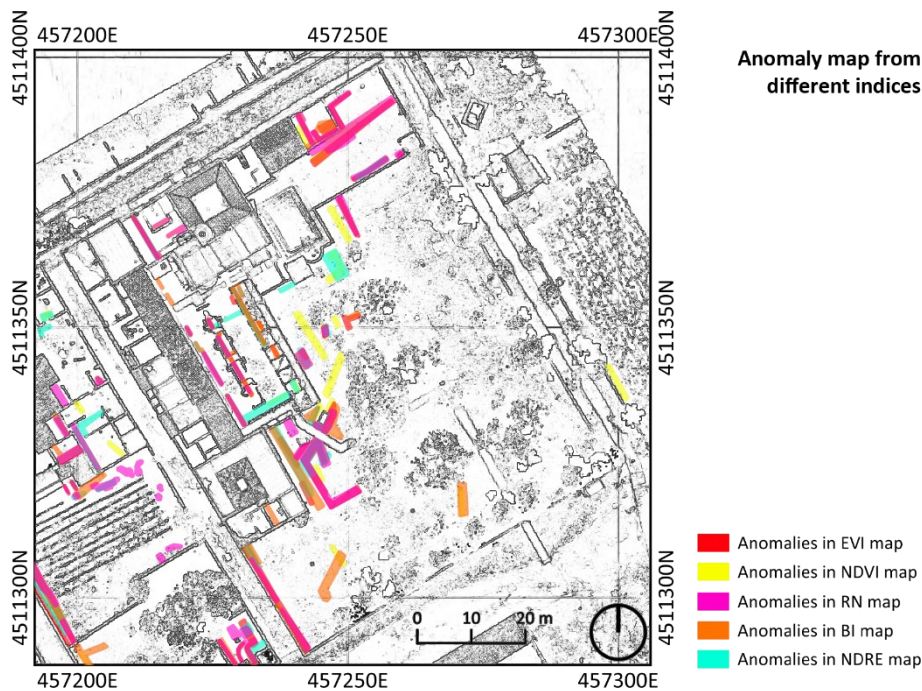
the hortus from the praedia alley, further validating the patterns observed in the other index maps.

The RN index map presents a situation of detected anomalies very similar to those found by reading the EVI 2 index map.



▲ Figure 130 Sythesis excerpts of RN calculated from afternoon datasets, ranging the Praedia di Iulia Felix (left). Summary of the anomalies marked from RN index map (right).

Lastly, a comprehensive map synthesises all crop marks identified through the applied indices, highlighted in different colours, each corresponding to the specific index represented in ► Figure 131.



► Figure 131 Summary of anomalies detected in Praedia di Iulia Felix, overlapping on a line-drawing map

7.4. Results obtained and comparative analysis

To making the result and the method more convincing, the comparative analysis could become an efficient strategy especially with the reliable results using other methods. Past research and investigations in regio II have yielded positive results, including geophysical surveys conducted in Praedia di Iulia Felix and archaeological excavations based on the geophysical surveys (Anguissola & Olivito, 2022). This paragraph aims to present the comparative analysis based on these studies.

Strating from the result of the last paragraph, the comparison with the geophysical survey will be stated detailedly, including the workflow. This group considers the trend of anomalies on a larger scale.

One step more, the comparison with the archeological excavation will be presented through the same method but zooming in a smaller scale with more influence from the surrounding.

Apart from these comparison, a group of strong anomalies would be collected in the third section, as well as the consideration towards the method. Finally, a brief discussion would be stated for exploring the next step of this method.

7.4.1. Synthesis of comparison with geophysical survey

To confirm the results and method, the analysis and identification of spectral anomalies in the index maps was compared with the geophysical investigations planned based on the stratigraphic excavations of 1990s (Marchetti, Materni, & Sapia, 2022). As the investigations were limited and only focusing on directly examining the areas of interest suggested by the previous investigations, in this stage, the anomalies not related to the investigation areas will not be presented in the analysis. The main idea of this confirmation is to check if the result has a certain overlapping ratio with the known result from the geophysical survey.

The initial steps involved collecting and selecting the most relevant geophysical survey maps, which provided key insights for the subsequent localisation of the stratigraphic samples carried out by the archaeologists. These maps were then compared with the results of the Aerial Remote Sensing with UAV, using a common reference system within the GIS environment, which enabled a comparative analysis of both raster and vector data.

A further critical phase of the analysis aimed to synthesise the results of the spectral anomalies – derived from the analysis of the different index maps – in a single map. The frequency with which each index identified the same anomaly was quantified, and a confidence map was generated. This map summarises the findings using a gradient of red shades – ranging from more intense to less intense – based on the frequency of the anomaly occurrence across the different index maps.

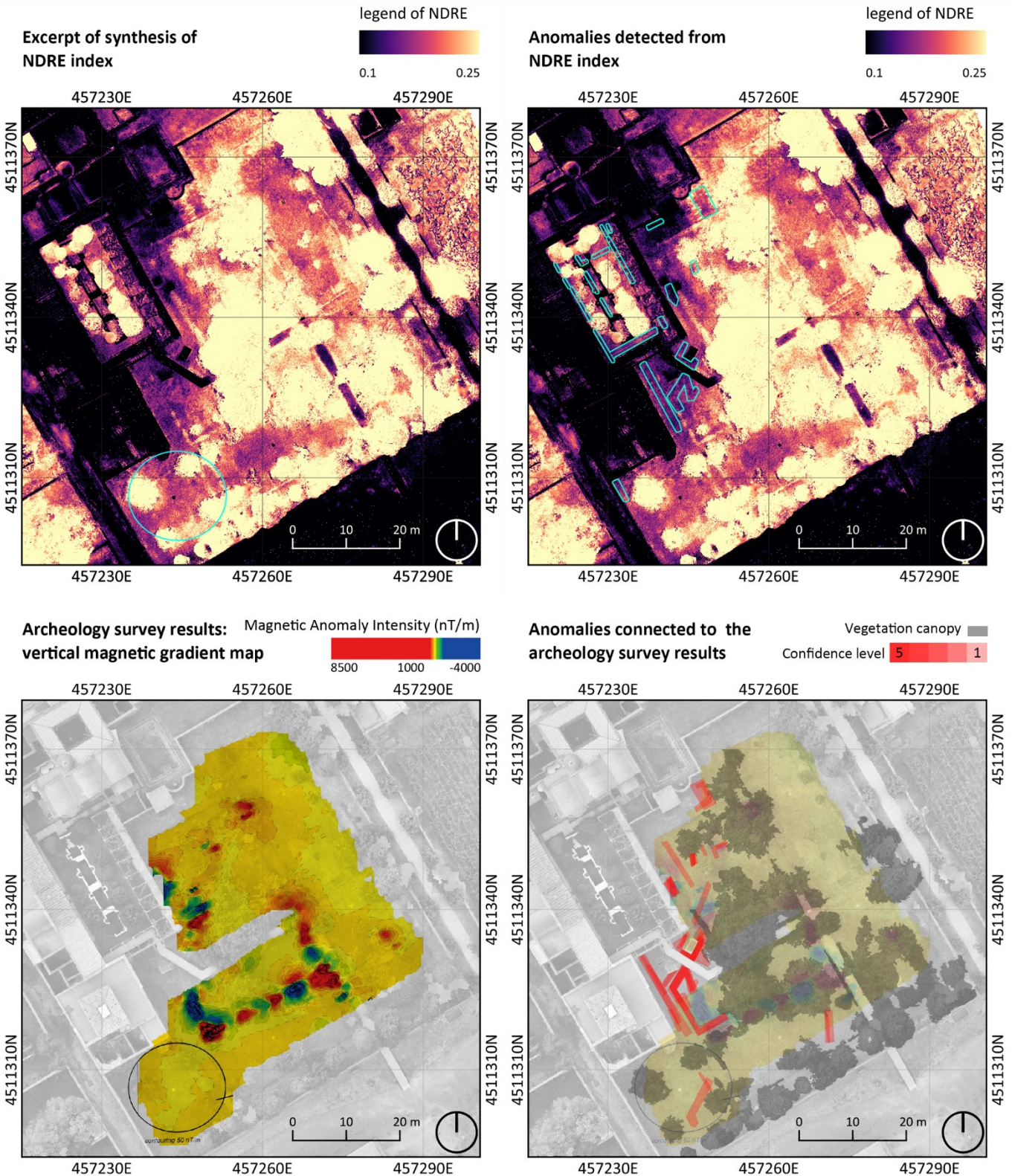
The comparison will be presented in 4 maps comprehensively: the first is the a suitable index map to show the working base, the following one is the related anomaly detection of this map. Apart from these, samples from the geophysical survey and the confirmation map overlapped would be presented for showing the overlap ratio and the general trend.

During the detection, it should be underlined is the known results from archaeologists and geophysicists can work as value guidance to identify the most appropriate index range for the specific vegetation conditions in the target area.

The first group is the comparison derived from a Vertical Magnetic Gradient map. the strong magnetic gradient values were interpreted in

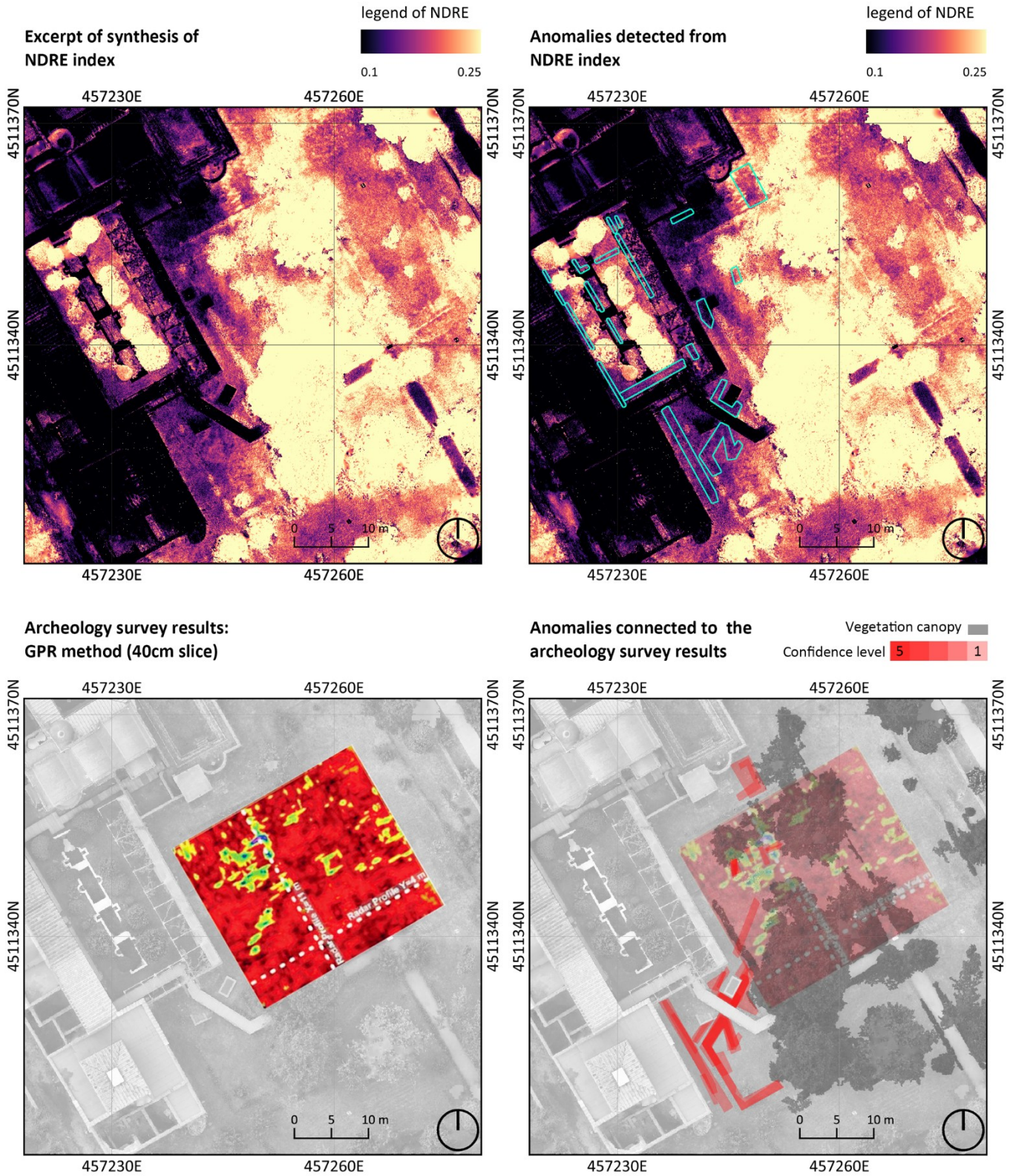
the centre of the hortus as suggesting the presence of strongly magnetised elements at low depths by the geophysics specialists (Marchetti, Materni, & Sapia, 2022). These elements probably have to be identified as modern buried hydric infrastructures. Instead, the anomaly along the northeast-southwest direction, which has weaker values, can be identified – in their opinion – with probable ancient structures. The index maps from Aerial Remote Sensing with UAV also identified the same feature, as indicated by the circles on the two maps.

▼ Figure 132 A group of images showing the workflow of the comparative analysis: including NDRE index map and anomaly detection (the first row); the vertical magnetic gradient map and the final anomalies detected with confidence view (the second row).



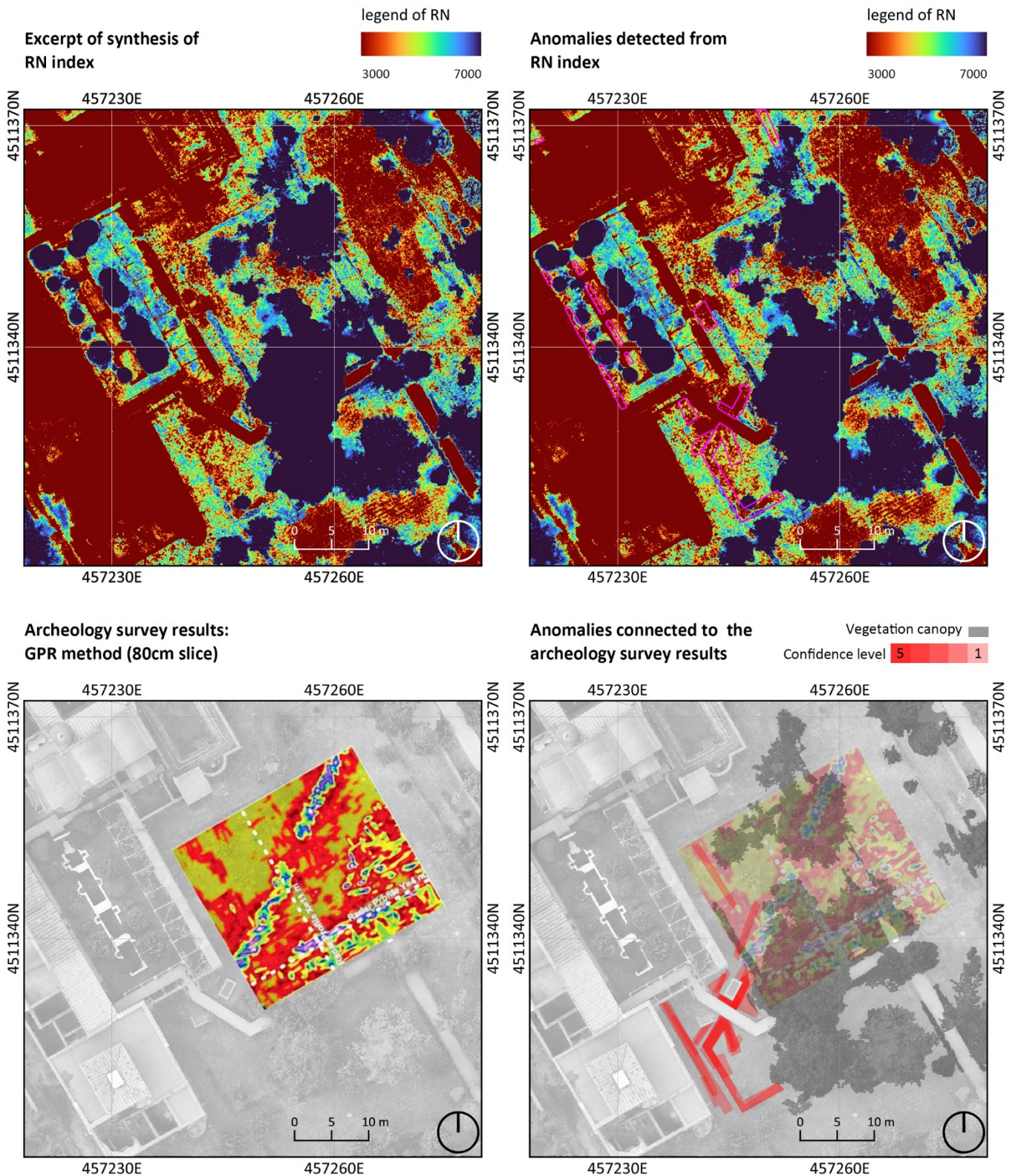
And the second group is comparison of a 40 cm depth slice GPR map. Regarding the second and third rows of the image: both the GPR maps highlight different structures at the two considered depths. The anomaly in this map corresponds to substructures of drainage systems. Though the area got influences from the treetops and human activities, some features matching the pattern of the GPR map appeared in the map were still catches during detention.

▼ Figure 133 A group of images showing the workflow of the comparative analysis: including NDRE index map and anomaly detection (the first row); the 40cm GPR map and the final anomalies detected with confidence view (the second row).



In the end, the last group of this section is showing a comparison of the 80 cm depth slice GPR map. As the map shows, a clear diagonal crossing masonry structure, which corresponds to the canal of the Conte of Sarno (Marchetti, Materni, & Sapia, 2022), which even the indices maps have easily identified despite the interruption due to the treetops.

▼ Figure 134 A group of images showing the workflow of the comparative analysis: including RN index map and anomaly detection (the first row); the 80cm GPR map and the final anomalies detected with confidence view (the second row).

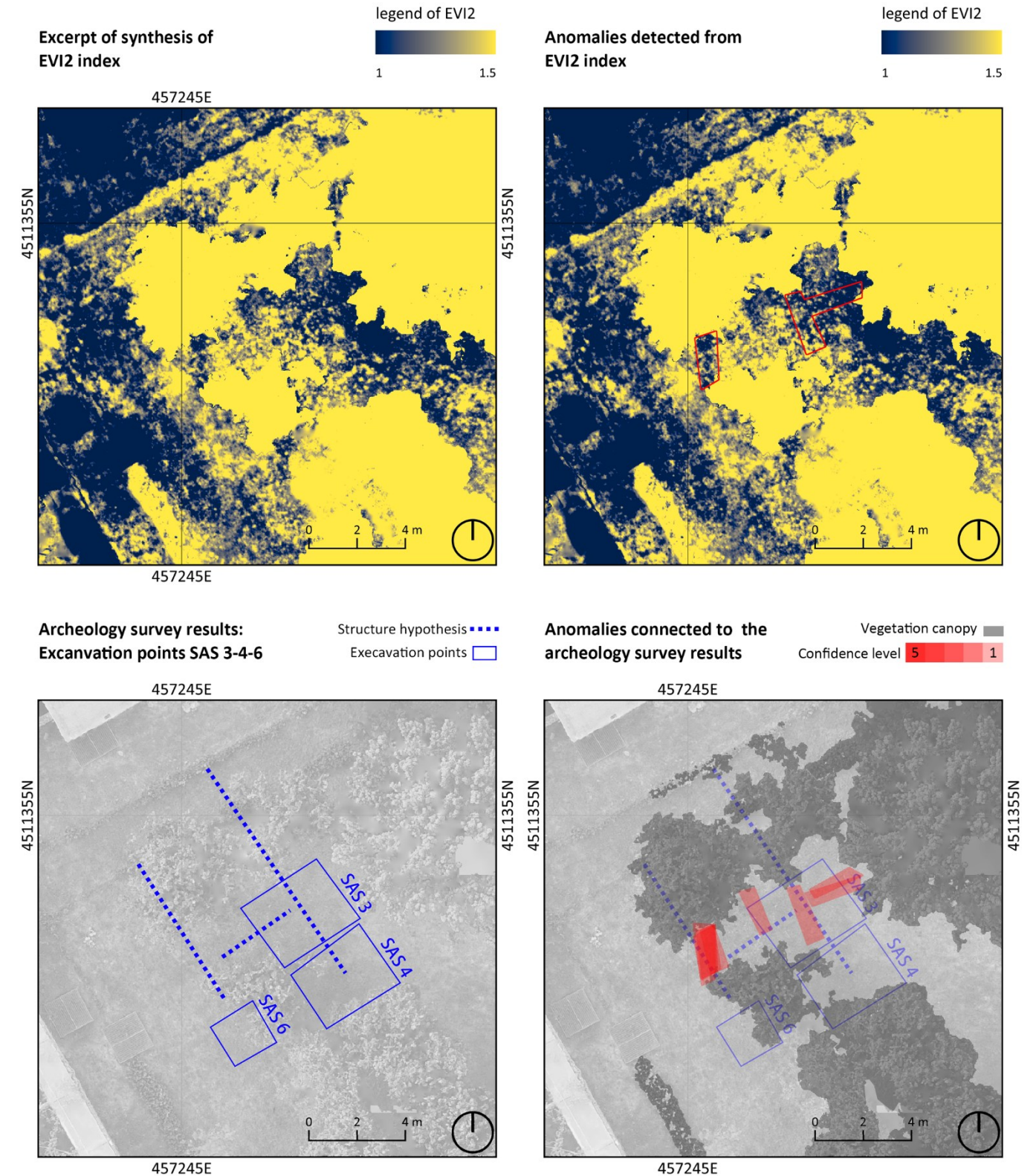


7.4.2. Synthesis of comparison with excavations

Following the geophysical investigations, the archeologists involved in the PRAEDIA project carried out 7 stratigraphic excavations trials in the Horus of Iulia Felix Praedia. These excavations provided valuable information on channel systems and helped in the reconstruction of the urban landscape, prior to the construction of the praedia (Anguissola & Olivito, Introduzione, 2022). Since the approach tested in the present research aimed to validate the capabilities of a relatively low-cost commercial sensor, used to develop Aerial Remote Sensing with UAV survey presented in this chapter, the focus was on the excavation areas that provided the most valuable insights from the archaeological work.

Similar to what emphasised in the last section, the comparison between the results of the archaeological excavations and the anomalies identified using the Aerial Remote Sensing method still highlighted its effectiveness. Apart from this, the presentation of the comparisons will obey the same layout in the last section. But due to the scale of analysis area and the positions, the projection of the treetops is also overlayed on the confidence map summarising the spectral anomalies, as the influence of the treetops is more stronger than the analysis in the last section. Also, based on the same reason, all the excavations are divided into 2 groups and presented in the maps.

The first group of analysis concerns a series of excavation trenches opened by the archeologists – prof. Anna Anguissola and prof. Riccardo Olivito – near the balneum latrine (excavation 3, 4, and 6) to verify Parslow's hypothesis, which suggested the possible existence of a road that divided the insula in two parts (Anguissola & Olivito, Introduzione, 2022). Although there was no confirmation found for the road infrastructure, many walls with north-south and east-west directions were identified, even the coverage of the canopies.

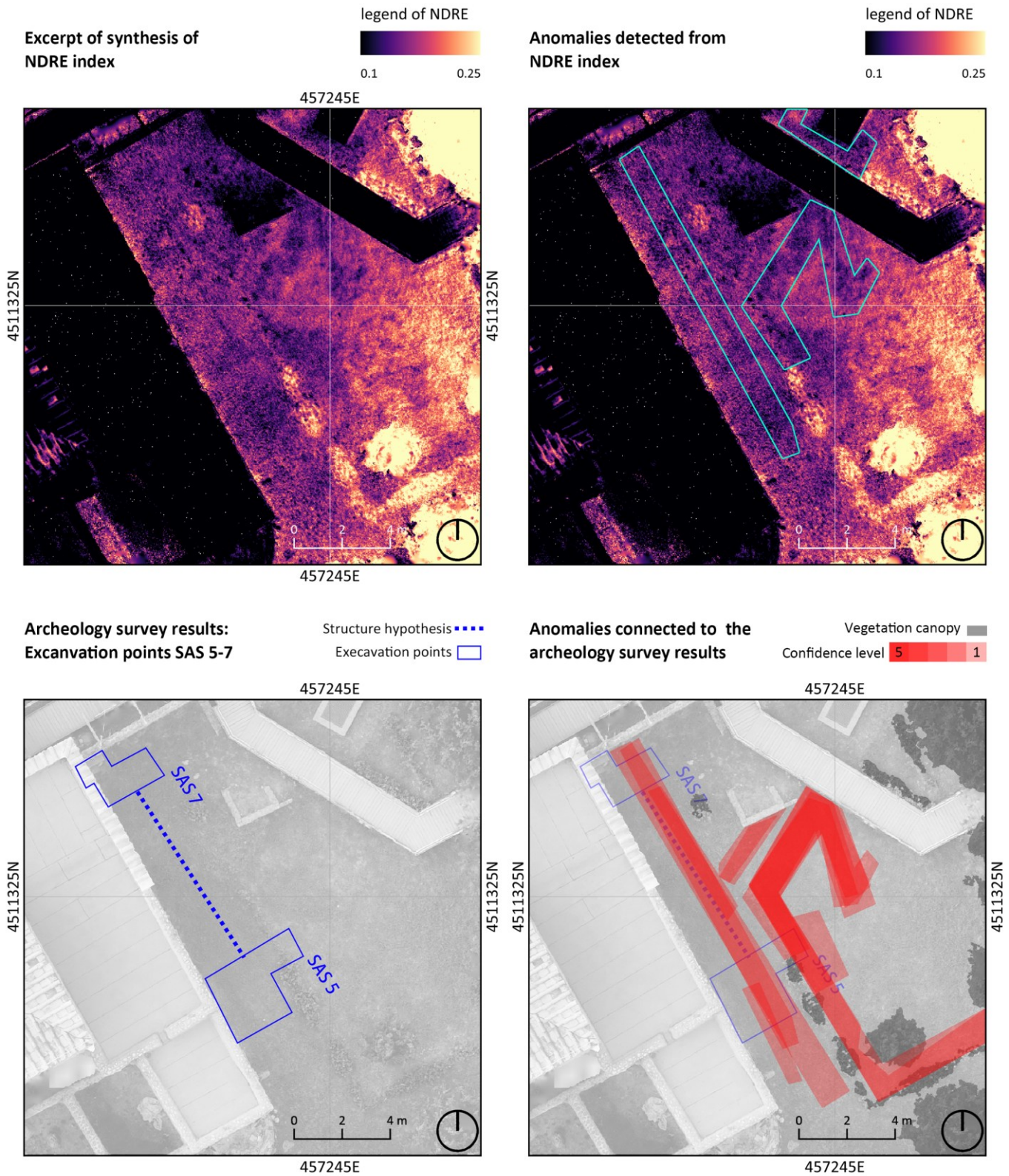


And the other group of analysis focuses on the excavation 5 and 7 which brought the richest and most complex findings: while the area 5 revealed a small channel coming from the viridarium, area 7 uncovered a stratified set of different channels and a water cistern. Three different channel systems were discovered from 3 different areas of the praedia, all directed towards the amphitheatre (Anguissola & Olivito, 2022). In this case, the spectral anomalies of the index maps presented the most challenging

▲ Figure 135 A group of images showing the workflow of the comparative analysis: including EVI 2 index map and anomaly detection (the first row); the excavation 346 traced and the final anomalies detected with confidence view (the second row).

situation, as marks are recognisable in all the different index maps. However, the general context may have been partially complicated by ground movement and backfill activities that occurred after the completion of the work on the trenches.

▼ Figure 136 A group of images showing the workflow of the comparative analysis: including NDRE index map and anomaly detection (the first row); the excavation 57 traced and the final anomalies detected with confidence view (the second row).



7.4.3. Summary of other significant anomalies

Apart from the anomalies in the hortus, there were a group of anomalies located out of the area of geophysical or archaeological surveys, which distributes in the northern part of the insula, the viridarium, the area near the boundary wall, and the region near the vineyard of the domus of the Venere in Conchiglia. This section will present the results briefly by a suitable index map as a reference and the confidence map overlapped on the gray scale visible orthophoto.

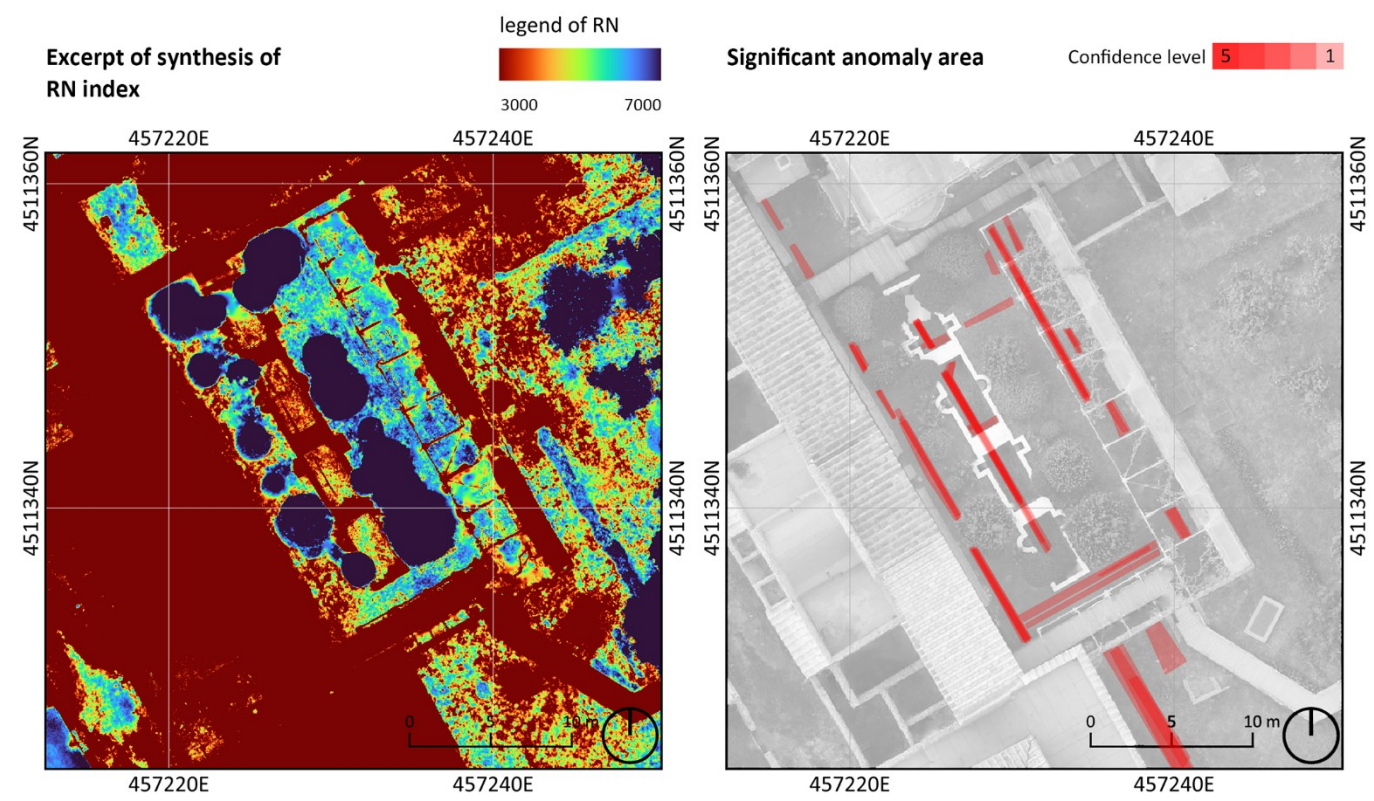
In the northern sector of the insula, a series of anomalies is visible along the walls, despite the absence of any corresponding evidence on the UAV orthophoto. Notably, even without comparative data from geophysical or archaeological surveys, the anomalies remain recognisable in the adjusted index map, where they exhibit a degree of regularity that suggests they are not random artefacts but potentially meaningful features.



The connections between anomalies appear more evident in the viridarium area. In this sector, a series of anomalies can be seen forming regular shapes that are clearly interrelated. Given the spatial context, some of these features may correspond to pipes running through the central pool, a hypothesis further supported by their apparent connection to water channels previously excavated by archaeologists outside the viridarium. Moreover, it is noteworthy that many of the anomalies in this area are expressed as fine double lines, a pattern that indicates both the

▲ Figure 137 Brief result presenting of an index map of the area (left) and a summary of anomalies detected with confidence view (right)

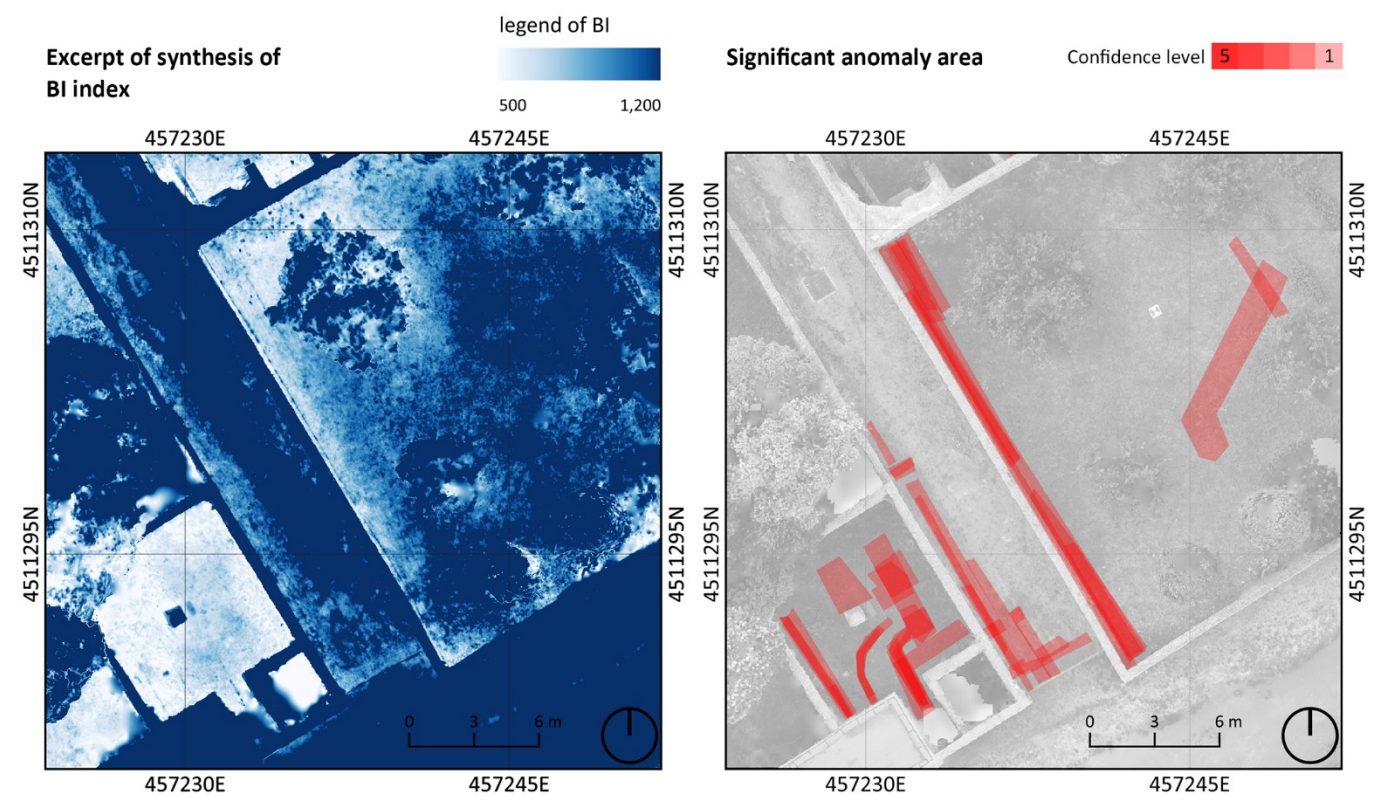
precision and the sensitivity of the method when applied to data of this GSD.



▲ Figure 139 Brief result presenting of an index map of the area (left) and a summary of anomalies detected with confidence view (right)

▼ Figure 138 Index map of the area (left) and a summary of anomalies detected with confidence view (right)

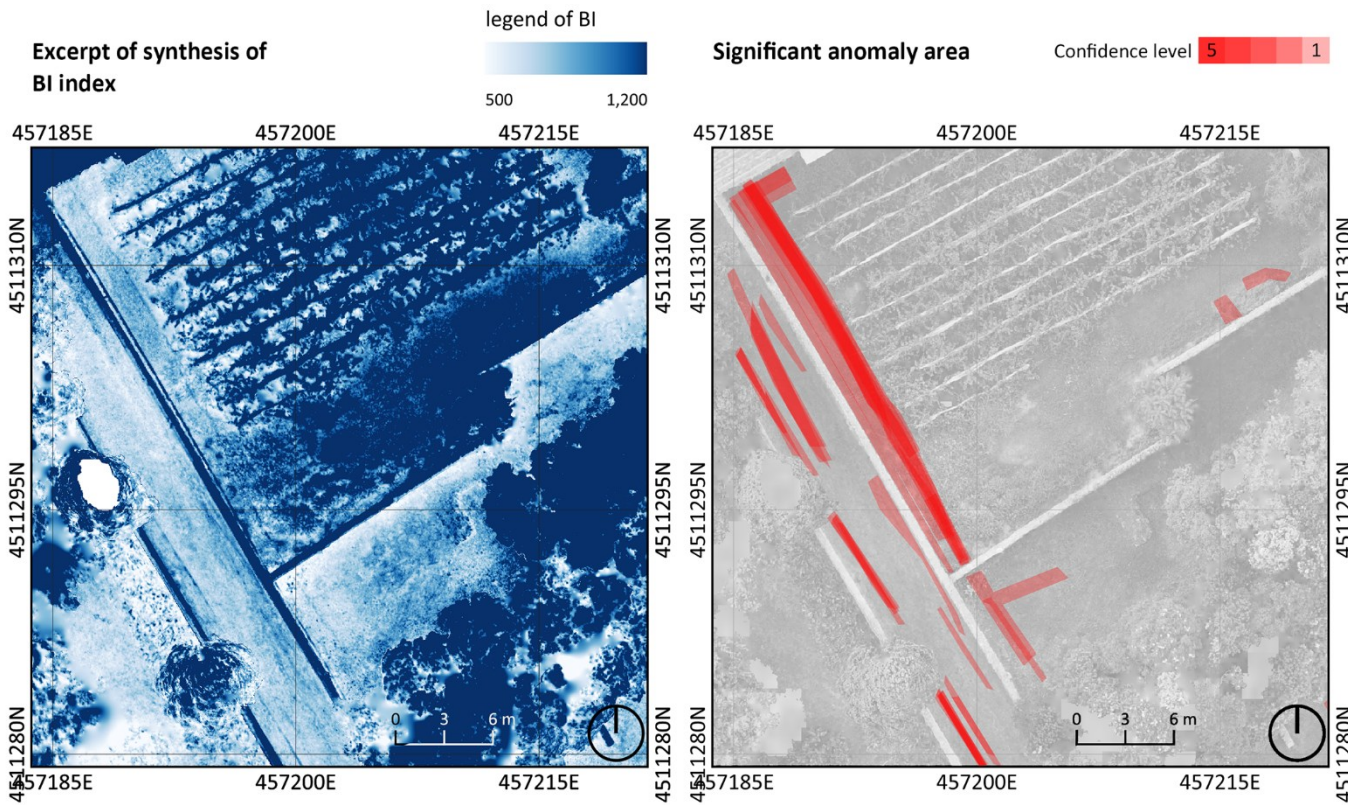
The exploration is also carried out at the edge of the geomagnetic survey area, which includes the edge of Praedia and a small courtyard in the adjacent insula, as well as the blocked alley between them. In this relatively remote area, the potential of this method is fully exposed - even in areas with relatively poor vegetation, anomalies can be clearly



identified - and the BI map's ability to display under current conditions is similar to other indices, even with clearer visual effects.

At the same time, the exploration also extended to the adjacent Insula vineyards. The anomalies in this area also exhibit similar features as in the previous example. However, it is worth mentioning that although the vegetation situation in this area is not uniform, combined with the exploration results of multiple indices, anomalies can still be clearly obtained

▼ Figure 140 Brief result presenting of an index map of the area (left) and a summary of anomalies detected with confidence view (right)



7.4.4. Discussion about the analysis

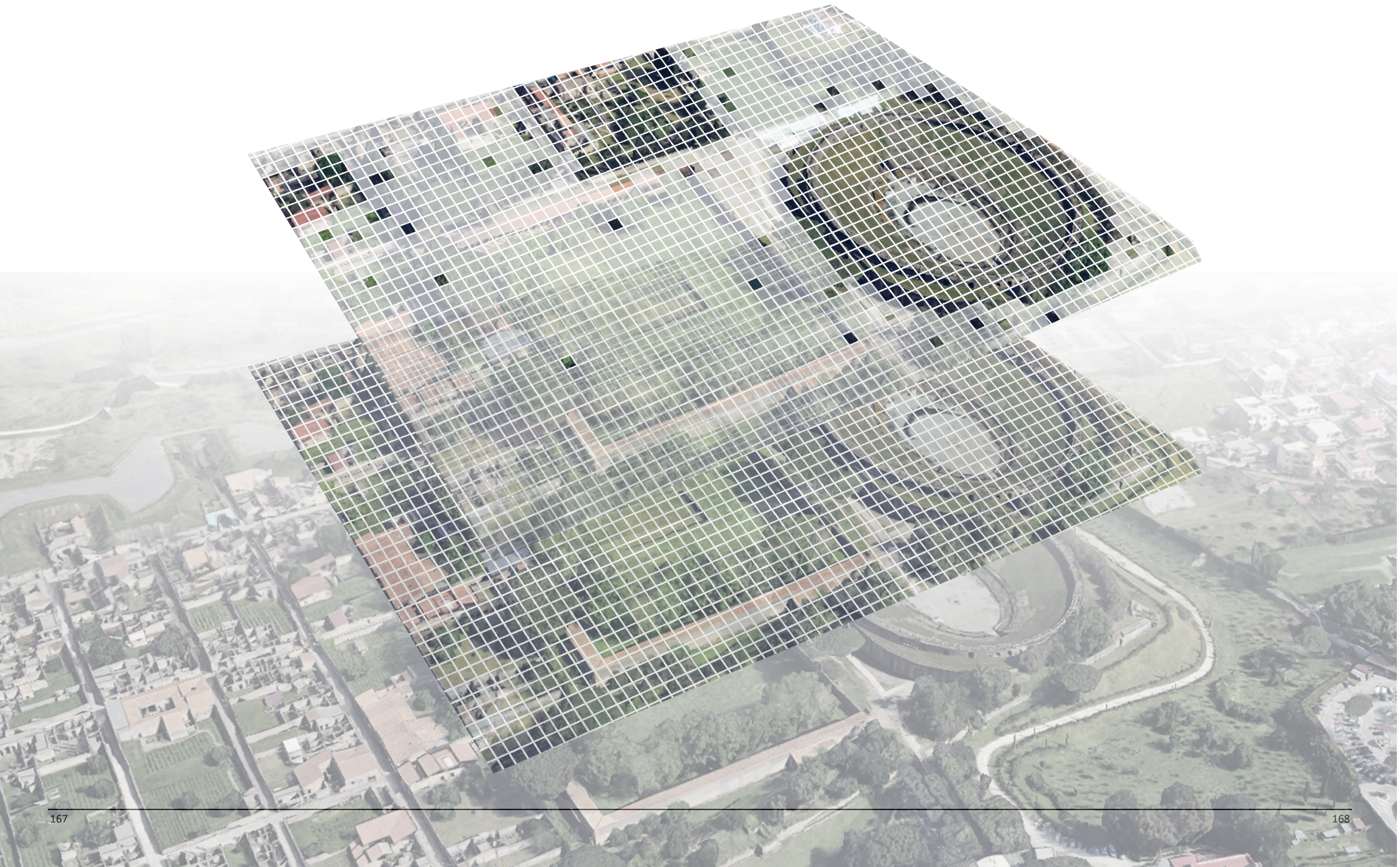
The multispectral photogrammetric analysis conducted at the Praedia of Iulia Felix in this case study, as demonstrated in previous sections, demonstrates the method's significant potential for detecting spectral anomalies that may correspond to buried archaeological features. In particular, the cross-correlation with data from previous geophysical and archaeological surveys provides strong support for the feasibility of using commercial multispectral drone sensors for archaeological exploration. The high heterogeneity of the Pompeii site—particularly in terms of the soil and vegetation types studied—makes it an ideal case for such studies.

The method itself utilizes a commercial drone multispectral sensor to efficiently and cost-effectively acquire high-resolution data, despite the limitations of the available spectral bands. However, similar analysis strategies can be applied to data analysis and anomaly detection, as long as the acquired bands include the three core R, RE, and NIR bands. While these bands perform different functions, they are considered effective for detecting anomalies in vegetation and soil.

However, it is certain that more indices relevant to vegetation studies could contribute to this approach if more bands were available, such as BLUE in the visible spectrum, or other sensors capable of collecting TIR or SWIR data.

From a methodological perspective, another aspect worth highlighting is the manual visual interpretation of anomalies. While crucial, this step is particularly time-consuming due to the large number of spectral index maps involved and the size of the site. To improve the reproducibility and sustainability of this method, the development of semi- or fully automated anomaly detection procedures would be beneficial, especially when applied to larger datasets.

8. Enhancements of analysis from AI



8.1. AI solutions for geomatics researchers

Strictly speaking, AI's impact on geomatics occurred when manual, human-centric workflows were transformed into automated, data-driven systems (Jocea, 2024). As various AI technologies continue to advance our understanding, machine learning, including deep learning, has already made its mark in the field of geomatics (Janga, Asamani, Sun, & Cristea, 2023). This involves using algorithms to automate basic tasks such as land cover classification and object detection in satellite imagery.

At present, AI is enabling a wide range of advanced applications within geomatics, particularly by enhancing the processing and interpretation of the data on a scale that was previously unattainable. These applications extend across multiple domains, strengthening geomatics' capacity not only to analyse but also to model complex spatial data. This development is closely connected to the rapid increase in high-resolution, multi-source datasets—such as imagery from the Sentinel-2 satellite or LiDAR data acquired through drone surveys (Roche & Hummel, 2024). The sheer amount and speed at which the information is now acquired renders traditional manual methods of analysis insufficient, thereby creating a strong need for automated, AI-aided approaches (Jocea, 2024).

To reduce the barriers to entry and encourage wider adoption, software developers are increasingly providing tools that simplify and automate complex geomatic tasks. In recent years, a growing number of user-friendly, no-code and low-code platforms have emerged, enabling users with limited technical expertise to carry out advanced analyses. For instance, Esri's ArcGIS platform offers a streamlined interface together with pre-trained AI models, allowing users from diverse backgrounds to perform sophisticated geospatial operations with relative ease (Esri, 2025). Similarly, software such as CloudCompare integrates algorithmic models directly, supporting automated workflows for common geomatic applications. In addition, visual modular programming environments, often referred to as Visual Programming Languages, provide an accessible entry point. These systems allow users to design workflows through graphical components rather than traditional coding, making it easier to perform fundamental data processing tasks without extensive programming knowledge.

8.2. Application scenarios

Building on the previous discussion, this paragraph examines how AI can enhance the analysis of geomatics data when users have little or no coding experience. The 3 case studies presented in this paper are applied as exploratory scenarios through which different approaches are tested. They will be divided into 3 sections for discussion, and the sequence will be arranged respect the exploring depth:

- The Complesso dei Riti Magici, is the most easy case to segment 3D point cloud of a block, called insula, through a black box AI in a commercial software.
- The amphitheatre, contributes a point cloud with atypical shape to explore an algorithms with high degree of freedom installed on open source software.
- Praedia di Iulia Felix, as the analysis presented, the enhancing part was pick for anomalies detecting on the index maps, using a basic ML visual programming language platform.

Within each scenario, the study evaluates the effectiveness of AI tools in supporting data preprocessing as well as their contribution to improving the overall quality and interpretability of the results.

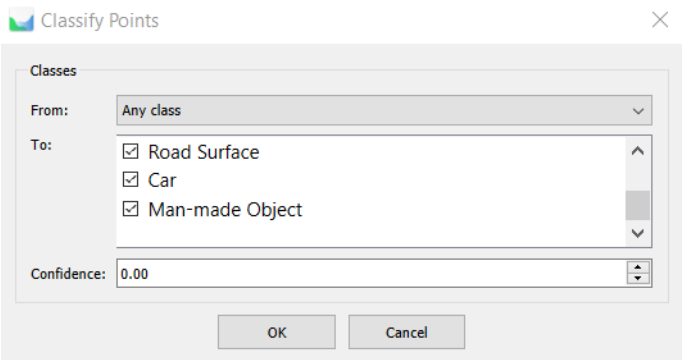
8.2.1. Block scale point cloud segmentation

This section focuses on the segmentation of a block-scale point cloud containing the entire insula where the Complesso dei Riti Magici is located, as illustrated in Figure 141. As noted earlier, Metashape is a robust commercial software, equipped with a semantic segmentation algorithm capable of automatically classifying point clouds. A key challenge in this case arises from the nature of the point cloud, which represents an area where most buildings lost their roofs. Consequently, the algorithm may not have sufficient relevant training data, even though the structures are easily recognisable to the human eye.



► Figure 141 Isometric view of the point cloud tested, under the colour view mode

This tool has a low flexibility, with only the classified point cloud set (i.e. "from"), the classified set (i.e. "to"), and the confidence. It has greatly reduced the difficulty of understanding and the threshold for operation, but has also lost its potential to be used in more diverse contexts. And the black box attribute of the algorithm makes this even more serious.



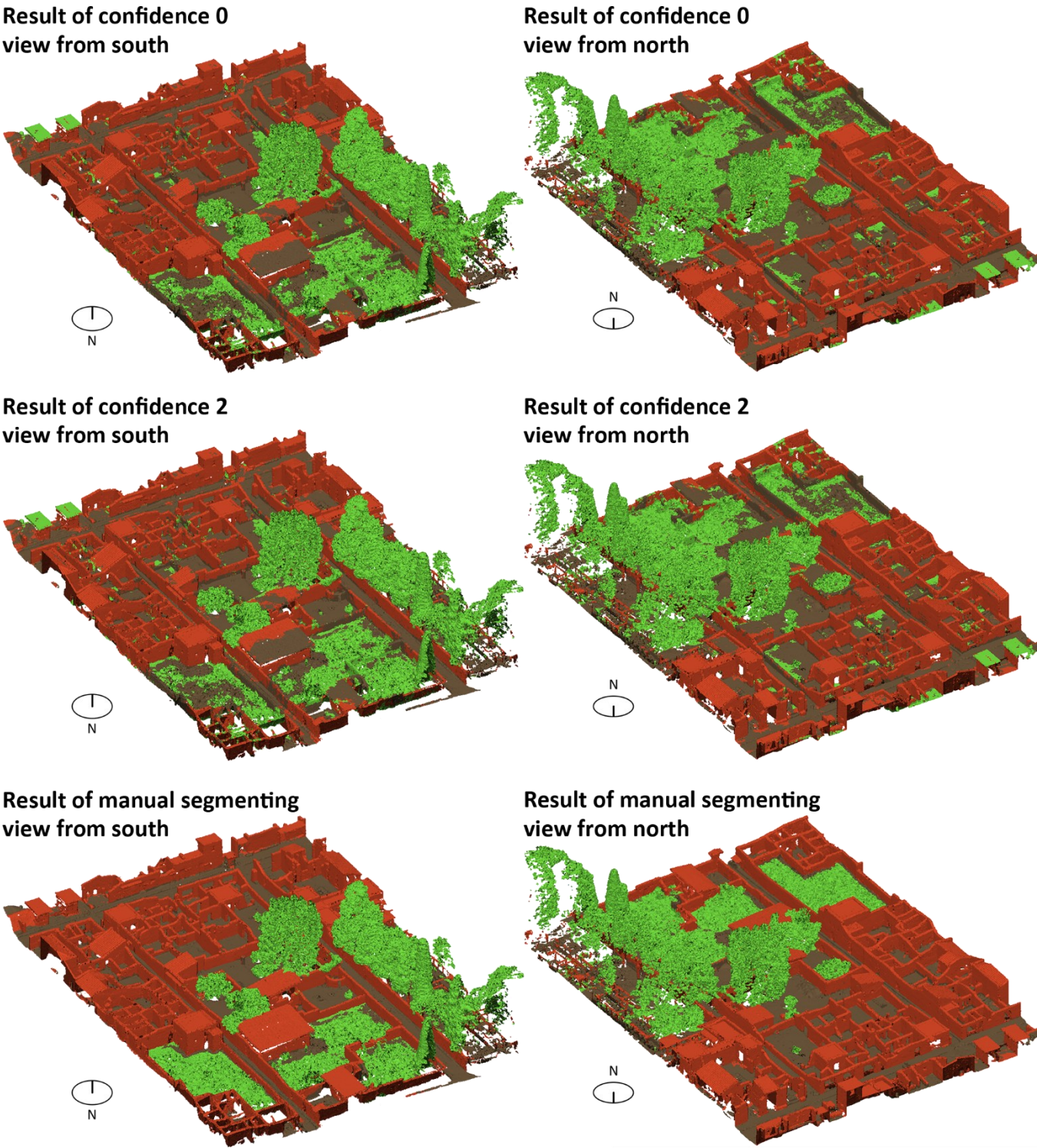
► Figure 142 Interface of the AI tool using for point classifying

The test attempted to adjust the confidence to a minimum value of 0 and a maximum value of 2 while maintaining a fixed number of categories of 3 and label types. From the time spent on the operation, different

parameters have almost no impact on the results. Unfortunately, the impact on the results of point cloud classification is also minimal. The following is a comparison between two test results and manual segmentation results:

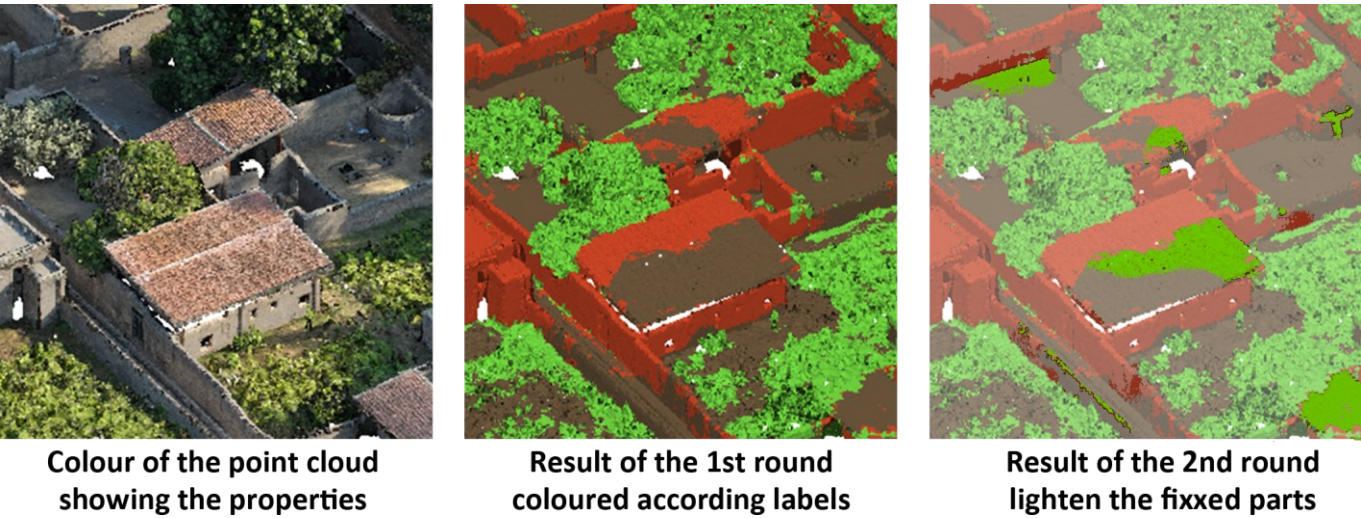
Firstly, the results obtained from different confidence calculations are similar. Secondly, if it is necessary to compare the differences between the two, in the region of difference, the result represented by confidence 0 is relatively closer to manual recognition. In addition, atypical object shapes may indeed affect the recognition of algorithms, and even elements such as walls and roofs have a large number of confused parts.

▼ Figure 143 The comparison of test results and the manual segmentation



The practice of repeatedly using this algorithm has also been attempted for the parts that have been segmented incorrectly. But as seen in Figure 144, semantic recognition has become even more chaotic. This undoubtedly further proves the narrow application scope and adjustment space of this tool.

▼ Figure 144 The comparison of the results of different rounds



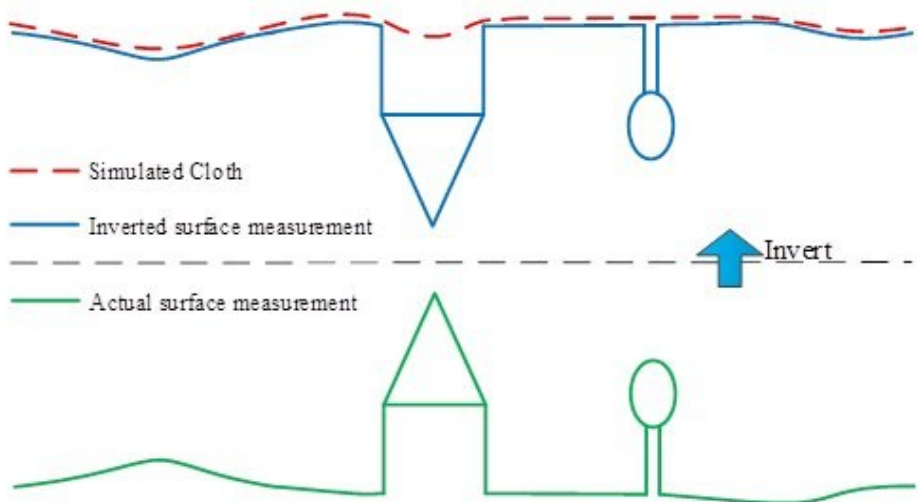
It can be seen from the above results that this algorithm is not ideal when applied to architectural complexes like Pompeii. And the number of point clouds does not have a significant impact on the accuracy of segmentation results, but the processing time required is indeed proportional to it. In addition, preprocessing such as early segmentation does not significantly improve the accuracy of the results when the shape of the point cloud is not typical enough.

However, it is worth noting that even with such chaotic results, it greatly saves the time required to manually segment the same point cloud. Therefore, this algorithm can be used as a tool for classification assistance rather than the main force.

8.2.2. Atypical architecture scale point cloud segmentation

Further from the unchangeable black box AI, AI that can adjust parameters to adapt to different classification rules may have higher efficiency. Therefore, this section chooses to use an algorithm called Cloth Simulation Filter equipped on Cloud Compact to segment the point cloud of Amphitheatre, aiming to separate the complete building structure, and the ground including the remaining underground space.

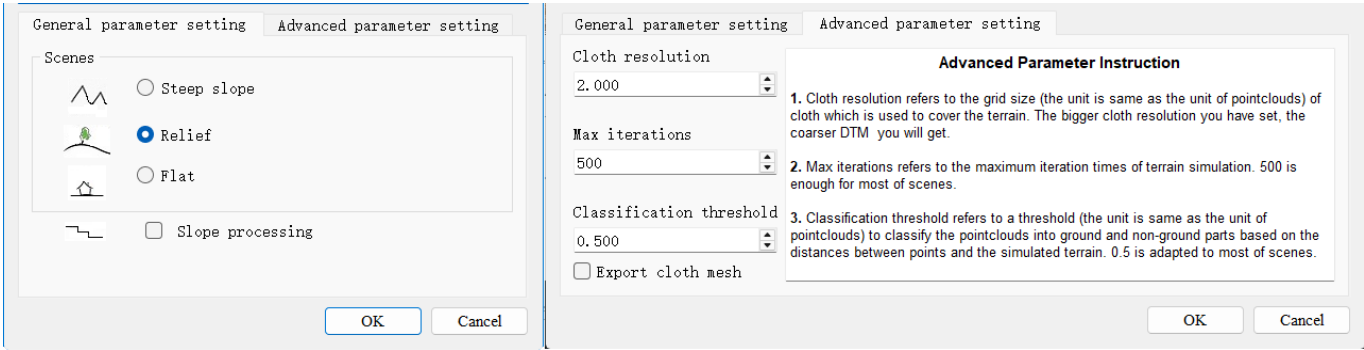
This method is based on cloth simulation on a LiDAR point cloud inverted, and then a rigid cloth is used to cover the inverted surface (Zhang W. , Qi, Wan, & Wang). By examining the interactions between the cloth nodes and the corresponding LiDAR points, it is possible to determine the positions of the cloth nodes and, in turn, generate an approximation of the ground surface. Once this surface has been established, the ground points can then be extracted from the LiDAR point cloud by comparing the original LiDAR data with the generated surface model (Zhang W. , et al., 2016).



◀ Figure 145 Principle of CSF method (CloudCompare wiki, 2016)

This tool supports calculations through both general and advanced parameters, which not only enhances users' understanding of data and algorithm principles, but also greatly expands the tool's adaptability to different datasets.

▼ Figure 146 The interface of CSF tool in Cloudcompare (general parameter & advanced parameter)

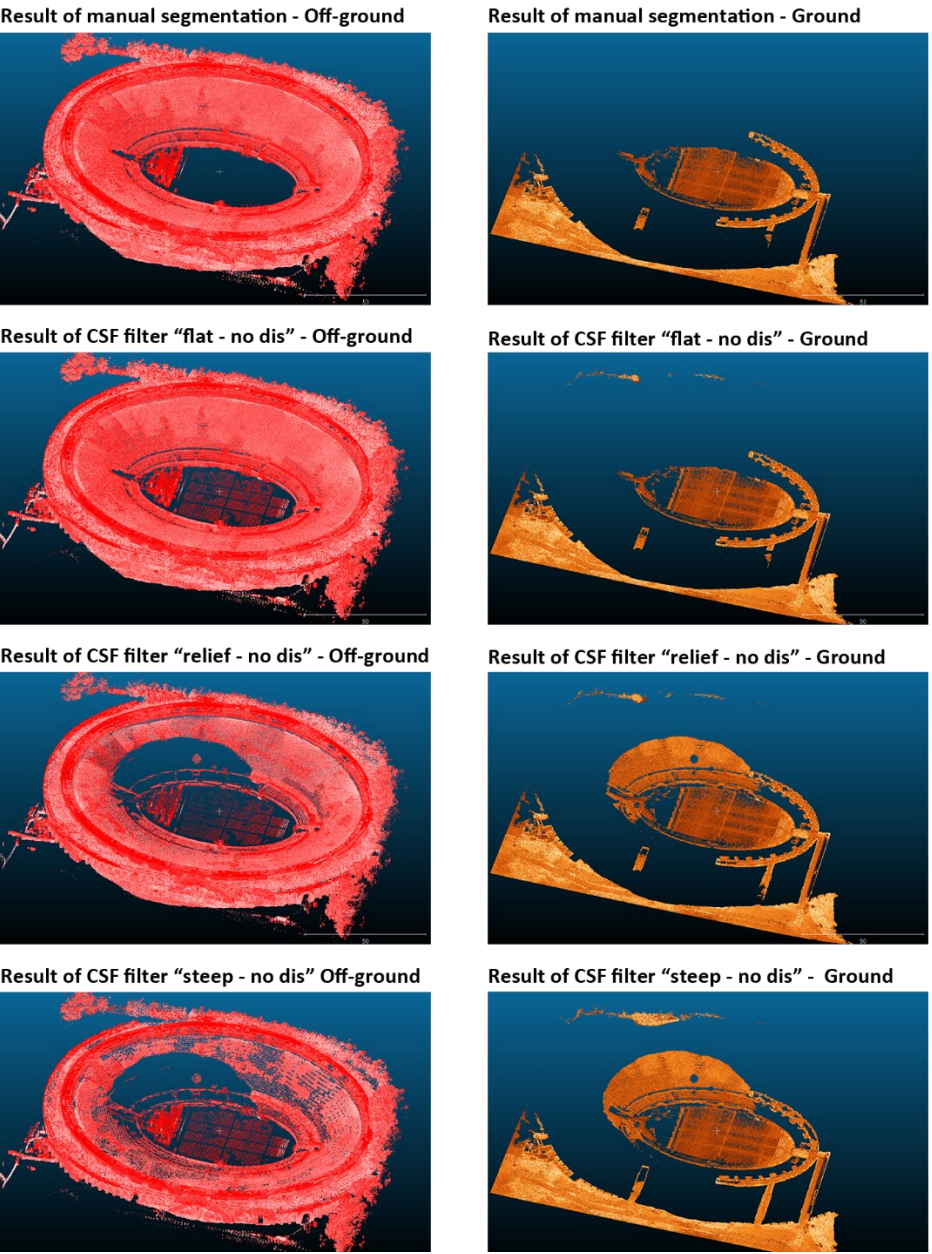


Firstly, it should be noted that this point cloud, which exceeds 200 million points even after subsampling, still places a considerable burden on personal laptops when running the algorithm. For this reason, data preprocessing must take into account both machine performance and dataset size. When these factors are excessive, it is advisable to reduce the computational load by either splitting the dataset or applying further subsampling. Moreover, certain algorithms—such as the one used in this case—allow adjustments through calculated parameters; however, such changes can significantly affect the accuracy of the results.

With an understanding of the geometric characteristics of point clouds, fixed high-level parameters such as cloth resolution, maximum iterations, and classification threshold were first determined through preliminary testing in order to balance computation time with output accuracy. Following this, different operational parameters were tested and compared to evaluate whether improved solutions could be achieved.

As shown in the figure, different parameters in this algorithm have a greater impact on the results compared to the previous case. And the combination of “Flat - no disconnection” achieved almost the same results as manual segmentation.

Firstly, it needs to be acknowledged that the flexibility of algorithm tools does contribute greatly to the adaptability of the algorithm. By changing parameters, the details of the algorithm can be closer to the analyzed dataset. Secondly, because the rules of the algorithm are transparent, although it increases the user's threshold for use, it is also more conducive to the rational use of the algorithm's rules.



► Figure 147 The comparison of test results and the manual segmentation

8.2.3. Image segmentation on index maps

After testing various AI tools available within the software, the third exploratory scenario applies ML to detect anomalies on the achived index maps. This approach is intended to replicate the anomaly detection process previously carried out manually in Chapter 7, but with AI performing the task instead of a human operator. The final detection outputs generated by ML will then be overlaid with the manual results, allowing for a direct comparative analysis of performance and accuracy.

QGIS provides a versatile environment for conducting a wide range of analyses, as it not only includes numerous tools for processing geographic information but also supports the integration of Python scripts, which greatly extends its functionality. However, for users without coding skills, the inability to locate highly specialised functions within QGIS often means that algorithmic operations must be transferred to other, more user-friendly platforms.

One such platform is Orange, an open-source toolkit for data visualisation, machine learning, and data mining. It features a visual programming interface that supports exploratory qualitative analysis and interactive visualisation. For users already familiar with node-based software environments such as Grasshopper or Dynamo, Orange is generally straightforward to adopt.

As outlined earlier, the index map is composed of index values attached to individual pixels. Software like Orange, however, does not natively support direct processing of such image-based data. This makes data transmission a critical step in the workflow. QGIS is able to convert the attribute information associated with raster pixels (or vectorised representations) into structured data columns. This conversion enables the seamless transfer of data into platforms such as Orange, where further computational analysis can be carried out.

▼ Figure 148 Screenshot of a part of data table derived from the raster layers by QGIS

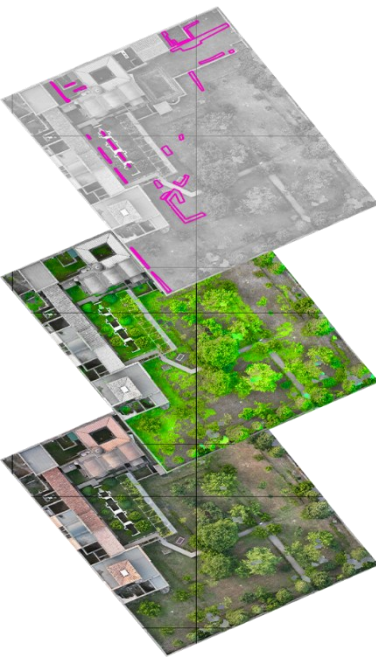
id	ndvi_pm1	ndvi_am1	ndre_pm1	ndre_am1	evi2_pm1	evi2_am1	bi_pm1	bi_am1	RN_pm1	RN_am1	R	B	G	X	Y	
2401573	0.319532	0.212205	0.183668	0.092353	0.528879	0.34361	4150.998	3309.646	0.515689	0.649886		142	133	131	457255.8	4511399
1	0.26852	0.188373	0.158827	0.068821	0.433473	0.289466	6696.76	3434.964	0.57664	0.685704		193	183	177	457255.7	4511399
2	0.391447	0.193598	0.22721	0.078761	0.671904	0.316635	3734.458	3497.309	0.437353	0.675606		203	186	181	457255.8	4511399
3	0.412089	0.212584	0.208985	0.095006	0.714932	0.365008	3483.916	3555.085	0.416341	0.64937		133	116	109	457255.8	4511399
4	0.406345	0.257754	0.221224	0.117313	0.702865	0.467926	3290.693	3180.445	0.422126	0.553705		166	153	138	457255.9	4511399
5	0.3639	0.210684	0.209487	0.074163	0.615885	0.28288	4212.048	3824.162	0.466383	0.651959		175	161	152	457255.6	4511399
6	0.343995	0.15102	0.215426	0.025417	0.576378	0.170971	5951.088	4916.384	0.488101	0.73759		156	155	144	457255.7	4511399
7	0.344525	0.177618	0.173804	0.066946	0.577422	0.299345	6381.441	3866.89	0.487515	0.677451		229	222	203	457255.7	4511399
8	0.380048	0.200239	0.203424	0.077043	0.648537	0.326589	4600.227	3801.671	0.449224	0.666335		141	129	123	457255.8	4511399
9	0.4092	0.215011	0.221693	0.090208	0.70886	0.328944	4113.878	4236.735	0.419245	0.646075		145	132	126	457255.8	4511399
10	0.405183	0.211469	0.214762	0.073985	0.700432	0.418882	3492.899	2935.231	0.423302	0.586669		174	158	150	457255.9	4511399
11	0.389909	0.247588	0.148038	0.088928	0.668732	0.388108	3748.233	3354.74	0.438944	0.603093		128	116	112	457255.5	4511399
12	0.365756	0.180117	0.185297	0.035248	0.61961	0.251232	4184.262	5067.628	0.464391	0.718886		158	150	142	457255.6	4511399
13	0.345774	0.1381	0.198568	0.013019	0.579879	0.187521	6060.308	5029.762	0.486134	0.757315		169	158	150	457255.6	4511399
14	0.365026	0.141049	0.219013	0.047239	0.618153	0.235227	5856.156	4537.249	0.465174	0.752773		126	116	103	457255.7	4511399
15	0.385636	0.182885	0.208757	0.064677	0.659959	0.289168	4533.566	4818.586	0.443381	0.68596		138	130	122	457255.7	4511399
16	0.340886	0.208607	0.181703	0.078957	0.57027	0.344576	4287.168	3573.281	0.491551	0.654797		163	151	143	457255.8	4511399
17	0.361479	0.250927	0.173461	0.115524	0.611032	0.391683	3632.668	3325.418	0.46899	0.598815		202	194	189	457255.8	4511399
18	0.372715	0.231748	0.186808	0.033436	0.633632	0.36821	3140.403	2556.57	0.456966	0.623209		171	161	157	457255.9	4511399
19	0.337393	0.244865	0.176964	0.085964	0.563425	0.42642	2652.236	1643.583	0.495446	0.6066		176	169	169	457255.9	4511399
20	0.319384	0.198394	0.207147	0.079377	0.528601	0.341159	5504.991	3484.284	0.515859	0.668901		163	151	142	457255.5	4511399

Undoubtedly, this type of tool offers a level of flexibility far greater than the previous two approaches. However, this freedom also comes with the requirement that users construct the algorithmic logic themselves, which in turn demands a deeper understanding of both the algorithms and the underlying data. In this case, the chosen method is the K-means algorithm, which is applied to filter pixels in the image according to specific values.

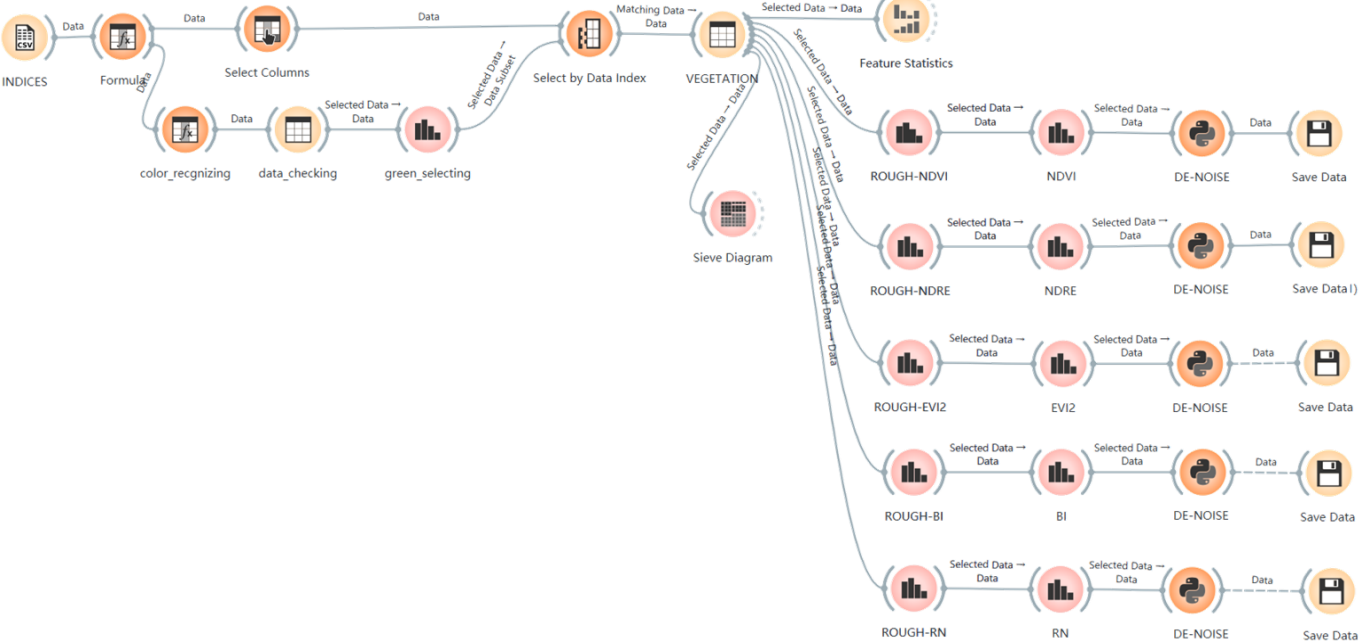
In the analysis described in Chapter 7, anomalies were identified within index maps by focusing on areas covered by vegetation. Translated into algorithmic terms, this process involves first filtering the dataset to isolate pixels corresponding to vegetation and then applying further filtering to detect abnormal values across the different spectral indices.

Fortunately, in the target area only vegetation appears green, which means that the visual dataset can readily serve as the basis for identifying and isolating vegetation. By applying an initial filter to select specific ranges of RGB values, the analysis is able to focus exclusively on green vegetation areas in subsequent stages. This targeted approach not only improves accuracy but also helps reduce the computational complexity of the second-step algorithm.

Another important consideration emerges when detecting anomalies manually. In this case, the index values of vegetation-covered areas are concentrated within a relatively narrow range, and the corresponding outliers are confined to an even narrower interval. Although it is not possible to identify every anomaly solely by relying on a single precise index value, it is feasible to define a limited interval that encompasses all potential outliers. For this reason, the second step of the algorithm involves constraining the anomalous interval by means of Orange's visual programming module, thereby enabling systematic detection within the defined range.

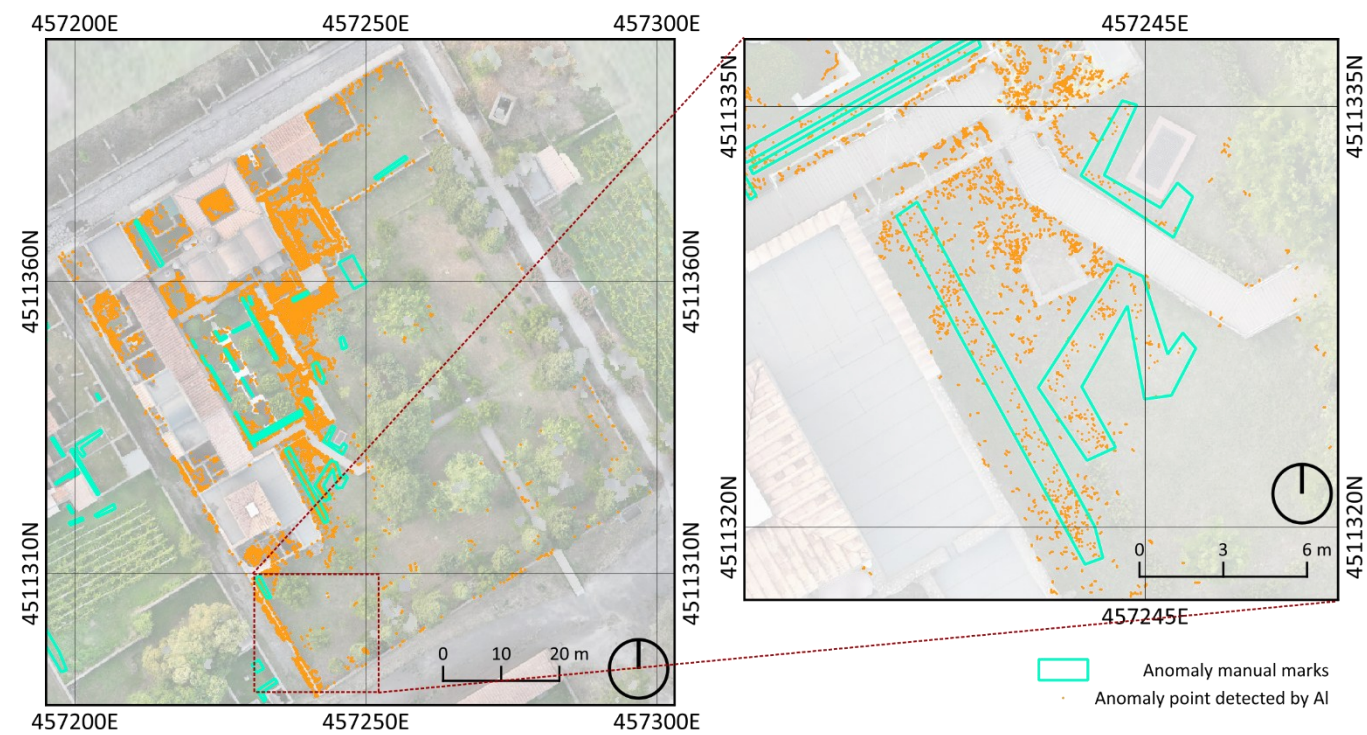
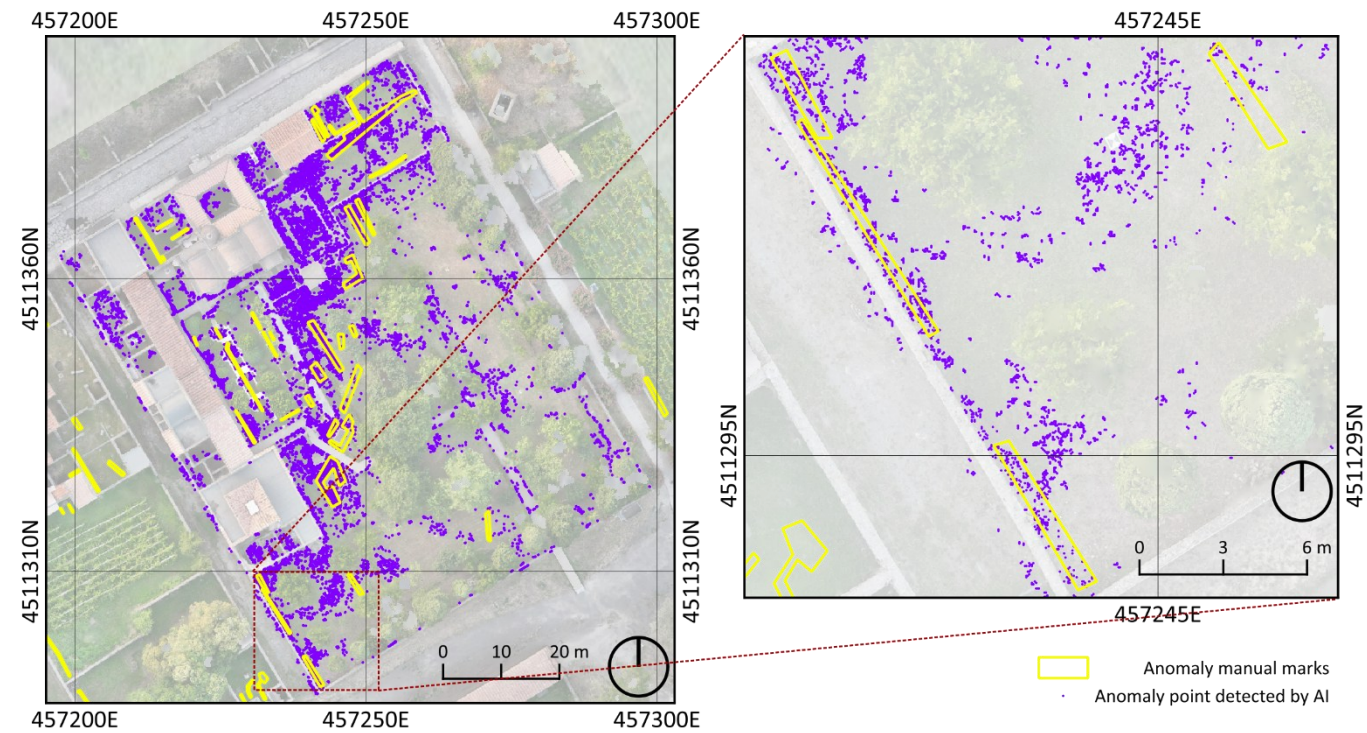


▲ Figure 149 Scheme of the analysis logic



▼ Figure 150 screenshot of the algorithm in orange

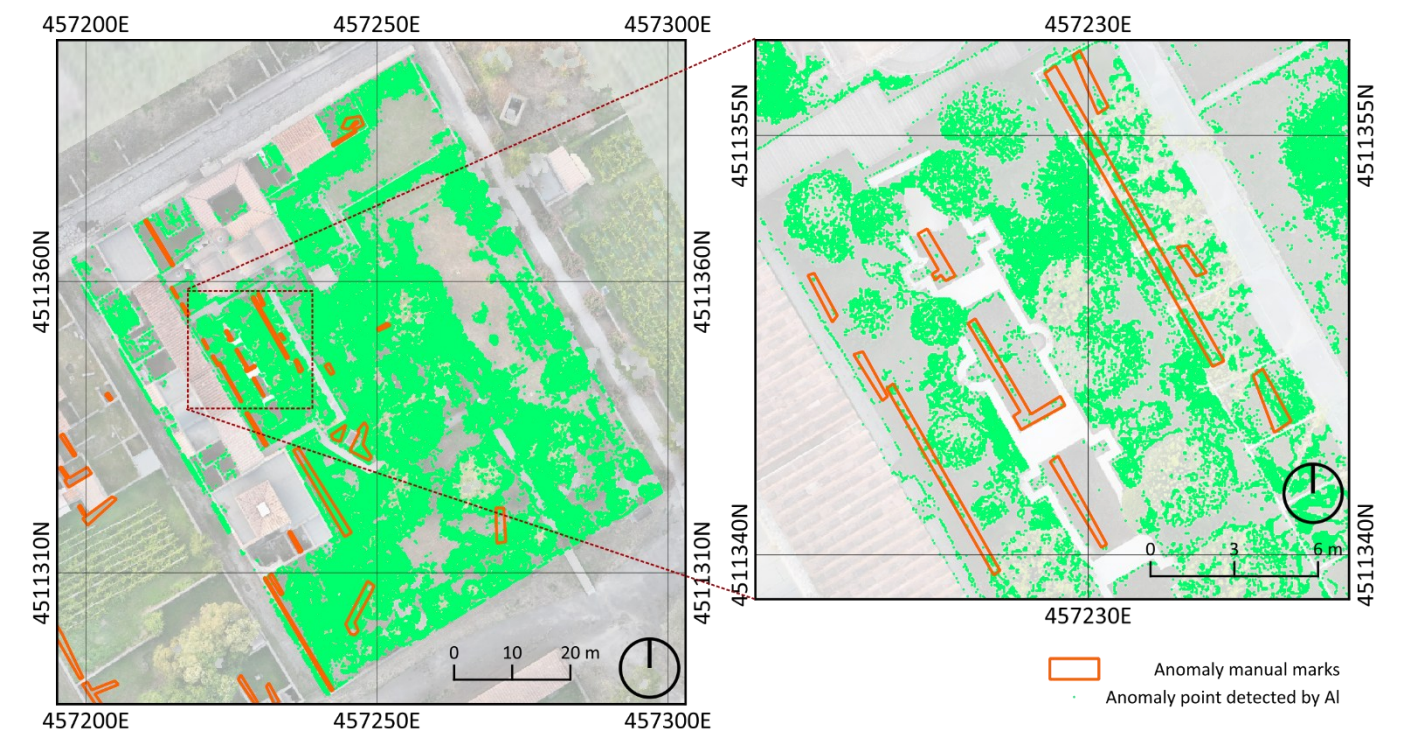
▼ Figure 151 Result of NDVI index computed through the algorithm, overlapped with the UAV map and visual interpretation



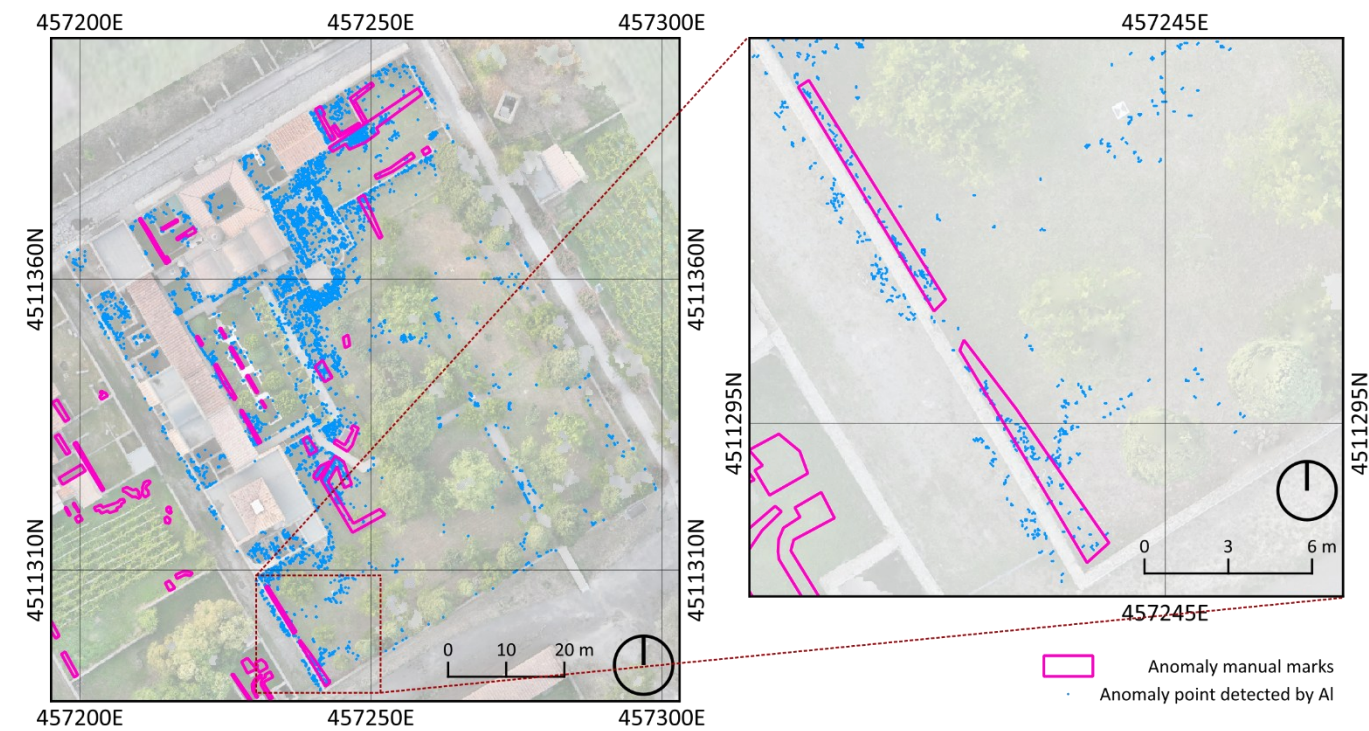
▲ Figure 152 Result of EVI 2 index computed through the algorithm, overlapped with the UAV map and visual interpretation

outliers manually filtered. But different indices have different degrees of adaptability to this analysis method. For example, the results reflected by BI are significantly different from those manually screened and cannot be optimized, while RN has become the best performing one.

▼ Figure 154 Result of NDRE index computed through the algorithm, overlapped with the UAV map and visual interpretation



▲ Figure 153 Result of BI index computed through the algorithm, overlapped with the UAV map and visual interpretation



▲ Figure 155 Result of RN index computed through the algorithm , overlapped with the UAV map and visual interpretation

In terms of results, the outcome may be regarded as a relatively positive indication. The algorithms not only assist in locating the areas where anomalies occur but also enable the rapid processing of large volumes of data. Although the outputs generated by current algorithms still require interpretation by experienced researchers, the time demands are considerably lower than those associated with purely manual analysis.

While the algorithm demonstrates considerable potential for refinement—for example, through the integration of multiple indices to support multi-criteria screening and thereby strengthen the robustness of anomaly detection—its current reliance on general-purpose software tools restricts its professional applicability. Such tools are not specifically designed to address the specialised requirements of advanced analytical tasks or the nuanced needs of heritage-focused research, which limits their effectiveness in these contexts.

9. Conclusions

This thesis examines 3 case studies from Regio II in Pompeii, with a particular focus on the role of geomatics in documenting and analysing architectural and landscape heritage. The study highlights the interdisciplinary use of innovative data acquisition technologies and the GIS environment, which together have enabled the creation of a structured archive of information on Regio II. This archive brings together multi-need and multi-scale data in an organised system. Building on this dataset, the thesis also explores the application of basic AI for data analysis, specifically in ways accessible to users without programming skills.

In addition to recording the present condition of Pompeii's heritage as a means of preserving its memory, the project also gathers information about features that remain buried or are needed to be recovered. The aim is to combine expertise from different disciplines to investigate the existing heritage through methods that are non-invasive and sustainable. By integrating regional history with the social context of the Roman era, the study also seeks to link the daily lives of Pompeii's ancient citizens with the ruins that remain today.

The thesis places particular emphasis on the innovative 3D measurement techniques applied in these case studies, which include topographic surveying, laser scanning, and drone photogrammetry, supplemented by multispectral analysis. During the survey campaign and the data processing, technologies with different characteristics and varying levels of accuracy are brought together to document elements of different scales and environments within each case study. Each of these 3 case studies presents a unique combination of rapid mapping methods, adapted to address underground or submerged structures or remains. This thesis carefully examines how well these technologies meet the requirements of each case, evaluating their accuracy, operational features, and how they work in combination with one another. This integrated approach allows for multi-level surveys and results in the creation of a rich archive of data, all organised under a single reference system and including diverse 3D metric products.

A particularly significant aspect of the final case study is the acquisition and processing of multispectral data, which was subsequently applied in detailed analysis. This approach not only provided new insights into the specific case but also demonstrated how spectral indices can be more widely applied within geomatics. Data from beyond the visible spectrum—particularly from the red edge and infrared bands—was combined with visible light data to study subsoil structures in the hortus. The analyses produced highly positive results, which were further supported by findings from geophysics and archaeology.

The research also explores how AI tools, already integrated into different software packages, can be used to process the data produced. These tools can be accessed by researchers with a general background in architecture or heritage studies, even without specialist programming knowledge. While AI techniques offer clear advantages in automating and standardising aspects of analysis, such as data segmentation, they also present limitations, particularly as their outputs cannot yet be independently verified without additional expert review. It is worth mentioning that in all cases, the verification of results is from a qualitative perspective. In order to study and optimize the algorithms used, quantitative research on robustness will become a new direction of work.

The central aim of this thesis was to assess the contribution of geomatics methods to the documentation and analysis of cultural heritage, while also evaluating the potential benefits of AI in this context. To achieve this, the research followed detailed methodologies agreeing with the standards of the discipline, which ensured the production of accurate results rich in detail. While some aspects of the findings require further validation or supplementary investigation, they are still in the same direction with the thesis's primary objectives and underline the potential of these combined methods.

Finally, the study expresses the hope that the integration of innovative investigative and analytical methods with archival documentation and historical mapping will encourage further research along similar lines. This may extend even to other disciplines, as demonstrated by the interdisciplinary findings already presented here. Beyond its methodological contributions, the study is also driven by a desire to preserve the extraordinary city of Pompeii and the vivid civic life it once embodied. In this sense, the research provides both insights and inspiration for developing more sustainable ways of coexisting with cultural heritage in the future.

10. bibliography

Abderrazak, B., Kadhem, G., El Battay, A., Mohamed, N., & Rouai, M. (2016). Assessment of Land Erosion and Sediment Accumulation Caused by Runoff after a Flash-Flooding Storm Using Topographic Profiles and Spectral Indices. *Advances in Remote Sensing*. doi:10.4236/ars.2016.54024

Agapiou, A., Hadjimitsis, D., & Alexakis, D. (2012). Evaluation of Broadband and Narrowband Vegetation Indices for the Identification of Archaeological Crop Marks. *Remote Sensing*. doi:https://doi.org/10.3390/rs4123892

Agostinacchio, d. M. (2021). *Pompei-Le pitture dei misteri (2parte)*. Retrieved 2025, from <https://www.scrignodipandora.it/pompei-le-pitture-dei-misteri-2parte/#:~:text=Esprimeva%20un%20atteggiamento%20concettuale%20popolare%20rispetto%20alla,con%20movimenti%20del%20corpo%20e%20suoni%2C%20danze>

Alfonso, I. (2016). *Handbook of Research on Emerging Technologies for Architectural and Archaeological Heritage*. IGI Global.

Alvarado, E. (2021). 237 Ways Drone Applications Revolutionize Business. *Report | Drone Application Report 2021*. Retrieved from <https://droneii.com/237-ways-drone-applications-revolutionize-business>

Anguissola, A., & Olivito, R. (2022). Introduzione. In A. Anguissola, & R. E. Olivito, *In Edizione degli scavi nei Praedia di Iulia Felix e studi sulla Regio II*. Pisa University Press: Pisa.

Anguissola, A., & Olivito, R. I. (2022). saggi di scavo 2019-2020 nell’hortus dei Praedia di Iulia Felix. In A. A., & Olivito R., *scavi nei Praedia di Iulia Felix e studi sulla Regio II*. Pisa University Press.

Ankareddy, R., & Delhibabu, R. (2025). Dense Segmentation Techniques Using Deep Learning for Urban Scene Parsing: A Review. *IEEE Access*, 34496-34517. doi:10.1109/ACCESS.2025.3543944

Aptella Pty Ltd. . (n.d.). *Different Types of Survey Drones and How They Take Off, Fly and Land. Position Partners*. Retrieved 5 2025, from <https://www.positionpartners.com.au/position-partners/survey-drones/>

Archaeological Park of Pompeii. (2021). *POMPEII PREPARES FOR CLIMATE CHANGE*. Retrieved 2025, from Pompeii: <https://pompeisites.org/en/comunicati/pompeii-prepares-for-climate-change/>

Archaeological Park of Pompeii. (2025). *PRAEDIA project, ricerca archeologica nei Praedia di Giulia Felice a Pompei*. Retrieved from Pompeii: <https://pompeisites.org/progetti-di-scavo/praedia-project-ricerca-archeologica-nei-praedia-di-giulia-felice-a-pompei/>

Archaeological Park of Pompeii. (n.d.). *Iulia Felix*. Retrieved 2025, from Pompeii: <https://pompeisites.org/en/exhibitions-and-events/julia-felix/>

Argyrou, A., & Agapiou, A. (2022). A Review of Artificial Intelligence and Remote Sensing for Archaeological Research. *Remote Sensing*. doi:https://doi.org/10.3390/rs14236000

Arianna, P., Teza, G., & Bonali, E. (2011). Terrestrial Laser Scanner Resolution: Numerical Simulations and Experiments on Spatial Sampling Optimization. *Remote Sensing* 3, pp. 167-184. doi:https://doi.org/10.3390/rs3010167

Armesto-González, J., Riveiro-Rodríguez, B., González-Aguilera, D., & Rivas-Brea, M. T. (2010). Terrestrial laser scanning intensity data applied to damage detection for historical buildings. *Journal of Archaeological Science*. doi:https://doi.org/10.1016/j.jas.2010.06.031

ASPRS. (2015). ASPRS Positional Accuracy Standards for Digital Geospatial Data. *Photogrammetric Engineering & Remote Sensing*.

Awati, R., Zola, A., & Fontecchio, M. (2024). *Definition: spatial data*. Retrieved 2025, from TechTarget: <https://www.techtarget.com/searchdatamanagement/definition/spatial-data>

Baiocchi, V. B. (2020). Integrated Geomatic Techniques for Georeferencing and Reconstructing the Position of Underground Archaeological Sites: The Case Study of the Augustus Sundial (Rome). *Remote Sensing*, 4064. doi:https://doi.org/10.3390/rs12244064

Barone, P. M., Bellomo, T., Mattei, E., Lauro, S. E., & Pettinelli, E. (2011). Ground-penetrating Radar in the Regio III (Pompeii, Italy): Archaeological Evidence. *Archaeological prospection*, 187-194. doi: <https://doi.org/10.1002/arp.405>

Beard, M. (2009). *Pompeii: The Life of a Roman Town*. Profile Books.

Berndt, S. (2018). The hand gesture and symbols of Sabazios. *Opuscula Annual of the Swedish Institutes at Athens and Rome*. doi:10.30549/opathrom-11-08

Berni, J. A., Zarco-Tejada, P. J., Suarez, L., & Fereres, E. (2009). Thermal and Narrowband Multispectral Remote Sensing for Vegetation Monitoring From an Unmanned Aerial Vehicle. *IEEE Transactions on Geoscience and Remote Sensing*, 722-738. doi:10.1109/TGRS.2008.2010457

Berra, E. F., & Peppas, M. V. (2020). Advances and Challenges of UAV SFM MVS Photogrammetry and Remote Sensing: Short Review. *2020 IEEE Latin American GRSS & ISPRS Remote Sensing Conference (LAGIRS)*. doi:10.1109/LAGIRS48042.2020.9285975

Bettini, A. (2016). *A Course in Classical Physics 4 - Waves and Light*. Springer Cham. doi:https://doi.org/10.1007/978-3-319-48329-0

Bomgardner, D. (2021). *The Story of the Roman Amphitheatre*.

Britannica. (2025). *The visible spectrum*. Retrieved 2025, from Britannica: <https://www.britannica.com/science/color/The-visible-spectrum>

Burrough, A., & McDonnell, A. (1998). *Principles of Geographical Information Systems*. Oxford University Press.

Byrne, A., & Hilbert, D. R. (Eds.). (1997). *Readings on Color* (Vol. Volume 2: The Science of Color). MIT Press.

Cappellazzo, M., Patrucco, G., & Spanò, A. (2024). ML Approaches for the Study of Significant Heritage Contexts: An Application on Coastal Landscapes in Sardinia. *Heritage* 7. doi: <https://doi.org/10.3390/heritage7100261>

Carmona, J. Á., Quirós, E., Mayoral, V., & Charro, C. (2020). Assessing the potential of multispectral and thermal UAV imagery from archaeological sites. A case study from the Iron Age hillfort of Villasviejas del Tamuja (Cáceres, Spain). *Journal of Archaeological Science: Reports*. doi:doi.org/10.1016/j.jasrep.2020.102312

Carnow, A. (2024). *Top 5 Tech Trends in Public Works & The Role of GIS*. Retrieved 2025, from esri: <https://www.esri.com/en-us/industries/blog/articles/top-5-tech-trends-in-public-works-the-role-of-gis>

Chang, K.-T. (2019). *Introduction to geographic information systems*. McGraw-Hill Education.

Chen, Z., Xu, H., Chen, W., Zhou, Z., Xiao, H., Sun, B., . . . Kang, W. (2023). PointDC:Unsupervised Semantic Segmentation of 3D Point Clouds via Cross-modal Distillation and Super-Voxel Clustering. *International Conference on Computer Vision (ICCV) 2023*. doi:http://doi.org/10.48550/arXiv.2304.08965

Cheng, J., Li, H., Li, D., Hua, S., & Sheng, V. (2022). A Survey on Image Semantic Segmentation Using Deep Learning Techniques. *Computers, Materials & Continua*. doi:10.32604/cmc.2023.032757

CIE. (2020). *ILV: International Lighting Vocabulary, 2nd Edition*. International Commission on Illumination. doi:10.25039/S017.2020

CloudCompare wiki. (2016). *CSF (plugin)*. Retrieved from CloudCompare wiki: [https://www.cloudcompare.org/doc/wiki/index.php/CSF_\(plugin\)](https://www.cloudcompare.org/doc/wiki/index.php/CSF_(plugin))

Costanza, M. (2024). *Climate Change Puts Ancient Pompeii at Risk*. Retrieved 2025, from Protect Earth Foundation: <https://protectearth.foundation/climate-change-puts-ancient-pompeii-at-risk/>

Csurka, G., Volpi, R., & Chidlovskii, B. (2022). Semantic Image Segmentation: Two Decades of Research. *Foundations and Trends® in Computer Graphics and Vision*, 1-162. doi:http://dx.doi.org/10.1561/06000000095

Cyron, M. (2006). *wikipedia: Pompeii*. Retrieved 2025, from <https://commons.wikimedia.org/wiki/File:PlanPompeji3.jpg>

Cyron, M. (2006). *Wikipedia: Pompeii*. Retrieved 2025, from https://en.wikipedia.org/wiki/File:Map_of_setteling_phases_of_Pompeii.png

D'Ambra, E. (2012). Women in the Bay of Naples. In S. Dillon, & S. James, *A Companion to Women in the Ancient World*. Blackwell Publishing Ltd.

De Caro, S. (2015). Excavation and conservation at Pompeii: a conflicted history. *The Journal of Fasti Online*.

De Francesco, A. M., Guido, A., Cipriani, M., Maruca, G., Musella, M., Sabbatucci, P., . . . Barca, D. (2025). Characterization of Stone Tesserae from “Praedia Iuliae Felicis” Mosaics (Pompeii—Italy). *Heritage*. doi:https://doi.org/10.3390/heritage8030094

De Vos, A., & De Vos, M. (1982). *Pompeii, Herculaneum, Stabia, Rome*. Giuseppe Laterza & figli Publishing House.

Delegido, J., Verrelst, J., Meza, C., Rivera, J., Alonso, L., & Moreno, J. (2013). A red-edge spectral index for remote sensing estimation of green LAI over agroecosystems. *European Journal of Agronomy*. doi:doi.org/10.1016/j.eja.2012.12.001

Dobbins, J., & Foss, P. (2007). *The World of Pompeii*. New York: Routledge. Taylor and Francis Group.

Drummond, A. (1993). *The World of the Romans*. Oxford University Press.

Elaksher, A., Ali, T., & Alharthy, A. (2023). A Quantitative Assessment of LIDAR Data Accuracy. *Remote Sensing*. doi:https://doi.org/10.3390/rs15020442

Elhashash, M., Hessah, A., & Rongjun, Q. (2022). A Review of Mobile Mapping Systems: From Sensors to Applications. *Sensors* 22. doi:https://doi.org/10.3390/s22114262

Enge, P., & Misra, P. (2006). *The global positioning system: Signals, measurements, and performance*. Ganga-Jamuna Press.

Ershad, M., & Ali, E. (2020). Geographic Information System (GIS): Definition, Development, Applications & Components. *Urbanisation in India: Causes, Growth, Trends, Patterns, Consequences & Remedial Measures*, 1-13.

Esri. (2025). *Geospatial AI: Artificial intelligence in GIS*. Retrieved from ArcGIS: Esri's comprehensive geospatial platform: https://www.esri.com/en-us/geospatial-artificial-intelligence/overview

Esri. (2025). *History of GIS*. Retrieved 2025, from Esri: https://www.esri.com/en-us/what-is-gis/history-of-gis

Etienne, R. (1992). *Daily Life in Pompeii*. Arnoldo Mondadori Editore.

Europe, C. o. (2005). *Convention on the Value of Cultural Heritage for Society*. Retrieved from https://www.coe.int/en/web/culture-and-heritage/faro-convention

European Space Agency. (2009). *Spectral signatures*. Retrieved 2025, from ESA-Eduspace: https://www.esa.int/SPECIALS/Eduspace_EN/SEMPNQ3Z2OF_0.html

FARO. (n.d.). *What Is SLAM?* Retrieved 2025, from FARO: https://www.faro.com/it-IT/Resource-Library/Article/What-is-SLAM

Faster Capital. (2025). *Image Processing: A Picture s Worth: Image Processing in Feature Engineering*. Retrieved 2025, from FasterCapital: https://www.fastercapital.com/content/Image-Processing--A-Picture-s-Worth--Image-Processing-in-Feature-Engineering.html

Fritsch, D. K. (2018). 3D preservation of buildings – Reconstructing the past. *Multimed Tools Appl*, 9153–9170. doi:https://doi.org/10.1007/s11042-017-4654-5

Global GPS Systems . (2023). *Overcoming Signal Interference in GPS Land Surveying*. Retrieved 2025, from https://globalgpsystems.com/

Gomarasca, M. A. (2009). *Basics of Geomatics*. Springer Science & Business Media.

Grewal, M. S. (2011). Global navigation satellite systems. *WIREs Computational Statistics*, 289-384.

Guidi, G. (2014). TERRESTRIAL OPTICAL ACTIVE SENSORS THEORY & APPLICATIONS. In F. Remondino, & S. Campana, *3D Recording and Modelling in Archaeology and Cultural Heritage: Theory and best practices*. University of Michigan Press.

Guo, Y., Wang, H., Hu, Q., Liu, H., Liu, L., & Bennamoun, M. (2021). Deep Learning for 3D Point Clouds: A Survey. *IEEE Transactions on Pattern Analysis and Machine Intelligence*. doi:10.1109/TPAMI.2020.3005434

Haraldur, S., Stanford, Cashdollar, & Stephen, R. J. (1982). The Eruption of Vesuvius in A. D. 79: Reconstruction from Historical and Volcanological Evidence. *American Journal of Archaeology*.

Harrap, R., & Lato, M. (2010). An overview of LIDAR: collection to application. *NGI publication*, 1-9.

Harshit, H., Kushwaha, S. K., & Jain, K. (2022). GEOMETRIC FEATURES INTERPRETATION OF PHOTOGRAMMETRIC POINT CLOUD FROM UNMANNED AERIAL VEHICLE. *ISPRS Annals of the Photogrammetry Remote Sensing and Spatial Information Sciences*. doi:10.5194/isprs-annals-X-4-W2-2022-83-2022

Hassani, F. (2015). Documentation of cultural heritage; techniques, potentials, and constraints. *The International Archives of the Photogrammetry, Remote Sensing and Spatial Information Sciences*. doi:https://doi.org/10.5194/isprsarchives-XL-5-W7-207-2015

Helmenstine, A. M. (2025). *Electromagnetic Radiation Definition*. Retrieved from ThoughtCo: https://www.thoughtco.com/definition-of-electromagnetic-radiation-605069

Huang, S. T., Hupy, J. P., Wang, Y., & Shao, G. (2021). A commentary review on the use of normalized difference vegetation index (NDVI) in the era of popular remote sensing. *Journal of Forestry Research*. doi:https://doi.org/10.1007/s11676-020-01155-1

HUETE, A. R., JACKSON, D., R., & POST, D. F. (1985). Spectral Response of a Plant Canopy with Different Soil Backgrounds. *REMOTE SENSING OF ENVIRONMENT*.

Huete, A., & Justice, C. (1999). *Algorithm Theoretical Basis Document*. Retrieved 2025, from MODIS Vegetation Index (MOD 13): https://modis.gsfc.nasa.gov/data/atbd/atbd_mod13.pdf

ISO/TR-19122. (2004). Geographic information/Geomatics — Qualification and certification of personnel.

Janga, B., Asamani, G. P., Sun, Z., & Cristea, N. (2023). A Review of Practical AI for Remote Sensing in Earth Sciences. *Remote Sensing*. doi:https://doi.org/10.3390/rs15164112

Jean-Michel, F., Jean-François, G., Ana-Maria, O.-R., & David, S. (2019). The Origins of Imperfection in Geographic Data. In B.-H. Mireille, D. Eric, & P. François, *Geographic Data Imperfection 1: From Theory to Applications* (pp. 25-44). doi: https://doi.org/10.1002/9781119507284.ch3

Jiang, S., Jiang, W., & Wang, L. (2022). Unmanned Aerial Vehicle-Based Photogrammetric 3D Mapping: A survey of techniques, applications, and challenges. *IEEE Geoscience and Remote Sensing Magazine*, 135-171. doi:10.1109/MGRS.2021.3122248

Jiang, Z., Huete, A. R., Didan, K., & Miura, T. (2008). Development of a two-band enhanced vegetation index without a blue band. *Remote Sensing of Environment*. doi:https://doi.org/10.1016/j.rse.2008.06.006

Jocea, A. F. (2024). Impact of Artificial Intelligence in the Geospatial Field: from Geospatial Data to Intelligent Decision Making. *Journal of Military Techn*. doi:10.32754/JMT.2024.2.03

Joncic, N., & Jan, Z. (2017). 3D SCANNING. *3D DIGITAL RECORDING OF ARCHAEOLOGICAL, ARCHITECTURAL AND ARTISTIC HERITAGE*. doi:10.4312/9789612378981

Kang, X. (2024). Research on the Application of Total Stations and Drones in Urban Building Survey. *Journal of Environmental and Building Engineering*. doi:https://doi.org/10.70767/jebe.v1i2.343

Kaplan, E. D., & Hegarty, C. (2017). *Understanding GPS/GNSS: Principles and Applications*. Artech House.

Kim, M., Jason, S., Jeffrey, I., Jeffrey, D., & Seonkyung, P. (2022). Absolute Accuracy Assessment of Lidar Point Cloud Using Amorphous Objects. *Remote Sensing*. doi:https://doi.org/10.3390/rs14194767

Kovanič, Ľ., Branislav, T., Patrik, P., Peter, B., Marcela, B. G., & Monika, B. (2023). Review of Photogrammetric and Lidar Applications of UAV. *Applied Sciences* 13. doi:https://doi.org/10.3390/app13116732

Kovanič, Ľ., Topitzer, B., Peťovský, P., Blišťan, P., Gergeľová, M., & Blišťanová, M. (2023). Review of Photogrammetric and Lidar Applications of UAV. *Applied Sciences*. doi:https://doi.org/10.3390/app13116732

Koza, J., Bennett, F., Andre, D., & Keane, M. (1996). Automated Design of Both the Topology and Sizing of Analog Electrical Circuits Using Genetic Programming. In J. Gero, & F. Sudweeks, *Artificial Intelligence in Design*. doi:https://doi.org/10.1007/978-94-009-0279-4_9

Kraus, K. (2007). *Photogrammetry: Geometry from Images and Laser Scans*. De Gruyter.

Kristiansen, K. (2002). The Birth of Ecological Archaeology in Denmark: history and researsh environments 1850-2000. In *In Fischer and Kristiansen 2002* (pp. 11–31).

Labster. (2025). *Electromagnetic spectrum*. Retrieved from Labster: <https://theory.labster.com/electromagnetic-spectrum/>

Labster. (2025). *Electromagnetic Waves*. Retrieved from Labster: <https://theory.labster.com/electromagnetic-waves/>

Lee, N. (2021). *What is spatial data and non-spatial data?* Retrieved 2025, from FME Blog: <https://fme.safe.com/blog/2021/10/non-spatial-data-difference-fme/#:~:text=Spatial%20data%2C%20also%20known%20as,is%20independent%20of%20geographic%20location.>

Li, B., Shi, Y., Qi, Z., & Chen, Z. (2018). A Survey on Semantic Segmentation. *2018 IEEE International Conference on Data Mining Workshops (ICDMW)*. doi:10.1109/ICDMW.2018.00176

Liebe, C. C., & Coste, K. (2013). Distance Measurement Utilizing Image-Based Triangulation. *IEEE Sensors Journal*. doi:10.1109/JSEN.2012.2212428

Lirer, L. P. (2001). Long-term volcanic hazard forecasts based on Somma-Vesuvio past eruptive activity. *Bull Volcanol*, 63, 45-60. doi:https://doi.org/10.1007/s004450000121

Lowe, D. (2004). Distinctive Image Features from Scale-Invariant Keypoints. *International Journal of Computer Vision*, 91-110. doi:https://doi.org/10.1023/B:VISI.0000029664.99615.94

Luhmann, T., Robson, S., Kyle, S., & Boehm, J. (2020). *Close-Range Photogrammetry and 3D Imaging*. Boston: De Gruyter. doi:https://doi.org/10.1515/9783110607253

Lundgren, A. (2023). Review: Roman Material Culture and Female Agency in the Bay of Naples. *CLARA*.

Maguire, D. (1991). An Overview and Definition of GIS. In D. Maguire, M. Goodchild, & D. Rhind, *Geographical Information Systems: Principles and Applications* (pp. 9-22).

Marchetti, M., Materni, V., & Sapia, V. (2022). Indagini geofisiche nell'hortus dei Praedia di Iulia Felix. In A. A., & E. Olivito R., *scavi nei Praedia di Iulia Felix e studi sulla Regio II*. Pisa University Press.

Marx, A., Clasen, A., May, J., König, S., Kleinschmit, B., & Förster, M. (2024). Imaging spectroscopy for bark beetle detection in Norway spruce and the relevance of the red-edge spectral range. *International Journal of Applied Earth Observation and Geoinformation*. doi:https://doi.org/10.1016/j.jag.2024.104100

Matsushita, B., Yang, W., Chen, J., Onda, Y., & Qiu, G. (2007). Sensitivity of the Enhanced Vegetation Index (EVI) and Normalized Difference Vegetation Index (NDVI) to Topographic Effects: A Case Study in High-density Cypress Forest. *Sensors* 7. doi:https://doi.org/10.3390/s7112636

Maxwell, A. E., Warner, T. A., & Fang, F. (2018). Implementation of Machine-Learning Classification in Remote Sensing: An Applied Review. *International Journal of Remote Sensing*. doi:10.1080/01431161.2018.1433343

Mazzaglia, A. (2021). The Information System of Pompeii Sustainable Preservation Project. A Tool for the Collection, Management and Sharing of Knowledge Useful for Conservation and Renovation of Archaeological Monuments. *Environmental Sciences Proceedings*. doi:https://doi.org/10.3390/environsciproc2021010014

Ndehedehe, C. (2013). Understanding Errors and Their Measurement in Geoinformation. *Journal of Environmental Sciences and Resource Management*, 74-87.

Nex, F., & Remondino, F. (2013). UAV for 3D mapping applications: a review. *Applied Geomatics*, 1-15. doi:https://doi.org/10.1007/s12518-013-0120-x

Nielsen, F., & Nock, R. (2003). On region merging: The statistical soundness of fast sorting, with applications. *2003 IEEE Computer Society Conference on Computer Vision and Pattern Recognition*. doi:10.1109/CVPR.2003.1211447

Njambi, R. (2021). *LiDAR accuracy, explained—and when to use stereo satellite imagery for elevation modeling*. Retrieved 2025, from <https://up42.com/blog/lidar-accuracy-explained-and-when-to-use-stereo-satellite-imagery>

NOAA. (2024). *What is lidar?* Retrieved 5 2025, from National Ocean Service website: <https://oceanservice.noaa.gov/facts/lidar.html>

Notarian, M. (2023). A Spatial Network Analysis of Water Distribution from Public Fountains in Pompeii. *American Journal of Archaeology*. doi:https://doi.org/10.1086/722233

Ohlinger, J. (2021). *Red Edge detects vegetative stress earlier in plant growth cycle*. Retrieved 2025, from up42: <https://up42.com/blog/red-edge-detects-vegetative-stress-earlier-in-plant-growth-cycle#:~:text=On%20the%20electromagnetic%20spectrum%2C%20the%20Red%20Edge,Technical%20Manager%20at%20HEAD%20Aerospace%20in%20France.>

Okwuenu, C., Igboke, E., & Anyadiegwu, P. (2024). Topographic Survey of Comprehensive Secondary School Nawfia, Anambra State. *International Journal of Research Publication and Reviews*, 2036-2042.

Olivito, R., & Anguissola, A. (2023). Il Progetto PRAEDIA a Pompei: le indagini nel Complesso dei Riti Magici (2021-2022). *AGOGI*. Retrieved from <https://iris.imtlucca.it/handle/20.500.11771/24438?mode=full>

Pan, H., Zahmatkesh, M., Rekabi-Bana, F., Arvin, F., & Hu, J. (2025). T-STAR: Time-Optimal Swarm Trajectory Planning for Quadrotor Unmanned Aerial Vehicles. *IEEE Transactions on Intelligent Transportation Systems*, 1-16.

Panella, E. (n.d.). *Daily life in ancient Pompeii*. Retrieved 2025, from Pompeii: <https://www.pompei.it/pompeii/daily-life-pompeii.htm>

Petrie, G., & Toth, C. (2009). Terrestrial Laser Scanners. In S. Jie, *Topographic laser ranging and scanning: principles and processing*. CRC Press.

PIRTI, A. (2021). Evaluating the accuracy of post-processed kinematic (PPK) positioning technique. *Geodesy and Cartography*. doi:https://doi.org/10.3846/gac

Pompei Online. (2025). *Gladiatorial games in Pompeii*. Retrieved 2025, from Pompei Online: <https://www.pompeionline.net/en/archaeological-park-of-pompeii/pompeian-curiosities/gladiatorial-games-in-pompeii#:~:text=Gladiator%20games%20in%20Pompeii%20were,the%20city%2C%20near%20the%20walls.>

Pompeii, A. P. (2025). *The Great Pompeii Project*. Retrieved from Pompeii: <https://pompeisites.org/en/the-great-pompeii-project/>

Praedia Project. (2025). *Pompeian Residential Architecture. Environmental, Digital, Interdisciplinary Archive*. Retrieved from PRAEDIA: <https://www.praediaproject.com/>

QGIS community. (n.d.). *QGIS - The Leading Open Source*. Retrieved 2025, from QGIS: <https://static.qgis.org/en/site/about/index.html>

Rahaman, H. (2021). Photogrammetry: What, How, and Where. In E. M. Champion, *Virtual Heritage: A Guide*. London: Ubiquity Press. doi:https://doi.org/10.5334/bck.d

Redazione Web of University of Pisa. (2022). *A Pompei si torna a scavare con il PRAEDIA Project*. Retrieved from University of Pisa: <https://old.unipi.it/index.php/presentazione/item/23916>

Remondino, F., Barazzetti, L., Nex, F., Scaioni, M., & Sarazzi, D. (2011). UAV photogrammetry for mapping and 3D modeling: current status and future perspectives. In H. Eisenbeiss, M. Kunz, & H. Ingensand, *Proceedings of the International Conference on Unmanned Aerial Vehicle in Geomatics (UAV-g)* (pp. 14-16). Zurich.

Remondino, F., Barazzetti, L., Nex, F., Scaioni, M., & Sarazzi, D. (2011). UAV photogrammetry for mapping and 3D modeling: current status and future perspectives. In H. Eisenbeiss, M. Kunz, & H. Ingensand, *Proceedings of the International Conference on Unmanned Aerial Vehicle in Geomatics (UAV-g)* (pp. 14-16). Zurich.

Remondio, F. (2014). PHOTOGRAMMETRY: THEORY. In F. Remondio, & S. Campana, *3D Recording and Modelling in Archaeology and Cultural Heritage: Theory and best practices: Theory and best practices* (pp. 65-73). University of Michigan Press. doi:10.30861/9781407312309

Riedorf, A., Daub, C., & Loef, P. (2006). Precise Positioning in Real-Time using Navigation Satellites and Telecommunication. *PROCEEDINGS OF THE 3rd WORKSHOP ON POSITIONING, NAVIGATION AND COMMUNICATION*. doi:10.1.1.581.2400

Riisgaard, S. (2005). SLAM for Dummies: A tutorial approach to Simultaneous Localization and Mapping. *Citeulike.org*. doi:<https://doi.org/10.1017/S0025315400002526>

Roche, I., & Hummel, P. (2024). *The Future of AI Using LiDAR*. Retrieved from Dell technologies : <https://infohub.delltechnologies.com/zh-cn/p/the-future-of-ai-using-lidar/>

Roller, S. (2021). *Pompeii*. Retrieved 2025, from Historyhit: <https://www.historyhit.com/locations/pompeii/>

Ronchi, D. L. (2020). Correlation among Earthwork and Cropmark Anomalies within Archaeological Landscape Investigation by Using LiDAR and Multispectral Technologies from UAV. *Drones*. doi:<https://doi.org/10.3390/drones4040072>

Rosidi, N. (2023). *A Comprehensive Overview of 3 Popular Machine Learning Models*. Retrieved 2025, from stratascratch: <https://www.stratascratch.com/blog/a-comprehensive-overview-of-3-popular-machine-learning-models/>

Sahragard, E., Farsi, H., & Mohamadzadeh, S. (2025). Advancing semantic segmentation: Enhanced UNet algorithm with attention mechanism and deformable convolution. *PloS one*. doi:<https://doi.org/10.1371/journal.pone.0305561>

Sammartano, G., & Spano, A. (2018). Point clouds by SLAM-based mobile mapping systems: accuracy and geometric content validation in multisensor survey and stand-alone acquisition. *Applied Geomatics*, 10. doi:10.1007/s12518-018-0221-7

Santoro, V., Patrucco, G., Lingua, A., & Spano', A. (2023). MULTISPECTRAL UAV DATA ENHANCING THE KNOWLEDGE OF LANDSCAPE HERITAGE. *INTERNATIONAL ARCHIVES OF THE PHOTOGRAMMETRY, REMOTE SENSING AND SPATIAL INFORMATION SCIENCES*, 1419–1426.

Schuurman, N., & Cinnamon, J. (2013). *Geographic Information Science*. doi:10.1093/obo/9780199874002-0023

Scolamiero, V., Boccardo, P., & Riccia, L. L. (2025). Mobile Mapping System for Urban Infrastructure Monitoring: Digital Twin Implementation in Road Asset Management. *Land* 14. doi:<https://doi.org/10.3390/land14030597>

Seepompeii. (2025). *Fighting and games: what was done in Pompeii's Amphitheater*. Retrieved 2025, from Seepompeii.

Shahraki, M., Elamin, A., & El-Rabbany, A. (2025). SAMNet++: A Segment Anything Model for Supervised 3D Point Cloud Semantic Segmentation. *Remote Sensing* 17. doi:<https://doi.org/10.3390/rs17071256>

Shan, J., & Toth, K. C. (2018). *Topographic Laser Ranging and Scanning: Principles and Processing*. CRC Press.

Shin, Y.-H. S.-Y.-T. (2023). UAV-Based Remote Sensing for Detection and Visualization of Partially-Exposed Underground Structures in Complex Archaeological Sites. *Remote Sensing*, 15, no. 7: 1876. doi:<https://doi.org/10.3390/rs15071876>

Simeone, O. (2018). A Very Brief Introduction to Machine Learning With Applications to Communication Systems. *IEEE Transactions on Cognitive Communications and Networking*, 648-664. doi:10.1109/TCCN.2018.2881442

Smith, M., & Park, D. (2000). Absolute and exterior orientation using linear features. *International Archives of Photogrammetry and Remote Sensing*, 850-857.

Spano, A. (2019). Rapid Mapping methods for archaeological sites. *2019 IMEKO TC4 International Conference on Metrology for Archaeology and Cultural Heritage*. MetroArchaeo.

Spanò, A. (2019). Rapid Mapping terrestre e da fotogrammetria UAV per il patrimonio a rischio. Tecnologia SLAM.

Spano, A. (2024). Concept of error, Theory of measures. *Course Presentation*.

Spanò, A. T., & Sammartano, G. (2014). Quick mapping by mobile sensors for landscape values monitoring and conservation. *TERRITORIO ITALIA*. doi:10.14609/Ti_2_14_3e

Spano, A., Sammartano, G., & Calantropio, A. (2019–2020). Digital Photogrammetry and images capturing. *Course Presentation*.

Sparks, E. (2025). *QGIS: An Introduction to an Open-Source Geographic Information System*. Retrieved 2025, from Mississippi state university extension: <http://extension.msstate.edu/publications/qgis-introduction-open-source-geographic-information-system>

Suraci, S. S., & de Oliveira, C. L. (2019). OUTLIER=GROSS ERROR? DO ONLY GROSS ERRORS CAUSE OUTLIERS IN GEODETIC NETWORKS? ADDRESSING THESE AND OTHER QUESTIONS. *Boletim de Ciências Geodésicas*. doi:10.1590/s1982-21702019000s00004

Tao, C. (2000). Mobile mapping technology for road network data acquisition. *Journal of Geospatial Engineering*.

Tapete, D., & Cigna, F. (2021). Satellite Technologies for Monitoring Archaeological Sites at Risk. (A. Traviglia, L. Milano, C. Tonghini, & R. Giovanelli, Eds.) *Stolen Heritage 2021, Antichistica* 29, 155-167.

Tatiraju, S., & Mehta, A. (2008). Image Segmentation Using k-Means Clustering, EM and Normalized Cuts. *University Of California-Irvine*.

Teppati Losè, L., Chiabrando, F., & Giulio Tonolo, F. (2020). Boosting the Timeliness of UAV Large Scale Mapping. Direct Georeferencing Approaches: Operational Strategies and Best Practices. *ISPRS International Journal of Geo-Information*. doi:<https://doi.org/10.3390/ijgi9100578>

the Editors of the Madain Project. (2025). *Amphitheatre of Pompeii*. Retrieved 2025, from Madain Project: https://madainproject.com/amphitheatre_of_pompeii

the Editors of the Madain Project. (2025). *House of Julia Felix*. Retrieved 2025, from Madain Project: https://madainproject.com/house_of_julia_felix

The U.S. Geological Survey. (2024). *The U.S. Geological Survey Survey Manual*. Retrieved 2025, from Survey Manual: <https://www.usgs.gov/survey-manual>

the U.S. National Science Foundation. (n.d.). *earthscope consortium*. Retrieved 2025, from <https://www.earthscope.org/what-is/tls/>

Torelli, M., & Osanna, M. (2006). *Sicilia ellenistica, consuetudo italica : alle origini dell'architettura ellenistica d'Occidente : Spoleto, Complesso monumentale di S. Nicolò, 5-7 novembre 2004*. Edizioni dell'Ateneo.

Touring Club Italiano. (2008). *Guida d'Italia – Naples and surroundings*. Touring Club Editore.

Travis, S. T. (2019). *Introduction to Laser Science and Engineering*. CRC Press. doi:<https://doi.org/10.1201/b22159>

Università di Pisa. (2023). *Resti di riti e sacrifici nel Complesso dei Riti Magici: conclusa la nuova campagna archeologica a Pompei*. Retrieved 2025, from <https://www.cfs.unipi.it/2023/08/01/resti-di-riti-e-sacrifici-nel-complesso-dei-riti-magici-conclusa-la-nuova-campagna-archeologica-a-pompei/>

UP42. (2025). *Spectral bands*. Retrieved 2025, from UP42 Documentation: <https://docs.up42.com/data/reference/spectral-bands#overview>

Urbini, S., Sapia, V., Materni, V., Marchetti, M., Anguissola, A., Taccola, E., & Olivito, R. (2021). Geophysical Survey in the Praedia Iuliae Felicis (Pompeii, II, 4). doi:<https://doi.org/10.13131/archelogicadata-eaz7-s858>

Verhoeven, G. J., Smet, P. F., Poelman, D., & Vermeulen, F. (2009). Spectral Characterization of a Digital Still Camera's NIR Modification to Enhance Archaeological Observation. *IEEE Transactions on Geoscience and Remote Sensing*. doi:10.1109/TGRS.2009.2021431

Wang, P., Liu, X., & Huang, F. (2009). *Research on Mobile Mapping System and its Application in Precision Agriculture*. Retrieved 2025, from Geospatial World: <https://geospatialworld.net/article/research-on-mobile-mapping-system-and-its-application-in-precision-agriculture/>

Wang, Q., Tan, Y., & Mei, Z. (2020). Computational Methods of Acquisition and Processing of 3D Point Cloud Data for Construction Applications. *Archives of Computational Methods in Engineering*. doi:10.1007/s11831-019-09320-4

Wasser, L., Jones, M. A., O'Brien, L., Stachelek, J., Wright, T., Teal, T., . . . Leinweber, K. (2025). *Data Carpentry Introduction to Geospatial Concepts*. (r. T. Swetnam, & Chris, Eds.) doi:<https://doi.org/10.5281/zenodo.1>

Wellesley College. (2017). *The Founding and History of Pompeii until 79 AD*. Retrieved 2025, from Piranesi in Rome: <http://omeka.wellesley.edu/piranesi-rome/exhibits/show/discovery-of-pompeii-and-hercu/founding-pompeii>

Widyaningsih, M., Priyambodo, T. K., Wibowo, M. E., & Kamal, M. (2023). Optimization Contrast Enhancement and Noise Reduction for Semantic Segmentation of Oil Palm Aerial Imagery. *International Journal of Intelligent Engineering & Systems*. doi:10.22266/ijies2023.0228.51

Wikipedia. (2025). *Conservation issues of Pompeii and Herculaneum*. Retrieved 2025, from https://en.wikipedia.org/wiki/Conservation_issues_of_Pompeii_and_Herculaneum

wikipedia. (2025). *QGIS*. Retrieved 2025, from <https://en.wikipedia.org/wiki/QGIS>

Wikipedia. (2025). *Wikipedia: Satellite navigation*. Retrieved 2025, from https://en.wikipedia.org/wiki/Satellite_navigation

Wikipedia. (n.d.). *Geographic information system software*. Retrieved 2025, from https://en.wikipedia.org/wiki/Geographic_information_system_software

Wilkinson, P. (2019). *Pompeii. An archaeological guide*. Bloomsbury Academic.

Wilson, A. (2011). City Sizes and Urbanization in the Roman Empire. In A. Bowman, & A. Wilson, *Settlement, Urbanization, and Population. Oxford Studies on the Roman Economy* (pp. 171–172). Oxford University Press.

Yang, S., Hou, M., & Li, S. (2023). Three-Dimensional Point Cloud Semantic Segmentation for Cultural Heritage: A Comprehensive Review. *Remote Sensing*. doi:<https://doi.org/10.3390/rs15030548>

Zanker, P. (1993). *Pompeii: society, urban images and forms of living*. Giulio Einaudi Editore.

Zanni, S., & De Rosa, A. (2019). Remote Sensing Analyses on Sentinel-2 Images: Looking for Roman Roads in Srem Region (Serbia). *Geosciences*.

Zhang, L. Z. (2022). Artificial Intelligence for Remote Sensing Data Analysis: A review of challenges and opportunities. *IEEE Geoscience and Remote Sensing*, 10, 270-294. doi:10.1109/MGRS.2022.3145854

Zhang, W., Qi, J., Wan, P., & Wang, H. (n.d.). Airborne LiDAR Data Filtering Algorithm Based on Cloth Simulation. Beijing Normal University.

Zhang, W., Qi, J., Wan, P., Wang, H., Xie, D., X., W., & Yan, G. (2016). An Easy-to-Use Airborne LiDAR Data Filtering Method Based on Cloth Simulation. *Remote Sensing*.

Zhao, Q., & Qu, Y. (2024). The Retrieval of Ground NDVI (Normalized Difference Vegetation Index) Data Consistent with Remote-Sensing Observations. *Remote Sensing* 16. doi:<https://doi.org/10.3390/rs16071212>